

**Shedding light on the nanoscale  
carrier dynamics and photogeneration in Quantum Dot systems**

Grimaldi, Gianluca

**DOI**

[10.4233/uuid:24aacb0a-1903-4b7e-8e8a-484bffcba12](https://doi.org/10.4233/uuid:24aacb0a-1903-4b7e-8e8a-484bffcba12)

**Publication date**

2019

**Document Version**

Final published version

**Citation (APA)**

Grimaldi, G. (2019). *Shedding light on the nanoscale: carrier dynamics and photogeneration in Quantum Dot systems*. [Dissertation (TU Delft), Delft University of Technology].  
<https://doi.org/10.4233/uuid:24aacb0a-1903-4b7e-8e8a-484bffcba12>

**Important note**

To cite this publication, please use the final published version (if applicable).  
Please check the document version above.

**Copyright**

Other than for strictly personal use, it is not permitted to download, forward or distribute the text or part of it, without the consent of the author(s) and/or copyright holder(s), unless the work is under an open content license such as Creative Commons.

**Takedown policy**

Please contact us and provide details if you believe this document breaches copyrights.  
We will remove access to the work immediately and investigate your claim.

Shedding light on the nanoscale:  
carrier dynamics and photogeneration  
in Quantum Dot systems

Gianluca Grimaldi



# Shedding light on the nanoscale: carrier dynamics and photogeneration in Quantum Dot systems

Proefschrift

ter verkrijging van de graad van doctor  
aan de Technische Universiteit Delft,  
op gezag van de Rector Magnificus prof.dr.ir. T.H.J.J. van der Hagen,  
voorzitter van het College voor Promoties,

in het openbaar te verdedigen op  
maandag 14 oktober 2019 om 10:00 uur

door

Gianluca GRIMALDI

Master of Science in Physics  
University of Milano-Bicocca, Italië  
geboren te Chicago, Verenigde Staten

Dit proefschrift is goedgekeurd door de promotoren.

Dr. A. J. Houtepen  
Prof. dr. L. D. A. Siebbeles

Samenstelling promotiecommissie bestaat uit:

Rector magnificus,	voorzitter
Dr. A. J. Houtepen	Technische Universiteit Delft, promotor
Prof. dr. L. D. A. Siebbeles	Technische Universiteit Delft, promotor

Onafhankelijke leden:

Prof.dr.ir. P. Geiregat	Universiteit Gent, België
Dr. B. Ehrler	AMOLF, Research Inst.
Prof.dr. A.F. Otte	Technische Universiteit Delft
Prof.dr. A. Meijerink	Universiteit Utrecht
Prof.dr. P. Dorenbos	Technische Universiteit Delft

This work received financial support from the Stichting voor de Technische Wetenschappen (STW), within the project “Stable and Non-Toxic Nanocrystal Solar Cells” (no. 13903).





# Table of contents

---

<b>Chapter 1</b> - Introduction	1
<b>Chapter 2</b> - Hot-electron transfer in quantum-dot heterojunction films	27
<b>Chapter 3</b> - Engineering the band-alignment in QD heterojunction films <i>via</i> ligand exchange	61
<b>Chapter 4</b> - Model to Determine a Distinct Rate Constant for Carrier Multiplication from Experiments	89
<b>Chapter 5</b> - Spectroscopic evidence for the contribution of holes to the bleach of Cd-chalcogenide quantum dots	109
<b>Chapter 6</b> - Kinetic Monte Carlo modeling of temperature dependent spectral diffusion in InP QD films	147
<b>Summary</b>	173
<b>Samenvatting</b>	177
<b>List of publications</b>	181
<b>Acknowledgments</b>	185
<b>Curriculum Vitae</b>	191



# Chapter 1

---

## Introduction

*"Maar ik maak steeds wat ik nog niet kan om het te leren kunnen."*

*"But I keep on making what I can't do yet, in order to learn to be able to do it."*

- Vincent Van Gogh, "Aan Anthon van Rappard", brief (letter)

**1****1.1 Introduction to the nanoscale**

This thesis has a measurable size, a measurable thickness, and a measurable weight. If the readers throw this thesis away, they can set it in motion with any speed they like, from the gentlest touch to the hardest push their arms allow. Whether it's flying away or sitting still on a desk, it's position can be satisfyingly determined, with an accuracy seemingly limited by one's commitment to perform a precise measurement.

These properties set this thesis squarely in the realm of macroscopic objects, the objects known to our senses. Objects belonging to this category have dimensions, mass and speed which are not extremely different from the dimensions, mass and speed typically possessed by our own human bodies. From Newton's discovery of the laws of motion to the beginning of the 20th century, scientists have developed a remarkably accurate description for the motion of macroscopic objects in the presence of external forces, developing a scientific toolset collectively known as "classical physics". Although the prediction of classical physics can be challenging to compute, their interpretations are deeply rooted in our intuitive picture of the world, quantitatively attributing to the fundamental components of the world the same properties we can qualitatively attribute to balls or PhD theses.

Despite its success in the description of the macroscopic world, applying a classical interpretation to the behavior of atoms, subatomic particles and electrons produces paradoxical answers. The observation that atoms absorb radiation only in precise amount, called "quanta", opened the floodgates for the discovery of a class of atomic and sub-atomic phenomena irreconcilable with classical phenomena. The interpretation of these phenomena built the foundation of the theory called "quantum mechanics", allowing extremely precise predictions of particle behavior, while departing from an intuitive picture of reality.

Nanomaterials, whose scale is in the order of  $10^{-9}$  m, are intermediate between the macroscopic and the atomic world. Electrons inside nanometer-sized objects can be delocalized over the whole object, and yet have properties similar to those of electrons confined inside atoms: they develop a discrete series of allowed energy levels. Quantum effects dominate the electronic behavior of these objects, and yet they can be assembled into large-scale films, centimeters-wide, giving rise to macroscopic properties that depend on the nanoscale size of the objects. Nanoscale systems offer unique opportunities to observe quantum mechanical properties and to exploit them in real-world device, providing answers for the large societal challenges that we need to face in the energy transition.

But before we dive into the quantum properties of nanomaterials, let's first quickly look at a particular class of solids, i.e. semiconductors, and at what happens when a macroscopic semiconductor absorbs light.

**1.2 Photoexcitation in bulk semiconductors**

In an infinitely extended crystal, electrons are delocalized over the whole system and their wavefunction is given by:

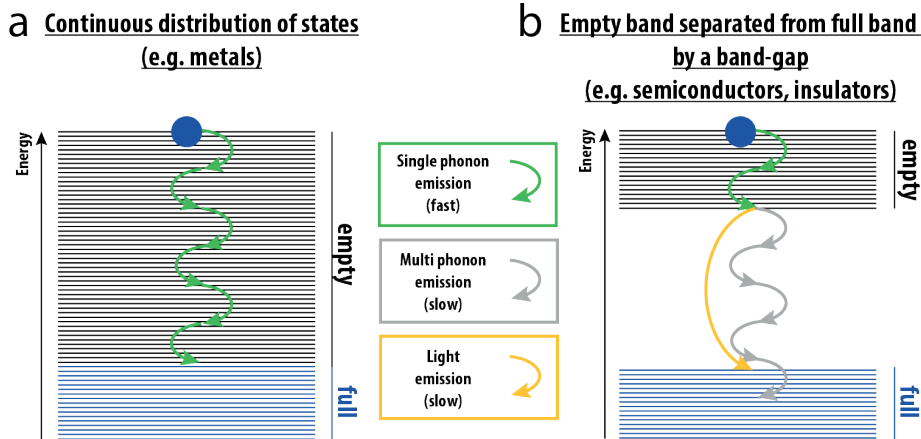


**Figure 1.1.** **a**, Schematics of electron relaxation through a continuous distribution of energy states. Single phonon emission causes the electron to quickly perform small ( $\leq 20$  meV) energy relaxation steps, allowing the system to return to its ground-state in a sub-ps time-scale. **b**, Schematics of electron relaxation through a distribution of energy states with a band-gap separating the empty states (conduction band) from the full states (valence band). Once the electron reaches the conduction band edge, single phonon emission cannot bridge the energy gap with the first lower energy state, and further relaxation requires either multi-phonon emission or light emission, both occurring on a longer time-scale.

$$\psi(\vec{r}) = u_{\vec{k}}(\vec{r})e^{i\vec{k}\vec{r}} \quad 1.1$$

where  $u_{\vec{k}}(\vec{r})$  is a function with the same periodicity as the crystal, and  $e^{i\vec{k}\vec{r}}$  is a running wave with crystal momentum  $\vec{k}$ . The presence of the periodic potential induces the formation of energy bands, allowed energy ranges separated from each other by gaps of forbidden energies. Semiconductors are characterized by the presence of a completely full band (valence band) separated from an empty band (conduction band) by a gap of forbidden energies (band-gap) that is not too large (typically between 0.5 and 3 eV).

The presence of this modest bandgap confers semiconductors peculiar optoelectronic properties. In a continuous, unbroken energy distribution, electrons promoted to higher energy levels by the absorption of a photon quickly lose energy via interaction with vibrational mode of the material, returning to their unexcited state in a 100 fs – 1 ps timescale. The emission of a single phonon in a vibrational mode subtracts a small amount of energy ( $\leq 20$  meV) from the electron, and repeated phonon emission allows the electron to efficiently relax through the continuous density of state (See Figure 1.1a).

The band-gap slows down electronic relaxation significantly. To dissipate the energy produced by the relaxation of the electron over the band-gap, multiple phonon-emission events need to happen to simultaneously, decreasing the likelihood of the relaxation event. Consequently, photoexcitation of semiconductors leads to rapid relaxation of electrons

## 1



**Figure 1.2.** **a**, TEM micrograph of a QD sample. The inset show a 3D representation of a single QDs capped with oleate ligands. **b**, Picture showing the effect of QD size on the color of QD solutions, due to the shift in the wavelength of the first absorption feature. **c**, Absorption spectra of different sizes of QDs.

and holes towards the band-edges (intraband relaxation), followed by a much slower interband relaxation, mediate by multi-phonon emission or by the emission of light (See Figure 1.1b).

### 1.3 Quantum Dots: an overview

Quantum Dots (QDs) are a class of semiconductor nanoparticles in which the electronic properties are strongly influenced by the size of the particle, an effect called quantum confinement. Colloidal QDs are synthesized via solution-based methods, typically via hot-injection synthesis<sup>1</sup>. In this synthesis, a QD precursor is rapidly injected into a flask containing a hot solution of the second QD precursor as well as ligands that bind both to the precursors and the QD surface, leading to a burst of formation of small QD nuclei. After the nucleation burst, the concentration of the QD precursors in solution drops, preventing further nucleation but allowing the growth of the existing nuclei. After the reaction is completed, QDs are suspended in the reaction mixture, together with unwanted reaction by-products. The QDs can be purified via precipitation, adding an antisolvent and centrifuging the mixture, until the precipitated QDs form a pellet on the bottom of the centrifuging vial, from which they can be re-dispersed in a suitable solvent.

The solution-based synthesis of QD samples allows facile QD assembly into QD solids, that can be obtained via solution-based methods such as dropcasting, spin-coating or dip-coating. The ligands on the surface of the QDs can be exchanged for stronger binding ligands, immersing the QD solid into an anti-solvent containing the desired new ligand. The film fabrication process leads to the formation of a QD solid, whose level of disorder varies depending on the fabrication conditions<sup>2-5</sup>. The QD film fabrication process does not require the high-temperatures and high-vacuum conditions required for epitaxial growth techniques, and can therefore be adopted for deposition on large scale surface.

QDs are characterized by a strong absorption cross section and by a sharp emission feature at the band-gap energy, that increases in energy as the QD size get smaller (quantum-size-effect). Their excellent thermal- and photo-stability give QDs an advantage over molecular emitters for applications in light emitting devices.

## 1.4 Quantum Dots: a (simple) physicist's picture

What happens if the delocalized electron states found in bulk crystals are confined into a finite volume? The simplest model showing the effects of confinement on the energy and wavefunction of a particle is the particle-in-a-box model.

In a spherical potential-well of radius  $R$  with infinite barriers, the Schrödinger equation for the particle is given by:

$$H\psi(\vec{r}) = \frac{p^2}{2m}\psi(\vec{r}) + V(r)\psi(\vec{r}) = HE\psi(\vec{r}) \quad 1.2$$

where  $m$  is the mass of the particle,  $p$  is the momentum operator and  $V$  the potential experienced by the particle. In spherical coordinates, the momentum operator can be expanded as:

$$p^2 = -\hbar^2 \left( \frac{\partial^2}{\partial r^2} + \frac{2}{r} \frac{\partial}{\partial r} - \frac{L^2}{r^2 \hbar^2} \right) \quad 1.3$$

Each term in the Hamiltonian depends either on the radial coordinate alone or on the total angular momentum operator  $L^2$ . The operators  $L^2$  and  $L_z$  (projection of the total angular momentum along a fixed axis) act only on the angular coordinates, and consequently commute with the terms containing only the radial coordinate. Furthermore,  $L_z$  commutes with  $L^2$ , and thus with the entire Hamiltonian, implying that it is possible to find solutions of eq. 1.2 that are simultaneously eigenfunctions of the two angular momentum operators. Thus, the wavefunctions for the particle can be written as:

$$\psi(\vec{r}) = f(r)Y_{lm}(\vartheta, \varphi) \quad 1.4$$

where  $Y_{lm}(\theta, \varphi)$  are spherical harmonics. Substituting eq. 1.3-1.4 in eq. 1.2 leads to:

$$-\frac{\hbar^2}{2m} \left( \frac{\partial^2}{\partial r^2} + \frac{2}{r} \frac{\partial}{\partial r} - \frac{l(l+1)}{r^2} \right) f(r) + V(r)f(r) = Ef(r) \quad 1.5$$

Taking the potential inside the sphere equal to zero, eq. 1.5 becomes the spherical Bessel differential equation, and the full wavefunction inside the sphere can be expressed as:

$$\psi(\vec{r}) = j_l(kr)Y_{lm}(\vartheta, \varphi) \quad 1.6$$

where  $k = \sqrt{2mE/\hbar^2}$  is the wavevector of the particle and  $j_l$  is the spherical Bessel function of the first kind. Imposing that the potential goes to zero at the edge of the sphere (impenetrable potential wall), the allowed wavevector values are determined by:

$$kR = z_{n,l} \quad 1.7$$

where  $z_{n,l}$  is the  $n$ -th zero of the  $j_l$  function. Consequently, the energy eigenvalues are determined via:

$$E = \frac{\hbar^2 k^2}{2m} = \frac{\hbar^2 z_{n,l}^2}{2mR^2} \quad 1.8$$

The function  $z_{n,l}$  increases as a function of the indices  $n$  and  $l$ . For  $l=0$  (nS wavefunctions), the allowed energies are given by:

$$E = \frac{\hbar^2 \pi^2 n^2}{2mR^2} \quad 1.9$$

Examining the allowed energy values, it can be noticed that:

Although the particle-in-a-box model is extremely simplified, it captures the most important features of zero-dimensional systems: the size-dependence of the energy levels and the presence of a discrete distribution of allowed states.

The potential experienced by electrons inside a QD is very different from potential of the particle-in-a-box model, varying strongly as a function of the position, as electrons are attracted to the atomic cores and are repelled by the other electrons. However, the particle-in-a-box model can be used to give a surprisingly effective description of the qualitative features of the properties of photoexcited QDs.

Upon photoexcitation, the excited electron and hole attract each other, while their electric field polarizes the crystal. In the effective mass approximation, the behavior of the interacting pair, called exciton, can be described by the Hamiltonian:

$$H = -\frac{\hbar^2}{2m_e} \nabla_e^2 - \frac{\hbar^2}{2m_h} \nabla_h^2 - \frac{e^2}{4\pi\epsilon\epsilon_0 |\vec{r}_e - \vec{r}_h|} + V_{e,self} + V_{h,self} + V_{eh,cross} \quad 1.10$$

where  $m_{e/h}$  is the effective mass of the electron/hole,  $\vec{r}_{e/h}$  the position of the electron/hole, and  $\epsilon$  is the dielectric function of the QD.  $V_{e/h,self}$  is the self-polarization term, the potential energy resulting from the interaction of a charge with the polarization induced by the same charge.  $V_{eh,cross}$  is the cross-polarization term, resulting from the interaction of each carrier with the polarization produced by the other carrier<sup>6</sup>. In the limit of strong confinement, in which the energy associated to the confined motion of the carriers dominates over their electrostatic interaction, the ground-state wavefunction for the electron-hole pair in the QD can be expressed as a product of two uncorrelated electron and hole wavefunctions, ground-state solutions of the Schrödinger equation for a particle of mass  $m_{e/h}$  inside a spherical potential well with infinite barriers:

$$\psi_{eh}(\vec{r}_e, \vec{r}_h) = \phi_e(\vec{r}_e) \phi_h(\vec{r}_h) \quad 1.11$$

$$\phi(\vec{r}) = j_1(kr) Y_{0,0}(\theta, \varphi) \quad 1.12$$

Evaluating the expectation values of the Hamiltonian in eq. 1.10 on the wavefunctions in eq. 1.11, leads to an approximation for the ground-state energy of the exciton inside the QD, called Brus equation<sup>6</sup>:

$$E_{ex} = E_g + \frac{\hbar^2 \pi^2}{2R^2} \left( \frac{1}{m_e} + \frac{1}{m_h} \right) - 1.8 \frac{e^2}{4\pi\epsilon\epsilon_0 R} + E_{cross} + E_{self} \quad 1.13$$

The excitonic energy levels predicted by Brus equation capture qualitatively the size-dependence of the band-edge absorption energy observed experimentally for QD samples<sup>1</sup> (See Figure 1.2c).

## 1.5 Quantum Dots: band-edge bleach

A large fraction of this thesis is devoted to measuring changes in the absorption of QDs upon light absorption, from which it is possible to obtain a large amount of information about the distribution of energy states and the dynamics of electrons populating those states.

1. Unlike the continuous distribution of energy values that a free particle can take, inside the box the particle can take only discrete values.
2. The lowest energy for the particle, corresponding to the indices  $n=1$  and  $l=0$ , is higher than the potential value inside the box ( $V=0$ ). This energy increase is called the ground-state confinement energy.
3. The ground-state confinement energy increases quadratically as the size of the box decreases.

To see how changes in the absorption can be related to the electronic population of the QD states, let's consider the results of the previous section on the nature of QD states. The discrete nature of the QD states leads to strong non-linearity of the band-gap absorption, as the presence of photoexcited carriers significantly decreases the number of available band-edge states, thus decreasing the band-gap absorption cross-section. Assuming that each transition from a valence band edge to a conduction band edge state has the same oscillator strength, that the transitions properties (energy, oscillator strength) are independent of the carrier population, and momentarily assuming that the transitions are independent on the electron spin state, the band-gap absorbance can be expressed as:

$$A_0 = A^* g_e g_h \quad 1.14$$

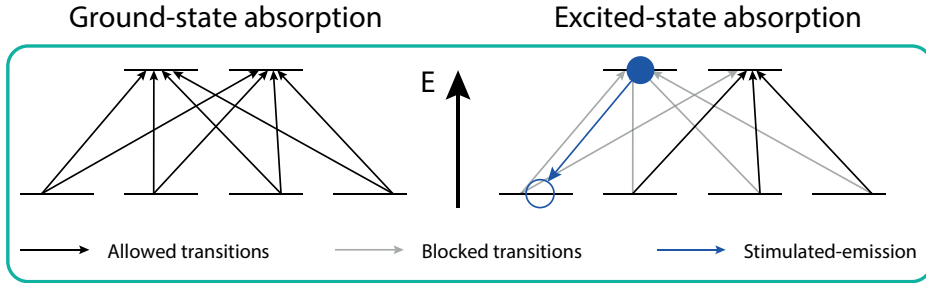


**Figure 1.3.** Scheme of the possible optical transitions between a full and an empty electronic level, both discrete and with finite degeneracy, represented by the number of horizontal lines at the same energy. The left part of the scheme shows the absorption transitions possible in the unexcited system, while the left side shows the effect of an excited electron and an exciton hole on the absorption. The excited species reduce the amount of absorption transitions possible, while allowing stimulated emission to occur, further decreasing the absorption.

where  $A^*$  is the absorbance of of each transition,  $g_e$  is the degeneracy of the conduction band-edge state, and  $g_h$  is the degeneracy of the valence band-edge state. When an excited electron or hole is added to the band-edge, all the absorption transitions involving the occupied state are blocked, since Pauli-exclusion principle prevents placing two electrons in the same quantum state (state-filling). Furthermore, if both electrons and holes are present at the band-edge, the light at band-gap energy that interacts with the system can stimulate the emission of another photon, identical to the incoming photon, via the radiative recombination of an electron-hole pair. The process, called stimulated emission occurs with the same efficiency as the absorption process, and is accounted in the total absorbance via a negative absorption transition (as it increases the transmittance through the system).

Thus, in presence of  $n \leq \max(g_e, g_h)$  photoexcited electron-hole pairs, the excited state absorbance will be given by:

$$A' = A^* (g_e - n)(g_h - n) - A^* n^2 \quad 1.15$$

The fractional difference between the excited state absorbance and the steady-state absorbance, is given by:

$$\Delta A / A_0 = -n \frac{g_e + g_h}{g_e g_h} \quad 1.16$$

This result implies that the band-gap absorbance in the presence of photoexcited carriers decreases proportionally to the number of electron-hole pairs, reaching a fraction of the steady-state absorbance determined by the degeneracy of the band-edge states. The decrease in intensity of an absorption transition due to the presence of photoexcited carriers in the initial or final state is called “absorption bleach”.

The differential absorbance  $\Delta A$  resulting from photoexcitation can be determined in a transient absorption (TA) measurement. Measuring TA on QD samples reveals the presence of a band-gap bleach, developing after photoexcitation, proportional to the absorbed photon fluence. According to eq. 1.16, the time-dependence of the band-gap bleach reflects the time-dependence of the carriers in the band-edge states, and can be used to obtain information about the dynamics of the photoexcited carriers.

Furthermore, understanding the behavior of the differential absorbance in QD samples has important consequences for lasing applications. When the band-edge bleach exceeds the steady-state absorption, shining light on the sample leads to the emission of additional light. This behavior, called optical gain, is required to achieve lasing, and its onset as a function of the carrier population can be determined via TA or spectroelectrochemical measurements on the QD samples<sup>7-8</sup>.

In equation 1.16, both electrons and holes contribute to decrease the band-edge absorbance. However, in cadmium chalcogenide QDs samples, the band-edge bleach is attributed entirely to the presence of photoexcited electrons, neglecting any contribution from photoexcited holes. Despite the lack of consensus on the reason for the apparent absence of a hole contribution to the bleach, this assumption has been commonly used to interpret TA results on cadmium chalcogenide QD samples. However, the presence of efficient optical gain in samples of CdSe QDs suggest a significant hole contribution to the bleach, and increased understanding of the relationship between band-edge bleach and density of excited carriers is required to model the onset of optical gain in QD samples (see Chapter 5: Hole contribution to the bleach of cadmium chalcogenide quantum dots).

## 1.6 Quantum Dots: plenty of room at surface

In the naïve QD description outlined in the previous sections, the surface of the QD acts primarily as a boundary, after which core wavefunctions decay into vacuum. However, from the early days of QD spectroscopy it was clear that QD surfaces play a very big role in the determination of the properties of QD samples, crucially determining the presence of trap states<sup>9-14</sup>, the characteristic of the vibrational modes in the QD system (both core and surface)<sup>15-18</sup>, the electron affinity<sup>19-23</sup>, and the position of the Fermi level<sup>2, 23-25</sup>. In the current state of QD research, selecting appropriate surface passivation is a fundamental step in the fabrication of QD samples with the required properties. The pivotal role played by QD surfaces can be easily understood looking at the fraction of all the atoms in a QD that reside on the surface. For a 5 nm CdSe QD, approximately 35% of the atoms are on the surface, and the percentage increases for smaller QDs.

In recent years, increased control of surface passivation techniques has allowed remarkable increases in sample quality, and unlocked new properties. Saturation of surface-localized traps, achieved by targeted binding of Z-type ligands increases dramatically the photoluminescence quantum yield of II-VI and III-V QDs<sup>13</sup>. Similar effects can be achieved filling trap states electrochemically, which does not remove the trap states but prevents photoexcited species to relax into them. Electrochemical control over the degree of trap filling allows to tune the involvement of trap states in the photoluminescence

## 1

process<sup>26-28</sup> or allowing charge transfer to occur between different QD species<sup>29</sup>. Changes in the chemical species present at the QD surface have been found to significantly affect the rigidity of the QD structure, affecting the intensity of electron-phonon coupling<sup>17</sup>.

Furthermore, the control over the chemical species bound on the QD surface can be used to tune the band-alignment in QD systems. Brown et al. demonstrated the possibility to control the electron affinity in PbS QD sample by variation of the ligands on the QD surface<sup>20</sup>. In the following years, various reports have shown the extent of the ligand-shift control over electron affinities<sup>21-23, 30</sup> and electron band-gaps<sup>31-33</sup>, and ligand exchange strategies have been employed to control the energy alignment in QD homojunctions<sup>21, 30</sup>. These effects add new possibility to the already remarkable degree of energy control of QD systems, potentially allowing full control over the energetics of QD-based heterostructures (See Chapter 3: “Band-alignment engineering in CdSe-PbSe QD heterojunction film via ligand-exchange”).

## 1.7 Quantum Dot Heterostructures

Most optoelectronic devices rely on the ability of semiconductor heterostructures to engineer the behavior of electrical carriers, spatially separating carriers of opposite charge or concentrating them in the same region, increasing the chances of recombination.

Core-shell heterostructures have had a tremendous impact on the QD field, both for fundamental studies<sup>34-35</sup> and for practical applications<sup>7, 36-37</sup>. They are formed when a semiconductor QD core is surrounded by a concentric layer of a different material, called shell (Figure 1.4a).

The most wide-spread use of core-shell heterostructure consist in the choice of a large band-gap shell material in a type-I alignment with the core band-gap, i.e. the lower band-gap is contained within the larger band-gap (Figure 1.4a). This energy structure confines any excited carriers to the QD core, preventing interactions with the external surface. At the same time, the shell material passivates the states at the surface of the core, effectively cleaning the materials band-gap from localized trap states. Because of the high degree of overlap between the electron and hole wavefunction maintained in the heterostructure, and the suppression of trapping processes, type-I core-shell can greatly enhance the photoluminescence efficiency of the core material, up to unity values for the quantum yield<sup>38-39</sup>. Furthermore, the fabrication of graded type-I shells, whose composition vary gradually from the core interface to the shell's surface, have been shown to suppress the rate of Auger recombination, allowing long multiexcitonic lifetimes and high biexcitonic photoluminescence quantum yield<sup>39-42</sup>.

The photoluminescence enhancement, defect passivation and Auger suppression associated with type-I core-shell QDs have allowed efficient QD-based LEDs and efficient lasing in QD films<sup>7, 36-37</sup>. From a fundamental standpoint, suppression of surface-mediated effects allows to study the carrier dynamics of the intrinsic core states, potentially obscured by the presence of fast trapping processes in unpassivated samples (see Chapter 5, Hole contribution to the bleach of cadmium chalcogenide quantum dots).

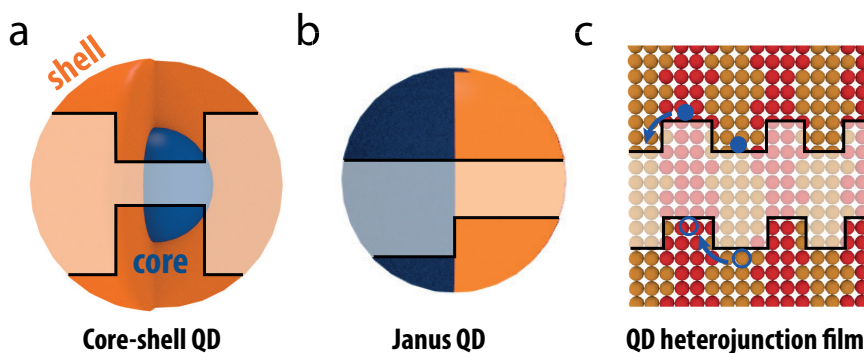


**Figure 1.4.** a, Scheme of a type-I energy alignment in a core-shell heterostructure geometry. b, Scheme of a Janus QD with quasi-type-II band-alignment. c, Scheme of a QD heterojunction film with type-II band-alignment.

Beside type-I aligned heterostructures, other energy alignment schemes are possible, enabling different optoelectronic behaviors. Type-II heterostructures are characterized by a staggered band-alignment, occurring when the highest valence band and the lowest conduction band are located in two different materials. This energy alignment leads to the separation of photoexcited electrons and holes, as they relax towards their energy minima in the system. Reduced electron-hole overlap in a type-II heterostructure increases the radiative recombination lifetime of the carriers, while reducing the energy of the emission.

Finally, an energy structure in which two conduction (or valence) bands have the same energy and the other two valence (or conduction) band have different energy is said to be in a quasi-type-II alignment. This alignment structure is characterized by the presence of a wavefunction delocalized over the whole system for the carriers in the aligned bands, while the other carrier type is localized in the lowest band-gap material. Quasi-type-II heterostructures can find use in the optimization of QD-based solar cells, as they can be used to reduce the energy threshold for the carrier multiplication process<sup>43-44</sup> (see Section “QD-based solar cells” in the current Chapter).

In addition to core-shell heterostructures, other heterostructure geometries, such as Janus QDs and QD heterojunction films, can be employed to tailor the behavior of charge carriers in the QD-based systems. Janus QDs are composed of two lobes of different materials, as shown schematically in Fig. 1.4b. As opposed to type-II core-shell structures, in which charge separation localizes one of the two carriers inside the QD core, hampering carrier extraction and thus decreasing its mobility, in type-II Janus structures both carriers interact with the surface and can be extracted from the particle. Kroupa et al. demonstrated the possibility to use quasi-type-II Janus heterostructure to enhance carrier multiplication<sup>44</sup>, exploiting the advantages of the heterostructure while maintaining the possibility to harvest the photo-generated carriers. Similar advantages are offered by QD heterojunction films (Fig. 1.4c), films composed of layers of two different core-only QD materials, coupled by short molecular linker and assembled in alternating layers of the two materials<sup>45-46</sup>. The short inter-QD spacing ensures electronic coupling between adjacent QDs, allowing the formation of a heterojunction even in the absence of

## 1

epitaxial connections between QDs. Talgorn et al. demonstrated the possibility to enhance the photoconductivity of a QD film via charge separation in a type-II QD heterojunction film<sup>45</sup>. Furthermore, the possibility to control the ligands on the surface of each QD species via ligand exchange during the layer-by-layer fabrication provides the possibility to tune the energy alignment between different QD species, via the band-shift caused by ligand-induced surface dipoles (See Section “Quantum Dots: plenty of surface” in the current Chapter, and Chapter 3: “Band-alignment engineering in CdSe-PbSe QD heterojunction film via ligand-exchange”).

## 1.8 Electronic transport in QD solids

One of the reason QDs materials are good candidate for use in optoelectronic devices is the ease in which they can be casted from QD solutions into thin-films, forming QD solids. However, the long ligands passivating the QD surface after synthesis make QD films insulating, limiting their device applications. Substituting the original ligand for shorter ones leads to significant increases in the mobility of both carrier species<sup>47-52</sup>. High carriers mobilities are required for the development of QD-based transistors and solar cells. For the latter, in particular, the probability to collect a photo-generated carrier at an electrode depends on the diffusion length of the carrier, in turn depending on the carrier mobility and on the carrier lifetime. For the same carrier lifetime, samples with higher mobility will be able to collect more photoexcited carriers, thus increasing the efficiency of the device. Consequently, understanding the factors limiting the mobility in QD films remains an important issue.

Electronic transport through QD films is typically described via site-to-site hopping, a thermally activated process, whose rates can be described via the Miller-Abrahams model:

$$k = k_0 \exp(-\beta d) \begin{cases} \exp\left(-\frac{E_2 - E_1}{k_b T}\right), & \text{for } E_2 > E_1 \\ 1, & \text{for } E_1 \geq E_2 \end{cases} \quad 1.17$$

where  $E_2$  is the energy of the final state,  $E_1$  the energy of the initial state,  $\beta$  is an effective barrier length, dependent on the ligands separating the QDs, and  $d$  is the distance between QDs.

An alternative description of charge transfer process in the nanoscale is offered by Marcus theory, developed for transfer of electrons between dielectric spheres and commonly used to describe charge transfer between molecules<sup>53</sup>. In the Marcus model, the rate of electron transfer between different sites can be expressed as:

$$k = \frac{k_0}{\sqrt{TE_\lambda}} e^{-\frac{(\Delta E - E_\lambda)^2}{4k_b TE_\lambda}} \quad 1.18$$

where  $E_\lambda$  is the reorganization energy, the energy required to change the polarization of the environment induced by the charge transfer process, and  $\Delta E$  is the energy difference between the final and the initial state.

Although the Miller-Abrahams model has been used extensively to describe hopping process, Chu et al. showed that the Marcus model can be used to describe carrier transport in QD solids<sup>54</sup>. The two models impose different temperature-dependences for the transfer rates. In particular, equation 1.18 contains a  $T^{-1/2}$  factor, allowing the presence of a temperature range in which hopping rates are temperature de-activated. As such, in considering the presence of temperature de-activated transport in low mobility QD samples, the possibility that the Miller-Abrahams model does not capture the temperature-dependence of hopping rates need to be considered (See Chapter 6: Kinetic Monte-Carlo modeling of temperature dependent mobilities in InP QD films).

The distribution of band-edge carrier energies in QD films is determined by the size distribution of the QDs, as quantum confinement is less strong in larger QDs, leading to lower energy levels, while the smaller, more quantum-confined QDs have higher carrier energies. As carrier hop through a QD film, they tend to move more efficiently to the lower energy site (upward energy jump in eq. 1.17), implying preferential occupation of the larger QDs. In conductive QD solids, carrier funneling into the larger QDs increases the impact of Auger recombination on carrier lifetime, as multiexcitons are formed into the larger QDs even at moderate fluences<sup>55</sup>. The effect of the shift of the carrier populations towards the larger QDs can be observed optically, monitoring the energy of the QD band-edge bleach, induced by the presence of carriers at the QD band-edges (see Section “Quantum Dots: band-edge bleach” of the current Chapter). As carrier move to lower energies, the bleach of the high band-gap part of the QD population decreases, while the bleach of the low band-gap part of the QD population increases, resulting in a shift in average bleach towards lower energies (red-shift). Comparison of the time-dependent red-shift of the band-edge bleach, which can be obtained via transient absorption measurements, with simulations of carrier hopping with Miller-Abrahams rates allows to extract estimates for the hopping rates and the diffusion coefficient associated with the hopping process<sup>56-57</sup>. Diffusion coefficient and carrier mobility are related via Einstein-Smoluchowski equation:

$$D = \frac{k_b T}{e} \mu \quad 1.18$$

where  $D$  is the diffusion coefficient and  $\mu$  the mobility.

With increasing mobility reported for ligand exchanged QD films (up to tens of  $\text{cm}^2/(\text{Vs})$ ), some reports have suggested the presence of band-like transport in QD solids, inferred from the presence of a temperature de-activated mobility regime<sup>51, 58-59</sup>. Gilmore et al. have reported a similar temperature de-activate behavior in QD films with lower carrier mobility, although they attributed the effect to a temperature-induced contraction of the interparticle distance. Shedding light on the temperature dependence of carrier mobility in QD films could provide valuable insights on the nature of the electronic motion in these systems, aiding in the improvement of the performances of QD films (see Chapter

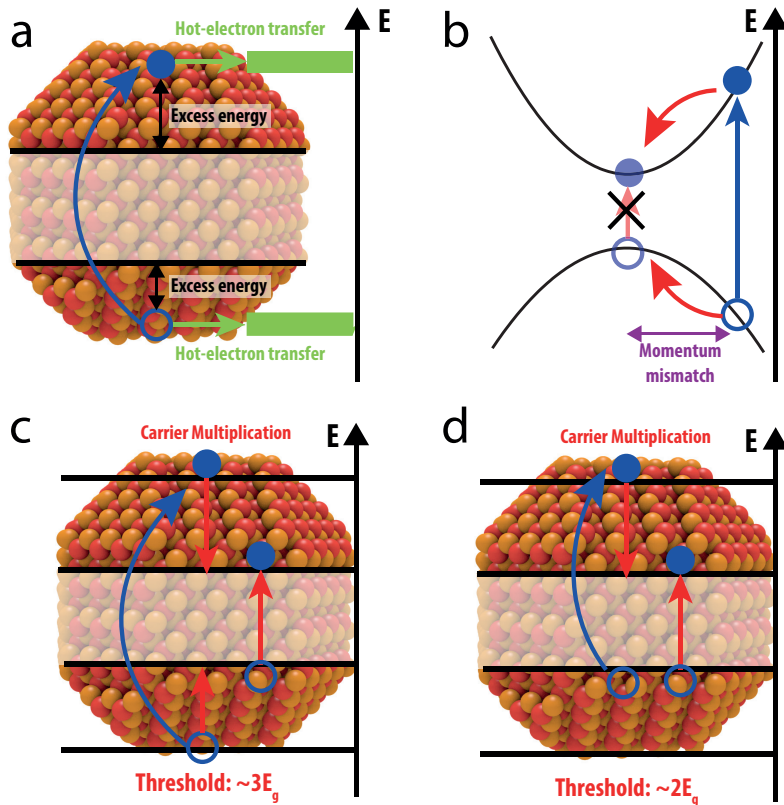


**Figure 1.5.** a, Energy scheme representing the hot-electron transfer process. b, Energy scheme, highlighting how carrier multiplication is hampered by the momentum mismatch between the high-energy and the low-energy state. c-d, Energy scheme, depicting carrier multiplication for symmetric (c) and asymmetric (d) excitation.

6: Kinetic Monte-Carlo modeling of temperature dependent mobilities in InP QD films).

## 1.9 QD-based solar cells

The design of the next generation of solar cells is centered around the ability to convert an increasing fraction of the solar power incident on the cell into an external current. This result can be achieved via different routes, and solar cell concepts have been proposed to eliminate channels for efficiency losses. In particular, QD have been suggested as a material candidate for next generation solar cell concepts exploiting carrier multiplication or hot-electron transfer.

### 1.9.1 Hot-electron transfer

In traditional solar cells, the largest source of losses is due to carrier thermalization<sup>60</sup>. When photons with an energy higher than the band-gap of the solar cell are absorbed, they produce carriers above (or below) the band-edge position. The energy difference

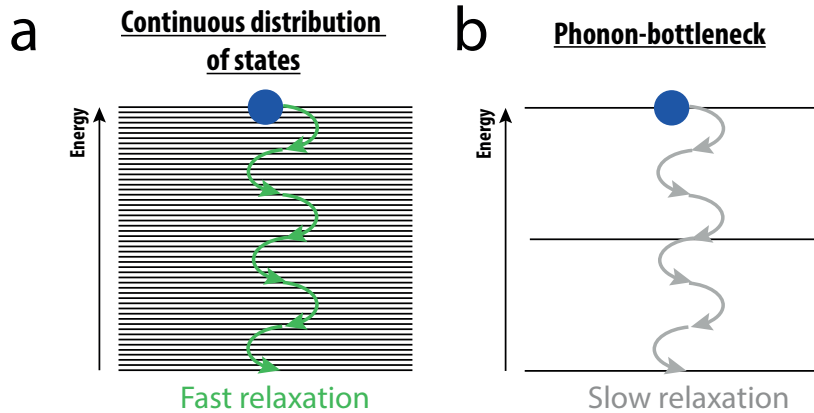


**Figure 1.6.** Schematics of electron relaxation in a continuous distribution of energy states (a) and in the presence of a phonon-bottleneck (b). While for a continuous distribution of states single phonon emission events allow efficient electron cooling, in the presence of a phonon-bottleneck multiple-phonon events are needed to progress cooling further.

between the initial carrier energy and its band-edge is called excess energy, and the sum of the two excess energies is equal to the difference between the photon energy and the material band-gap (Fig. 1.5a). This excess energy is rapidly transferred from the carriers to lattice vibrations (i.e. is dispersed as heat), thus reducing the output power of the cell. In addition, the resulting increase in the temperature of the system has additional deleterious effects on the performance of solar cells, including changes in the material band-gap and increased thermodynamic losses<sup>60</sup>.

One of the solar cell concepts put forward to circumvent thermalization losses is the hot-electron solar cell. In a hot-electron solar cell, high-energy carriers are efficiently extracted by energy selective contacts (hot-electron transfer), preventing their thermalization. However, efficient hot-electron transfer alone is not sufficient to provide any improvement in solar cell performance. In fact, a solar cell whose contacts extract high-energy electrons would be prevented from extracting the lower energy ones, and would behave similarly to a higher band-gap solar cell with a high-density of trap states in the band gap. However, if efficient carrier-carrier interactions are present, after the extraction of a high-energy carrier, cold carriers are quickly scattered into the higher excess energy states. If both carrier-extraction and carrier-carrier interaction are faster than carrier thermalization, a steady stream of high energy carriers are extracted from the system, potentially increasing the maximum power conversion efficiency from 33% to 66%.

In the past, semiconductor QD have been proposed as material platform for the efficient use of hot-electrons. In QDs, quantum confinement spreads the bulk density of states into a discrete set of energy levels, whose separation increases as the size of the QD decreases. If the energy difference between two neighboring energy states becomes larger than the phonon energies in the system, more than a single phonon is necessary to mediate the relaxation process, leading to a decrease in the cooling rate. This process,

## 1

called phonon-bottleneck, could slow down thermalization in a hot-electron solar cell architecture, benefiting the competing processes (carrier extraction and carrier-carrier scattering). However, despite reports suggesting the presence of a phonon-bottleneck in QDs<sup>61-64</sup>, typical carrier relaxation processes in QD samples occur on the same timescale as in bulk materials<sup>65-70</sup>. Phonon-bottlenecks can be circumvented via the presence of Auger-mediated cooling<sup>71-72</sup>, efficient multiphonon emission<sup>17,66</sup>, and via the contributions of surface-related effects<sup>65,73</sup>.

Despite the lack of a clear phonon-bottleneck in most QD materials, the size-dependence of their energy levels is a valuable resource in the energetic fine-tuning required for the energy-selective contacts, and the presence of hot-electron transfer between different QD components shows that a QD heterostructure satisfies one of the conditions required for a functioning hot-electron solar cell (see Chapter 2: “Hot-electron transfer in QD heterojunction films”).

### 1.9.2 Carrier Multiplication

In the carrier multiplication (CM) process, a high-energy electron-hole pair scatters with valence band electrons, cooling to the band-edges and creating additional electron-hole pairs as a result<sup>74-77</sup>. The effect enables to use the energy of the high-energy photons to increase the photocurrent, preventing losses due to carrier thermalization<sup>75-76,78</sup>. The CM process is the inverse of the Auger recombination process, in which an electron-hole pair recombines promoting a spectator charge to higher energy. The two processes share the same matrix element, as they differ only by a reversal of the initial and final state. In bulk materials, momentum conservation makes both Auger and CM processes inefficient<sup>79-80</sup>, as depicted in Figure 1.5b. As the momentum operator is related with translation of the physical system, momentum conservation is valid only in systems with translation symmetry, and does not hold for QDs. Breaking of momentum conservation increases the rate of the Auger and CM processes.

Since CM originates from high-energy carriers, it competes with phonon-mediated cooling, which removes energy from the electron-hole pair releasing it as lattice vibrations. As in the case of hot-electron transfer, the presence of a phonon-bottleneck for electronic cooling in QDs would increase CM efficiencies, allowing CM to outcompete the phonon emission.

The impact of CM on solar cell performances depends strongly on the efficiency of the CM process and on the energy onset of the process, i.e. the minimum photon energy required to obtain CM. Modeling of solar cell efficiencies in the presence of CM revealed the importance of having the lowest CM threshold possible<sup>81</sup>. Since energy needs to be conserved in the process, the minimum photon energy allowing the production of two electron-hole pairs via CM is equal to twice the material band-gap. On the other hand, if the energy of the photon is distributed equally between the photoexcited electron and hole, to undergo carrier multiplication each carrier needs to have an energy distance from its band-edge equal to the band-gap, as depicted in Figure 1.5c. Thus, symmetric excitation leads to a CM onset of  $3E_g$ , and an asymmetry in the distribution of the initial photon energy is required to shift the CM onset towards  $2E_g$ <sup>80</sup>. While a CM threshold of  $3E_g$  leads to only minor increases in the maximum power-conversion efficiency of a solar cell, lowering the onset leads to a sharp increase. In the presence of step-like (no

thermalization losses) CM with a threshold at  $2E_g$ , the maximum power-conversion efficiency is increased from 33% to 42%.

Asymmetric energy distribution might be achieved via the presence of optical transitions involving a band-edge state and a state inside one of the bands<sup>80</sup> (Figure 1.5d). Alternatively, instead of relying on the presence of appropriately positioned transitions in a material's band-structure, it is possible to engineer custom energy structures via the use of heterojunctions<sup>43</sup>. In a quasi-type-II heterojunction, excitations of the high band-gap material deliver one of the two carriers at the band-edge of the whole system, while the other carrier can lower its energy transferring to the lower band-gap material, possibly undergoing CM in the process. Heterojunction enhancement of CM efficiency has been demonstrated by Cirloganu et al. for core-shell QDs<sup>43</sup>, opening the possibility to substantially increase the impact of CM on the performance of QD-based solar cells.

## 1.10 Thesis outline

This work stems from an attempt to increase the understanding of charge transfer, carrier transport and carrier photogeneration in QD films.

In Chapter 2 we demonstrate the presence of hot-electron transfer occurring between two different QD species in a QD heterojunction film. In Chapter 3 we examine the effect of ligand-induced energy shift on the band-alignment of the two QD species characterized in Chapter 2, showing a shift from a type-I to type-II energy alignment. In Chapter 4 we present a model for the extraction of carrier multiplication rate from carrier multiplication yield measurements and carrier cooling times, allowing the first experimental determination of carrier multiplication rates. In Chapter 5 we present evidence for the contribution of holes to the band-edge bleach of cadmium chalcogenides QDs, demonstrating that their contribution becomes appreciable for passivated samples. In Chapter 6 we present the results of Kinetic Monte-Carlo modeling of spectral shifts in conductive InP QD films, obtained as a function of temperature, revealing the presence of a temperature deactivated mobility-regime and analyzing its causes.

## References

1. Murray, C. B.; Norris, D. J.; Bawendi, M. G., Synthesis and Characterization of Nearly Monodisperse CdE (E = S, Se, Te) Semiconductor Nanocrystallites. *J. Am. Chem. Soc.* 1993, 115, 8706-8715.
2. Luther, J. M.; Law, M.; Song, Q.; Perkins, C. L.; Beard, M. C.; Nozik, A. J., Structural, optical and electrical properties of self-assembled films of PbSe nanocrystals treated with 1,2-ethanedithiol. *ACS Nano* 2008, 2 (2), 271-280.
3. Evers, W. H.; Goris, B.; Bals, S.; Casavola, M.; de Graaf, J.; van Rooij, R.; Dijkstra, M.; Vanmaekelbergh, D., Low-dimensional semiconductor superlattices formed by geometric control over nanocrystal attachment. *Nano Lett* 2013, 13 (6), 2317-23.
4. Suchand Sandeep, C. S.; Azpiroz, J. M.; Evers, W. H.; Boehme, S. C.; Moreels, I.; Kinge, S.; Siebbeles, L. D. A.; Infante, I.; Houtepen, A. J., Epitaxially Connected

- PbSe Quantum-Dot Films: Controlled Neck Formation and Optoelectronic Properties. *ACS Nano* 2014, 8 (11), 11499-11511.
5. Geuchies, J. J.; van Overbeek, C.; Evers, W. H.; Goris, B.; de Backer, A.; Gantapara, A. P.; Rabouw, F. T.; Hilhorst, J.; Peters, J. L.; Konovalov, O.; Petukhov, A. V.; Dijkstra, M.; Siebbeles, L. D.; van Aert, S.; Bals, S.; Vanmaekelbergh, D., In situ study of the formation mechanism of two-dimensional superlattices from PbSe nanocrystals. *Nat. Mater.* 2016, 15 (12), 1248-1254.
  6. Brus, L. E., Electron-electron and electron-hole interactions in small semiconductor crystallites: The size dependence of the lowest excited electronic state. *J. Chem. Phys.* 1984, 80 (9), 4403.
  7. Bisschop, S.; Geiregat, P.; Aubert, T.; Hens, Z., The Impact of Core/Shell Sizes on the Optical Gain Characteristics of CdSe/CdS Quantum Dots. *ACS Nano* 2018, 12 (9), 9011-9021.
  8. Wang, C.; Wehrenberg, B.; Woo, C. Y.; Guyot-Sionnest, P., Light Emission and Amplification in Charged CdSe Quantum Dots. *J. Phys. Chem. B* 2004.
  9. Bae, W. K.; Joo, J.; Padilha, L. A.; Won, J.; Lee, D. C.; Lin, Q.; Koh, W.-k.; Luo, H.; Klimov, V. I.; Pietryga, J. M., Highly Effective Surface Passivation of PbSe Quantum Dots through Reaction with Molecular Chlorine. *J. Am. Chem. Soc.* 2012, 134 (49), 20160-20168.
  10. Carey, G. H.; Kramer, I. J.; Kanjanaboos, P.; Moreno-Bautista, G.; Voznyy, O.; Rollny, L.; Tang, J. A.; Hoogland, S.; Sargent, E. H., Electronically Active Impurities in Colloidal Quantum Dot Solids. *ACS Nano* 2014, 8 (11), 11763-9.
  11. Woo, J. Y.; Ko, J.-H.; Song, J. H.; Kim, K.; Choi, H.; Kim, Y.-H.; Lee, D. C.; Jeong, S., Ultrastable PbSe Nanocrystal Quantum Dots via in Situ Formation of Atomically Thin Halide Adlayers on PbSe(100). *J. Am. Chem. Soc.* 2014, 136 (25), 8883-8886.
  12. du Fossé, I.; ten Brinck, S.; Infante, I.; Houtepen, A. J., Role of Surface Reduction in the Formation of Traps in n-Doped II-VI Semiconductor Nanocrystals: How to Charge without Reducing the Surface. *Chem. Mater.* 2019, 31 (12), 4575-4583.
  13. Kirkwood, N.; Monchen, J. O. V.; Crisp, R. W.; Grimaldi, G.; Bergstein, H. A. C.; du Fosse, I.; van der Stam, W.; Infante, I.; Houtepen, A. J., Finding and Fixing Traps in II-VI and III-V Colloidal Quantum Dots: The Importance of Z-Type Ligand Passivation. *J Am Chem Soc* 2018.
  14. Ip, A. H.; Thon, S. M.; Hoogland, S.; Voznyy, O.; Zhitomirsky, D.; Debnath, R.; Levina, L.; Rollny, L. R.; Carey, G. H.; Fischer, A.; Kemp, K. W.; Kramer, I. J.; Ning, Z.; Labelle, A. J.; Chou, K. W.; Amassian, A.; Sargent, E. H., Hybrid passivated colloidal quantum dot solids. *Nat. Nanotechnol.* 2012, 7 (9), 577-582.

15. Schnitzenbaumer, K. J.; Dukovic, G., Comparison of Phonon Damping Behavior in Quantum Dots Capped with Organic and Inorganic Ligands. *Nano Lett* 2018.
16. Mack, T. G.; Jethi, L.; Andrews, M.; Kambhampati, P., Direct Observation of Vibronic Coupling between Excitonic States of CdSe Nanocrystals and Their Passivating Ligands. *The Journal of Physical Chemistry C* 2019, 123 (8), 5084-5091.
17. Yazdani, N.; Bozyigit, D.; Vuttivorakulchai, K.; Luisier, M.; Infante, I.; Wood, V., Tuning Electron-Phonon Interactions in Nanocrystals through Surface Termination. *Nano Lett* 2018, 18 (4), 2233-2242.
18. Lifshitz, E., Evidence in Support of Exciton to Ligand Vibrational Coupling in Colloidal Quantum Dots. *J Phys Chem Lett* 2015, 6 (21), 4336-47.
19. Soreni-Harari, M.; Yaacobi-Gross, N.; Steiner, D.; Aharoni, A.; Banin, U.; Millo, O.; Tessler, N., Tuning energetic levels in nanocrystal quantum dots through surface manipulations. *Nano Lett* 2008, 8 (2), 678-84.
20. Brown, P. R.; Kim, D.; Lunt, R. R.; Zhao, N.; Bawendi, M. G.; Grossman, J. C.; Bulović, V., Energy Level Modification in Lead Sulfide Quantum Dot Thin Films through Ligand Exchange. *ACS Nano* 2014, 8 (6), 5863-5872.
21. Chuang, C.-H. M.; Brown, P. R.; Bulović, V.; Bawendi, M. G., Improved performance and stability in quantum dot solar cells through band alignment engineering. *Nat. Mater.* 2014, 13 (8), 796-801.
22. Crisp, R. W.; Kroupa, D. M.; Marshall, A. R.; Miller, E. M.; Zhang, J.; Beard, M. C.; Luther, J. M., Metal Halide Solid-State Surface Treatment for High Efficiency PbS and PbSe QD Solar Cells. *Sci. Rep.* 2015, 5, 9945.
23. Kroupa, D. M.; Voros, M.; Brawand, N. P.; McNichols, B. W.; Miller, E. M.; Gu, J.; Nozik, A. J.; Sellinger, A.; Galli, G.; Beard, M. C., Tuning colloidal quantum dot band edge positions through solution-phase surface chemistry modification. *Nat. Commun.* 2017, 8, 15257.
24. Law, M.; Luther, J. M.; Song, Q.; Hughes, B. K.; Perkins, C. L.; Nozik, A. J., Structural, optical, and electrical properties of PbSe nanocrystal solids treated thermally or with simple amines. *J. Am. Chem. Soc.* 2008, 130 (18), 5974-5985.
25. Ning, Z.; Voznyy, O.; Pan, J.; Hoogland, S.; Adinolfi, V.; Xu, J.; Li, M.; Kirmani, A. R.; Sun, J.-P.; Minor, J.; Kemp, K. W.; Dong, H.; Rollny, L.; Labelle, A.; Carey, G.; Sutherland, B.; Hill, I.; Amassian, A.; Liu, H.; Tang, J.; Bakr, O. M.; Sargent, E. H., Air-stable n-type colloidal quantum dot solids. *Nat. Mater.* 2014, 13 (8), 822-828.

26. van der Stam, W.; de Graaf, M.; Gudjonsdottir, S.; Geuchies, J. J.; Dijkema, J. J.; Kirkwood, N.; Evers, W. H.; Longo, A.; Houtepen, A. J., Tuning and Probing the Distribution of Cu(+) and Cu(2+) Trap States Responsible for Broad-Band Photoluminescence in CuInS<sub>2</sub> Nanocrystals. *ACS Nano* 2018, 12 (11), 11244-11253.
27. van der Stam, W.; du Fossé, I.; Grimaldi, G.; Monchen, J. O. V.; Kirkwood, N.; Houtepen, A. J., Spectroelectrochemical Signatures of Surface Trap Passivation on CdTe Nanocrystals. *Chem. Mater.* 2018, 30 (21), 8052-8061.
28. Boehme, S. C.; Azpiroz, J. M.; Aulin, Y. V.; Grozema, F. C.; Vanmaekelbergh, D.; Siebbeles, L. D. A.; Infante, I.; Houtepen, A. J., Density of trap states and Auger-mediated electron trapping in CdTe quantum-dot solids. *Nano Lett.* 2015, 15 (5), 3056-3066.
29. Boehme, S. C.; Walvis, T. A.; Infante, I.; Grozema, F. C.; Vanmaekelbergh, D.; Siebbeles, L. D. A.; Houtepen, A. J., Electrochemical Control over Photoinduced Electron Transfer and Trapping in CdSe-CdTe Quantum-Dot Solids. *ACS Nano* 2014, 8 (7), 7067-7077.
30. Bronstein, N. D.; Martinez, M. S.; Kroupa, D. M.; Voros, M.; Lu, H.; Brawand, N. P.; Nozik, A. J.; Sellinger, A.; Galli, G.; Beard, M. C., Designing Janus Ligand Shells on PbS Quantum Dots using Ligand-Ligand Cooperativity. *ACS Nano* 2019.
31. Xia, P.; Liang, Z.; Mahboub, M.; van Baren, J.; Lui, C. H.; Jiao, J.; Graham, K. R.; Tang, M. L., Surface Fluorination for Controlling the PbS Quantum Dot Bandgap and Band Offset. *Chem. Mater.* 2018, 30 (15), 4943-4948.
32. Giansante, C.; Infante, I.; Fabiano, E.; Grisorio, R.; Suranna, G. P.; Gigli, G., "Darker-than-Black" PbS Quantum Dots: Enhancing Optical Absorption of Colloidal Semiconductor Nanocrystals via Short Conjugated Ligands. *J. Am. Chem. Soc.* 2015, 137 (5), 1875-86.
33. Giansante, C., Surface Chemistry Control of Colloidal Quantum Dot Band Gap. *J. Phys. Chem. C* 2018, 122 (31), 18110-18116.
34. Dabbousi, B. O.; Rodriguez-Viejo, J.; Mikulec, F. V.; Heine, J. R.; Mattoussi, H.; Ober, R.; Jensen, K. F.; Bawendi, M. G., (CdSe) ZnS core-shell quantum dots: synthesis and characterization of a size series of highly luminescent nanocrystallites. *J. Phys. Chem. B* 1997, 101 (46), 9463-9475.
35. Jha, P. P.; Guyot-Sionnest, P., Trion decay in colloidal quantum dots. *ACS Nano* 2009, 3 (4), 1011-5.
36. Fan, F.; Voznyy, O.; Sabatini, R. P.; Bicanic, K. T.; Adachi, M. M.; McBride, J. R.; Reid, K. R.; Park, Y. S.; Li, X.; Jain, A.; Quintero-Bermudez, R.; Saravanapavanantham,

- M.; Liu, M.; Korkusinski, M.; Hawrylak, P.; Klimov, V. I.; Rosenthal, S. J.; Hoogland, S.; Sargent, E. H., Continuous-wave lasing in colloidal quantum dot solids enabled by facet-selective epitaxy. *Nature* 2017, 544 (7648), 75-79.
37. Lim, J.; Park, Y.-S.; Klimov, V. I., Optical gain in colloidal quantum dots achieved with direct-current electrical pumping. *Nat. Mater.* 2017, 17 (1), 42-49.
38. Li, Y.; Hou, X.; Dai, X.; Yao, Z.; Lv, L.; Jin, Y.; Peng, X., Stoichiometry-Controlled InP-Based Quantum Dots: Synthesis, Photoluminescence, and Electroluminescence. *J Am Chem Soc* 2019, 141 (16), 6448-6452.
39. Hanifi, D. A.; Bronstein, N. D.; Koscher, B. A.; Nett, Z.; Swabeck, J. K.; Takano, K.; Schwartzberg, A. M.; Maserati, L.; Vandewal, K.; van de Burgt, Y.; Salleo, A.; Alivisatos, A. P., Redefining near-unity luminescence in quantum dots with photothermal threshold quantum yield. *Science* 2019, 363 (6432), 1199-1202.
40. Park, Y. S.; Bae, W. K.; Baker, T.; Lim, J.; Klimov, V. I., Effect of Auger Recombination on Lasing in Heterostructured Quantum Dots with Engineered Core/Shell Interfaces. *Nano Lett* 2015, 15 (11), 7319-28.
41. Park, Y. S.; Lim, J.; Makarov, N. S.; Klimov, V. I., Effect of Interfacial Alloying versus "Volume Scaling" on Auger Recombination in Compositionally Graded Semiconductor Quantum Dots. *Nano Lett* 2017.
42. Jain, A.; Voznyy, O.; Hoogland, S.; Korkusinski, M.; Hawrylak, P.; Sargent, E. H., Atomistic Design of CdSe/CdS Core-Shell Quantum Dots with Suppressed Auger Recombination. *Nano Lett* 2016, 16 (10), 6491-6496.
43. Cirloganu, C. M.; Padilha, L. A.; Lin, Q.; Makarov, N. S.; Velizhanin, K. A.; Luo, H.; Robel, I.; Pietryga, J. M.; Klimov, V. I., Enhanced carrier multiplication in engineered quasi-type-II quantum dots. *Nat. Commun.* 2014, 5, 4148.
44. Kroupa, D. M.; Pach, G. F.; Voros, M.; Giberti, F.; Chernomordik, B. D.; Crisp, R. W.; Nozik, A. J.; Johnson, J. C.; Singh, R.; Klimov, V. I.; Galli, G.; Beard, M. C., Enhanced Multiple Exciton Generation in PbS|CdS Janus-like Heterostructured Nanocrystals. *ACS Nano* 2018, 12 (10), 10084-10094.
45. Talgorn, E.; de Vries, M. A.; Siebbeles, L. D. A.; Houtepen, A. J., Photoconductivity Enhancement in Multilayers of CdSe and CdTe Quantum Dots. *ACS Nano* 2011, 5 (5), 3552-3558.
46. Boehme, S. C.; Vanmaekelbergh, D.; Evers, W. H.; Siebbeles, L. D. A.; Houtepen, A. J., In situ spectroelectrochemical determination of energy levels and energy level offsets in quantum-dot heterojunctions. *J. Phys. Chem. C* 2016, 120 (9), 5164-5173.

47. Talgorn, E.; Moysidou, E.; Abellon, R. D.; Savenije, T. J.; Goossens, A.; Houtepen, A. J.; Siebbeles, L. D. A., Highly Photoconductive CdSe Quantum-Dot Films: Influence of Capping Molecules and Film Preparation Procedure. *J. Phys. Chem. C* 2010, 114 (8), 3441-3447.
48. Gao, Y.; Aerts, M.; Suchand Sandeep, C. S.; Talgorn, E.; Savenije, T. J.; Kinge, S.; Siebbeles, L. D. A.; Houtepen, A. J., Photoconductivity of PbSe Quantum-Dot Solids: Dependence on Ligand Anchor Group and Length. *ACS Nano* 2012, 6 (11), 9606-9614.
49. Klem, E. J. D.; Shukla, H.; Hinds, S.; MacNeil, D. D.; Levina, L.; Sargent, E. H., Impact of dithiol treatment and air annealing on the conductivity, mobility, and hole density in PbS colloidal quantum dot solids. *Appl. Phys. Lett.* 2008, 92 (21).
50. Kovalenko, M. V.; Scheele, M.; Talapin, D. V., Colloidal Nanocrystals with Molecular Metal Chalcogenide Surface Ligands. *Science* 2009, 324 (5933), 1417-1420.
51. Lee, J.-S.; Kovalenko, M. V.; Huang, J.; Chung, D. S.; Talapin, D. V., Band-like transport, high electron mobility and high photoconductivity in all-inorganic nanocrystal arrays. *Nat. Nanotechnol.* 2011, 6 (6), 348-352.
52. Crisp, R. W.; Callahan, R.; Reid, O. G.; Dolzhenkov, D. S.; Talapin, D. V.; Rumbles, G.; Luther, J. M.; Kopidakis, N., Photoconductivity of CdTe Nanocrystal-Based Thin Films: Te<sub>2</sub>- Ligands Lead To Charge Carrier Diffusion Lengths Over 2  $\mu\text{m}$ . *J. Phys. Chem. Lett.* 2015, 4815-4821.
53. Marcus, R. A.; Sutin, N., Electron transfer in chemistry and biology. *Biochim. Biophys. Acta* 1985, 811, 265-322.
54. Chu, I.-H.; Radulaski, M.; Vukmirovic, N.; Cheng, H.-P.; Wang, L.-W., Charge Transport in a Quantum Dot Supercrystal. *The Journal of Physical Chemistry C* 2011, 115 (43), 21409-21415.
55. Gao, Y.; Suchand Sandeep, C. S.; Schins, J. M.; Houtepen, A. J.; Siebbeles, L. D., Disorder strongly enhances Auger recombination in conductive quantum-dot solids. *Nat. Commun.* 2013, 4, 2329.
56. Gilmore, R. H.; Lee, E. M.; Weidman, M. C.; Willard, A. P.; Tisdale, W. A., Charge carrier hopping dynamics in homogeneously broadened PbS quantum dot solids. *Nano Lett* 2017, 17 (2), 893-901.
57. Gilmore, R. H.; Winslow, S. W.; Lee, E. M. Y.; Ashner, M. N.; Yager, K. G.; Willard, A. P.; Tisdale, W. A., Inverse Temperature Dependence of Charge Carrier Hopping in Quantum Dot Solids. *ACS Nano* 2018.

58. Choi, J.-H.; Fafarman, A. T.; Oh, S. J.; Ko, D.-K.; Kim, D. K.; Diroll, B. T.; Muramoto, S.; Gillen, J. G.; Murray, C. B.; Kagan, C. R., Bandlike Transport in Strongly Coupled and Doped Quantum Dot Solids: A Route to High-Performance Thin-Film Electronics. *Nano Lett.* 2012, 12 (5), 2631-2638.
59. Talgorn, E.; Gao, Y.; Aerts, M.; Kunneman, L. T.; Schins, J. M.; Savenije, T. J.; van Huis, M. A.; van der Zant, H. S.; Houtepen, A. J.; Siebbeles, L. D., Unity quantum yield of photogenerated charges and band-like transport in quantum-dot solids. *Nat. Nanotechnol.* 2011, 6 (11), 733-9.
60. Wang, A.; Xuan, Y., A detailed study on loss processes in solar cells. *Energy* 2018, 144, 490-500.
61. Geiregat, P.; Delerue, C.; Justo, Y.; Aerts, M.; Spoor, F.; Van Thourhout, D.; Siebbeles, L. D. A.; Allan, G.; Houtepen, A. J.; Hens, Z., A Phonon Scattering Bottleneck for Carrier Cooling in Lead Chalcogenide Nanocrystals. *ACS Nano* 2015, 9 (1), 778-788.
62. Pandey, A.; Guyot-Sionnest, P., Slow electron cooling in colloidal quantum dots. *Science* 2008, 322 (5903), 929-932.
63. Urayama, J.; Norris, T. B.; Singh, J.; Bhattacharya, P., Observation of phonon bottleneck in quantum dot electronic relaxation. *Phys Rev Lett* 2001, 86 (21), 4930-3.
64. Heitz, R.; Born, H.; Guffarth, F.; Stier, O.; Schliwa, A.; Hoffmann, A.; Bimberg, D., Existence of a phonon bottleneck for excitons in quantum dots. *Phys. Rev. B* 2001, 64 (24).
65. Cooney, R. R.; Sewall, S. L.; Anderson, K. E. H.; Dias, E. A.; Kambhampati, P., Breaking the Phonon Bottleneck for Holes in Semiconductor Quantum Dots. *Phys. Rev. Lett.* 2007, 98 (17), 177403.
66. Schaller, R. D.; Pietryga, J. M.; Goupalov, S. V.; Petruska, M. A.; Ivanov, S. A.; Klimov, V. I., Breaking the phonon bottleneck in semiconductor nanocrystals via multiphonon emission induced by intrinsic nonadiabatic interactions. *Phys Rev Lett* 2005, 95 (19), 196401.
67. Klimov, V. I.; McBranch, D. W., Femtosecond 1P-to-1S electron relaxation in strongly confined semiconductor nanocrystals. *Phys. Rev. Lett.* 1998, 80 (18), 4028-4031.
68. Klimov, V. I.; McBranch, D. W.; Leatherdale, C. A.; Bawendi, M. G., Electron and hole relaxation pathways in semiconductor quantum dots. *Phys. Rev. B* 1999, 60 (19), 13740-13749.

69. Guyot-Sionnest, P.; Shim, M.; Matranga, C.; Hines, M., Intraband relaxation in CdSe quantum dots. *Phys. Rev. B* 1999, 60 (4), R2181-R2184.
70. Spoor, F. C. M.; Kunneman, L. T.; Evers, W. H.; Renaud, N.; Grozema, F. C.; Houtepen, A. J.; Siebbeles, L. D. A., Hole Cooling Is Much Faster than Electron Cooling in PbSe Quantum Dots. *ACS Nano* 2016, 10 (1), 695-703.
71. Efros, A. L.; Kharchenko, V. A.; Rosen, M., Breaking the phonon bottleneck in nanometer quantum dots: Role of Auger-like processes. *Solid State Communications* 1995, 93 (4), 281-284.
72. Hendry, E.; Koeberg, M.; Wang, F.; Zhang, H.; de Mello Donega, C.; Vanmaekelbergh, D.; Bonn, M., Direct observation of electron-to-hole energy transfer in CdSe quantum dots. *Phys Rev Lett* 2006, 96 (5), 057408.
73. Kilina, S. V.; Kilin, D. S.; Prezhdo, O. V., Breaking the Phonon Bottleneck in PbSe and CdSe Quantum Dots: Time-Domain Density Functional Theory of Charge Carrier Relaxation. *ACS Nano* 2009, 3 (1), 93-99.
74. Schaller, R. D.; Klimov, V. I., High efficiency carrier multiplication in PbSe nanocrystals: implications for solar energy conversion. *Phys Rev Lett* 2004, 92 (18), 186601.
75. Hanna, M. C.; Nozik, A. J., Solar conversion efficiency of photovoltaic and photoelectrolysis cells with carrier multiplication absorbers. *J. Appl. Phys.* 2006, 100 (7), 074510.
76. Klimov, V. I., Detailed-balance power conversion limits of nanocrystal-quantum-dot solar cells in the presence of carrier multiplication. *Appl. Phys. Lett.* 2006, 89 (12), 123118.
77. Aerts, M.; Suchand Sandeep, C. S.; Gao, Y.; Savenije, T. J.; Schins, J. M.; Houtepen, A. J.; Kinge, S.; Siebbeles, L. D. A., Free Charges Produced by Carrier Multiplication in Strongly Coupled PbSe Quantum Dot Films. *Nano Lett.* 2011, 11 (10), 4485-4489.
78. Semonin, O. E.; Luther, J. M.; Choi, S.; Chen, H.-Y.; Gao, J.; Nozik, A. J.; Beard, M. C., Peak External Photocurrent Quantum Efficiency Exceeding 100% via MEG in a Quantum Dot Solar Cell. *Science* 2011, 334 (6062), 1530-1533.
79. Delerue, C.; Allan, G.; Pijpers, J. J. H.; Bonn, M., Carrier multiplication in bulk and nanocrystalline semiconductors: Mechanism, efficiency, and interest for solar cells. *Phys. Rev. B* 2010, 81 (12).
80. Spoor, F. C. M.; Grimaldi, G.; Delerue, C.; Evers, W. H.; Crisp, R. W.; Geiregat, P.; Hens, Z.; Houtepen, A. J.; Siebbeles, L. D. A., Asymmetric Optical Transitions

Determine the Onset of Carrier Multiplication in Lead Chalcogenide Quantum Confined and Bulk Crystals. ACS Nano 2018.

81. Beard, M. C.; Midgett, A. G.; Hanna, M. C.; Luther, J. M.; Hughes, B. K.; Nozik, A. J., Comparing multiple exciton generation in quantum dots to impact ionization in bulk semiconductors: implications for enhancement of solar energy conversion. Nano Lett. 2010, 10 (8), 3019-27.



# Chapter 2

## Hot-electron transfer in quantum-dot heterojunction films

### *Abstract*

Thermalization losses limit the photon-to-power conversion of solar cells at the high-energy side of the solar spectrum, as electrons quickly lose their energy relaxing to the band edge. Hot-electron transfer could reduce these losses. We demonstrate fast and efficient hot-electron transfer between lead selenide and cadmium selenide quantum dots assembled in a quantum-dot heterojunction solid. In this system, the energy structure of the absorber material and of the electron extracting material can be easily tuned via a variation of quantum-dot size, allowing to tailor the energetics of the transfer process for device applications. The efficiency of the transfer process increases with excitation energy as a result of the more favorable competition between hot-electron transfer and electron cooling. The experimental picture is supported by time-domain density functional theory calculations, showing that electron density is transferred from lead selenide to cadmium selenide quantum dots on the sub-picosecond timescale.

Based on: Gianluca Grimaldi, Ryan W. Crisp, Stephanie ten Brinck, Felipe Zapata, Michiko van Ouwendorp, Nicolas Renaud, Nicholas Kirkwood, Wiel Evers, Sachin Kinge, Ivan Infante, Laurens D. A. Siebbeles and Arjan J. Houtepen. *Nature Communications*, 2018, 9 (1), 2310.

## 2.1 Introduction

Semiconductor quantum-dots (QDs) have drawn considerable interest due to their low-cost solution-based synthesis and unique photophysics, controllably bridging the divide between molecular and bulk material properties<sup>1,2</sup>. As the size of a semiconductor crystal is decreased to below the bulk exciton Bohr-radius, quantum-confinement starts breaking the continuous band-structure into discrete electronic levels. It has been suggested that the sparse density of states in QDs could slow electron cooling<sup>3</sup>, as single phonon emission does not suffice to bridge the energy between levels and slower multi-phonon emission events are needed to dissipate the electron energy. Such a “phonon-bottleneck” would enable making use of high energy (“hot”) carriers before they thermalize, for instance via carrier multiplication (CM)<sup>4</sup> or hot-electron transfer (HET), provided appropriate quenching of surface related relaxation channels<sup>3,5,6</sup>. In addition to posing an interesting scientific problem, these processes may also find applications in solar energy conversion via suppression of thermal losses. Hot-electron solar cells in particular can theoretically enhance the maximum power conversion efficiency of solar cells from 33% to 66%.<sup>7</sup> In practice, experimental evidence concerning slowing of carrier cooling in QDs remains scattered<sup>3,8</sup> and cooling rates are usually high<sup>9</sup>. At the same time, CM and HET have been demonstrated using QDs. The interplay of cooling and CM or HET in nanostructure remains largely understood.

The HET process involves high-energy carriers, transferring between different species before thermalizing, and occurs in any materials where electron transfer outcompetes cooling. In recent years HET has been demonstrated to occur from QDs to metal-oxides<sup>10,11</sup>, acceptor molecules<sup>12</sup> and localized surface states<sup>13-15</sup>. However, harvesting of hot-electrons to increase solar cell efficiency requires careful choice of both the absorber material band-gap and the energy of the extraction level. The latter is difficult to control in the previously reported hot-electron acceptors, requiring a change in the materials used for extraction.

In this work, we demonstrate ultrafast HET across PbSe-CdSe QD-heterostructures in QD heterojunction (QDHJ) films coupled by molecular linkers. We demonstrate that HET occurs in these QD HJs with an efficiency that increases as the excitation photon energy increases. Our results suggest that the facile control over the energetics of QDHJs can be used to spectrally tune photon absorption and electron injection without requiring changes in material composition.

## 2.2 Films characterization

QD heterojunction films were prepared by depositing alternating layers of PbSe and CdSe QDs on a quartz substrate (See Appendix, Fig. 2.6-7), and exchanging the insulating ligands on the surface of the QDs with short conductive linkers<sup>16,17</sup>. The spectroscopic investigation focused on a sample fabricated with 1,2-ethanedithiol (EDT) linkers, while similar results are obtained treating each layer with 1,2-ethanediamine (EDA) (See Appendix, Fig. 2.3-4). Figure 2.1a shows a transmission electron microscope (TEM) image of a reference film prepared with a single cycle of PbSe and CdSe QD deposition,

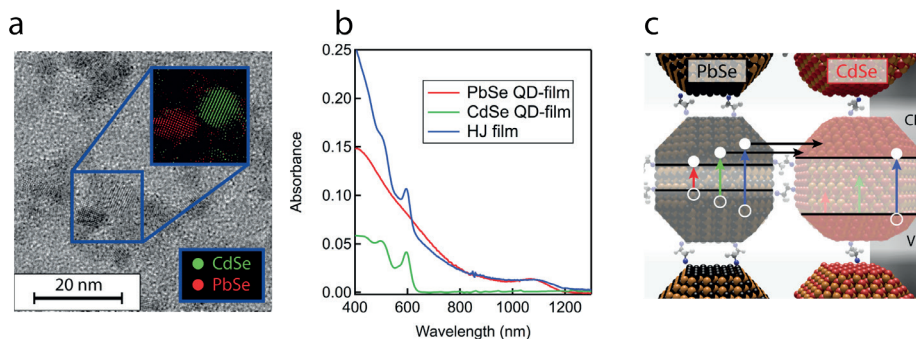


**Figure 2.1. Film properties.** **a**, High resolution transmission electron microscope (TEM) image showing PbSe and CdSe quantum dots (QDs) drop-casted on a TEM grid and subsequently treated with 1,2-ethanedithiol (EDT). The inset displays the result of a Fourier bandpass analysis of the image, distinguishing the two QD materials via their atomic lattices, and showing close proximity between the two components. **b**, linear absorption spectra of the combined PbSe-CdSe QDHJ film and of the single material films. **c**, schematic of the energy alignment in the system.

displaying close proximity between the different QD components. The optical absorption spectra of the QDHJ film and of the reference single-material films are shown in Figure 2.1b.

The energy alignment was investigated *via* spectro-electrochemical measurements on the QDHJ films (See Appendix, Fig. 2.10). A type I alignment with a 1S energy level offset of 0.25 eV was found, in agreement with trends reported in literature<sup>18</sup>. This small conduction band offset, in conjunction with a significant difference in band gaps, allows selective study of the transfer of hot-electrons from PbSe to CdSe QDs. As shown schematically in Figure 2.1c, upon low-energy photoexcitation (red and green lines) PbSe QDs are selectively photoexcited, while higher energy light is required to also photoexcite CdSe QDs (blue line). Excitation above the PbSe band gap may provide the electron with sufficient energy to transfer to the CdSe QD, while the hole is prevented from transferring by the large valence band offset.

### 2.3 Hot-electron transfer probed by Transient Absorption Spectroscopy

Transient absorption (TA) spectroscopy can be used to detect and quantify electron transfer between the two QD species. Upon selective photoexcitation of the PbSe QDs, electrons transferring to the CdSe QDs induce a decrease in the 1S CdSe absorption, commonly known as an absorption bleach, due to state filling and stimulated emission<sup>19</sup>. The differential absorbance  $\Delta A_{1s}$  is proportional to the number of electrons in the CdSe 1S state, while holes contribute negligibly, on account of the higher degeneracy of hole states<sup>20-22</sup>. The CdSe  $\Delta A_{1s}$  signal can then be used to quantify the number of electrons transferring to the initially unoccupied CdSe QDs.

In order to identify PbSe and CdSe QD contributions to the TA response of QDHJ films

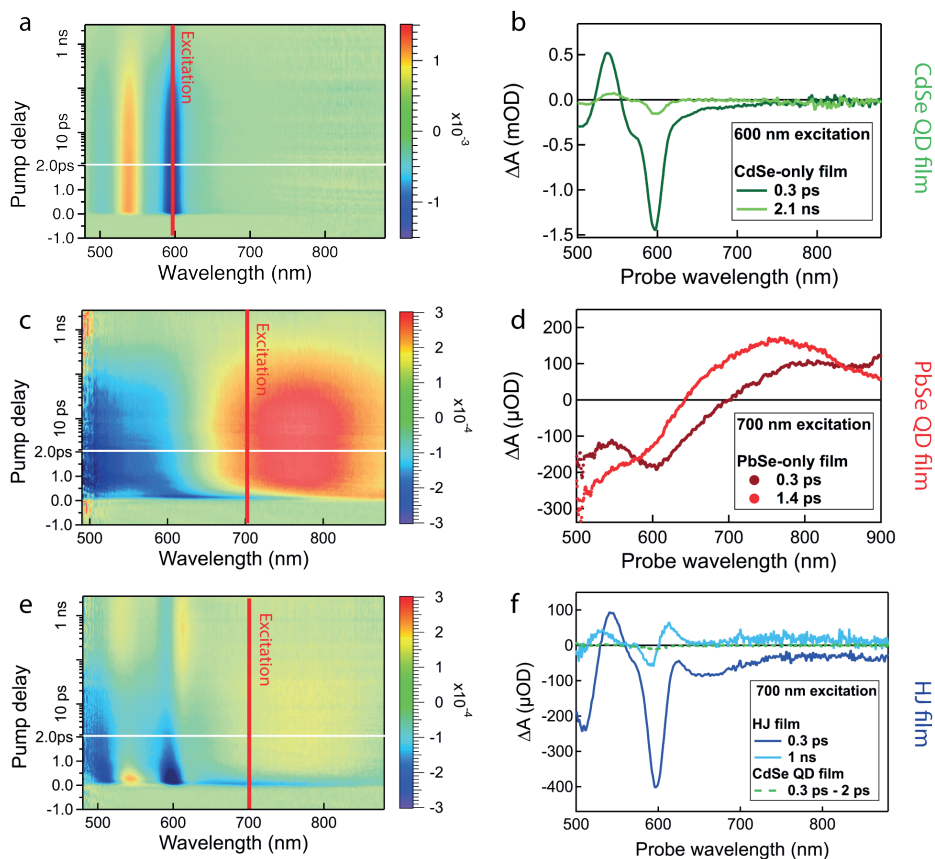


**Figure 2.2. Transient Absorption (TA) on QD-films.** **a**, color map showing the differential absorbance of a film composed of 4.5 nm CdSe QDs, excited at 600 nm with a fluence of  $1.27 \cdot 10^{13}$  photons/cm<sup>2</sup> per pulse (0.07 excitons per CdSe QD). **b**, spectral cuts of figure 2a, showing the TA response for two delay times after photoexcitation. **c**, color map showing the differential absorbance of a film composed of 2.3 nm PbSe QDs, excited at 700 nm with a fluence of  $9.84 \cdot 10^{13}$  photons/cm<sup>2</sup> per pulse (0.39 excitons per PbSe QD). **d**, spectral cuts of figure 2c. **e**, color map showing the differential absorbance of a QD/HJ film, composed of 4.5 nm CdSe QDs and 2.3 nm PbSe QDs. The film is excited at 700 nm with a fluence of  $1.19 \cdot 10^{14}$  photons/cm<sup>2</sup> per pulse (0.36 excitons per PbSe QD), closely resembling the excitation conditions of the PbSe QD film. **f**, spectral cuts of figure 2e, showing the comparison between the TA response of the HJ film (dark and light blue) and the response of the CdSe QD film excited with the same conditions; i.e. 700 nm excitation with a fluence of  $1.19 \cdot 10^{14}$  photons/cm<sup>2</sup> per pulse.

in the CdSe 1S spectral range, we characterized the response of films composed of the individual components. Figure 2.2a-b shows a TA measurement on an EDT-treated 4.5 nm CdSe QD film, whose absorption spectrum is shown in Figure 2.2b, excited at 600 nm, clearly showing an absorption bleach at the CdSe 1S energy. The shape of the feature is maintained throughout the 3 ns window of the measurement, decreasing in amplitude as a result of charge carrier recombination (radiative and non-radiative).

Figure 2.2c-d shows the result of a TA measurement on EDT-treated 2.3 nm PbSe QD film,

excited at 700 nm. At wavelengths in the visible, absorbance changes are characterized by the presence of a broad increase in absorbance (650-900 nm) and by an absorption bleach at the high-energy side of the probe window (500-650 nm). The photo-induced absorption feature is always observed in TA measurements of PbSe QDs, and has been attributed to biexciton shifts of the absorption spectrum<sup>23,24</sup>, while the bleach feature is typically seen in transient absorption or spectro-electrochemical measurement on PbSe QD films<sup>25</sup>, but not on dispersions. The nature of this broad absorption bleach has yet to be identified.

The TA response of the combined PbSe-CdSe film, excited at 700 nm, i.e. below the CdSe bandgap, is shown in Figure 2.2e-f. As can be noted from the early time TA signal, both sets of TA features present in the individual films can be seen in the combined film response. In particular, the negative peak at the CdSe bandgap is associated with bleaching of the CdSe 1S transition, implying the presence of electrons at the CdSe conduction band edge. The spectral cut of the TA measurement in Figure 2.2f compares the TA response of the combined film (continuous line) with the TA response of the CdSe-only film (dotted line), both excited at 700 nm with identical incoming photon fluence, proving that the bleach of the CdSe 1S feature in absence of neighbouring PbSe QDs is negligible. We conclude that, as CdSe QDs are not directly photoexcited, electrons are transferred from PbSe to CdSe QDs. The excitation energy dependence of the rise time of the CdSe 1S bleach feature is in line with the suggested pathway (See Appendix, Fig. 2.11).

The bleach at the CdSe 1S energy quickly decreases in a few ps. Considering the type I energy level structure (Fig. 2.1c) it is to be expected that after HET electrons quickly transfer back to the PbSe QD. To verify that this back-transfer is efficient we performed a separate experiment where we excited the CdSe 1S feature directly and quantified the efficiency of electron transfer by monitoring the ingrowth of the absorption bleach at the PbSe QDs 1S position (See Appendix, Fig. 2.12). In that case we observe fast electron transfer from the CdSe to the PbSe QDs with a near unity efficiency. Thus we conclude that the fast decay of the CdSe 1S bleach after HET observed in Figures 2.2e,f is due to back transfer to PbSe QDs. On a longer timescale of 50-100 ps, an anti-symmetric negative-positive feature appears at the CdSe 1S position and remains constant throughout the 3 ns measurement time. A second antisymmetric feature appears around 520 nm. This type of TA feature, resembling the first derivative of the absorption spectrum, is usually associated with an electric field induced shift of the absorption spectrum<sup>26,27</sup>.

The PbSe-related induced absorption between 650-850 nm decreases with the same time-constant as the shift features increase. These observations suggest that as charges depopulate the CdSe and PbSe QDs core states, excited carriers accumulate in proximity of CdSe QDs, electrostatically influencing the QDs and shifting the energy of the 1S and 1P absorption features. We tentatively attribute this to carrier trapping at the surface of the CdSe and/or PbSe QDs. However, for the current discussion the important observation is that CdSe 1S states are populated after selective excitation of PbSe QDs, indicating ultrafast HET from PbSe to CdSe QDs.

We measured TA on the QDHJ film in both the visible (450 nm – 900 nm) and NIR (1150 nm – 1600 nm) spectral regions, varying the excitation energy to characterize the dependence of HET on the initial energy of the electron. Figure 2.3a-d shows the TA

2

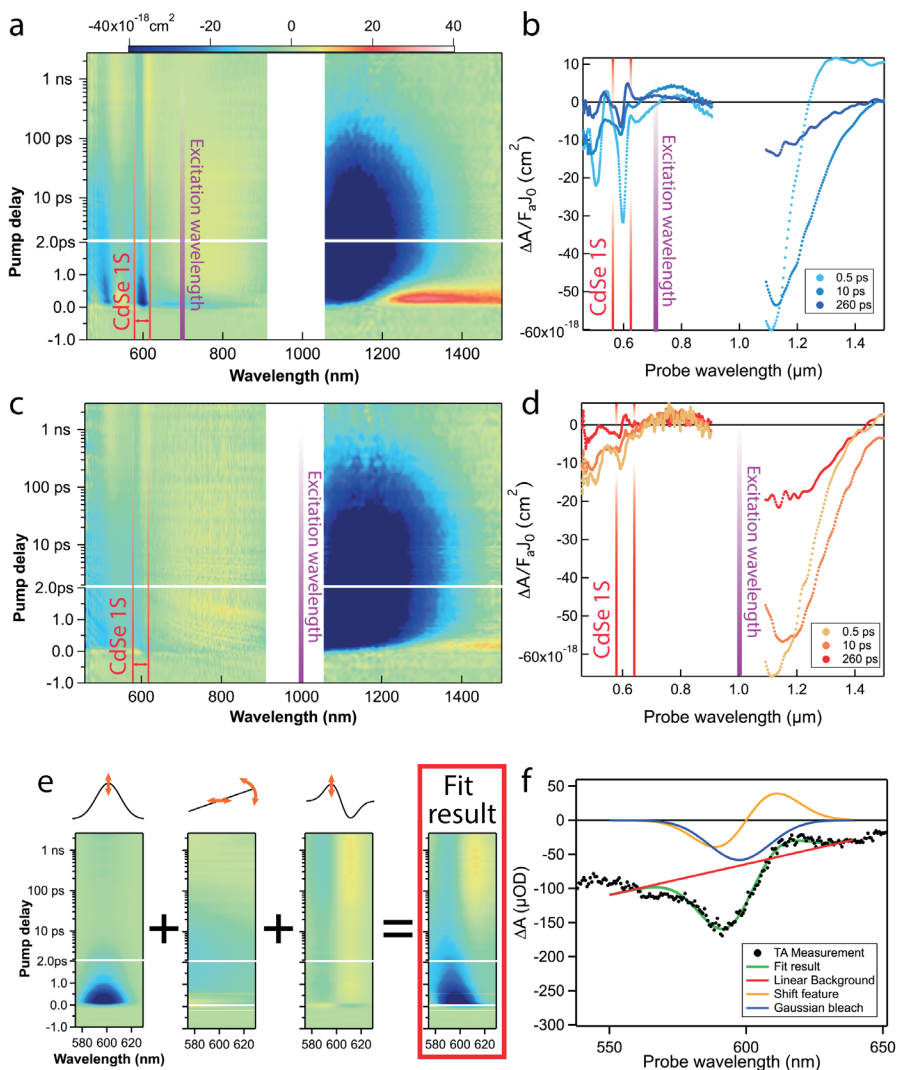


**Figure 2.3. Heterojunction-film (HJ-film) TA response for different excitations and fitting method.** **a**, TA color map showing the differential absorbance per absorbed fluence of the combined PbSe-CdSe film, photoexcited at 700 nm with an absorbed fluence of  $1.4 \cdot 10^{13}$  photons/cm<sup>2</sup> x pulse (0.36 excitons per PbSe QD). **b**, spectral slices of the color map 3a. **c**, TA color map of the combined film photoexcited at 1000 nm with an absorbed fluence of  $3.4 (3.0) \cdot 10^{13}$  photons/cm<sup>2</sup> x pulse in the visible (NIR) range ( $\sim 0.07$  excitons per PbSe QD). **d**, spectral cuts of color map 3c. **e**, color maps showing the different contributions to the fit of the TA response around the CdSe 1S feature; i.e. a Gaussian bleach, a linear background and a shift feature, as described in the text. The orange arrows represent the 4 fit parameters (See Supporting Info). **f**, spectral slice of a TA measurement showing the agreement between fit and experimental trace, together with the shape of the different contributions.

response of the QDHJ film normalized for the absorbed fluence (i.e.  $\Delta A/F_a J_0$ , where  $J_0$  the incident photon fluence and  $F_a$  the fraction of absorbed light)<sup>28</sup>, excited at 700 and 1000 nm. For both excitations the NIR response is dominated by the absorption bleach of the lowest PbSe transition, while for 700 nm excitation an induced absorption feature is visible immediately after photoexcitation, which is related to a hot-carriers induced biexciton shift<sup>23, 24, 29</sup>. Besides the differences in the first picosecond, related to differences in carrier cooling, the NIR PbSe bleach remains largely the same for the two different excitations. In stark contrast, the CdSe TA features in the visible range differ significantly. For 1000 nm excitation, the CdSe 1S bleach is barely visible on top of the negative TA signal arising from PbSe QDs, indicating a much lower efficiency of hot-electron injection to the CdSe QDs compared to the measurement performed with 700 nm excitation wavelength.

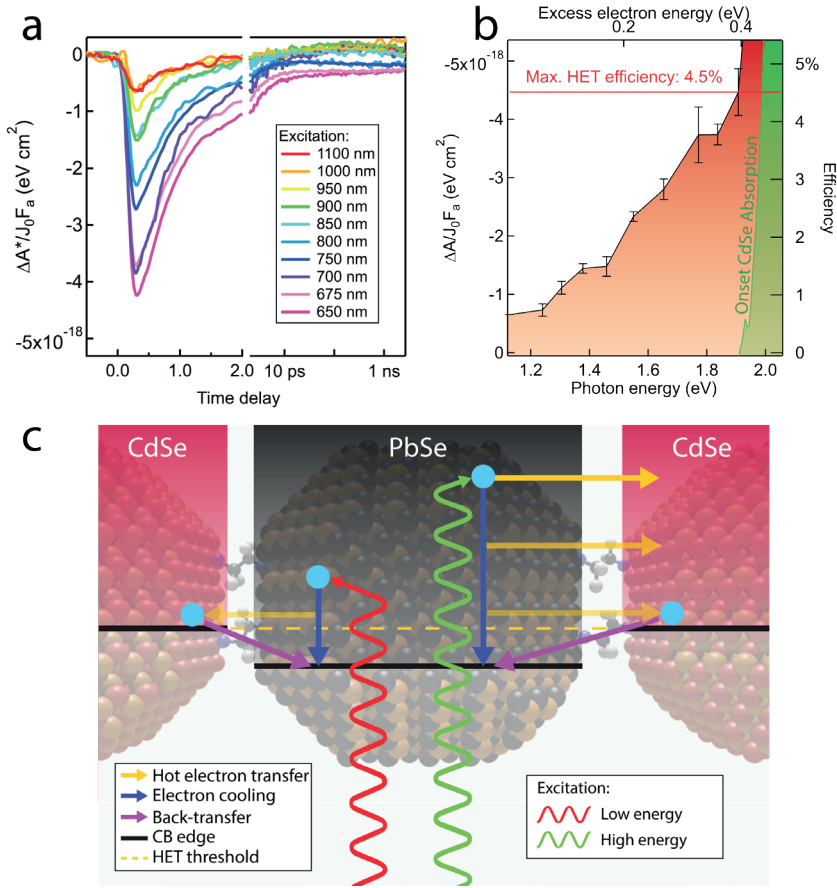
## 2.4 Hot-electron transfer efficiency

Figure 2.3 qualitatively shows that HET process depends on the energy of the absorbed photon. To quantify the HET efficiency and rate, the TA bleach of the CdSe 1S feature needs to be separated from other spectrally overlapping contributions, namely the slowly varying background, related to photoexcitation of PbSe QDs, and the shift feature prominent for  $t > 100$  ps .

To separate the different contributions, we fitted the TA spectrum obtained at each delay-time with a superposition of a Gaussian bleach and a derivative-like shift feature, while the slowly varying PbSe contribution is approximated by a line<sup>30</sup> (See Appendix, Fig. 2.13). The color maps in figure 2.3e show the results of the fit to the TA measurement displayed in figure 2.3a, highlighting the behavior of the different contributions, while Figure 2.3f displays the excellent match between the fitted function and the experimental data. This fitting method allows to extract the amplitude of the CdSe bleach component and to follow its time evolution. Furthermore, integrating the Gaussian profile over the entire 1S feature corrects for the effect of inhomogeneous broadening of the 1S feature and thus facilitates comparison between different samples. We will indicate this quantity as  $\Delta A^* = \int_{1S} \Delta A \, dE$ .

We measured TA varying the excitation energy between 650 nm, the onset of the CdSe absorption (See Fig. 2.1b), and 1100 nm. Figure 2.4a shows the energy-integrated, absorbed fluence-rescaled differential absorbance of the CdSe 1S feature  $\Delta A^*/F_a J_0$ . The time dynamics shows a  $\sim 200$  fs ingrowth of the signal (similar to the instrumental response limit), followed by decay with a  $\tau_{1/2}$  of  $\sim 600$  fs. A clear trend is observed in the excitation energy dependence of  $\Delta A^*$ , with a 7-fold signal increase between 1100 nm and 650 nm excitation. Sub-bandgap excitation of the CdSe QD reference film showed at least 20 times lower bleach signals than the combined film excited with equal photon fluence (See Appendix, Fig. 2.14-15), thus demonstrating that direct CdSe excitation contributes negligibly to the combined film response.

To quantify the efficiency of the transfer process, we followed the procedure reported by Boehme et al.<sup>28</sup> We first determine the bleach of the 1S absorption due to a single exciton by direct excitation in a CdSe QD reference film, i.e. the bleach cross-section (derived in



**Figure 2.4. Excitation energy dependence of Hot-electron transfer (HET).** **a**, fitted amplitude of the CdSe bleach component as a function of time, plotted for different excitation wavelengths. The plot shows an increase of the maximum bleach amplitude for shorter excitation wavelengths. **b**, plot of the bleach amplitude maxima as a function of excitation energy. The right axis shows the HET efficiency corresponding to each bleach value. Error bars are obtained from the standard deviation of the amplitude maxima, obtained from repeated measurements. **c**, schematics of the HET dynamics. Upon higher-energy excitation electrons have longer time available to transfer to CdSe QDs before cooling below the HET threshold than electrons excited at lower energy. In addition, transfer rates are expected to be larger for high-energy electrons, due to an increased amount of final CdSe states and more pronounced electron delocalization. The fast decrease of the CdSe bleach is attributed to back-transfer of electron from CdSe to PbSe QDs.

the Appendix):

$$\sigma_b = \frac{(\Delta A^*)_{\max} \ln(10)}{F_a J_0} \quad 2.1$$

The efficiency of HET to CdSe QDs for selective excitation of PbSe QDs in a QDHJ film

can then be expressed as:

$$\eta_{\text{HET}} = \frac{(\Delta A^*)_{\text{max}} \ln(10)}{F_d J_0 \sigma_b} \quad 2.2$$

where  $(\Delta A^*)_{\text{max}}$  is the peak of the integrated differential absorbance.

Figure 2.4b shows that the estimated HET efficiency increases as a function of excitation energy, a behavior recently observed for HET from QDs to molecular acceptors<sup>12</sup>. Exciting the system just below the CdSe absorption onset leads to a HET efficiency of 4.5%. For higher energy excitations, electron injection from PbSe to CdSe QDs is mixed with the contribution stemming from direct photoexcitation of the CdSe QDs, which represents the dominant contribution to the CdSe bleach.

The observed trend in the electron injection efficiency can be understood within the HET picture schematically depicted in Figure 2.4c. Electrons excited high in the manifold of PbSe conduction band states lose their energy quickly. When the energy of the electron drops below the CdSe QD 1S state, transfer is no longer possible. This implies that higher energy electrons have a longer time-window to undergo HET. At the same time the increase of the QD density of states as a function of electron energy leads to a higher number of available CdSe states, increasing the rate of electron transfer.

In these experiments, only electrons in the CdSe QD 1Se level contribute to the bleach, while undetected higher energy electrons can back-transfer to the PbSe QD component before reaching the conduction band-edge. Therefore, the highest extracted HET efficiency of 4.5% represents a lower limit for the real HET efficiency. Furthermore, higher transfer efficiencies may be achieved by further increasing the initial electron energy, although direct absorption from CdSe QDs prevents us from determining the transfer efficiencies at higher excitation energies.

## 2.5 Rate-equation modeling

To obtain an estimate of the rate associated with the HET process from the HET efficiency, it is required to model the competition between HET and electron cooling. We employed a very simple rate-equation model, describing the conduction bands of the two materials as a discrete set of levels with equal energy spacing and electron transfer rates that are constant in energy and equal for forward and back transfer (See Appendix, Fig. 2.16). The model was fitted to the dynamics of the CdSe 1S<sub>c</sub> population in the QDHJ film, with the transfer rate and the energy-loss rates in the two materials as fitting parameters. Figure 2.5a shows the experimentally determined CdSe 1S<sub>c</sub> population for 675 nm excitation (black), together with the fit of the population with the rate-equation model (blue). An electron transfer rate of 1.1 ps<sup>-1</sup> and energy-loss rates of 2.2 eV/ps and 0.5 eV/ps for PbSe and CdSe, respectively, are extracted from the fit. Figure 2.5a also shows the comparison between the fractional CdSe 1S<sub>c</sub> population and the total HET efficiency (green), accounting for the charges that back-transfer before reaching the lowest CdSe excited state. In this way, a total HET efficiency of 6.2% is found.

The estimated energy-loss rates are in agreement with values reported in the literature<sup>9</sup>.

<sup>30, 31</sup>. The electron transfer rate of  $1.1 \text{ ps}^{-1}$  is similar to rates observed for “cold” electron transfer between CdTe and CdSe nanocrystals<sup>28</sup> and for electron transfer between differently sized PbSe QDs<sup>32</sup>. Despite the strong oversimplifications, the model is able to describe the kinetics of the experimental signal, yielding reasonable values for the cooling and transfer rates.

## 2

## 2.6 DFT modeling

To verify the extracted efficiency and rate of HET and to test the physical description of the competition between HET, cooling, and back transfer we also modelled the QDHJ system with density functional theory (DFT) calculations on a system composed of a PbSe QD and CdSe QD, bound covalently by a EDT bridge. To achieve the experimentally reported type-I band alignment, we employed a  $\sim 1.2 \text{ nm}$  CdSe QD passivated with methane-thiol ligands and a  $\sim 1.8 \text{ nm}$  PbSe QD passivated with formate ligands. After geometrical relaxation, we analyzed the electronic structure of this system at the DFT/PBE level of theory<sup>33, 34</sup> using the CP2k code (Figure 2.5b)<sup>35</sup>. In this representation, each line corresponds to a molecular orbital (MO), and the color of the line represents the contribution of each fragment to this MO: the PbSe fragment is depicted in red, CdSe in green, and the organic bridge in black.

At energies near the CB edge, the MOs are mostly localized on the PbSe QD, with the exception of the  $1S_c$  state of CdSe appearing at an energy of  $\sim 0.7 \text{ eV}$  above the overall conduction band edge. At higher excess energies ( $> 1.2 \text{ eV}$ ) MO mixing occurs between the CdSe and PbSe states. Such overlap is associated with the small inter-dot distance provided by the EDT bridge, and is reduced if longer bridge molecules are used (Fig. 2.17-18). On the right of Figure 2.5b, four different molecular orbitals are depicted: (1) a PbSe-localized MO located near the CB edge, (2) the  $1S_c$  CdSe state that shows little mixing with PbSe, (3) a delocalized MO at high excess energies, showing contribution of all three fragments, and (4) a PbSe-localized MO also present at high excess energies. We then performed time-domain non-adiabatic molecular dynamic (NAMD) simulations (see computational details) to analyze the electron-phonon relaxation dynamics. Because we are interested only in the electron relaxation, we fixed the hole at the VB edge, and we started our NAMD simulations at different excess electron energies:  $\sim 1.2 \text{ eV}$  (denoted A in figure 2.5b),  $\sim 1.5 \text{ eV}$  (B), and  $\sim 1.8 \text{ eV}$  (C). Figure 2.5c shows the results of the NAMD simulations. For all simulations, electron density is seen to transfer rapidly from the PbSe QD to the CdSe QD on a  $\sim 50 \text{ fs}$  timescale. Afterwards, the electron density is transferred back to PbSe, and after about 600 fs, electrons are again fully localized on the PbSe QD. Figure 2.5c also shows that by starting the dynamics at higher energy in the CB, the fraction of electron density transferred to CdSe increases, in agreement with the experimental observations presented above. The maximum fraction of electron density transferred to the CdSe QDs is 20% in the TDDFT calculation. This number, which includes electrons in all CdSe QD levels, not just the  $1S_c$  level, is somewhat higher than the experimentally extracted 6.2%. The fact that the theoretical efficiency peaks at 20% is simply due to the fact that the electron density spreads over both the PbSe and CdSe QD states before localizing fully at the PbSe QD in the  $1S_c$  level.

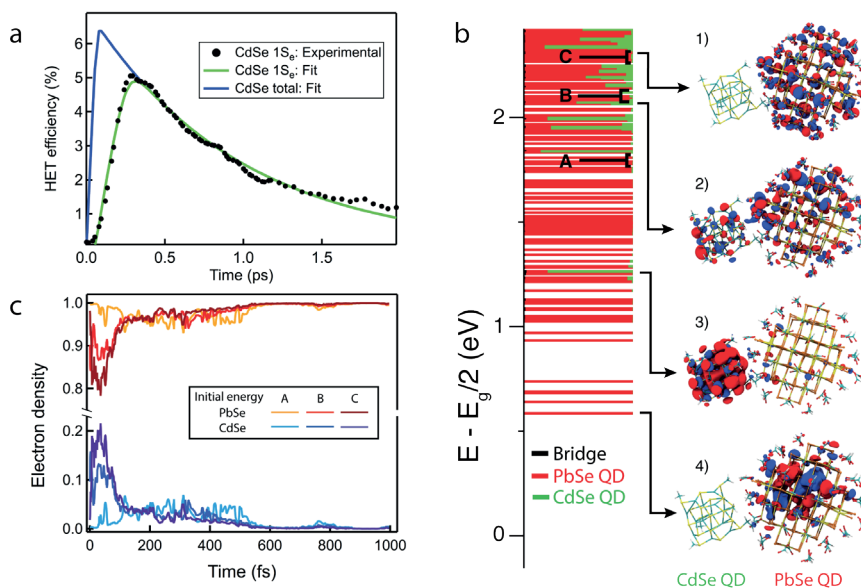


**Figure 2.5. Modeling of HET.** **a**, fit of the experimentally determined HET efficiency (black) with the rate-equation model discussed in the main text. The blue curve shows the fitted efficiency of charge injection in the CdSe  $1S_e$  level, while the green curve indicates the total fraction of electrons injected in any CdSe state. The TA measurement is performed exciting the HJ film with 650 nm laser light, with a fluence of  $4.14 \times 10^{12}$  photons/(cm<sup>2</sup>·pulse). **b**, Computed electronic structure at the DFT/PBE level of theory of the PbSe-CdSe model system, which is composed of a PbSe QD and a CdSe QD coupled by a EDT molecule (bridge). The horizontal bars specify what fraction of each molecular orbital is localized on the PbSe QD (red), on the CdSe QD (green) and on the bridge (black). The contribution of the EDT bridge is almost negligible. The figure also shows the molecular orbital plots associated with 1) a high-energy state mostly localized on PbSe, 2) a high-energy state delocalized over both CdSe and PbSe, 3) the CdSe  $1S_e$  state, and 4) the PbSe  $1S_e$  state. **c**, NAMD simulations illustrating the electron dynamics started from three different initial conditions indicated in Figure 5b as A, B and C. Electrons are rapidly injected into the CdSe QD, and transfer back on a longer timescale. The data show an increase in the maximum transferred electron density for initial states with higher energy.

The combination of the experimental observation of HET and the DFT calculations shows that HET between QDs can indeed take place on very short timescales provided that the QDs are strongly coupled and wave functions at high energy are significantly delocalized over both QDs. This strong coupling is evident in the calculated wave functions and, given the good match with the experimental results, likely also occurs in the experimental QDHJ film. Using longer ligands to space the QDs will slow down both the HET process and the back-recombination rate. Engineering the coupling could potentially lead to an optimum between HET and back transfer, as has been shown for electron transfer from molecular dyes to TiO<sub>2</sub> in dye sensitized solar cells<sup>36</sup>.

The above experiments show that HET between QDs is fast and feasible. However, for applications that aim to make use of hot-carriers it is clear that a pathway away from the CdSe QD – PbSe QD interface must be provided to avoid back transfer and to allow

extraction of the carriers.

## 2.7 Conclusions

In conclusion, we have demonstrated ultrafast hot-electron transfer between two different quantum dot species. A maximum of 4.5% was observed for the transfer efficiency just below the CdSe QD absorption onset. Exciting above this threshold should give higher transfer efficiencies. Electrons injected in CdSe QDs are quickly transferred back to PbSe QDs, due to the type-I energy alignment. TDDFT calculations confirm the presence of sub-ps electron transfer between the two QDs and the dependence of the HET efficiency on the initial electron energy.

An efficient hot-carrier solar cell requires selective contacts, allowing only carriers within a narrow energy range to be extracted<sup>7</sup>. Hence, in addition to efficient HET, hot-carrier solar cells require control over the energy levels of both the donor and the acceptor in the HET process. The QDHJ system allows such control over the energy level of both the donor and the acceptor and, as demonstrated here, may also show efficient HET, indicating QDs as a promising material candidate for both light-absorbing and hot-electron extracting materials in HET solar cells.

## 2.8 Methods

**Synthesis of CdSe QDs.** CdSe QDs were obtained via a hot-injection synthesis method, adapted from van Embden et al.<sup>37</sup>. The QDs were synthesized by swift injection of a Se-precursor solution in a hot Cd-precursor solution held at 260° and kept under nitrogen atmosphere, followed by multiple injections of both solutions to sustain further QD growth. The Se injection solution was obtained dissolving 0.327 g Se powder in a solution of 2.5 g trioctylphosphine (TOP, tech grade 90%), 2.5 g 1-octadecene (ODE, tech grade 90%) and 6 g oleylamine (OAm, tech grade 70%), yielding a clear and slightly yellow solution, stored in a nitrogen-filled glovebox. The Se growth solution was obtained dissolving 0.25 g of Se powder in 1.55 g TOP in a nitrogen-filled glovebox, yielding a clear solution. The Cd-precursor growth solution was obtained adding 0.22 g CdO (99.999%), 0.970 g oleic acid (OA, 90%), and 6.23 g ODE to a 3-neck round-bottom flask (BPF) attached to a Schlenk line. The solution was degassed under vacuum (< 1 mbar) for 1 hour at 80°, it was heated to 260° under nitrogen atmosphere until it turned clear and then cooled back to room temperature. Oleylamine (1.13 mL, tech grade 70%) was added to the Cd-solution during cooling. The Cd growth solution was stored in a glovebox. Finally 0.22 g CdO, 3 g OA and 30 g ODE were added to a 3-neck BPF flask, degassed under vacuum for 1 hour at 80° and heated to 260° until the solution turned clear. The Se injection solution was loaded into a 24 mL syringe equipped with a 16G needle and quickly injected into the cadmium solution at 260°. The temperature of the reaction solution was allowed to recover to 250°, where it was held for QD growth. After 20 min, 2 mL of cadmium growth solution and 0.2 mL of selenium growth solution were added dropwise to the reaction. After 3 additions, one every 10 min, the reaction was allowed to proceed further for 10 minutes at 250°, then cooled at room temperature. The reaction solution was washed three times via QD precipitation, induced by the addition of acetone and centrifugation, and resuspension in toluene. After the last precipitation step, the QDs were resuspended in hexane and were stored in a glovebox.

**Synthesis of PbSe QDs.** PbSe QDs were obtained via a hot-injection synthesis method, adapted from Steckel et al.<sup>38</sup>. The QDs were synthesized by swift injection of a Se-precursor solution in a hot

Pb-precursor solution held at 120° and kept under nitrogen atmosphere. The Se injection solution was prepared dissolving 0.553 g Se powder in 19 mL TOP and adding 0.13 mL diphenylphosphine (DPP, 98%). The reaction solution was prepared adding to a 3-neck BPF flask 1.35 g PbO (99,999%), 17 mL ODE and 4 mL OA. The flask was connected to a Schlenk line, where the solution was degassed under vacuum (<1 mbar) for 1 hour, then heated to 125° under nitrogen atmosphere, until it turned clear. The solution was further degassed under vacuum at 100° for half an hour, then heated back to 180° under nitrogen atmosphere. The Se injection solution was loaded into a 20 mL syringe equipped with a 16G needle, and quickly injected into the reaction solution. The solution temperature dropped to approximately 120° after injection. The reaction was allowed to proceed for 30 s, after which it was quenched by immersing the flask in water bath. The reaction solution was diluted in hexane, with addition of ethanol to induce QDs precipitation upon centrifuging. The washing procedure was repeated three times, then the QDs were resuspended in hexane and stored in a glovebox.

**TEM analysis.** HR-TEM images were obtained from a JEOL-JEM 3200 FSC microscope. PbSe and CdSe QDs were deposited on a copper TEM grid covered with a 3 nm thick carbon supporting layer. A single dip-coating cycle was used for each QD material, to obtain roughly a monolayer coverage of the grid. A Fast Fourier Transform (FFT) analysis performed on the TEM images revealed the presence of two lattice periodicities. Applying a band-pass Fourier filter to the TEM image, in order to selectively display one of the two lattice spacing, we found that the smallest lattice spacing correspond to smaller QDs. Furthermore, FFT analysis of individual QDs revealed a square geometry for the reciprocal space points for the smallest spacing component, with a d-spacing of 3.08 nm, compatible with the expected values for a {200} PbSe plane. For the other component, a d-spacing of 3.7 was observed, which can be associated with a {111} plane in wurtzite CdSe. We conclude that both QD species are present on the TEM grids and that intimate contact is possible between QDs of the two materials.

**Film fabrication.** The heterojunction films were fabricated via layer-by-layer growth with a mechanical dip-coater (DC Multi-8, Nima Technology), performed inside a nitrogen-filled glovebox. Each layer is obtained by dipping for 30 seconds a quartz substrate in a solution of QDs (PbSe or CdSe) in hexane, followed by 20 second drying outside the solution, 30 seconds dipping in a solution of the linker molecule (EDT or EDA) in acetonitrile. The concentration of the QD solution was 0.1 mM, determined from the linear absorption of the solutions and from the size-dependent extinction coefficient reported in literature<sup>39, 40</sup>, while the ligand solution had a concentration of 10 mM for EDT and 1 M for EDA. The LbL procedure was repeated 14 times for the EDT capped film (12 for the EDA capped), yielding 7 (6) layers of each of the two QD materials. For each HJ film, two reference individual-QD films were fabricated, employing only one of the two QD solution and half of the total LbL cycles. Thickness measurements were performed scratching a QD film with a razor blade and measuring the depth of the scratch with a profilometer (DEKTAK 8, Veeco). A film thickness of 75 nm was measured for a HJ film fabricated with similar conditions as the EDT-capped HJ film measured in Transient Absorption, while the reference CdSe QD film had a thickness of 47 nm. These values correspond to a layer thickness of 1.6 QDs per layer for the CdSe QD component and 1.8 QDs per layer for the PbSe QD component.

**Transient Absorption.** Pump-probe TA measurements are performed on solid state samples placed inside an air-tight holder, loaded inside a nitrogen filled glovebox. Two quartz windows on opposite sides of the holder allow to perform optical measurements on the sample. A Yb:KGW oscillator (Light Conversion, Pharos SP) is used to produce 180 fs pulses with a 1028 nm wavelength, at a 5 kHz frequency. The pump beam is obtained by sending the fundamental beam through an Optical Parametric Amplifier (OPA) equipped with a second harmonic module (Light Conversion, Orpheus), performing non-linear frequency mixing and producing an output beam whose wavelength can be tuned in the 310-1330 nm window. A small fraction of the fundamental beam power is used to produce a broadband probe spectrum (500-1600nm), by supercontinuum generation in a sapphire crystal. The pump beam is transmitted through a mechanical chopper operating at 2.5 kHz, allowing

one every two pump pulses to be transmitted. Pump and probe beam overlap at the sample position with a small relative angle ( $\sim 8^\circ$ ), with a relative time delay controlled by an automated delay-stage. After transmission through the sample, the pump beam is dumped while the probe is collected at a detector (Ultrafast Systems, Helios). The differential absorbance is obtained via  $\Delta A = \ln(I_{\text{on}}/I_{\text{off}})$ , where  $I$  is the light incident on the detector with either pump on or pump off. TA data are corrected for probe-chirp via a polynomial correction to the coherent artifact. Pump photon fluence was estimated by measuring with a thermopile sensor (Coherent, PS19Q) the pump beam transmission through a pinhole of 1 mm radius.

**TDDFT calculations of a coupled PbSe QD – CdSe QD system.** To computationally investigate the electron injection between PbSe and CdSe QDs, we employed one of the most powerful approaches to study the electron-phonon relaxation dynamics: the non-adiabatic molecular dynamics (NA-MD) method. NA-MD combines a classical description of the nuclei motion and a time-dependent description of the electronic evolution, which includes quantum transition between electronically excited states. In this framework, electrons move in the potential energy surface of a single adiabatic electronic excited state, while the whole set of excited states, is computed “on-the-fly” at each step of the trajectory. Quantum transitions between different electronic states are evaluated stochastically using the fewest switches surface hopping (FSSH) method developed by Tully<sup>41</sup>. When implemented in the time-domain Kohn-Sham (TDKS)<sup>42</sup>, TDKS-FSSH can be used to study electronic transitions for large systems, whereas multi-electronic excited states are derived from one-electron transitions between the computed Kohn-Sham (KS) orbitals.

The time-dependent wave function of the system is calculated in the basis of KS orbitals by:

$$|\psi(\mathbf{x}, t)\rangle = \sum_{k=1}^N c_{pk}(t) |\varphi_p(\mathbf{x}; R)\rangle \quad 2.3$$

Where  $c_{pk}(t)$  are the time-dependent expansion coefficients and  $\varphi_p(\mathbf{x}; R)$  is the adiabatic wave function representing the electronic excited state  $p$ . The electronic solution is obtained by solving the time-dependent Schrödinger equation:

$$i\hbar \frac{\partial}{\partial t} |\psi(\mathbf{x}, t)\rangle = H(\mathbf{x}, t) |\psi(\mathbf{x}, t)\rangle \quad 2.4$$

By combining the two equations above, we obtain the time-dependent Schrödinger equation in the basis of the expansion coefficients:

$$i\hbar \frac{\partial}{\partial t} c_k(t) = \sum_m^{N_e} c_m(t) (\varepsilon_m \delta_{km} + d_{km}) \quad 2.5$$

where  $\varepsilon_m$  is the energy of the excited state  $m$  and  $d_{km}$  is the time-derivative non-adiabatic coupling vector between states  $k$  and  $m$ , and can be reformulated as:

$$d_{km} = -i\hbar \left\langle \varphi_k \left| \frac{\partial}{\partial t} \varphi_m \right. \right\rangle \quad 2.6$$

Typically, a standard electronic structure package provides the energies and the coefficients of the KS orbitals, while a separate module is needed to compute non-adiabatic couplings in (4). For this purpose, we have implemented a new module called QMflows-NAMD [<https://github.com/SCM-NV/qmflows>], which interfaces several quantum chemical codes with PYXAID, a program that describes the time evolution of electronically excited states as illustrated in equation 2.5<sup>43, 44</sup>. QMflows-NAMD

is used to compute the molecular orbital coefficients, energies, and the nonadiabatic coupling elements between KS states at the DFT level of theory using the CP2k code. The non-adiabatic couplings are evaluated numerically using the Meek-Levine formula<sup>45</sup>. Additionally, a min-cost algorithm, implemented in QMflows-NAMD, is used to track the nature of each electronically excited state along the whole trajectory<sup>46</sup>. Finally, the non-adiabatic couplings and excited state energies are written on file in a format readable by PYXAID, which is then used to study the time evolution of the excited states. Here we employed the neglect the back-reaction approximation to decouple the electron dynamics from the nuclear dynamics, and ultimately using the ground state trajectory as the only meaningful one<sup>47</sup>. Such approximation has been demonstrated to be valid for large nanocrystals<sup>48</sup>.

To study the electron dynamics, we first relaxed the PbSe-CdSe system to its most stable structural configuration. We then performed an equilibration NVT dynamics using ab-initio DFT/PBE molecular dynamics simulation at 300 K using a velocity rescaling thermostat. Once the system had reached an equilibrium, we performed a production run with an NVE ensemble for 2 ps.

For each simulation, we used a single initial condition at  $t=0$ , and we solved stochastically between 7-14 hopping trajectories, depending on the number of available PbSe-localized states available in between CdSe-localized states at different excess energies.

2

### References

1. Brus, L. E. Electron-electron and electron-hole interactions in small semiconductor crystallites: The size dependence of the lowest excited electronic state. *J. Chem. Phys.* 80, 4403 (1984).
2. Banin, U., Cao, Y. W., Katz, D. & Millo, O. Identification of atomic-like electronic states in indium arsenide nanocrystal quantum dots. *Nature* 400, 542-544 (1999).
3. Pandey, A. & Guyot-Sionnest, P. Slow electron cooling in colloidal quantum dots. *Science* 322, 929-932 (2008).
4. Klimov, V. I. Detailed-balance power conversion limits of nanocrystal-quantum-dot solar cells in the presence of carrier multiplication. *Appl. Phys. Lett.* 89, 123118 (2006).
5. Cooney, R. R., et al. Breaking the Phonon Bottleneck for Holes in Semiconductor Quantum Dots. *Phys. Rev. Lett.* 98, 177403 (2007).
6. Kambhampati, P. Hot Exciton Relaxation Dynamics in Semiconductor Quantum Dots: Radiationless Transitions on the Nanoscale. *J. Phys. Chem. C* 115, 22089-22109 (2011).
7. Ross, R. T. & Nozik, A. J. Efficiency of hot-carrier solar energy converters. *J. Appl. Phys.* 53, 3813-3818 (1982).
8. Guyot-Sionnest, P., Wehrenberg, B. & Yu, D. Intraband relaxation in CdSe nanocrystals and the strong influence of the surface ligands. *J. Chem. Phys.* 123, 074709 (2005).
9. Gao, Y., et al. Enhanced hot-carrier cooling and ultrafast spectral diffusion in



- strongly coupled PbSe quantum-dot solids. *Nano Lett.* 11, 5471-5476 (2011).
10. Tisdale, W. A., et al. Hot-electron transfer from semiconductor nanocrystals. *Science* 328, 1543-1547 (2010).
  11. Robel, I., Kuno, M. & Kamat, P. V. Size-dependent electron injection from excited CdSe quantum dots into TiO<sub>2</sub> nanoparticles. *J. Am. Chem. Soc.* 129, 4136-4137 (2007).
  12. Li, M., et al. Slow cooling and highly efficient extraction of hot carriers in colloidal perovskite nanocrystals. *Nat. Commun.* 8, 14350 (2017).
  13. Pandey, A. & Guyot-Sionnest, P. Hot electron extraction from colloidal quantum dots. *J. Phys. Chem. Lett.* 1, 45-47 (2010).
  14. Sewall, S. L., et al. State-resolved studies of biexcitons and surface trapping dynamics in semiconductor quantum dots. *J. Chem. Phys.* 129, 084701 (2008).
  15. Tyagi, P. & Kambhampati, P. False multiple exciton recombination and multiple exciton generation signals in semiconductor quantum dots arise from surface charge trapping. *J. Chem. Phys.* 134, 094706 (2011).
  16. Law, M., et al. Structural, optical, and electrical properties of PbSe nanocrystal solids treated thermally or with simple amines. *J. Am. Chem. Soc.* 130, 5974-5985 (2008).
  17. Luther, J. M., et al. Structural, optical and electrical properties of self-assembled films of PbSe nanocrystals treated with 1,2-ethanedithiol. *ACS Nano* 2, 271-280 (2008).
  18. Boehme, S. C., et al. In situ spectroelectrochemical determination of energy levels and energy level offsets in quantum-dot heterojunctions. *J. Phys. Chem. C* 120, 5164-5173 (2016).
  19. Klimov, V. I. Optical nonlinearities and ultrafast carrier dynamics in semiconductor nanocrystals. *J. Phys. Chem. B* 104, 6112-6123 (2000).
  20. Klimov, V. I., McBranch, D. W., Leatherdale, C. A. & Bawendi, M. G. Electron and hole relaxation pathways in semiconductor quantum dots. *Phys. Rev. B* 60, 13740-13749 (1999).
  21. Sewall, S. L., et al. State-to-state exciton dynamics in semiconductor quantum dots. *Phys. Rev. B* 74, 235328 (2006).
  22. Fan, F., et al. Continuous-wave lasing in colloidal quantum dot solids enabled by facet-selective epitaxy. *Nature* 544, 75-79 (2017).

23. Geiregat, P., et al. Coulomb shifts upon exciton addition to photoexcited PbS colloidal quantum dots. *J. Phys. Chem. C* 118, 22284-22290 (2014).
24. Kambhampati, P. Multiexcitons in Semiconductor Nanocrystals: A Platform for Optoelectronics at High Carrier Concentration. *J. Phys. Chem. Lett.* 3, 1182-1190 (2012).
25. Alimoradi Jazi, M., et al. Transport properties of a two-dimensional PbSe square superstructure in an electrolyte-gated transistor. *Nano Lett.* 17, 5238-5243 (2017).
26. Empedocles, S. A. & Bawendi, M. G. Quantum-confined stark effect in single CdSe nanocrystallite quantum dots. *Science* 278, 2114-2117 (1997).
27. Trinh, M. T., et al. Nature of the second optical transition in PbSe nanocrystals. *Nano Lett.* 8, 2112-2117 (2008).
28. Boehme, S. C., et al. Electrochemical Control over Photoinduced Electron Transfer and Trapping in CdSe-CdTe Quantum-Dot Solids. *ACS Nano* 8, 7067-7077 (2014).
29. De Geyter, B., et al. Broadband and picosecond intraband absorption in lead-based colloidal quantum dots. *ACS Nano* 6, 6067-6074 (2012).
30. Spoor, F. C., et al. Hole cooling is much faster than electron cooling in PbSe quantum dots. *ACS Nano* 10, 695-703 (2016).
31. Guyot-Sionnest, P., Shim, M., Matranga, C. & Hines, M. Intraband relaxation in CdSe quantum dots. *Phys. Rev. B* 60, R2181-R2184 (1999).
32. Gao, Y., et al. Disorder strongly enhances Auger recombination in conductive quantum-dot solids. *Nat. Commun.* 4, 2329 (2013).
33. Perdew, J. P., Burke, K. & Ernzerhof, M. Generalized Gradient Approximation Made Simple. *Phys. Rev. Lett.* 77, 3865-3868 (1996).
34. Azpiroz, J. M., Ugalde, J. M. & Infante, I. Benchmark Assessment of Density Functional Methods on Group II-VI MX (M = Zn, Cd; X = S, Se, Te) Quantum Dots. *J. Chem. Theory Comput.* 10, 76-89 (2014).
35. Hutter, J., Iannuzzi, M., Schiffmann, F. & VandeVondele, J. cp2k:atomistic simulations of condensed matter systems. *Wiley Interdiscip. Rev.: Comput. Mol. Sci.* 4, 15-25 (2014).
36. Kroeze, J. E., et al. Alkyl chain barriers for kinetic optimization in dye-sensitized solar cells. *J. Am. Chem. Soc.* 128, 16376-16383 (2006).

37. van Embden, J. & Mulvaney, P. Nucleation and growth of CdSe nanocrystals in a binary ligand system. *Langmuir* 21, 10226-10233 (2005).
38. Steckel, J. S., Yen, B. K., Oertel, D. C. & Bawendi, M. G. On the mechanism of lead chalcogenide nanocrystal formation. *J. Am. Chem. Soc.* 128, 13032-13033 (2006).
39. Moreels, I., et al. Composition and size-dependent extinction coefficient of colloidal PbSe quantum dots. *Chem. Mater.* 19, 6101-6106 (2007).
40. Jasieniak, J., et al. Re-examination of the size-dependent absorption properties of CdSe quantum dots. *J. Phys. Chem. C* 113, 19468-19474 (2009).
41. Tully, J. C. Molecular dynamics with electronic transitions. *J. Chem. Phys.* 93, 1061-1071 (1990).
42. Craig, C. F., Duncan, W. R. & Prezhdo, O. V. Trajectory surface hopping in the time-dependent Kohn-Sham approach for electron-nuclear dynamics. *Phys. Rev. Lett.* 95, 163001 (2005).
43. Akimov, A. V. & Prezhdo, O. V. The PYXAID Program for Non-Adiabatic Molecular Dynamics in Condensed Matter Systems. *J. Chem. Theory Comput.* 9, 4959-4972 (2013).
44. Akimov, A. V. & Prezhdo, O. V. Advanced Capabilities of the PYXAID Program: Integration Schemes, Decoherence Effects, Multiexcitonic States, and Field-Matter Interaction. *J. Chem. Theory Comput.* 10, 789-804 (2014).
45. Meek, G. A. & Levine, B. G. Evaluation of the Time-Derivative Coupling for Accurate Electronic State Transition Probabilities from Numerical Simulations. *J. Phys. Chem. Lett.* 5, 2351-2356 (2014).
46. Fernandez-Alberti, S., et al. Shishiodoshi unidirectional energy transfer mechanism in phenylene ethynylene dendrimers. *J. Chem. Phys.* 137, 22A526 (2012).
47. Akimov, A. V. & Prezhdo, O. V. in *Encyclopedia of Nanotechnology, Theory of Nonadiabatic Electron Dynamics in Nanomaterials* (ed. Bhushan, B.) 1-20. (Springer Netherlands 2014).
48. Akimov, A. V., Neukirch, A. J. & Prezhdo, O. V. Theoretical insights into photoinduced charge transfer and catalysis at oxide interfaces. *Chem. Rev.* 113, 4496-4565 (2013).
49. Sandeep, C. S. S., et al. Epitaxially Connected PbSe Quantum-Dot Films:

- Controlled Neck Formation and Optoelectronic Properties. *ACS Nano* 8, 11499-11511 (2014).
50. Gao, Y., et al. Photoconductivity of PbSe Quantum-Dot Solids: Dependence on Ligand Anchor Group and Length. *ACS Nano* 6, 9606-9614 (2012).
51. Boehme, S. C., et al. Electrochemical charging of CdSe quantum dot films: dependence on void size and counterion proximity. *ACS Nano* 7, 2500-2508 (2013).

## Appendix

2

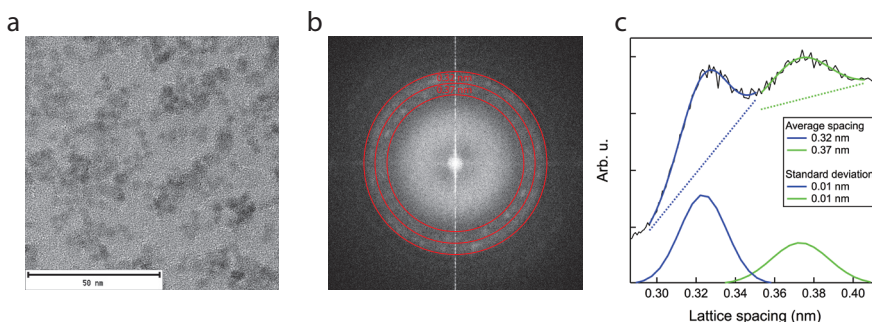


**Figure 2.6. Identification of the two quantum dot (QD) components via Transmission Electron Microscopy (TEM).** a, TEM image of a sample fabricated dipcoating a TEM grid one time in a PbSe QD solution, one time in a CdSe QD solution, and ligand exchanging for EDT linkers between the cycles. b, Fourier transform of Figure 2.6a, highlighting the presence of two rings of diffraction features. c, radial integration of Figure 2.6b, fitted with a Gaussian feature and a line.

#### Fourier analysis of TEM images

Figure 2.6a shows a TEM image of a substrate dipped once in a solution of PbSe QDs (2.3 nm) and in a solution CdSe QDs (4.5nm), followed by ligand exchange with ethanedithiol (EDT) linkers. The small size of the PbSe QDs and the material contrast of the CdSe QDs did not allow us to resolve the two QD components with our TEM setup. Therefore, we performed a Fourier transform of the images, displayed in Figure 2.6b, highlighting the presence of two resolvable lattice distances.

Radial integration of the Fourier transform, displayed in Figure 2.6c, revealed the presence of two intensity peaks superimposed on a varying background. Fitting the two peaks with a Gaussian profile and a linear slope, approximately describing the background, yielded a d-spacing for the two features of 0.32 nm and 0.37 nm.

**Table 2.1. d-spacings for planes in rocksalt-PbSe.**

Rocksalt-PbSe Miller indices	d-spacing (nm)
{200}	0.306
{2-20}	0.217
{4-2-2}	0.126
{4-40}	0.109

**Table 2.2. d-spacings for planes in wurtzite-CdSe.**

Wurtzite-CdSe Miller indices	d-spacing (nm)
{100}	0.372
{002}	0.351
{101}	0.329
{102}	0.255

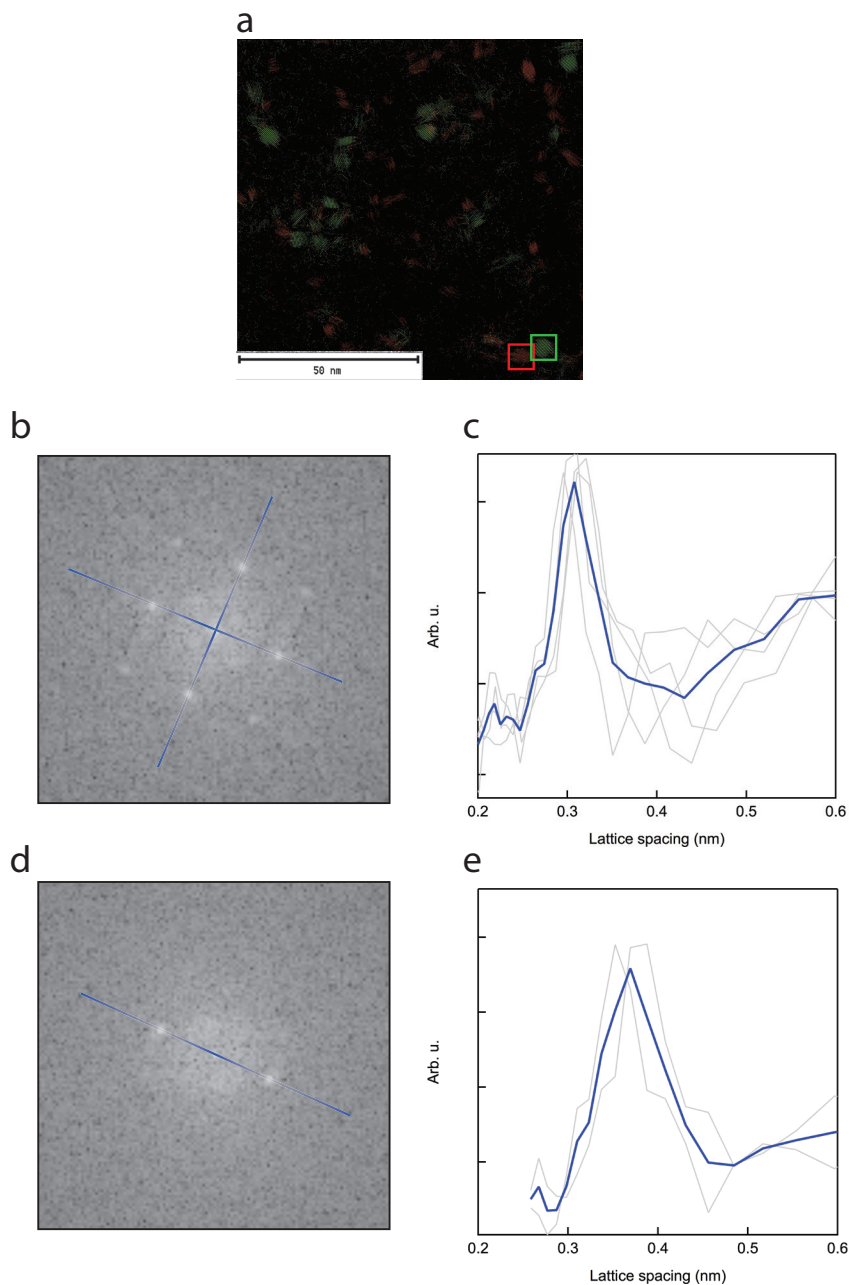


**Figure 2.7. Fourier analysis of neighboring QDs.** **a**, superposition of two images obtained applying to the image in Figure 2.6a two different Fourier bandpass filters, selecting the periodicity  $0.32 \pm 0.02$  nm (red) and  $0.38 \pm 0.02$  nm (green). **b**, Fourier transform of the portion of Figure 2.7a contained in the green square. **c**, plot of the intensity of the diffraction features in Figure 2.7b along the radial direction (blue lines). **d**, Fourier transform of the portion of Figure 2.7a contained in the red square. **e**, plot of the intensity of the diffraction features in Figure 2.7d along the radial direction (blue line).

Applying a bandpass filter to the image, centered to one of the two periodicities, and taking the inverse Fourier transform of the image, we produce two images containing only the atomic features corresponding to the selected lattice spacing. Figure 2.7a shows the superposition of the two images: the atomic feature corresponding to the  $0.32 \pm 0.02$  nm periodicity (highlighted in red), those corresponding to the  $0.38 \pm 0.02$  nm periodicity (in green). Table 2.1 and Table 2.2 show the calculated lattice spacing of different planes for rocksalt PbSe and wurtzite CdSe, respectively. It must be noted that, while the 0.38 nm can be unambiguously assigned to the periodicity of the {100} plane of wurtzite CdSe, the Fourier peak at 0.32 nm can contain contributions from both the CdSe {101} plane and the PbSe {200} plane. From Figure 2.7a it can be seen how the QDs corresponding to the 0.32 nm periodicity have a smaller size than the other QDs, suggesting this periodicity can be attributed primarily to the presence of the smaller PbSe QDs. Applying the Fourier transform on the two neighbouring QDs shown in Figure 2.1a (red and green rectangles in Figure 2.7a), produces the Fourier images in Figure 2.7b and Figure 2.7d. Figure 2.7b corresponds to the QD with 0.32 nm spacing

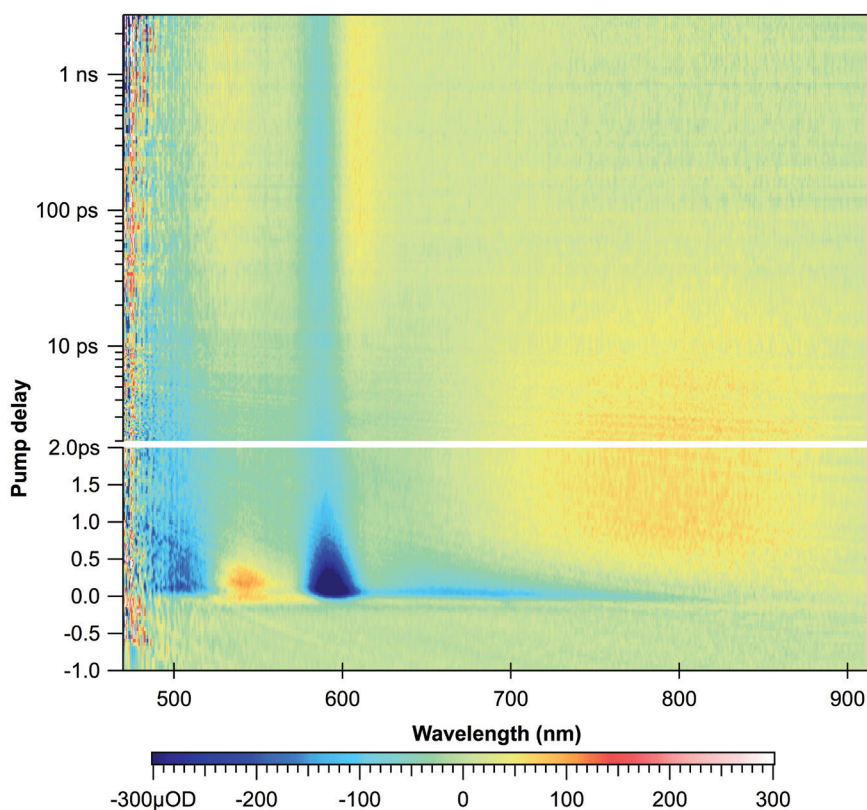


**Figure 2.8.** TA response of an EDA-capped HJ film. Color map showing the differential absorbance of a HJQD film composed of 4.5 nm CdSe QDs and 2.3 nm PbSe QDs, treated with EDA. The film is excited at 700 nm with an absorbed fluence of  $9.03 \cdot 10^{12}$  photons/cm<sup>2</sup> per pulse.

(red highlights) and clearly shows a square arrangement of the diffraction points. The d-spacing, shown by the intensity peaks in Figure 2.7c, closely matches the predicted 0.306 nm spacing of {200} planes in PbSe. Similar analysis of the other QD (green highlights) reveals diffraction peaks with centered at 0.37 nm, closely matching the periodicity of {100} facets in wurtzite CdSe. Hence, we attribute the two QDs to the two different materials and note that they are in close proximity to each other but that they remain distinct particles.

### Transient Absorption results for an EDA-treated film

This section shows the result of a TA investigation on the HJQD film treated during the layer-by-layer processing with ethanediamine (EDA) instead of EDT. The treatment is expected to reduce inter-particle distance via removal of the original ligands, leading to QD necking<sup>49,50</sup>.

Figure 2.8 shows a TA measurement performed on the EDA-treated HJQD film with 700 nm excitation, showing the same behavior observed for the EDT treated films: the appearance of a CdSe bleach upon photoexcitation, which decays in a sub-ps timescale; on a longer time-scale (~100 ps) a derivative-like feature appears at the CdSe bandgap energy. The traces in Figure 2.9a show the normalized CdSe bleach of the EDA-HJQD film obtained fitting TA measurements performed with different excitation wavelengths. The initial value of the bleach increases for decreasing excitation wavelength, as observed for the EDT-treated films. HET efficiency values obtained for the measurements are shown in Figure 2.9b, which are in line with the values obtained for the EDT-treated sample.

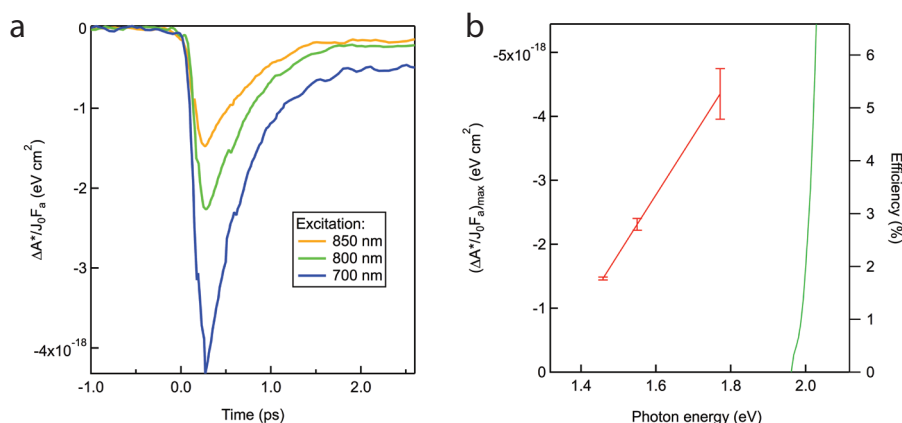


**Figure 2.9. Hot-electron transfer in an EDA-capped HJ film.** **a**, fitted amplitude of the CdSe bleach component of the EDA-HJQD film, plotted for different excitation wavelengths. **b**, plot of the bleach amplitude maxima as a function of excitation energy. The right axis shows the HET efficiency corresponding to each bleach value. Error bars are obtained from the standard deviation of the amplitude maxima, obtained from repeated measurements. The green line indicates the onset of the CdSe QD absorption. Error bars are obtained from the standard deviation of the bleach amplitude maxima obtained in repeated measurements.

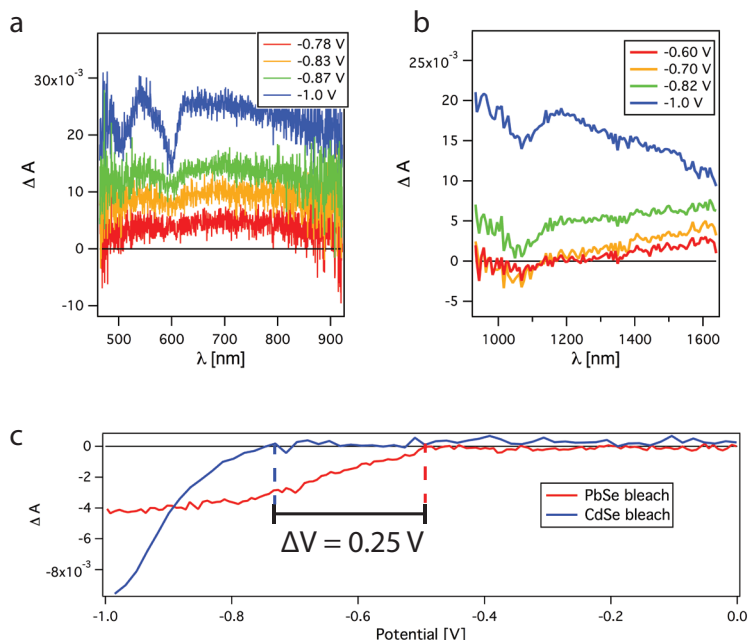


**Figure 2.10. Spectro-electrochemical determination of conduction band offset.** a-b, differential absorbance of the QDHJ film as a function of the applied potential, for the visible (a) and NIR (b) spectral regions, highlighting the presence of two bleach features at the bandgap of the two QD materials. c, Amplitude of the Gaussian features fitted to the PbSe and CdSe bleach as a function of the applied potential.

### Spectro-electrochemical determination of conduction-band offset in heterojunction film

The HJ film used for the spectro-electrochemical measurements was prepared depositing alternating layers of the same QD materials used for the TA study, using a layer-by-layer dipcoating processing on an ITO substrate. During each deposition cycle the film is dipped into the QD solution, slowly extracted, leaving a layer of QDs on the substrate, and then ligand exchanged with ethanedithiol (EDT).

The spectro-electrochemical measurement was performed in a previously reported setup<sup>51</sup>. The sample was immersed in a LiClO<sub>4</sub> electrolyte solution in acetonitrile, with a Ag wire pseudoreference electrode and a Pt counter electrode. The potential of the sample was controlled with a PGSTAT128N (Autolab) potentiostat, while changes in the sample absorbance were monitored simultaneously with a USB2000 (Ocean Optics) spectrometer (300-1000 nm) and a NIRQuest 256 (Ocean Optics) spectrometer (900-2500 nm). In the following text, reported values of the potential are relative to the potential of the Ag electrode.

The CV scan was performed with a scan rate of 20 mV/s, scanning from 0 to -1 V. Figure 2.10a shows the absorbance changes of the QDHJ film in the visible range. No absorbance change is observed up to -0.7 V, after which a positive background

starts increasing, remaining roughly constant over the visible range. Around  $-0.8$  V a bleach feature appears on top of the positive background at the wavelength of CdSe 1S absorption (597 nm), indicating the injection of electrons in the conduction band of CdSe QDs. Figure 2.10b shows the same potential scan, monitored in the NIR range. From  $\sim -0.6$  V a bleach feature appears at the wavelength of the PbSe 1S absorption (1068 nm), indicating electron injection to the conduction band of PbSe QDs. When the potential is lowered further, a broad induced absorption feature start increasing, and eventually dominates the signal for the lowest potentials. The spectral traces obtained from the two measurements were fitted at each applied potential, to separate the bleach contribution from the induced absorption background. The visible range data were fitted with the sum of a Gaussian term (CdSe bleach) and a constant background. The NIR signal was fitted with a Gaussian term (PbSe bleach) and a linear term, to empirically take into account the shape of the NIR background. Figure 2.10c shows the amplitudes of the two Gaussian terms, allowing us to extract the potential difference between the onsets of the bleach features; i.e.  $\Delta V = 0.25$  V. The measured offset probably provides an upper limit for the actual conduction band offset, as additional energy is required to overcome charging effects.

### Rise dynamics of CdSe QDs bleach signal

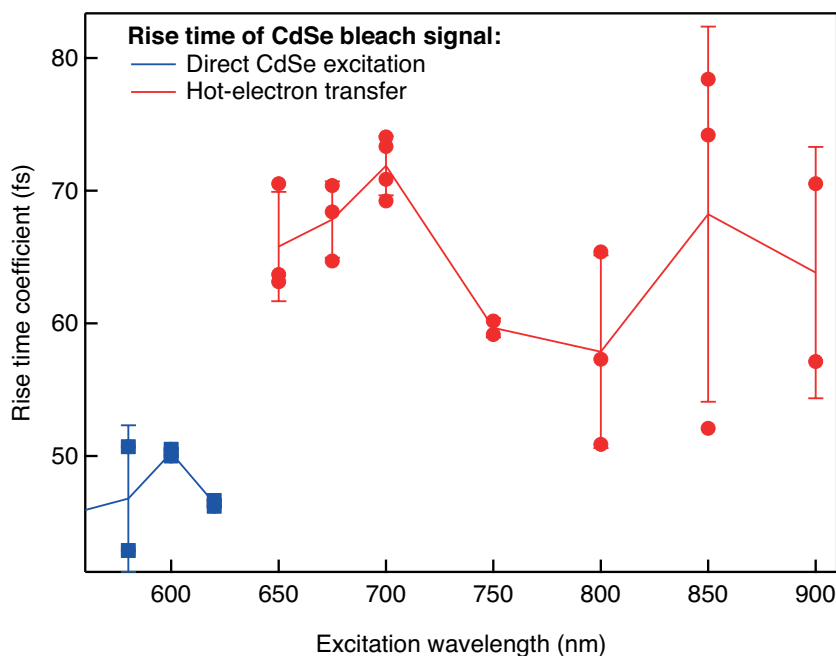


**Figure 2.11. Rise time coefficient for the CdSe QD bleach signal as a function of excitation energies.** Going from direct excitation of CdSe QDs to the hot-electron transfer excitation regime leads to a sharp increase in the rise time, arising from the electron transfer pathway. Error bars represent the standard deviation of the rise time coefficients at each excitation wavelength, obtained from repeated measurements.

In order to quantify the rise time of the CdSe QDs bleach signal, we fitted the experimental bleach traces to the equation:

$$f(t) = A \left( 1 + \operatorname{erf} \left( \frac{t - t_0}{\sqrt{2}\sigma} \right) \right) \quad 2.7$$

Where  $\sigma$  is a coefficient indicating how quickly does the bleach signal rise. Figure 2.11 shows a plot of  $\sigma$  for different excitation wavelengths, indicating that the CdSe bleach rise time increases sharply going from direct CdSe QD excitation to a sub-CdSe bandgap excitation of the system. In this regime, the electron needs first to transfer from PbSe to CdSe QDs, and subsequently cool within the manifold of CdSe excited states, thus resulting in a longer build-up time for the bleach signal.

### Estimate of electron back-transfer from CdSe to PbSe QDs

TA measurements on the QDHJ film show that the CdSe bleach decays rapidly after photoexcitation, for both below and above CdSe bandgap excitation, indicating that electrons leave the CdSe QDs. The measured type-I band alignment between the two QD materials suggests electrons would favorably transfer from CdSe to PbSe QDs.

To confirm this relaxation pathway, we measured the TA response at the bandedge of the PbSe QD component, comparing the PbSe bleach measured with different excitation energies. Upon below CdSe bandgap excitation, only a small fraction of the excited electrons populate CdSe QDs (Fig. 2.4b). Conversely, above CdSe bandgap excitation results in more than 15% of the charges localizing on CdSe QDs, estimated with the same method employed to calculate HET efficiencies: rescaling the initial normalized bleach by the bleach cross section. Figure 2.12 displays in as red dots the normalized PbSe bleach for below CdSe-bandgap excitation. Errors bars, when present, are obtained repeating the measurement with different excitation fluence and taking the standard deviation of the results. This procedure is allowed because of the linearity of the measured bleach signal with power. Comparing the average value of the PbSe bleach for below CdSe-bandgap excitation (red line) with the values obtained for above CdSe-bandgap excitation (green points), it is possible to notice that the difference is not statistically significant. Thus, within the accuracy of the measurement, initial excitation of a significant fraction of electrons in CdSe QDs doesn't result in an appreciable change in the final electron population of the PbSe QDs. We then estimated the expected decrease in PbSe bleach in the absence of electron transfer, multiplying the average PbSe bleach with the fraction of charges initially photoexcited on PbSe QDs. The estimated bleach values (Figure 2.12, blue dots) are significantly lower than what is experimentally observed. The result suggests near unity yield of the transfer process from CdSe to PbSe QDs.

### Fitting method for TA measurements

To solve the spectral overlap between the TA features of the two QDs in the visible range we fitted each TA spectrum with the function:

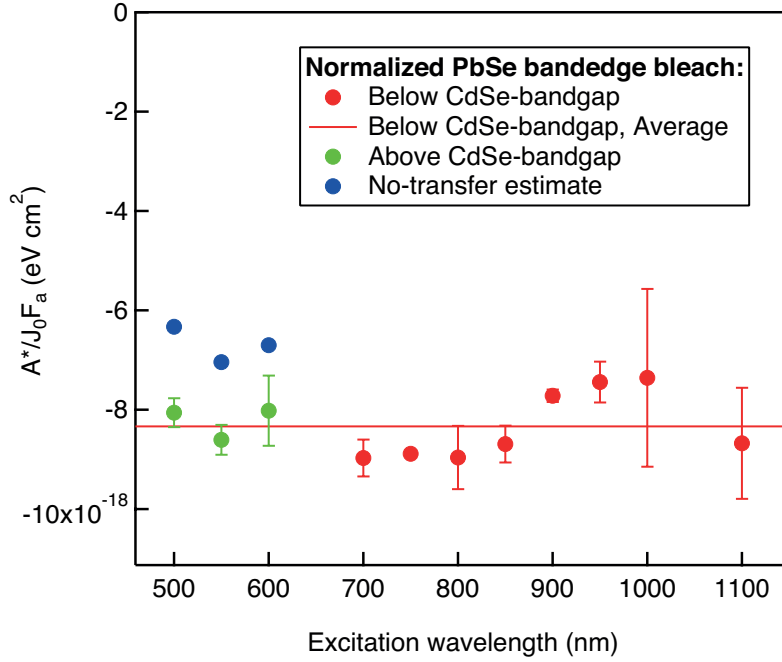


**Figure 2.12. Normalized PbSe TA bleach as a function of excitation wavelength.** The red dots indicate the value of PbSe bleach for below CdSe-bandgap excitation, while the green dots show the PbSe bleach for above CdSe-bandgap excitation. Comparing the average value of the PbSe bleach for below CdSe-bandgap excitation (red line) with the green dot values indicates that the two excitation regimes produce the same amount of PbSe bleach, within experimental errors. Furthermore, estimating the reduction of PbSe bleach in the case of negligible electron transfer (blue dots) indicates that the constant PbSe bleach value is associated with efficient transfer from CdSe to PbSe QDs. Error bars are obtained repeating the measurement with the same excitation wavelength multiple times and calculating the standard deviation of the normalized TA bleach.

$$\begin{aligned}
 f(\lambda, t) = & A_g(t) \exp\left[-\frac{(\lambda - \lambda_g)^2}{2\sigma_g^2}\right] + A_s(t) \left\{ \exp\left[-\frac{(\lambda - \lambda_g)^2}{2\sigma_g^2}\right] - \exp\left[-\frac{(\lambda - \lambda_g - \Delta\lambda_{sh})^2}{2\sigma_g^2}\right] \right\} \\
 & + A_{bg}(t)(\lambda - \lambda_{bg}(t))
 \end{aligned} \tag{2.8}$$

The first term, a Gaussian peak, accounts for the bleach of the Gaussian-shaped CdSe 1S feature. The second term describes the TA signal produced by a shift of the linear absorption associated with electrostatic interaction: it is obtained by subtracting the Gaussian feature of the unperturbed CdSe 1S absorption by the same Gaussian feature shifted by  $\Delta\lambda_{sh}$ . The last term is a line, empirically describing the shape of the slowly varying PbSe induced absorption background in a small wavelength range around the CdSe 1S feature. Of the 7 fit parameters, 3 are held constant:  $\lambda_g$  and  $\sigma_g$  are extracted from a fit of the CdSe 1S linear absorption in a CdSe-only film;  $\Delta\lambda_{sh}$  is fixed at 5 nm, chosen to be a reasonable value for a Stark-shift of the CdSe 1S transition (more details on the

choice for  $\Delta\lambda_{\text{sh}}$  are provided in the following section). Thus the TA signal originating from the CdSe QDs is fitted changing the amplitudes of two fixed-shape features, while the line describing the PbSe background is left unconstrained.

2

The bleach amplitude  $A_g(t)$ , extracted from the fit, is multiplied by  $\sqrt{2\pi} \sigma_g$  to obtain the energy integrated bleach amplitude  $\Delta A_g^*(t)$ , whose value divided by the absorbed photon fluence is shown in Figure 2.4a for different excitation energy.

#### Effect of the choice of $\Delta\lambda_{\text{sh}}$ on the TA fit

The  $\Delta\lambda_{\text{sh}}$  parameter of the TA fit was held at a constant value of 5 nm, corresponding to a 17 meV redshift of the CdSe absorption spectrum. Similar shift values were obtained in electric-field dependent PL measurements on CdSe QDs under a  $\sim 100$  kV/cm electric field<sup>26</sup>. Figure 2.13 shows the CdSe bleach rescaled by the absorbed photon fluence, obtained fitting the same TA measurement (700 nm excitation,  $1.05 \cdot 10^{13}$  photons/cm<sup>2</sup>·pulse) with  $\Delta\lambda_{\text{sh}}$  values between 3 and 10 nm. While the choice for  $\Delta\lambda_{\text{sh}}$  affects appreciably the bleach estimate in the 10 ps – 3 ns range, the peak value of the bleach remains largely unaffected. Thus the HET efficiency, based on the peak value of the bleach, can be safely estimated considering any  $\Delta\lambda_{\text{sh}}$  value in the 3 – 10 nm range.

#### Response of CdSe QD film in TA measurements with below-bandgap excitation

As mentioned in the main text, exciting a CdSe QD film below the onset of its linear absorption still results in bleaching of the CdSe bandedge absorption, which is however negligible compared to the magnitude of bleach arising in the HJ film excited at the same wavelength with comparable power (Figure 2.2f).

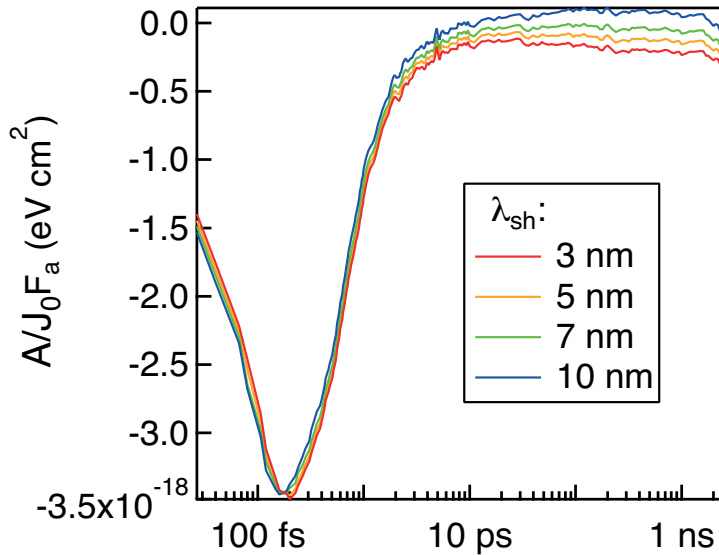


**Figure 2.13. Influence of  $\Delta\lambda_{\text{sh}}$  on the fit of the CdSe 1S bleach.** Time-dependence of CdSe rescaled bleach obtained fitting a TA measurement with different values of the  $\Delta\lambda_{\text{sh}}$  parameter. The TA measurement was performed exciting at 700 nm, with a fluence of  $1.05 \cdot 10^{13}$  photons/cm<sup>2</sup>·pulse.

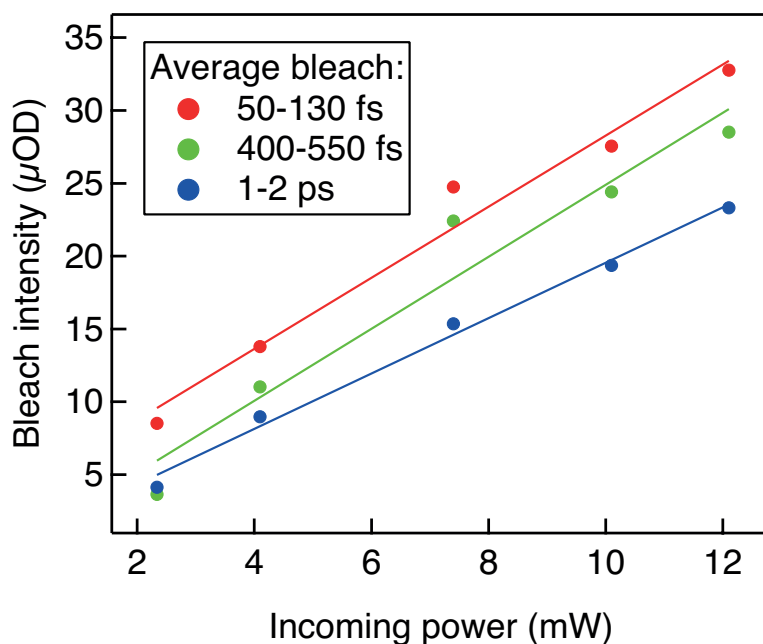


**Figure 2.14. Power dependence of below-bandgap excitation response in a CdSe QD film.** Exciting a CdSe QD film with 700 nm light, a small bleach of the CdSe 1S feature develops. The intensity of the bleach signal scales linearly with the incoming power.

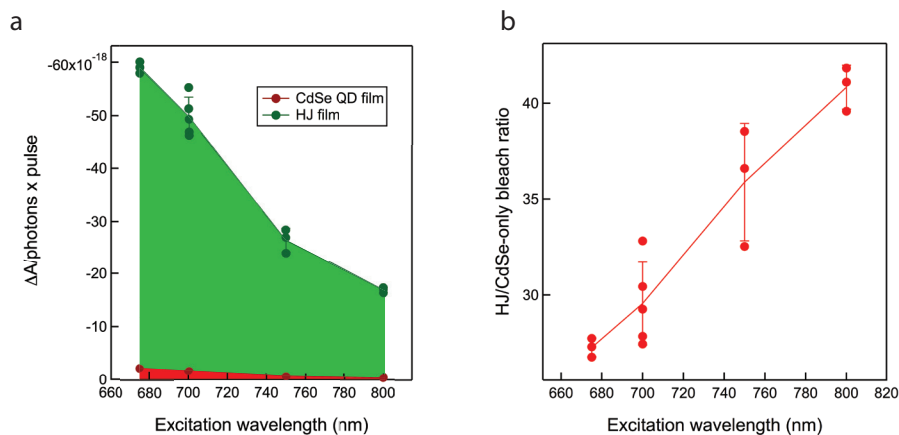


**Figure 2.15. Estimate of the contribution of direct CdSe excitation to the CdSe 1S bleach.** **a**, bleach per incoming photon per pulse in the HJ and CdSe QD film, as a function of excitation wavelength. The graph makes clear that the bleach arising from CdSe QDs alone does not contribute significantly to the signal observed in the HJ film. **b**, ratio between the CdSe bleach amplitude observed in the HJ film and the same quantity measured in the CdSe QD film. Error bars represent the standard deviation of the ratios at each excitation wavelength, obtained from repeated measurements.

We characterized the behavior of the CdSe QD film upon below-bandgap excitation, measuring the power-dependence of the bleach resulting upon 700 nm excitation. Figure 2.14 shows the power-dependence of the bleach signal, averaged over three different time intervals, showing a linear dependence.

The presence of a bleach feature in the CdSe QD film for below-bandgap excitation is clearly arising from a different process than the one proposed for the HJ film, involving transfer of hot-electron from PbSe to CdSe QDs. Thus, is crucial for our interpretation of the CdSe TA bleach in the 675-1100 nm excitation range that the bleach observed in the CdSe QD film is negligible compared to the same quantity measured in the HJ film. We compared the amplitude of the bleach feature in the CdSe QD film and HJ film, for excitations in the 675-800 nm range. The bleach amplitudes were rescaled by the number of incoming photons in each pulse, exploiting the linearity of the bleach with the incoming power, in order to compare measurements with different powers. Figure 2.15a shows the bleach per incoming photon in the two films. Figure 2.15b shows the ratio between the bleach amplitude in the HJ film and in the CdSe QD film, indicating that the HJ film signal remains more than 20 times higher than the signal observed in the CdSe QD film.

### Determination of the bleach cross-section of CdSe QDs

In order to quantify the efficiency of the transfer process, we need to estimate the bleach induced in a CdSe QD by a unit area density of electrons; i.e. the bleach cross-section  $\sigma_b$ . As reported by Boehme et al.<sup>28</sup>, the energy integrated differential absorption of the CdSe 1S feature can be related to the area-density of electrons  $N_e$ , by:

$$\Delta A^* = N_e \frac{\sigma_b}{\ln(10)} \quad 2.9$$

where  $\sigma_b$  is an energy integrated bleach cross-section and  $F_a J_0$  is the absorbed photon fluence. In a CdSe QD-film, directly excited and in absence of carrier multiplication or significant Auger recombination during the excitation pulse, each absorbed photon leads to the creation of one exciton. Thus, directly after photoexcitation,  $N_e = F_a J_0$  and the bleach cross-section can be determined as:

$$\sigma_b = \frac{\Delta A^*(t=0, \text{CdSe-only})}{F_a J_0} \ln(10) \quad 2.10$$

### Rate-equation model for the fitting of CdSe bleach dynamics

In order to rationalize the dynamics of the CdSe bleach observed in the TA measurements, we consider HET to be in competition with cooling and back-transfer of injected electrons to PbSe QDs, and employ a rate-equation model to qualitatively describe the process. The conduction bands of the two materials are modeled by two sets of electron levels, uniformly spaced in energy and displaced by a fixed conduction band offset, determined spectro-electrochemically. The energy spacing between levels,  $dE$ , is taken as small as possible, to simulate a continuous density of states. This choice is motivated by the lack of detailed information on the position of energy levels in the

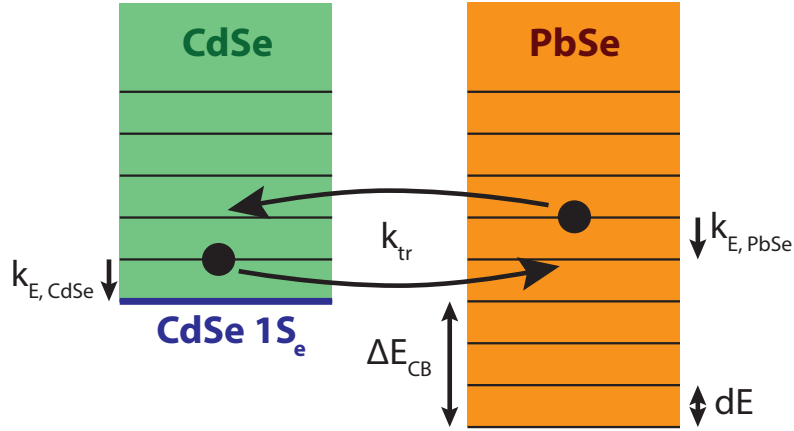


**Figure 2.16. Schematics of the energy structure in the rate-equation model.** The conduction bands of the two materials are represented via two sets of energy states, separated by an arbitrarily chosen energy spacing  $dE$ . The two cooling rates ( $k_{E,CdSe}$  and  $k_{E,PbSe}$ ) and the transfer rate ( $k_{tr}$ ) are constant in energy.

coupled QD film. The rate of population change of an electron level  $N_x$  ( $x = \text{CdSe}$  or  $\text{PbSe}$ ) is determined by:

$$\begin{aligned} \frac{dN_x(t, E)}{dt} = & k_{tr} (N_y(t, E) - N_x(t, E)) \Theta(E - E_{CdSe, CB}) \\ & + k_{E,x} (N_x(t, E + dE) - N_x(t, E)) \Theta(E - E_{x, CB}) \end{aligned} \quad 2.11$$

where  $k_{tr}$  and  $k_{E,x}$  are, respectively, the rate of transfer between the two QDs and a transition rate to the following lower energy state in the same QDs, while  $dE$  indicates the chosen energy step.  $\Theta$  indicates the Heaviside function, stopping the transfer between the two QDs for states below the lowest CdSe state and stopping the cooling at the conduction band edge of each material. The transfer rate and the cooling rate are assumed to be independent of electron energy and the transfer rate is assumed to be equal in both directions, in order to keep the model as simple as possible.

The simulation is initialized with the electron density completely localized on a single PbSe level at energy  $E_{max}$ , determined considering a symmetric division of the photon excess energy between electron and hole. As the simulation evolves, the electron density starts spreading to lower energies and transferring to the CdSe QD component. At each time  $t_i$ , the electron density  $N(t_i, E_i)$  is equal to the probability of finding an electron in  $E_i$  at time  $t_i$ , given an initial excitation at the energy  $E_{max}$ .

The model was used to fit the time-dependence of the fractional CdSe  $1S_e$  population, determined experimentally, using the transfer rate and the two materials cooling rates as fitting parameters (Figure 2.16). The rate  $k_{tr}$  sets the cooling dynamics in each of the two energy continua, and, as such, depends on the choice of the energy spacing between levels. We can relate the value of  $k_{tr}$  to the experimentally determined energy loss rate,  $\gamma_E = k_{tr} dE$ .

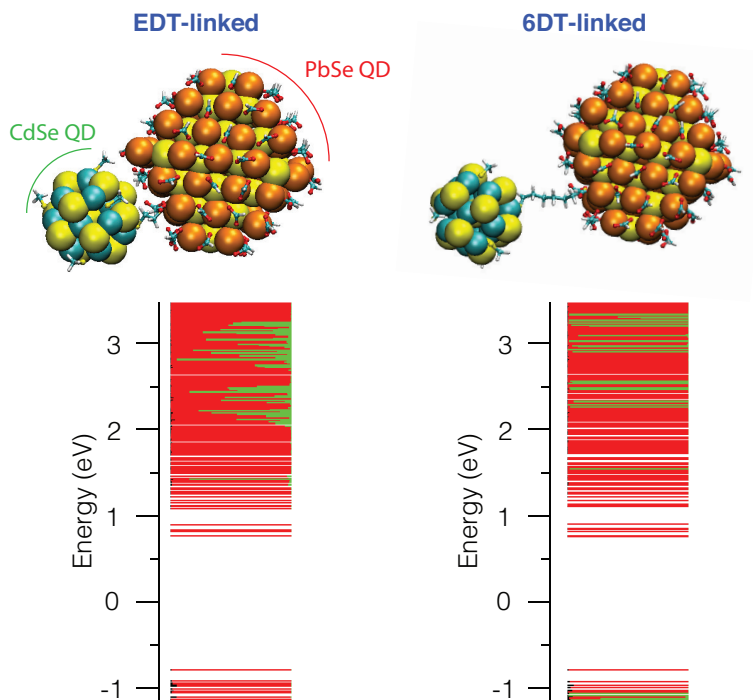


**Figure 2.17. Influence of ligand length on the electronic structure.** Conduction band electronic structure of a coupled CdSe QD – PbSe QD system (see Methods) for two different bridging molecules: ethanedithiol (EDT) and hexanedithiol (6DT). Each line corresponds to a molecular orbital (MO), and the color of the line represents the contribution of each fragment of the simulation to the MO: the PbSe fragment is depicted in red, CdSe in green, and the organic bridge in black. It can be seen that for the EDT linked system, most of the MOs with a contribution from the CdSe fragment have a significant contribution from the PbSe fragment, resulting in a high degree of electron delocalization. Conversely, for the 6DT-linked system, MOs are mostly localized on one of the two QDs.

### CdSe conduction band-edge state

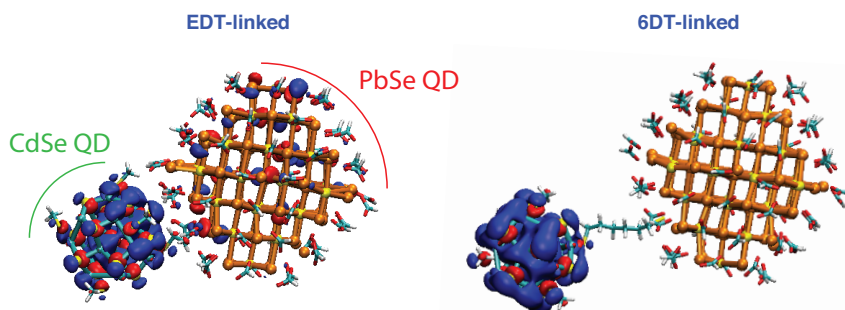


**Figure 2.18. Influence of ligand length on electron delocalization.** MO plot for the lowest energy MO with a significant contribution from the CdSe fragment. The EDT-linked system shows delocalization of the MO on the PbSe QD, while the 6DT-linked MO remains localized on the CdSe QD.





# Chapter 3

## Engineering the band-alignment in QD heterojunction films *via* ligand exchange

### *Abstract*

Colloidal Quantum Dots (QDs) allow great flexibility in the design of optoelectronic devices, thanks to their solution-processed thin-film assembly and their size-dependent optical and electronic properties. In particular, in QD-based heterojunctions, the bandgap of both components can be controlled by varying the size of the QDs. However, control over the band-alignment between the two materials is required to tune the dynamics of carrier transfer across an heterostructure.

We demonstrate that ligand-exchange strategies can be used to control the band-alignment of PbSe and CdSe QDs in a mixed QD solid, shifting it from a type-I to a type-II alignment. The change in alignment is observed in both spectroelectrochemical and transient absorption measurements, leading to a change in the energy of the conduction band-edges in the two materials and in the direction of electron transfer upon photoexcitation. Our work demonstrates the possibility to tune the band-offset of QD heterostructures via control over the chemical species passivating the QD surface, allowing full control over the energetics of the heterostructure without requiring changes in the QD composition.

Based on: Gianluca Grimaldi, Mark J. van den Brom, Indy du Fossé, Ryan W. Crisp, Nicholas Kirkwood, Solrun Gudjonsdottir, Jaco J. Geuchies, Sachin Kinge, Ivan Infante, Laurens D.A. Siebbeles and Arjan J. Houtepen. In preparation.

### 3.1 Introduction

Semiconductor heterojunctions provide control over the distribution and the motion of charge carriers, and thus are at the core of many optoelectronic devices. Semiconductor quantum dots (QDs) offer great flexibility in designing heterojunctions. The bandgap of QDs can be readily tuned *via* a change in the QD size, without requiring changes in material composition<sup>1-4</sup>. Colloidal solutions of QDs can be cast into thin films *via* solution-based processing, leading to densely packed films of QDs<sup>5-8</sup>. During film fabrication, the long, insulating ligands capping the surface of as-synthesized QDs can be exchanged for shorter, more conductive ligands<sup>8-15</sup>, allowing a high degree of electronic coupling between QDs while maintaining the quantum confined nature of QD states. These properties make QD solids excellent candidates for use in solar cells<sup>16-19</sup>, transistors<sup>10, 20-22</sup>, LEDs<sup>23-24</sup>, lasers<sup>25-28</sup> and photodetectors<sup>29-31</sup>. In contrast to bulk semiconductor heterojunctions, junctions formed between different QDs do not require epitaxial connections, which allows the fabrication of QD films composed of different, non-lattice-matched QD components, without building up strain in the system.

Beside the tunability of QD bandgaps, numerous studies have demonstrated that the ligands on the QD surface significantly affect the position of the QD band-edges with respect to the vacuum level<sup>15, 32-33, 36-40</sup>. This effect arises from changes in the surface dipoles induced by the different ligands: inward-pointing surface dipoles increase the electron affinity, i.e. the difference between the vacuum level and the conduction band, while outward-pointing surface dipoles decrease it<sup>32</sup>. The possibility to shift the energy structure of QDs *via* control of the capping ligands, depicted schematically in Figure 3.1a, can be used to control the band-offset in a junction. Chuang *et al.*<sup>36</sup> and Santra *et al.*<sup>37</sup> showed the effect of the ligand shift on working devices, by fabricating a homojunction with two different ligand treatments on PbS QDs, resulting in an increase of the photovoltaics performance of a QD-based solar cell.

In this work, we use ligand-exchange treatments to control the band alignment of QD heterojunctions. We fabricated films composed of alternating layers of PbSe and CdSe QDs *via* layer-by-layer dip-coating. The film structure is shown schematically in Figure 3.1b. During the fabrication step, the oleate ligands, capping the as-synthesized QDs, are exchanged for shorter ligands. In earlier work performed in our group, we characterized the band-alignment of PbSe-CdSe heterojunction films capped with ethanedithiolate ligands (EDT). We found a type-I alignment between the two materials, in which the band edges of the smaller bandgap component (PbSe) are located within the bandgap of the larger bandgap component (CdSe), as represented in Figure 3.1b<sup>34-35</sup>.

Although a type-I alignment is beneficial for optoelectronic applications involving radiative electron-hole recombination, such as LEDs or lasers, for many devices other band-alignment configurations are preferred. Type-II heterojunctions lead to separation of photoexcited electrons and holes, decreasing their recombination rate and thus increasing their lifetime. Such a configuration is preferred for light detection and photovoltaic applications. Alternatively, it could be beneficial to have a so-called quasi-type-II band-alignment, where the conduction band (CB) levels of both materials are resonant. This would be ideal in the context of optimizing carrier multiplication, where upon photon

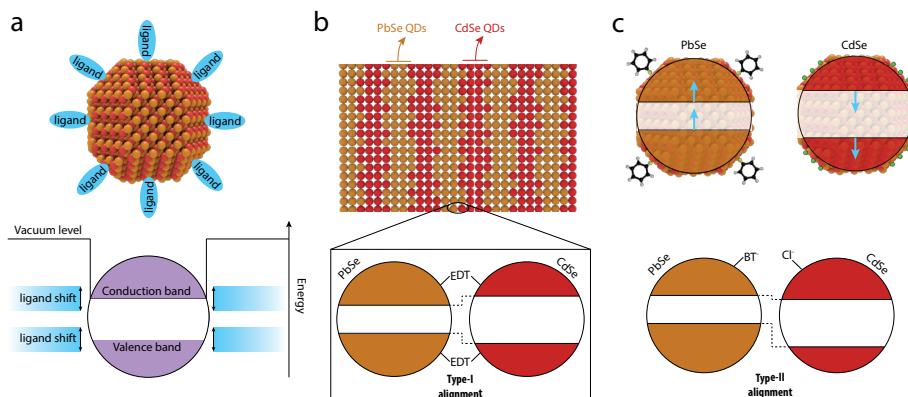


**Figure 3.1. Schematics of QD heterojunction films.** **a**, The band-edges of a semiconductor QD can be shifted by the presence of passivating ligands with different dipole moments<sup>15, 32-33</sup>. **b**, Structure of a PbSe-CdSe heterojunction QD film, fabricated by dip-coating alternating layers of PbSe and CdSe QDs, and ligand-exchanging the original ligands of the as-synthesized QDs for shorter linker molecules. The inset shows the heterojunction formed by CdSe and PbSe QDs treated with ethanedithiol (EDT), characterized by a type-I band-alignment<sup>34-35</sup>. **c**, Relative energy shift induced by the benzenethiol (BT, top left) and tetrabutylammonium chloride (TBACl, top right) ligand treatment with respect to the band-edge position in an EDT capped QD, as reported by Brown *et al.*<sup>32</sup>, together with the possible type-II heterojunction resulting from BT-treatment of PbSe QDs and TBACl-treatment of CdSe QDs.

absorption in the CdSe QDs, impact ionization of the hole can lead to the generation of multiple electron-hole pairs, as has been shown for CdSe/PbSe core-shell QDs<sup>41</sup> and Janus particles<sup>42</sup>. In general, it is clear that the ability to control the relative alignment of the energy levels increases the possibilities to form functional QD heterojunctions.

We demonstrate that the type-I band-alignment between CdSe and PbSe QDs, can be altered into a type-II alignment (see Figure 3.1c) by the functionalization of the two QD components with appropriate ligands. Considering the changes in electron affinity reported by Brown *et al.*<sup>32</sup>, we treated the PbSe QDs with benzenethiol (BT) ligands, leading to lower electron affinities than the EDT treatment. The CdSe QDs were treated with tetrabutylammonium chloride (TBACl), leading to higher electron affinities than the EDT treatment.

We performed spectroelectrochemical measurements on heterojunction QD films, confirming a type-I alignment for EDT capped heterojunctions, which is altered into a type-II band alignment following a BT-TBACl treatment. Transient absorption (TA) measurements confirm that this type-II offset leads to charge separation and longer charge carrier lifetimes, but also reveal the presence of a high density of interfacial trap states. Our results demonstrate the possibility to engineer the band-alignment of QD heterojunctions *via* control of the passivating ligands on the QD surface, enabling full control over the energetics of the heterojunction. At the same time, a high degree of electron trapping at interfacial states is observed, which hinders the usage of PbSe-CdSe QD heterojunctions. Density functional theory (DFT) calculations of CdSe-PbSe QD dimers suggest that the

presence of defect states is related to insufficient passivation of the QD surface, and not to states localized at the interface between the CdSe and PbSe QDs. Further improvement in the understanding and passivation of the heterojunction surface is needed to bridge the gap with device-grade heterojunctions.

### 3.2 Film fabrication

3

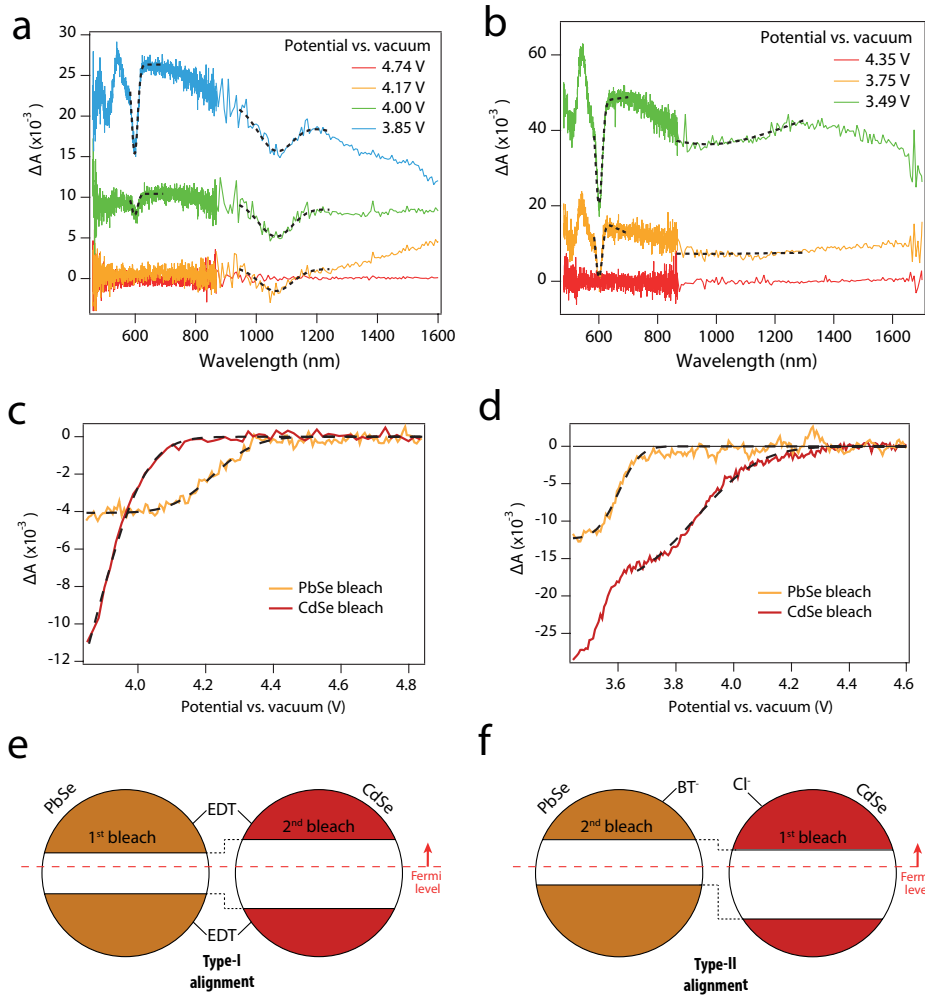
We fabricated QD heterojunction films composed of alternating layers of PbSe and CdSe QDs *via* layer-by-layer dip-coating of quartz or ITO substrates in QD solutions. Two solutions of 2.3 nm PbSe QDs and 4.5 nm CdSe QDs were used for dip-coating, which is a combination of sizes that we previously characterized to have a type-I alignment with a small conduction band-offset<sup>34-35</sup>. Each QD layer is ligand exchanged by dipping the substrate in a solution of the new ligand in a polar solvent (See Methods). For the TBACl-BT treatment, the layer-by-layer deposition technique used, which allows intimate contact between the CdSe and PbSe QDs, could lead to exposure of already ligand-exchanged QDs to the wrong ligand type, leading to the presence of benzenethiolate ligands on CdSe QDs and Cl<sup>-</sup> ligands on PbSe QDs. However, the electron affinity shifts observed in the spectroelectrochemical measurements are consistent with a predominant benzenethiolate passivation of PbSe QDs and Cl<sup>-</sup> passivation of CdSe QDs<sup>32</sup>.

### 3.3 Spectroelectrochemical determination of band-alignment

In order to determine the relative position of the conduction bands in the PbSe and CdSe QDs, we performed spectroelectrochemical measurements on the heterojunction QD films assembled on a conductive ITO substrate. In these measurements, the sample is immersed in an electrolyte solution (0.1 M lithium perchlorate in acetonitrile) and a potential is applied between the substrate and a Ag wire quasi reference electrode, while the absorbance of the sample is recorded. The potential of the quasi reference electrode was calibrated with the ferrocene/ferrocenium redox couple (See Appendix, Figure 3.6). All potentials are reported with respect to vacuum.

When the Fermi level of the system is raised above the conduction band edge of one of the QD components, charges are injected into the conduction band of the QDs, leading to a reduction of the band-edge absorption, an effect called absorption bleach<sup>43-50</sup>. Measuring the development of the absorption bleach of the two QD components as a function of the applied potential allows to reconstruct the band-alignment in the heterojunction: if the PbSe bleach develops at more positive potentials than the CdSe bleach, the PbSe band-edges lie within the CdSe bandgap, and the system is in a type-I alignment; vice versa, if the CdSe bleach develops first, the system is in a type-II alignment<sup>34</sup>.

Figure 3.2 shows the results of spectroelectrochemical measurements performed on an EDT-treated sample and on a TBACl-BT-treated sample. Figure 3.2a shows the differential absorbance of the EDT-treated film for different applied potentials. As the potential is decreased, a negative bleach feature appears at the PbSe bandgap wavelength (1030 nm), followed at lower potential by a bleach feature at the CdSe bandgap (603 nm). In contrast, for the TBACl-BT sample (Fig. 3.2b) the first absorption bleach is observed at the CdSe QD bandgap, while a PbSe absorption bleach becomes apparent at lower potential.



3

**Figure 3.2. Spectroelectrochemical determination of band-alignment in EDT and TBACl/BT heterojunction films.** **a,b,** Differential absorbance spectra of the a) EDT-treated and b) TBACl/BT film for different applied potentials. Dotted lines indicate fits of the data around the bandgap energies of the two QD components. For the EDT-treated film (a) the PbSe bleach appears at higher potential vs. vacuum than the CdSe bleach, while the order of appearance is reversed in the TBACl/BT film (b). **c,d,** Amplitude of the bleach component extracted from a fit to the data (see Appendix), plotted as a function of the applied potential. Dotted lines show error function fits to the experimental data, allowing to quantify the energy position of the conduction band levels (see Table 3.1). **e,f,** Schemes representing the band-alignment of the QD heterojunction consistent with the measured order of the PbSe and CdSe bleach features. As the potential versus vacuum is decreased, in the EDT-treated film (e) the PbSe QDs bleach first (type-I alignment), while in the TBACl-BT-treated film the CdSe QDs bleach first (type-II alignment).

Beside the presence of the band-edge bleaches, the measurement shows a broad induced absorption background, which is often observed in similar measurements on QD films<sup>34, 49</sup>, and is likely related to increased scattering and reflection due to the reduction of surface

cations<sup>51</sup>. To disentangle the potential dependence of the bleach features from the increase in the background, we performed a fit of the signal in a spectral range around each bleach feature, employing a Gaussian shape for the bleach and describing the slowly varying background with a straight line (dotted lines in Figure 3.2a and 3.2b). Figure 3.2c and 3.2d show the amplitude of the two bleach features as a function of the potential in the EDT (Fig. 3.2c) and in the TBACl-BT sample (Fig. 3.2d), clearly demonstrating that the PbSe bleach appears at higher potential in the EDT sample, while the CdSe bleach appears at higher potential in the TBACl-BT sample.

Figure 3.2e and 3.2f display the energy alignment inferred from the spectroelectrochemical results. In the EDT film, the PbSe CB edge lies at lower energy (higher potential) than the CdSe CB edge. Since the PbSe bandgap is smaller than the CdSe bandgap, the PbSe CB edges fall within the CdSe bandgap, as shown in Figure 3.2e. Vice versa, the fact that in the TBACl-BT film the CdSe bleach appears at lower energy (higher potential) than the PbSe bleach implies a type-II band-alignment, as shown in Figure 3.2f. These results demonstrate that the band-alignment in CdSe-PbSe QD heterojunction films can be switched between type-I and type-II *via* ligand treatments.

As shown in Figure 3.2d, the CdSe bleach amplitude in the TBACl-BT film shows a second increase in the bleach amplitude below 3.7 V, occurring in the same potential range where the PbSe bleach develops. The second bleach increase could be caused by pockets of CdSe QDs isolated from the rest of the CdSe QDs network by surrounding PbSe QDs. When electrons are present only in the CdSe conduction band, electron injection in the isolated CdSe QD is slow, and does not occur efficiently within the timescale of our experiment. When the Fermi level is raised above the PbSe conduction band, electrons can be injected into the PbSe QDs, increasing the conductivity of the entire film and allowing facile injection of electrons into the isolated CdSe QDs.

The potential dependence of the bleach amplitudes is well described by an error function (dotted black lines in Fig. 3.2c and 3.2d), describing progressive filling of a Gaussian density of states centered at the conduction band (CB) energy (see Appendix). Fitting the potential dependence of the bleach leads to a quantitative determination of the CB energy for the two ligand treatments, listed in Table 3.1.

**Table 3.1.** Conduction band energies for PbSe and CdSe QDs in the EDT and TBACl-BT film, determined *via* an error function fit to the bleach amplitude, shown in Fig. 3.2c and 3.2d.

	PbSe CB (eV)	CdSe CB (eV)	$\Delta E$ (eV)
EDT	-4.2	-3.9	0.3
TBACl-BT	-3.6	-3.9	-0.3

The CB energies extracted from the fit show that the band-offset,  $\Delta E = E_{\text{CB}}(\text{CdSe}) - E_{\text{CB}}(\text{PbSe})$ , changes sign between the two ligand treatments, shifting by 0.6 eV. The change is mostly due to the shift of the PbSe CB edge, while the CdSe CB edge is the same in the two films. The shift of the PbSe CB edge is twice as large as the shift observed by Brown *et al.* for PbS QDs<sup>32</sup>. The difference is perhaps associated with the difference in

material (PbSe vs. PbS). Furthermore, the energy required to inject an electron inside a material with the higher CB edge can be greater than the electron affinity of the material, e.g. due to electrostatic repulsion between the injected electrons<sup>34</sup>. While Boehme *et al.* have estimated that these effects contribute negligibly to the energy of the first electrons electrochemically injected in the system<sup>34</sup>, they could lead to an overestimation of the offset between the conduction band-edge energies of the two QD components. However, the relative position of the CBs, and hence the type-I vs. type-II band alignment can be trusted.

To summarize, spectroelectrochemical measurements on PbSe-CdSe heterojunction QD films demonstrate that the band-alignment in PbSe-CdSe heterojunctions can be changed from a type-I to a type-II alignment *via* ligand exchange with a BT treatment in the PbSe layers and with a TBACl treatment in the CdSe layers. The absolute energy position of the CB edges suggests that the shift is dominated by a change in the PbSe CB energy.

3

### 3.4 Electron dynamics in type-II QD heterojunctions measured by transient absorption spectroscopy.

In a type-II band alignment, photoexcited electrons and holes should transfer to opposite sides of the heterojunction. In particular, in the type-II structure assigned to the TBACl-BT-treated film, photoexcited electrons are expected to minimize their energy by occupying the CB edge of the CdSe QD component. Thus, photoexcitation of either the PbSe QDs or the CdSe QDs should lead to electrons bleaching the CdSe band-edge. Furthermore, the CdSe QD band-edge bleach induced by the electron should persist long after the initial thermalization, as electron-hole recombination should be slowed down by the spatial separation of the charges. To test the energy alignment determined above and to verify that charge separation takes place, we performed transient absorption (TA) measurements on a BT-TBACl film on a quartz substrate, photoexciting the system either below or above the bandgap of the CdSe QDs.

Figure 3.3a shows the results of a TA measurement of the TBACl-BT-treated type-II film, excited at 700 nm to obtain selective photoexcitation of the PbSe QD component, with an absorbed photon fluence of  $1.96 \cdot 10^{13}$  photons/cm<sup>2</sup> per pulse. At early times after photoexcitation the signal shows a bleach at the CdSe band gap (blue in the color-map), indicating the presence of electrons at the CdSe CB edge. This bleach feature decays rapidly and is replaced by a negative-positive anti-symmetric signal, resembling the first derivative of the first absorption peak (red trace in Figure 3.3d). The derivative-like feature is associated with an electrostatic shift of the QD absorption<sup>52-53</sup>, and can be linked to the presence of charge carriers close to the CdSe QDs, but not directly populating the CdSe CB edge. We associate the rapid decay of the bleach in the type-II system with the presence of a high density of electronic trap states. The presence of sub-ns trapping was also shown in our previous TA study on type-I CdSe-PbSe QD heterojunction films<sup>35</sup>. Very fast electron trapping was also observed in CdSe-CdTe type-II QD heterojunction films. In that case, electrochemical trap filling was required to observe efficient electron transfer from CdTe to CdSe QDs<sup>54</sup>.

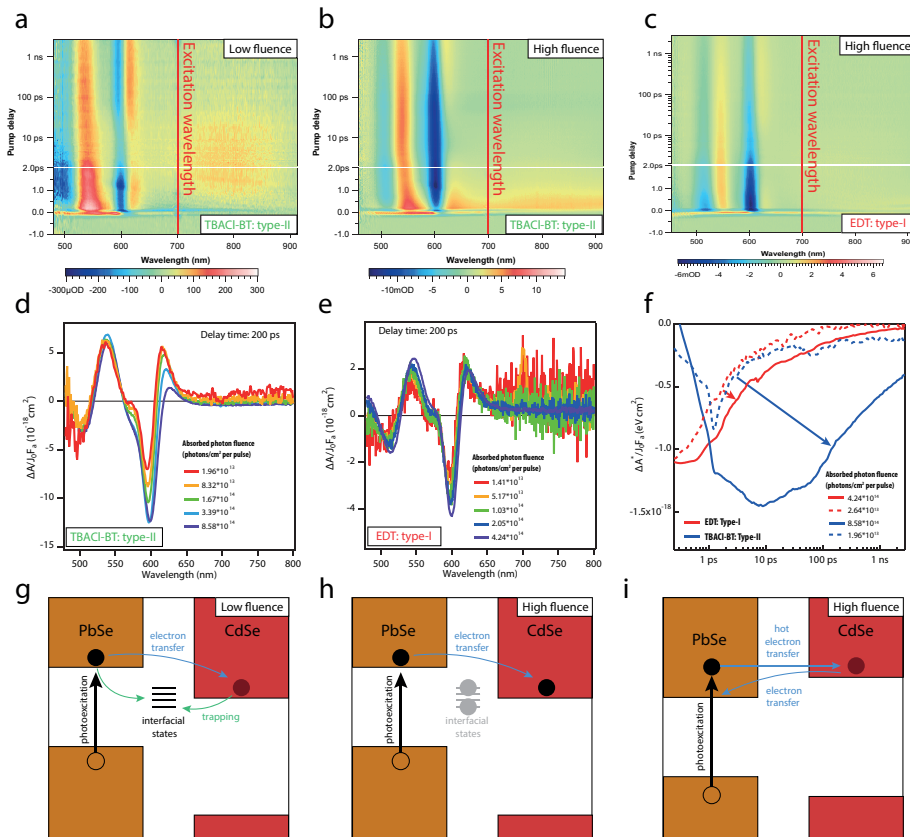


**Figure 3.3. Transient absorption (TA) measurements of electron dynamics in CdSe-PbSe QD heterojunction films upon selective PbSe excitation.** **a**, Color-map showing the results of a TA measurement performed on the TBACl/BT film, excited at 700 nm with an absorbed fluence of  $1.96 \cdot 10^{13}$  photons/cm<sup>2</sup> per pulse. At early time, the CdSe band-edge signal is characterized by a bleach feature, that decays rapidly and is replaced after 20 ps by a derivative-like feature. **b**, Color-map showing the results of the TA measurements performed on the TBACl/BT film, excited at 700 nm with an absorbed fluence of  $8.58 \cdot 10^{14}$  photons/cm<sup>2</sup> per pulse. A long-lived bleach is present at the CdSe band-edge and remains throughout the 3 ns time-range of the experiment. **c**, Color-map showing the results of the TA measurements performed on the EDT film, excited at 700 nm with an absorbed fluence of  $4.24 \cdot 10^{14}$  photons/cm<sup>2</sup> per pulse. The CdSe bleach is short lived, decaying with a half-life of 3.6 ps. The short lifetime of the CdSe bleach is compatible with the presence of hot-electron transfer in a type-I heterostructure<sup>35</sup>. **d**, Absorbed fluence-normalized differential absorbance of TA measurements on the TBACl/BT film excited at 700 nm with different photon fluences, obtained at a delay time of 200 ps. With increasing photon fluence, the shape of the signal shifts from a derivative-like feature to a Gaussian bleach, increasing in intensity. **e**, Absorbed fluence-normalized differential absorbance of TA measurements on the EDT film excited at 700 nm with different photon fluences, obtained at a delay time of 200 ps. The shape of the signal at the CdSe bandgap is weakly influenced by the absorbed fluence. **f**, Time-dependence of the energy-integrated bandgap signal (See Appendix) of the EDT sample (red) and TBACl-BT sample (blue), for low (dotted-line) and high (continuous line) fluence. As the fluence increases, the time-dependence of the bleach in the TBACl-BT film increases dramatically, while in the EDT sample it is hardly affected. **g,h,i**, Schemes representing electron transfer processes occurring in the type-II film (**g,h**) and in the type-I film (**i**). For the type-II film, at low fluence electrons are rapidly trapped at interfacial states (**g**), and higher fluence is needed to

saturate the trap states and allow long-lived electron occupation of the CdSe conduction band-edge (h). In the type-I film (i), the electron dynamics is described by hot-electron transfer to the CdSe QDs, followed by back-transfer to the PbSe QDs<sup>35</sup>.

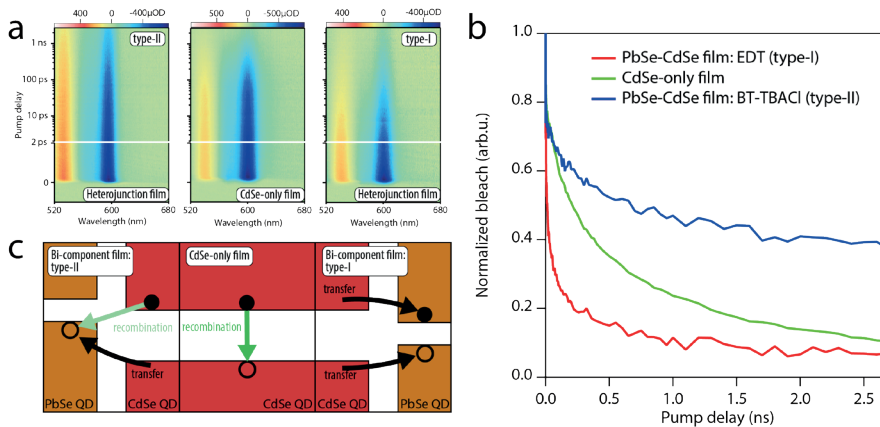
Similar to the electrochemical trap filling we employed for CdSe-CdTe QD heterojunction films, we sought to fill the traps here by increasing the excitation fluence. We find that the fast decay dynamics of the CdSe band-edge bleach change significantly as a function of excitation fluence. A TA measurement at a high absorbed photon fluence of  $8.58 \cdot 10^{14}$  photons/cm<sup>2</sup> per pulse is shown in Figure 3.3b. In this case the CdSe band edge response is characterized by a long-lived bleach feature, eventually decaying with a half-life of 400 ps, comparable with the band-edge bleach lifetime of a CdSe-only film (see also Fig. 3.4a, Fig. 3.4b and Appendix).

Figure 3.3c shows the differential absorbance of an EDT-treated type-I film obtained with measurement conditions similar to those in Figure 3.3b (700 nm excitation with an absorbed photon fluence  $4.24 \cdot 10^{14}$  photons/cm<sup>2</sup> per pulse). As previously reported for EDT-treated PbSe-CdSe QD films, excitation below the CdSe QD absorption onset results in a short-lived CdSe QD bleach, originating from hot-electron transfer from the PbSe QDs to the CdSe QDs, followed by back-transfer to the PbSe QDs<sup>35</sup>. While the CdSe QD absorption bleach in the type-II film decays with a half-life of 400 ps (Fig. 3.3b), the CdSe QD bleach in this type-I film decays with a short half-lifetime of 3.8 ps. This short decay time is attributed to fast electron back-transfer in the type-I heterojunction, confirming the difference in band-alignment between the two films.

Figure 3.3d shows the fluence-normalized TA spectra of the TBACl-BT sample obtained 200 ps after photoexcitation at the CdSe QD bandgap for varying absorbed photon fluences. While at low fluence the signal is dominated by the derivative-like feature, due to the trapping of photoexcited carriers, as the fluence increases the signal becomes dominated by a band-edge bleach, indicating the presence of electrons at the CdSe CB edge. In contrast to the type-II TBACl-BT sample, the type-I EDT sample shows little variation of the fluence-normalized band-edge TA signal with fluence, as shown in Figure 3.3e.

Figure 3.3f shows the time-dependence of the bleach signal for the TBACl-BT sample (blue lines) and EDT sample (red lines), measured in the low fluence (dotted lines) and high fluence (continuous lines) regime. The TA signal, here labelled  $\Delta A^*$ , is integrated over a spectral range centered at the CdSe QD bandgap (581 nm - 652 nm), to remove the contribution of the anti-symmetric positive-negative shift feature from the time-dependence of the bleach. The increase in absorbed photon fluence causes only a minor variation in the bleach lifetime for the EDT sample, while the dynamics of the bleach in the TBACl-BT film changes dramatically, going from a bleach decay half-life of 2.7 ps to 400 ps.

Our interpretation of the TA measurements on the type-II TBACl-BT sample is summarized by the schemes in Figure 3.3g and Figure 3.3h. Figure 3.3g shows the dynamics of the photoexcited electron in the low fluence regime, in which carrier trapping and electron



**Figure 3.4. Transient absorption (TA) measurements of electron dynamics upon direct CdSe excitation.** **a**, TA color-maps of a TBACl/BT heterojunction film (left), a CdSe-only film treated with TBACl (middle), and an EDT heterojunction film (right) excited at 570 nm, above the onset of CdSe absorption. The minimum of each color-scale is set to the lowest differential absorbance value (i.e. the maximum bleach amplitude). The TBACl/BT film shows the longest bleach lifetime, while the bleach of the EDT film is the shortest-lived. **b**, Normalized bleach amplitude for the TA measurements displayed in **a**), quantitatively showing the difference in bleach decay between the films. **c**, Proposed model for the dynamics of bleach decay upon direct CdSe excitation. The increased bleach lifetime in the TBACl/BT film is attributed to spatial separation between electrons and holes across the type-II heterojunction, reducing the recombination rate with respect to the CdSe-only film. In the type-I EDT-treated film, instead, electron transfer contributes to the depopulation of the CdSe band-edges, increasing the rate of bleach decay.

transfer both occur on a ps timescale, leading to a short-lived CdSe QD bleach and the development of a pronounced derivative-like feature at later times. However, in the high fluence regime (Figure 3.3h), the increased number of trapped electrons can saturate the density of trap states, allowing additionally photogenerated electrons to escape the trapping process and remain at the CdSe band-edge. The power-dependence of the bleach lifetime distinguishes the type-II TBACl-BT sample from the type-I EDT sample (Figure 3.3i). In the latter case, the bleach dynamics is dominated by the back-transfer of hot-electrons from CdSe QDs to PbSe QDs, which does not depend on the excitation fluence.

Since the fast trapping process is not observed in a PbSe-only or CdSe-only QD film (See Appendix, Figures 3.9 and 3.10), we tentatively assign these trap states to interfacial states, occurring at the PbSe-CdSe heterojunction interface. The presence of localized states at the interface between Pb-chalcogenides and Cd-chalcogenides has been predicted by DFT simulations of PbS-CdS Janus-particles<sup>55</sup> and of PbSe QDs embedded in a CdSe matrix<sup>55</sup>, suggesting that epitaxial contact between PbSe and CdSe nanostructures leads to the formation of localization centers. This is discussed in more detail below (see section Density functional theory calculations on PbSe-CdSe QD dimers).

To further demonstrate the effect of the band offset on the lifetime of photogenerated electrons, we excited mixed CdSe-PbSe and CdSe-only QD films above the CdSe QD bandgap, at 570 nm. Figure 3.4a compares the resulting TA response of the TBACl/BT

heterojunction film (Figure 3.4a, left), with the response of a CdSe-only film (Figure 3.4a, center) and of an EDT-treated heterojunction film (Figure 3.4a, right). In each color-map the blue edge of the color-scale is set to the minimum  $\Delta A$  value, in order to highlight the differences in the decay of the bleach signals. Figure 3.4b shows the time-dependence of the normalized bleach, highlighting the differences between the three films. It is evident that the bleach lifetime is longest in the TBACl/BT type-II heterojunction film, shortest in the EDT type-I heterojunction film and intermediate in the CdSe-only film.

The differences in the bleach decay can be attributed to differences in the carrier recombination rate induced by charge transfer, as depicted in Figure 3.4c. For the type-II film (left panel) an electron hole pair generated on CdSe QD in contact with a PbSe QD is separated, as the hole transfers to the PbSe QDs. Charge separation decreases the rate of recombination and increases the electron lifetime with respect to the CdSe-only film. On the contrary, in the type-I film, charge transfer between adjacent CdSe and PbSe QDs depopulates the band-edges of the CdSe QDs, thus increasing the rate of band-edge bleach decay. These TA measurements, with excitation both above and below the CdSe QD bandgap, confirm the type-I alignment of the EDT-treated QD heterojunction film and the type-II alignment of the TBACl-BT-treated film, in line with the spectroelectrochemical measurements.

3

### 3.5 Density functional theory calculations on PbSe-CdSe QD dimers

The TA measurements we have performed on PbSe-CdSe heterojunction QD films reveal the presence of fast trapping processes in both the type-I<sup>35</sup> and the type-II alignment, which are instead absent from PbSe-only and CdSe-only QD films. Density functional theory (DFT) calculations performed by Giberti *et al.* have predicted the presence of interfacial states within the bandgap of PbSe QDs embedded in a CdSe matrix<sup>55</sup>. Simulations of PbS-CdS Janus particles by Kroupa *et al.* have also reported localized interfacial states at the interface between the two materials<sup>42</sup>. The presence of interfacial states in the bandgap would hamper the use of PbSe-CdSe QD heterojunction films for practical applications. DFT calculations were carried out in order to obtain a better understanding of the trap formation at the PbSe-CdSe interface on an atomistic level. First, the structures of separate  $\text{Cd}_{176}\text{Se}_{147}\text{Cl}_{58}$  and  $\text{Pb}_{140}\text{Se}_{85}\text{Cl}_{110}$  QDs were optimized (see Methods for further details). Chloride ligands were used to passivate both QD surfaces<sup>56-57</sup>, due to their low computational cost compared to the benzenethiolate ligands used in the experiments. Although this choice could affect the band alignment between the two materials, it has little influence on the presence of localized interfacial states, which are mostly dependent on the coordination of interfacial atoms. Figure 3.5a shows the density of states (DOS) for the two materials, in which the molecular orbital (MO) of each state is represented by a horizontal line. The contribution of each atomic species to the MOs is represented by the length of the line segment of the corresponding color (blue for Cd, beige for Pb, brown for Se, green for Cl). As shown in Figure 3.5a, these pristine structures show clean bandgaps, i.e. without localized states, as expected from experimental results<sup>58</sup>.

Zhang *et al.* reported that the interface between CdSe-PbSe Janus particles formed by cation exchange develops along the {111} facets of the two materials<sup>59</sup>. They attribute the

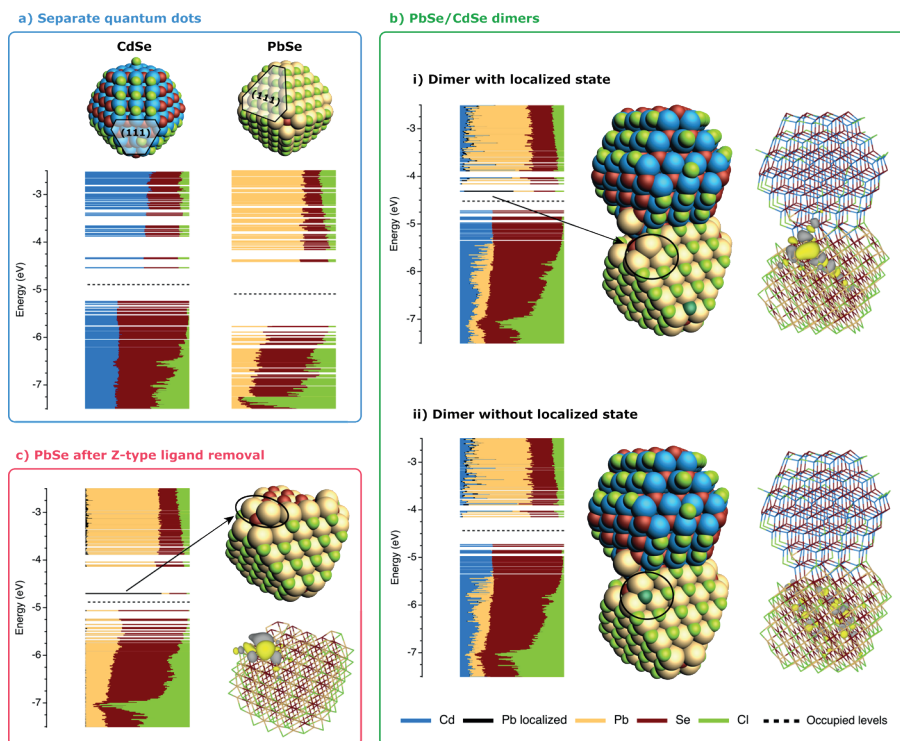


**Figure 3.5. DFT calculations of the electronic structure of PbSe-CdSe dimers.** **a**, Structure and DOS of the separate CdSe and PbSe QDs. The {111} planes at which the QDs will be attached to each other are indicated. For the DOS, each molecular orbital (MO) is represented by a horizontal line. The contribution of an element or group of atoms to a certain MO is indicated by the length of the line segment of the corresponding color. Levels below the dotted line are occupied, whereas the levels above are empty. **b**, DOS, structures and contour plots of PbSe-CdSe dimers i) with and ii) without a localized state. In i), the large black line segment in the DOS shows that the LUMO is largely localized on the three Pb-atoms indicated by the black circle. This can also be seen in the contour plot on the right. In ii) a chloride ligand (dark green) has been moved to these three Pb-atoms. Both the DOS and the contour plot of the LUMO indicate that this removes the localized state. **c**, DOS, structure and contour plot of the PbSe QD after removal of 12 Z-type  $\text{PbCl}_2$  ligands. The DOS shows that the LUMO is highly localized on the two Pb-atoms indicated by the black circle. The bottom right figure shows the contour plot of the LUMO level, which further highlights its localized character. All contour plots shown here use a contour plot value of  $0.015 \text{ e/bohr}^3$ .

preferential formation of {111} interfaces to the absence of strain along this plane, making it energetically favorable<sup>59</sup>. Therefore, we decided to attach the separate QDs at one of their {111} facets. To allow the formation of the PbSe-CdSe interface, we removed the minimal amount of Z-type  $\text{PbCl}_2$  ligands from the {111} facet of the PbSe QD to attach to the CdSe QD. In order to obtain a bare {111} surface on the CdSe QD, only one Cl had to be moved to an adjacent {111} facet. The ligand arrangement assigned to the system in the calculation could easily arise in the QD film, as a result of incomplete surface passivation and by the diffusion of ligands on the QD surface.

Optimization of the QD dimer that is created upon attaching the two QDs at their bare {111} facets gives the structure shown in Figure 3.5b-i. The black segment in the LUMO in Figure 3.5b-i represents the contribution of three adjacent Pb atoms, highlighted by a black circle in the structure, on which the orbital predominantly localizes. It can be noted that this localized orbital is situated on the edge of the PbSe-CdSe interface and not at the PbSe-CdSe interface itself. However, if a chloride ligand (dark green in Figure 3.5b-ii) is taken from a {111} facet on PbSe and placed in the middle of the aforementioned three Pb-atoms, optimization leads to a structure where the LUMO is no longer localized. Therefore, the formation of a localized state in the PbSe-CdSe QD dimer can be prevented by a rearrangement of the ligands.

These results suggest that the localized state is not directly related to the creation of an interface between PbSe and CdSe, but to the removal of Z-type ligands that is required for the formation of such an interface. It is likely that the removal of ligands leads to the formation of labile edge and corner atoms that may form localized states upon relaxation of the structure. This notion is supported by optimization of the PbSe QD after the removal of Z-type ligands, but before the addition of the CdSe moiety, as shown in Figure 3.5c. The LUMO of this structure is localized on two Pb-atoms in a similar manner as with the QD dimers in Figure 3.5b, indicating that localization is not necessarily related to the presence of a PbSe-CdSe interface.

These calculations suggest that the presence of localized states is related to an incomplete passivation of the QD surface, likely as a consequence of the ligand treatments employed to obtain the type-II alignment, and do not arise directly from the PbSe-CdSe heterostructure interface. In that case, the development of new ligand exchange or passivation strategies for the heterostructure QD films should aim at the suppression of electron trapping while maintaining the type-II alignment of the heterostructure.

### 3.6 Conclusions

Using spectroelectrochemistry and ultrafast transient absorption spectroscopy we have shown that the band alignment in CdSe/PbSe QD heterojunction films can be tuned from type-I, when the entire film is treated with ethanedithiol, to type-II alignment, when the PbSe QDs are treated with benzenethiol and the CdSe QDs with TBACl. Spectroelectrochemical measurements on TBACl-BT-treated and on EDT-treated films show a clear inversion in the order of the PbSe and CdSe conduction band-edge levels. Transient absorption measurements performed with a high photon fluence on the TBACl-BT-treated film show the presence of a long-lived CdSe QD bleach developing upon selective PbSe QD excitation, indicative of electron transfer from the PbSe QD to the CdSe QD conduction band-edge. Furthermore, direct CdSe QD photoexcitation in the TBACl-BT film results in a longer band-edge bleach lifetime compared to a CdSe-only QD film, characteristic of reduced recombination of spatially separated electrons and holes. Our results demonstrate the possibility to control the energy alignment of QD heterojunctions *via* ligand exchange, providing an additional handle to control the energetics of QD-based devices. On the other hand, low fluence TA measurements reveal the presence of a high density of trap states. DFT calculations suggest that these trap states

are not intrinsic to the PbSe-CdSe interface, but appear at undercoordinated Pb atoms at the edge of the interface. This highlights the importance of a greater understanding of the electronic passivation of QD heterojunctions in order to exploit their potential for optoelectronic applications.

### 3.7 Methods

3

**CdSe QD synthesis.** The CdSe QDs were synthesized following a recipe reported in our previous work<sup>35</sup>, in turn adapted from van Embden *et al.*<sup>60</sup>. The synthesis was performed injecting a Se-precursor into a flask containing hot Cd-precursor, followed by repeated injection of the Cd- and Se-precursor to further grow the QDs.

The Cd growth solution was prepared by adding 0.22 g CdO (99.999%), 0.970 g oleic acid (OA, 90%), and 6.23 g ODE to a 3-neck round-bottom flask (BPF). The flask was attached to a Schlenk line, degassed for 1 hour under vacuum (<1 mbar) at 80°C. The solution was then heated to 260°C under nitrogen atmosphere, until it turned clear, indicating the formation of the Cd-oleate complex. The solution was then allowed to reach room temperature, and oleylamine (1.13 mL, tech grade 70%) was added during cooling.

The Se growth solution was obtained by dissolving 0.25 g Se powder in 1.55 g trioctylphosphine (TOP, tech grade 90%) in a nitrogen-filled glove-box.

The Se injection precursor was prepared by dissolving 0.327 g Se powder in a solution of 2.5 g TOP, 2.5 g 1-octadecene (ODE, tech grade 90%) and 6 g oleylamine (OAm, tech grade 70%) in a nitrogen-filled glove-box.

The Cd-precursor for the hot-injection was prepared by adding 0.22 g CdO, 3 g OA, and 30 g ODE to a 3-neck BPF flask. The solution was degassed under vacuum for 1 hour at 80°C and then heated to 260°C under nitrogen atmosphere, until it turned clear.

The hot-injection was performed by loading the Se injection precursor in a syringe equipped with a 16G needle, and quickly injecting it into the 3-neck BPF flask containing the Cd-precursor, kept at a temperature of 260°C. After injection, the temperature was allowed to decrease to 250°C, where it was kept. After 20 min, 2 mL of Cd and Se growth precursors were added dropwise to the reaction solution. The growth precursor addition was repeated three times, waiting 10 minutes between each addition. After the last addition, the reaction was allowed to proceed at 250°C for 10 minutes and was subsequently stopped by cooling to room temperature. The reaction product was washed three times by QD precipitation, achieved adding an anti-solvent (ethanol) to the reaction solution and centrifuging the mixture (3500 rpm), followed by re-dispersion in hexane.

**PbSe QD synthesis.** The PbSe QDs were synthesized following a recipe reported in our previous work<sup>35</sup>, in turn adapted from Steckel *et al.*<sup>61</sup>. The synthesis was performed injecting a Se-precursor into a flask containing hot Pb-precursor. The Se injection precursor was prepared dissolving 0.553 g Se powder in 19 mL TOP and 0.13 mL diphenylphosphine (DPP, 98%). The Pb reaction solution was prepared adding 1.35 g PbO (99.999%), 17 mL ODE and 4 mL OA to a 3-neck BPF flask. The flask was connected to a Schlenk line and the solution was degassed under vacuum for 1 hour. The solution was then heated to 125°C under nitrogen atmosphere, until it turned clear, and then cooled to 100°C and degassed under vacuum for 30 minutes. To perform the injection reaction, the Pb-precursor solution was heated to 180°C and placed under nitrogen atmosphere. The injection was performed loading the Se injection precursor into a 20 mL syringe equipped with a 16G needle, and then quickly injecting the content into the Pb-precursor. The reaction was allowed to proceed for 10 seconds, after which it was quenched by immersing the flask in cold water. The reaction product was washed three times by precipitation, achieved adding an anti-solvent (ethanol) to the reaction solution and centrifuging the mixture (3500 rpm), and re-dispersion in hexane.

**Film fabrication.** The heterojunction QD films were fabricated by layer-by-layer deposition. For

every QD layer, the substrate (quartz or ITO) was dipped in a QD solution for 30 seconds, then was raised out of the solution, left to dry for 30 seconds and subsequently immersed for 30 seconds in a solution of the new ligands dissolved in a polar solvent. After 30 seconds of drying, the substrate was immersed in the pure polar solvent, to wash away unbound residues of the new ligands, and finally left to dry for 30 seconds before starting again the same cycle for the other QD material. The QD solutions were prepared with a QD concentration in hexane of 0.2 mM, determined from linear absorption measurements and from the values of the extinction coefficient provided in literature<sup>62-63</sup>. For the EDT capped films, the ligand exchange solution was a 10 mM solution of EDT in acetonitrile, and in the final washing step the substrate was immersed in acetonitrile. For the TBACl layers, the ligand exchange solution consisted of a 30 mM solution of TBACl in methanol, and in the final washing step the substrate was immersed in methanol. For the BT layers, the ligand exchange solution consisted of a 50 mM solution of BT in methanol, and in the final washing step the substrate was immersed in methanol.

**Transient Absorption.** The fundamental laser beam is generated by a Yb:KGW oscillator (Light Conversion, Pharos SP), producing a 1028 nm wavelength beam with 180 fs pulse width and 5 kHz repetition rate. The fundamental laser beam is sent to a beam-splitter, separating the beam into a low intensity and a high intensity component. The high intensity component (pump beam) is sent through an Optical Parametric Amplifier (OPA, Light Conversion, Orpheus), allowing to tune the wavelength of the beam between 312 and 1330 nm. The pump beam is then sent through a mechanical chopper rotating at 2.5 kHz, blocking one out of two laser pulses. After transmission through the chopper, the pump beam is sent to the sample, photoexciting it. The low intensity beam (probe beam) is converted into a broadband continuum (500 – 1600 nm) by transmission through a sapphire crystal, and then focused on the sample, where it overlaps spatially with the pump beam. After transmission through the sample, the probe beam is collected by a detector (Ultrafast Systems, Helios), measuring the spectrum of the probe pulse transmitted by the sample in the presence of a pump pulse ( $I_{on}$ ) and the probe pulse transmitted when the pump beam was blocked ( $I_{off}$ ). The differential absorbance is calculated *via*  $\Delta A = \ln(I_{on}/I_{off})$ . The chirp of the probe spectrum, produced by the different group velocities of different probe wavelengths, is corrected *via* a polynomial fit to the coherent artefact response<sup>64</sup>. The QD films were loaded into an air-tight sample holder inside a nitrogen-filled glovebox.

**Spectroelectrochemistry.** The spectroelectrochemical measurements were performed inside a nitrogen-filled glovebox. The samples were placed in an electrochemical cell, having the ITO substrate coated with the QD film as working electrode, a Ag wire as quasi reference electrode, and a Pt plate as counter electrode. The cell was placed inside a cuvette, immersed in an electrolyte (0.1 M lithium perchlorate solution in acetonitrile), and connected to a potentiostat (Autolab, PGSTAT128N). Acetonitrile was dried before use in an Innovative Technology PureSoly Micro column. The quasi reference electrode was calibrated measuring the redox potential of the ferrocene/ferrocenium redox couple, with a scan speed of the applied potential of 50 mV/s. Absorbance measurements were performed measuring the light transmitted through the sample for different applied potentials, using a deuterium halogen source (DH-2000, Ocean Optics) and measuring it on a USB2000+ spectrometer (Ocean Optics). Cyclic voltammograms measured on the PbSe-CdSe QD films were recorded with a scan speed of 10 mV/s.

**Density functional theory calculations on PbSe-CdSe dimers.** All calculations have been carried out at the DFT level, using the PBE exchange-correlation functional<sup>65</sup> and double- $\zeta$  basis set, as implemented in the CP2K quantum chemistry software package<sup>66</sup>. Relativistic effects were included through the use of effective core-potentials. All structures were optimized to the lowest energy at 0 K in the gas phase.

## References

1. Brus, L. E., Electron-electron and electron-hole interactions in small semiconductor crystallites: The size dependence of the lowest excited electronic state. *J. Chem. Phys.* 1984, 80 (9), 4403.
2. Ekimov, A. I.; Efros, A. L.; Onushchenko, A. A., Quantum size effect in semiconductor microcrystals. *Solid State Communications* 1985, 56 (11), 921-924.
3. Colvin, V. L.; Alivisatos, A. P.; Tobin, J. G., Valence-band photoemission from a quantum-dot system. *Phys Rev Lett* 1991, 66 (21), 2786-2789.
4. Ekimov, A. I.; Hache, F.; Schanne-Klein, M. C.; Ricard, D.; Flytzanis, C.; Kudryavtsev, I. A.; Yazeva, T. V.; Rodina, A. V.; Efros, A. L., Absorption and intensity-dependent photoluminescence measurements on CdSe quantum dots: assignment of the first electronic transitions. *J. Opt. Soc. Am. B* 1993, 10 (1), 100-107.
5. Kagan, C. R.; Lifshitz, E.; Sargent, E. H.; Talapin, D. V., Building devices from colloidal quantum dots. *Science* 2016, 353 (6302).
6. Colvin, V. L.; Schlamp, M. C.; Alivisatos, A. P., Light-emitting diodes made from cadmium selenide nanocrystals and a semiconducting polymer. *Nature* 1994, 370 (6488), 354-357.
7. Kagan, C. R.; Murray, C. B.; Nirmal, M.; Bawendi, M., Electronic Energy Transfer in CdSe Quantum Dot Solids. *Phys. Rev. Lett.* 1996, 76 (9).
8. Yu, D.; Wang, C.; Guyot-Sionnest, P., n-Type Conducting CdSe Nanocrystal Solids. *Science* 2003, 300 (5623), 1277-1280.
9. Law, M.; Luther, J. M.; Song, Q.; Hughes, B. K.; Perkins, C. L.; Nozik, A. J., Structural, optical, and electrical properties of PbSe nanocrystal solids treated thermally or with simple amines. *J. Am. Chem. Soc.* 2008, 130 (18), 5974-5985.
10. Talapin, D. V.; Murray, C. B., PbSe nanocrystal solids for n- and p-channel thin film field-effect transistors. *Science* 2005, 310 (5745), 86-89.
11. Jarosz, M. V.; Porter, V. J.; Fisher, B. R.; Kastner, M. A.; Bawendi, M. G., Photoconductivity studies of treated CdSe quantum dot films exhibiting increased exciton ionization efficiency. *Phys. Rev. B* 2004, 70 (19).
12. Luther, J. M.; Law, M.; Song, Q.; Perkins, C. L.; Beard, M. C.; Nozik, A. J., Structural, optical and electrical properties of self-assembled films of PbSe nanocrystals treated with 1,2-ethanedithiol. *ACS Nano* 2008, 2 (2), 271-280.

13. Kovalenko, M. V.; Scheele, M.; Talapin, D. V., Colloidal Nanocrystals with Molecular Metal Chalcogenide Surface Ligands. *Science* 2009, 324 (5933), 1417-1420.
14. Crisp, R. W.; Callahan, R.; Reid, O. G.; Dolzhenkov, D. S.; Talapin, D. V.; Rumbles, G.; Luther, J. M.; Kopidakis, N., Photoconductivity of CdTe Nanocrystal-Based Thin Films: Te<sup>2-</sup> Ligands Lead To Charge Carrier Diffusion Lengths Over 2  $\mu\text{m}$ . *J. Phys. Chem. Lett.* 2015, 4815-4821.
15. Crisp, R. W.; Kroupa, D. M.; Marshall, A. R.; Miller, E. M.; Zhang, J.; Beard, M. C.; Luther, J. M., Metal Halide Solid-State Surface Treatment for High Efficiency PbS and PbSe QD Solar Cells. *Sci. Rep.* 2015, 5, 9945.
16. Ganesan, A.; Houtepen, A.; Crisp, R., Quantum Dot Solar Cells: Small Beginnings Have Large Impacts. *Applied Sciences* 2018, 8 (10).
17. Zhang, H.; Kurley, J. M.; Russell, J. C.; Jang, J.; Talapin, D. V., Solution-Processed, Ultrathin Solar Cells from CdCl<sub>3</sub>(-)-Capped CdTe Nanocrystals: The Multiple Roles of CdCl<sub>3</sub>(-) Ligands. *J Am Chem Soc* 2016, 138 (24), 7464-7.
18. Semonin, O. E.; Luther, J. M.; Choi, S.; Chen, H.-Y.; Gao, J.; Nozik, A. J.; Beard, M. C., Peak External Photocurrent Quantum Efficiency Exceeding 100% via MEG in a Quantum Dot Solar Cell. *Science* 2011, 334 (6062), 1530-1533.
19. Sanehira, E. M.; Marshall, A. R.; Christians, J. A.; Harvey, S. P.; Ciesielski, P. N.; Wheeler, L. M.; Schulz, P.; Lin, L. Y.; Beard, M. C.; Luther, J. M., Enhanced mobility CsPbI<sub>3</sub> quantum dot arrays for record-efficiency, high-voltage photovoltaic cells. *Sci Adv* 2017, 3 (10), eaao4204.
20. Chung, D. S.; Lee, J.-S.; Huang, J.; Nag, A.; Ithurria, S.; Talapin, D. V., Low Voltage, Hysteresis Free, and High Mobility Transistors from All-Inorganic Colloidal Nanocrystals. *Nano Lett.* 2012, 12 (4), 1813-1820.
21. Kagan, C. R.; Mitzi, D. B.; Dimitrakopoulos, C. D., Organic-Inorganic Hybrid Materials as Semiconducting Channels in Thin-Film Field-Effect Transistors. *Science* 1999, 286 (5441), 945-947.
22. Bisri, S. Z.; Piliego, C.; Yarema, M.; Heiss, W.; Loi, M. A., Low Driving Voltage and High Mobility Ambipolar Field-Effect Transistors with PbS Colloidal Nanocrystals. *Advanced Materials* 2013, 25 (31), 4309-4314.
23. Shirasaki, Y.; Supran, G. J.; Bawendi, M. G.; Bulović, V., Emergence of colloidal quantum-dot light-emitting technologies. *Nature Photonics* 2012, 7 (1), 13-23.
24. Lim, J.; Park, Y. S.; Wu, K.; Yun, H. J.; Klimov, V. I., Droop-Free Colloidal Quantum

Dot Light-Emitting Diodes. *Nano Lett* 2018, 18 (10), 6645-6653.

25. Klimov, V. I.; Mikhailovsky, A. A.; Xu, S.; Malko, A.; Hollingsworth, J. A.; Leatherdale, C. A.; Eisler, H.; Bawendi, M. G., Optical gain and stimulated emission in nanocrystal quantum dots. *Science* 2000, 290 (5490), 314-7.
26. Klimov, V. I.; Ivanov, S. A.; Nanda, J.; Achermann, M.; Bezel, I.; McGuire, J. A.; Piryatinski, A., Single-exciton optical gain in semiconductor nanocrystals. *Nature* 2007, 447 (7143), 441-6.
27. Fan, F.; Voznyy, O.; Sabatini, R. P.; Bicanic, K. T.; Adachi, M. M.; McBride, J. R.; Reid, K. R.; Park, Y. S.; Li, X.; Jain, A.; Quintero-Bermudez, R.; Saravanapavanantham, M.; Liu, M.; Korkusinski, M.; Hawrylak, P.; Klimov, V. I.; Rosenthal, S. J.; Hoogland, S.; Sargent, E. H., Continuous-wave lasing in colloidal quantum dot solids enabled by facet-selective epitaxy. *Nature* 2017, 544 (7648), 75-79.
28. Lim, J.; Park, Y.-S.; Klimov, V. I., Optical gain in colloidal quantum dots achieved with direct-current electrical pumping. *Nat. Mater.* 2017, 17 (1), 42-49.
29. Konstantatos, G.; Howard, I.; Fischer, A.; Hoogland, S.; Clifford, J.; Klem, E.; Levina, L.; Sargent, E. H., Ultrasensitive solution-cast quantum dot photodetectors. *Nature* 2006, 442 (7099), 180-3.
30. Keuleyan, S.; Lhuillier, E.; Brajuskovic, V.; Guyot-Sionnest, P., Mid-infrared HgTe colloidal quantum dot photodetectors. *Nature Photonics* 2011, 5 (8), 489-493.
31. Deng, Z.; Jeong, K. S.; Guyot-Sionnest, P., Colloidal quantum dots intraband photodetectors. *ACS Nano* 2014, 8 (11), 11707-14.
32. Brown, P. R.; Kim, D.; Lunt, R. R.; Zhao, N.; Bawendi, M. G.; Grossman, J. C.; Bulović, V., Energy Level Modification in Lead Sulfide Quantum Dot Thin Films through Ligand Exchange. *ACS Nano* 2014, 8 (6), 5863-5872.
33. Kroupa, D. M.; Voros, M.; Brawand, N. P.; McNichols, B. W.; Miller, E. M.; Gu, J.; Nozik, A. J.; Sellinger, A.; Galli, G.; Beard, M. C., Tuning colloidal quantum dot band edge positions through solution-phase surface chemistry modification. *Nat. Commun.* 2017, 8, 15257.
34. Boehme, S. C.; Vanmaekelbergh, D.; Evers, W. H.; Siebbeles, L. D. A.; Houtepen, A. J., In situ spectroelectrochemical determination of energy levels and energy level offsets in quantum-dot heterojunctions. *J. Phys. Chem. C* 2016, 120 (9), 5164-5173.
35. Grimaldi, G.; Crisp, R. W.; Ten Brinck, S.; Zapata, F.; van Ouwendorp, M.; Renaud, N.; Kirkwood, N.; Evers, W. H.; Kinge, S.; Infante, I.; Siebbeles, L. D. A.; Houtepen, A. J., Hot-electron transfer in quantum-dot heterojunction films. *Nat.*

- Commun. 2018, 9 (1), 2310.
36. Chuang, C.-H. M.; Brown, P. R.; Bulović, V.; Bawendi, M. G., Improved performance and stability in quantum dot solar cells through band alignment engineering. *Nat. Mater.* 2014, 13 (8), 796-801.
  37. Santra, P. K.; Palmstrom, A. F.; Tanskanen, J. T.; Yang, N.; Bent, S. F., Improving Performance in Colloidal Quantum Dot Solar Cells by Tuning Band Alignment through Surface Dipole Moments. *The Journal of Physical Chemistry C* 2015, 119 (6), 2996-3005.
  38. Soreni-Harari, M.; Yaacobi-Gross, N.; Steiner, D.; Aharoni, A.; Banin, U.; Millo, O.; Tessler, N., Tuning energetic levels in nanocrystal quantum dots through surface manipulations. *Nano Lett* 2008, 8 (2), 678-84.
  39. Timp, B. A.; Zhu, X. Y., Electronic energy alignment at the PbSe quantum dots/ZnO(10 $\bar{1}$ 0) interface. *Surface Science* 2010, 604 (17-18), 1335-1341.
  40. Munro, A. M.; Zacher, B.; Graham, A.; Armstrong, N. R., Photoemission Spectroscopy of Tethered CdSe Nanocrystals: Shifts in Ionization Potential and Local Vacuum Level As a Function of Nanocrystal Capping Ligand. *ACS Applied Materials & Interfaces* 2010, 2 (3), 863-869.
  41. Cirloganu, C. M.; Padilha, L. A.; Lin, Q.; Makarov, N. S.; Velizhanin, K. A.; Luo, H.; Robel, I.; Pietryga, J. M.; Klimov, V. I., Enhanced carrier multiplication in engineered quasi-type-II quantum dots. *Nat. Commun.* 2014, 5, 4148.
  42. Kroupa, D. M.; Pach, G. F.; Voros, M.; Giberti, F.; Chernomordik, B. D.; Crisp, R. W.; Nozik, A. J.; Johnson, J. C.; Singh, R.; Klimov, V. I.; Galli, G.; Beard, M. C., Enhanced Multiple Exciton Generation in PbS|CdS Janus-like Heterostructured Nanocrystals. *ACS Nano* 2018, 12 (10), 10084-10094.
  43. Bawendi, M. G.; Wilson, W. L.; Rothberg, L.; Carroll, P. J.; Jedju, T. M.; Steigerwald, M. L.; Brus, L. E., Electronic structure and photoexcited-carrier dynamics in nanometer-size CdSe clusters. *Phys Rev Lett* 1990, 65 (13), 1623-1626.
  44. Dneprovskii, V. S.; Klimov, V.; Okorokov, D. K.; Vandyshev, Y. V., Strong optical nonlinearities and laser emission of semiconductor microcrystals. *Solid State Communications* 1992, 81 (3), 227-230.
  45. Woggon, U.; Gaponenko, S.; Langbein, W.; Uhrig, A.; Klingshirn, C., Homogeneous linewidth of confined electron-hole-pair states in II-VI quantum dots. *Phys Rev B Condens Matter* 1993, 47 (7), 3684-3689.
  46. Wang, C.; Shim, M.; Guyot-Sionnest, P., Electrochromic nanocrystal quantum dots. *Science* 2001, 291 (5512), 2390-2.

47. Wehrenberg, B. L.; Guyot-Sionnest, P., Electron and Hole Injection in PbSe Quantum Dot Films. *J. Am. Chem. Soc.* 2003, 125 (26), 7806-7807.
48. Guyot-Sionnest, P.; Wehrenberg, B.; Yu, D., Intraband relaxation in CdSe nanocrystals and the strong influence of the surface ligands. *J. Chem. Phys.* 2005, 123 (7), 074709.
49. Houtepen, A. J.; Vanmaekelbergh, D., Orbital occupation in electron-charged CdSe quantum-dot solids. *J. Phys. Chem. B* 2005, 109 (42), 19634-42.
50. Koole, R.; Allan, G.; Delerue, C.; Meijerink, A.; Vanmaekelbergh, D.; Houtepen, A. J., Optical Investigation of Quantum Confinement in PbSe Nanocrystals at Different Points in the Brillouin Zone. *Small* 2008, 4 (1), 127-133.
51. du Fossé, I.; ten Brinck, S.; Infante, I.; Houtepen, A. J., Role of Surface Reduction in the Formation of Traps in n-Doped II-VI Semiconductor Nanocrystals: How to Charge without Reducing the Surface. *Chem. Mater.* 2019, 31 (12), 4575-4583.
52. Empedocles, S. A.; Bawendi, M. G., Quantum-confined stark effect in single CdSe nanocrystallite quantum dots. *Science* 1997, 278 (5346), 2114-7.
53. Trinh, M. T.; Houtepen, A. J.; Schins, J. M.; Piris, J.; Siebbeles, L. D., Nature of the second optical transition in PbSe nanocrystals. *Nano Lett.* 2008, 8 (7), 2112-7.
54. Boehme, S. C.; Walvis, T. A.; Infante, I.; Grozema, F. C.; Vanmaekelbergh, D.; Siebbeles, L. D. A.; Houtepen, A. J., Electrochemical Control over Photoinduced Electron Transfer and Trapping in CdSe-CdTe Quantum-Dot Solids. *ACS Nano* 2014, 8 (7), 7067-7077.
55. Giberti, F.; Voros, M.; Galli, G., Design of Heterogeneous Chalcogenide Nanostructures with Pressure-Tunable Gaps and without Electronic Trap States. *Nano Lett* 2017, 17 (4), 2547-2553.
56. Voznyy, O.; Thon, S. M.; Ip, A. H.; Sargent, E. H., Dynamic Trap Formation and Elimination in Colloidal Quantum Dots. *The Journal of Physical Chemistry Letters* 2013, 4 (6), 987-992.
57. Drijvers, E.; De Roo, J.; Martins, J. C.; Infante, I.; Hens, Z., Ligand Displacement Exposes Binding Site Heterogeneity on CdSe Nanocrystal Surfaces. *Chem. Mater.* 2018, 30 (3), 1178-1186.
58. Kirkwood, N.; Monchen, J. O. V.; Crisp, R. W.; Grimaldi, G.; Bergstein, H. A. C.; du Fosse, I.; van der Stam, W.; Infante, I.; Houtepen, A. J., Finding and Fixing Traps in II-VI and III-V Colloidal Quantum Dots: The Importance of Z-Type Ligand Passivation. *J. Am. Chem. Soc.* 2018.

59. Zhang, J.; Chernomordik, B. D.; Crisp, R. W.; Kroupa, D. M.; Luther, J. M.; Miller, E. M.; Gao, J.; Beard, M. C., Preparation of Cd/Pb Chalcogenide Heterostructured Janus Particles via Controllable Cation Exchange. *ACS Nano* 2015, 9 (7), 7151-63.
60. van Embden, J.; Mulvaney, P., Nucleation and growth of CdSe nanocrystals in a binary ligand system. *Langmuir* 2005, 21 (22), 10226-33.
61. Steckel, J. S.; Yen, B. K.; Oertel, D. C.; Bawendi, M. G., On the mechanism of lead chalcogenide nanocrystal formation. *J. Am. Chem. Soc.* 2006, 128 (40), 13032-3.
62. Moreels, I.; Lambert, K.; De Muynck, D.; Vanhaecke, F.; Poelman, D.; Martins, J. C.; Allan, G.; Hens, Z., Composition and size-dependent extinction coefficient of colloidal PbSe quantum dots. *Chem. Mater.* 2007, 19 (25), 6101-6106.
63. Jasieniak, J.; Smith, L.; van Embden, J.; Mulvaney, P.; Califano, M., Re-examination of the size-dependent absorption properties of CdSe quantum dots. *J. Phys. Chem. C* 2009, 113 (45), 19468-19474.
64. Kunneman, L. T. Exciton and charge carrier dynamics in semiconductor nanorods and nanoplatelets. Delft University of Technology, 2015.
65. Perdew, J. P.; Burke, K.; Ernzerhof, M., Generalized gradient approximation made simple. *Phys. Rev. Lett.* 1996, 77 (18), 3865-3868.
66. Hutter, J.; Iannuzzi, M.; Schiffmann, F.; VandeVondele, J., CP2K: atomistic simulations of condensed matter systems. *Wiley Interdisciplinary Reviews-Computational Molecular Science* 2014, 4 (1), 15-25.
67. Ruch, P. W.; Cericola, D.; Hahn, M.; Kötz, R.; Wokaun, A., On the use of activated carbon as a quasi-reference electrode in non-aqueous electrolyte solutions. *J. Electroanal. Chem.* 2009, 636 (1-2), 128-131.

## Appendix

### Calibration of the Ag pseudoreference electrode for the spectroelectrochemical measurements

During a spectroelectrochemical measurement, a potential difference is applied across the electrochemical cell, setting the potential of the working electrode with respect to the reference electrode. In order to calibrate the potential values with respect to a standard reference for the potential (e.g. the potential of an electron in vacuum), we measured a cyclic voltammogram of a redox couple whose reaction potential is known with respect to the reference<sup>1</sup>. We measured the ferrocene/ferrocenium redox couple, scanning the applied potential over the redox potential. Figure 3.6 shows the result of a cyclic voltammogram of ferrocene/ferrocenium, performed with a scan rate of 50 mV/s. The position of the redox potential measured with respect to the pseudoreference electrode,  $V_{1/2}$  (pseudoref.), was determined taking the average of the potentials at which the reduction and oxidation peak current occur. The potential values recorded by the potentiostat are then calibrated using the formula:

$$\begin{aligned} V(\text{vacuum}) &= V(\text{pseudoref.}) + V_{\text{fc}/\text{fc}^+}(\text{vacuum}) - V_{1/2}(\text{pseudoref.}) \\ &= V(\text{pseudoref.}) + V_{\text{SCE}}(\text{vacuum}) + V_{\text{fc}/\text{fc}^+}(\text{SCE}) - V_{1/2}(\text{pseudoref.}) \end{aligned} \quad 3.1$$

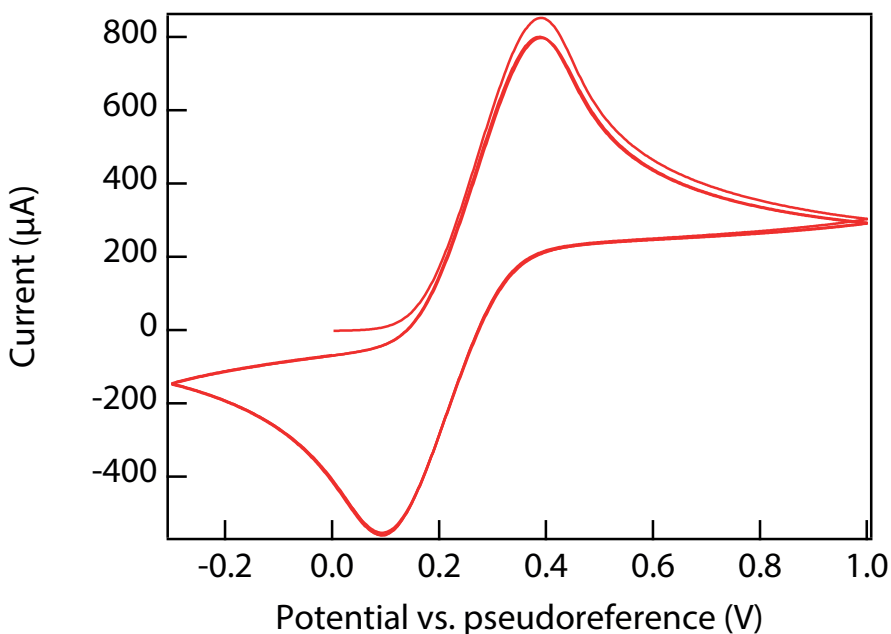


**Figure 3.6.** Cyclic voltammogram of the ferrocene/ferrocenium redox couple, measured with a potential scanning speed of 50 mV/s.

where  $V_{\text{SCE}}(\text{vacuum})$  is the redox potential of the saturated calomel electrode (SCE) measured versus vacuum (4.68 V), and  $V_{\text{Fc/Fc}^+}(\text{SCE})$  is the redox potential of the ferrocene/ferrocenium couple measured versus the SCE (0.46 V)<sup>67</sup>. To ensure proper calibration of the potential, a ferrocene/ferrocenium reference measurement was taken before each spectroelectrochemical measurement.

### Fit of QD bleach in the spectroelectrochemical measurements

The spectroelectrochemical signal at the PbSe and CdSe QD bandgap, composed of the superposition of a Gaussian bleach and of a slowly varying background (as discussed in the main text), is fitted using the function:

$$f(\lambda) = A + B\lambda + A_G \exp\left(-(\lambda - \lambda_G)^2 / (2\sigma_G^2)\right) \quad 3.2$$

where  $A_G$ ,  $\lambda_G$ , and  $\sigma_G$  are the amplitude, central wavelength and standard deviation of the Gaussian bleach, respectively. For the fit of the PbSe bleach in the TBACl-BT film and the CdSe bleach in the EDT film, the slope of the background in the wavelength range of the bleach feature was negligible, and a satisfactory fit could be achieved keeping the slope  $B$  fixed to 0 during the fit.

### Potential-dependence of spectroelectrochemical bleach amplitude

We assume a Gaussian density of states at the conduction band-edge of each QD component, originating from the presence of quantum confinement acting on a Gaussian size distribution and by the presence additional energy disorder throughout a QD film (e.g. variation in inter-QD coupling or the presence of impurity ions). In the presence of unity gate coupling, i.e. changes in the applied potential are equal to the changes of the Fermi level, the number of electrons injected into the band-edge state as a function of the applied potential is proportional to:

$$N_{\text{CB}} \propto \int_{-\infty}^V e^{-\frac{(V-V_{\text{CB}})^2}{2\sigma^2}} = \sqrt{\frac{\pi}{2}}\sigma \left(1 + \text{erf}\left(\frac{(V-V_{\text{CB}})}{\sqrt{2}\sigma}\right)\right) \quad 3.3$$

where  $V_{\text{CB}}$  and  $\sigma$  are the central potential and the standard deviation of the conduction band density of states, respectively.

Since the band-edge bleach of semiconductor QDs is proportional to the number of electrons populating the conduction band-edge states, the potential dependence of the experimental bleach can be described by the fit function:

$$f(V) = A \left(1 + \text{erf}\left(\frac{V - V_{\text{CB}}}{\sqrt{2}\sigma}\right)\right) \quad 3.4$$

Estimates of the gate coupling for electrochemical charging of porous QD films,

performed by Boehme *et al.*<sup>34</sup>, suggest a near unity value for low injected carrier density, allowing to reliably use spectroelectrochemical measurements to determine the band-edge energies. However, in a heterojunction film, the injection of carriers in the highest conduction band-edge occurs in the presence of a significant density of injected electrons in the system, potentially leading to energy penalties for further electronic injection due to imperfect screening of the Coulomb interactions in the system. Therefore, although the energy position of the lowest energy conduction band and the energy order of the conduction band-edge can be determined reliably with the spectroelectrochemical approach, the spectroelectrochemical estimate for the position of the highest conduction band-edge can be shifted upwards by the Coulomb energy penalties, increasing the energy distance between the two conduction band edges.

### Energy-integration of the transient absorption signal at the CdSe QD bandgap

In the transient absorption measurements of PbSe-CdSe QD films, the signal at the bandgap of the CdSe QDs is dominated by a bleach feature, prominent at early times,

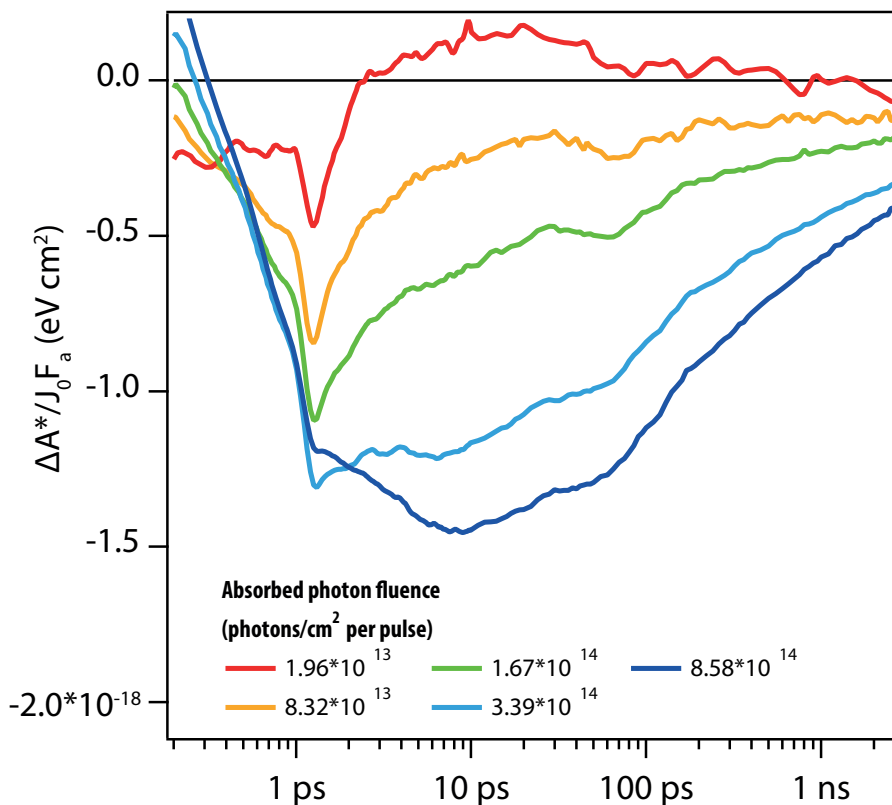


**Figure 3.7.** Time-dependence of the energy-integrated, fluence-normalized bleach for the TBACl-BT sample, obtained integrating the TA signal in an energy range around the CdSe QD bandgap (1.90 – 2.14 eV) and dividing it by the absorbed photon fluence.

and by a derivative-like feature, prominent at late times. Since the two features are spectrally overlapping, the time-dependence of the TA signal at a fixed wavelength contains contributions from both features. To disentangle the time-dependence of the bleach feature from the derivative-like feature, we integrated the TA signal in the energy window between 1.90 eV and 2.14 eV, containing the full bleach and derivative-like feature. Due to the anti-symmetry of the derivative-like feature, its contribution to the integral is null, and the integrated values reflects only the contribution of the bleach to the TA signal. The time-dependent bleaches shown in Figure 3.3f, Figure 3.7 and Figure 3.8 are obtained integrating the TA signal in the 1.90-2.14 eV range, and dividing the resulting integral by the absorbed photon fluence.

3

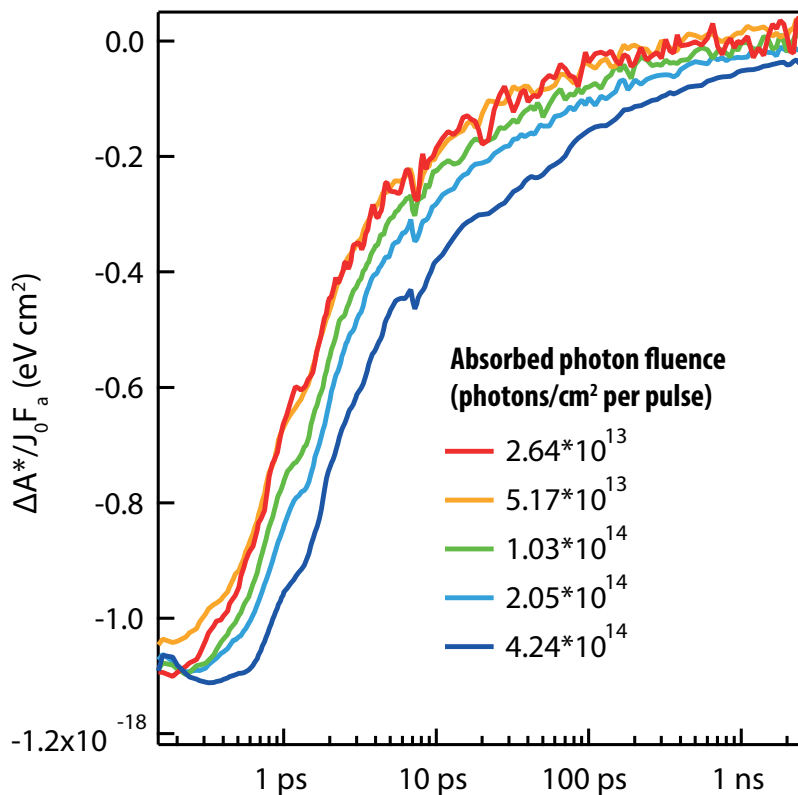


**Figure 3.8.** Time-dependence of the energy-integrated, fluence-normalized bleach for the EDT sample, obtained integrating the TA signal in an energy range around the CdSe QD bandgap (1.90 – 2.14 eV) and dividing it by the absorbed photon fluence.

### Power-dependence of the bleach decay time in the TBACI-BT treated film

**Table 3.2.** Bleach half-life of the TBACI-BT sample for different absorbed photon fluence, obtained from the time-dependence of the energy-integrated, fluence-normalized bleach, displayed in Figure 3.7.

Absorbed photon fluence (photons/cm <sup>2</sup> per pulse)	Bleach half-life (ps)
$1.96 \cdot 10^{13}$	1.7
$8.32 \cdot 10^{13}$	2.7
$1.67 \cdot 10^{14}$	15
$3.39 \cdot 10^{14}$	220
$8.58 \cdot 10^{14}$	450

### Power-dependence of the bleach decay time in the EDT-treated film

**Table 3.3.** Bleach half-life of the EDT sample for different absorbed photon fluence, obtained from the time-dependence of the energy-integrated, fluence-normalized bleach, displayed in Figure 3.8.

Absorbed photon fluence (photons/cm <sup>2</sup> per pulse)	Bleach half-life (ps)
$2.64 \cdot 10^{13}$	1.4
$5.17 \cdot 10^{13}$	1.7
$1.03 \cdot 10^{14}$	2.0
$2.05 \cdot 10^{14}$	2.4
$4.24 \cdot 10^{14}$	3.7

Transient absorption measurements of CdSe-only and PbSe-only films

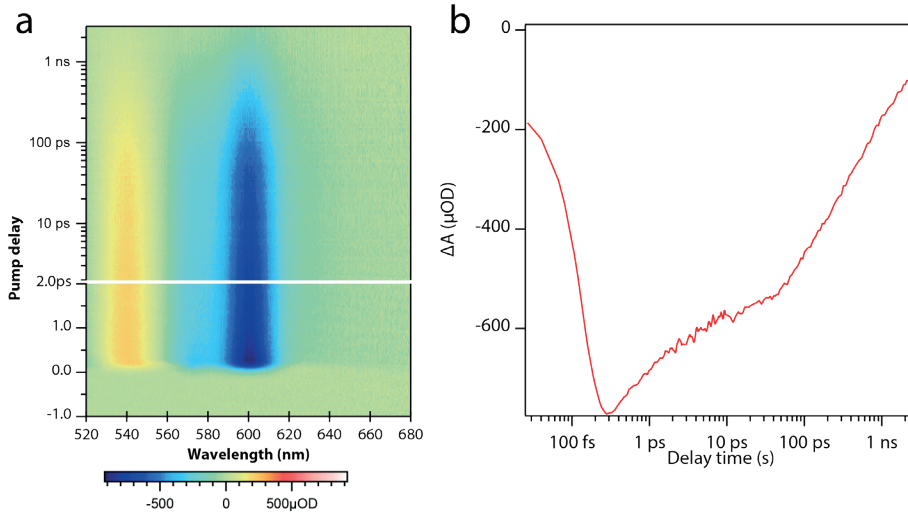


**Figure 3.9.** **a**, Color-map showing the TA response of a CdSe-only film ligand treated with a TBACl ligand solution, excited at 570 nm with an incoming photon fluence of  $9.76 \cdot 10^{12}$  photons/cm<sup>2</sup> per pulse. **b**, bleach amplitude extracted from a Gaussian fit of the band-edge bleach for each pump delay time.

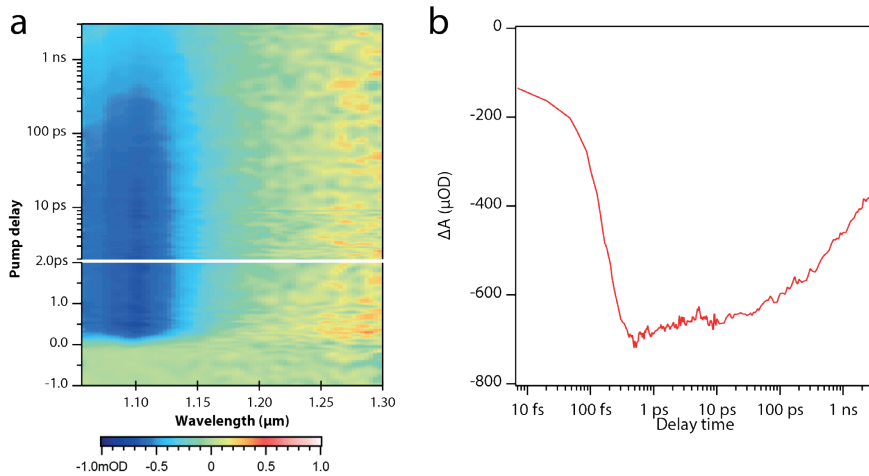


**Figure 3.10.** **a**, Color-map showing the TA response of a PbSe-only film ligand treated with a TBACl ligand solution, excited at 1100 nm with an incoming photon fluence of  $9.05 \cdot 10^{13}$  photons/cm<sup>2</sup> per pulse. **b**, bleach amplitude extracted from a Gaussian fit of the band-edge bleach for each pump delay time.

3



# Chapter 4

## Model to Determine a Distinct Rate Constant for Carrier Multiplication from Experiments

### *Abstract*

Carrier multiplication (CM) is the process in which multiple electron-hole pairs are created upon absorption of a single photon in a semiconductor. CM by an initially hot charge carrier occurs in competition with cooling by phonon emission, with the respective rates determining the CM efficiency. Up to now CM rates have only been calculated theoretically. We show for the first time how to extract a distinct CM rate constant from experimental data of the relaxation time of hot charge carriers and the yield of CM. We illustrate this method for PbSe quantum dots. Additionally, we provide a simplified method using an estimated energy loss rate to estimate the CM rate constant just above the onset of CM, when detailed experimental data of the relaxation time is missing.

Based on: Frank C. M. Spoor, Gianluca Grimaldi, Sachin Kinge, Arjan J. Houtepen and Laurens D. A. Siebbeles. ACS Applied Energy Materials, 2019, 2 (1), 721-728.

## 4.1 Introduction

Absorption of a sufficiently energetic photon in a semiconductor can initially create a hot electron-hole pair with the electron and/or the hole having excess energy exceeding the band gap. Such hot charge carriers can cool down to the band edge by phonon emission, and in addition by excitation of one or more additional electrons across the band gap. The latter process of carrier multiplication (CM) leads to generation of two or more electron-hole pairs for one absorbed photon.<sup>1,2</sup>

In the last decade, many nanomaterials with varying composition, size and shape have been investigated for the occurrence of CM.<sup>1-3</sup> CM has been found in 0D quantum dots (QDs) in solution<sup>4</sup> and in thin films,<sup>5,6</sup> 1D nanorods,<sup>7</sup> 2D nanosheets,<sup>8</sup> 2D percolative networks<sup>9</sup> and bulk material.<sup>10</sup> CM is a promising process to increase the efficiency of solar energy conversion and has been demonstrated to occur in photovoltaic devices and solar fuel cells based on 0D, 1D or 2D nanomaterials.<sup>11-15</sup>

The quantum yield (QY) for charge carrier photogeneration (number of charges carriers per absorbed photon) is the net result of the competitive relaxation of a hot electron-hole pair *via* CM and cooling by phonon emission. Therefore the competition between CM and cooling has been studied intensively.<sup>16-18</sup> Relaxation times have been experimentally determined in many materials, with a particular focus on lead selenide (PbSe) QDs, owing to their well-controlled synthesis and large range of possible band gap energies through tuning their size.<sup>19</sup> The outcome is that cooling at high energies relevant to CM is similar in QDs and bulk material.<sup>20-22</sup> However, according to theoretical calculations CM rates in QDs differ from those for bulk.<sup>23-26</sup>

To our knowledge the most comprehensive study aimed at finding CM and cooling rates by theoretical analysis of measured QYs is that of Stewart *et al.*<sup>18</sup> However, in that work the rates were taken to be independent of the energy of the charge carrier. The latter does not agree with the aforementioned theoretical calculations, which indicate that the CM rate strongly depends on charge carrier energy. In addition, our earlier work shows that the cooling rate also depends on energy.<sup>22</sup> A model that allows one to extract an energy-dependent CM rate from experiments would be very valuable for the understanding of the factors that govern CM.

In this work, we derive a method to extract an energy-dependent CM rate constant from experimental measurements of the relaxation time of hot charge carriers to band edge states and the QY of electron-hole pairs. The method is valid up to a carrier excess energy (the energy of the carrier above the band edge, i.e.  $E_{\text{excess},e} = E_e - E_{\text{CB}}$  for electrons) of twice the band gap. In that case the hot charge carriers can undergo only one CM event. We use the method to determine an energy-dependent CM rate constant from our previous experimental data for PbSe QDs.<sup>22,27</sup> The method is however much more generally applicable and can be used to derive CM rate constants for any material of which experimental results of both the relaxation time and the QY are available. We also discuss a simplification to the method using an estimated energy loss rate instead of experimental data of the relaxation time. This simplified method can be used to find an estimate of the CM rate constant just above the energetic threshold of CM using only QY data when experimental data of the relaxation time of hot charge carriers is not available, as is the case for many materials that are studied for CM.

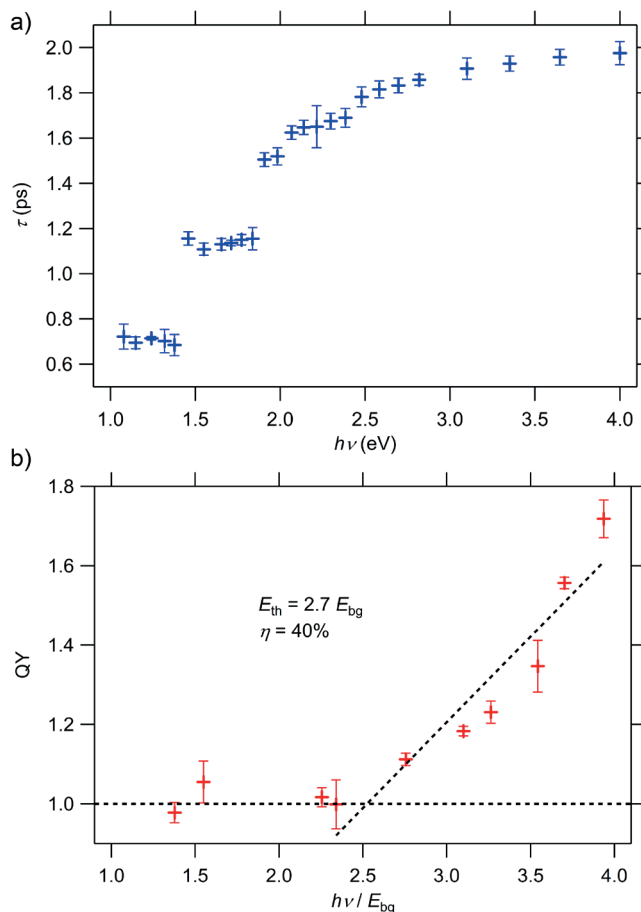


**Figure 4.1.** **a**, Electron relaxation times as a function of photoexcitation energy and **b**, QY as a function of photoexcitation energy scaled by the band gap energy for 3.9 nm PbSe QDs as reported in our previous works.<sup>22, 27</sup>

## 4.2 Experimental relaxation time and QY

In our previous work we reported energetic relaxation of electrons and holes to the band edges as a function of photoexcitation energy  $h\nu$  for 3.9 nm PbSe QDs with a band gap of 0.95 eV.<sup>22</sup> Here we focus on electrons only, for which we have accurately determined the relaxation time. Near the band gap we found that electrons relax between energy levels in fixed times. At photoexcitation energies relevant for CM, starting at twice the band gap energy, the relaxation time for electrons increases continuously as a function of photon energy. We show the relaxation time for electrons in 3.9 nm PbSe QDs as a function of photoexcitation energy in Figure 4.1a. For the same 3.9 nm PbSe QDs we reported the QY in our follow-up work.<sup>27</sup> We show this QY as a function of photoexcitation energy normalized by the band gap energy in Figure 4.1b. A straight line is fitted to the data points above unity to find the CM threshold at 2.7 times the band gap energy and a CM

efficiency given by  $\eta = \frac{QY - 1}{h\nu / E_{bg}} \cdot 100\% = 40\%$ .

### 4.3 Model of the electronic structure

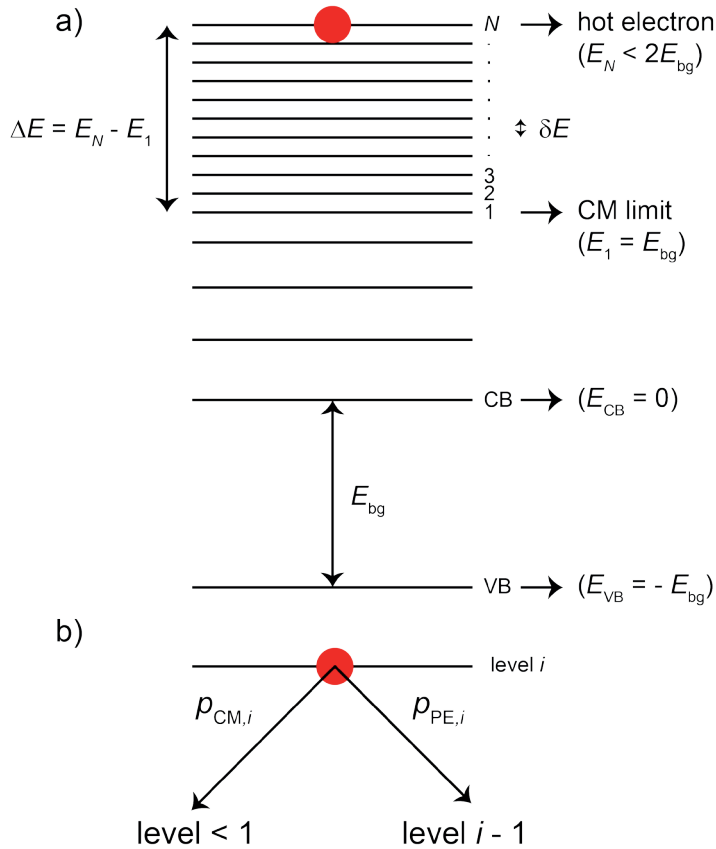
From the data in Figure 4.1 we wish to extract a rate constant for CM. To do so we first need to define an electronic structure for PbSe QDs. Many calculations of the PbSe QD electronic structure exist,<sup>22,28,29</sup> yielding a high density of states (DOS) at energies relevant for CM. The situation of a high DOS ensures that electronic states are always available for energy conservation upon phonon emission by a charge carrier. Indeed, carrier relaxation was shown to be governed by phonon emission for charge carriers with high excess energy over the band gap, similar to bulk material.<sup>20-22</sup> As an approximation, we can therefore use an electronic structure consisting of  $N$  equidistant energy levels, with the distance determined by the phonon energy,  $\delta E$ , at energies relevant for CM. We ignore the exact electronic structure near the band edge, since CM cannot occur from these energy levels. We show such an electronic structure in Figure 4.2a. We label the valence band (VB), conduction band (CB) and the higher energy levels (with indices 1 to  $N$ ) from which CM can occur. Setting the CB energy to 0, the electron energy for which CM can occur must be at least one band gap energy  $E_{bg}$ . Taking into account only states relevant for CM, we take level 1 at an energy equal to  $E_{bg}$ . The highest energy level, at which we create a hot electron, is labeled  $N$ .

In the electronic structure of Figure 4.2a, an electron in an energy level  $i$  has two possibilities. It either cools down to the energy level  $i - 1$  below by emitting a phonon or undergoes CM, as illustrated in Figure 4.2b. Upon CM, it decays to a level  $i < 1$ . If the electron energy is larger than twice the band gap energy, the electron theoretically could undergo CM to a level  $i \geq 1$  and hence undergo CM twice. We consider only single CM events and therefore consider the highest carrier energy to be just below twice the band gap energy. This determines our limit for energy level  $N$  ( $E_N < 2E_{bg}$ ). When an electron in our analysis decays to a level  $i < 1$  it is not considered further, since CM is no longer energetically allowed. We now define  $k_{PE,i}$  as the phonon emission rate constant from level  $i$ ,  $k_{CM,i}$  as the CM rate constant from level  $i$ ,  $\Delta E$  as the hot electron energy above the theoretical onset of CM (the electron energy in level  $N$  minus the electron energy in level 1) and  $\delta E$  as the phonon energy, which is the distance between energy levels, see Figure 4.2a. Since we assume that cooling is governed by phonon emission only, the overall relaxation rate constant equals  $k_{PE,i} + k_{CM,i}$ . The probability to either emit a phonon,  $p_{PE,i}$ , or undergo CM,  $p_{CM,i}$ , from a certain level  $i$  is expressed in terms of the rate constants as:

$$p_{PE,i} = \frac{k_{PE,i}}{k_{PE,i} + k_{CM,i}} \quad 4.1$$

$$p_{CM,i} = \frac{k_{CM,i}}{k_{PE,i} + k_{CM,i}}$$

### 4.4 Modeling carrier relaxation time and CM QY



4

**Figure 4.2.** **a**, Electronic structure for PbSe QDs. The CB energy is set to 0, such that the first energy level from which an electron can undergo CM has at least the band gap energy  $E_{bg}$ . This energy level is labeled 1. Above the minimal energy required for CM we assume equidistant energy levels with N the highest level at which we initially create a hot electron. Since we only consider single CM events, this energy must be lower than twice the band gap energy. **b**, Possible scenarios of phonon emission or CM from an energy level  $i$ .

Using the electronic structure of Figure 4.2a we can now identify the possible relaxation scenarios of a hot electron from any energy level  $i$  between 1 and N. For example, if an electron is created in energy level 2, it can either (i) undergo CM directly, (ii) emit a phonon in energy level 2 to cool down to energy level 1 and then undergo CM or (iii) emit a phonon in energy level 2 to cool down to energy level 1 and subsequently emit a phonon in energy level 1 to cool down below it. In all three scenarios, the electron ends up below level 1 and is no longer able to decay *via* CM. From this consideration, we can calculate the relaxation time from each energy level to below level 1 for comparison to Figure 4.1a. The first relaxation times are given by:

$$\begin{aligned}
\tau_1 &= p_{PE,1} \frac{1}{k_{PE,1}} + p_{CM,1} \frac{1}{k_{CM,1}} \\
\tau_2 &= p_{PE,2} p_{PE,1} \left( \frac{1}{k_{PE,2}} + \frac{1}{k_{PE,1}} \right) + p_{PE,2} p_{CM,1} \left( \frac{1}{k_{PE,2}} + \frac{1}{k_{CM,1}} \right) + p_{CM,2} \frac{1}{k_{CM,2}} \\
\tau_3 &= p_{PE,3} p_{PE,2} p_{PE,1} \left( \frac{1}{k_{PE,3}} + \frac{1}{k_{PE,2}} + \frac{1}{k_{PE,1}} \right) + p_{PE,3} p_{PE,2} p_{CM,1} \left( \frac{1}{k_{PE,3}} + \frac{1}{k_{PE,2}} + \frac{1}{k_{CM,1}} \right) \\
&\quad + p_{PE,3} p_{CM,2} \left( \frac{1}{k_{PE,3}} + \frac{1}{k_{CM,2}} \right) + p_{CM,3} \frac{1}{k_{CM,3}}
\end{aligned} \tag{4.2}$$

4

The corresponding QYs for comparison to Figure 4.1b can be calculated in a similar manner. Note that the QY is defined as the total number of charge carriers per absorbed photon. The QY is therefore always at least unity and becomes higher when CM occurs. The first QYs are given by:

$$\begin{aligned}
QY_1 &= 1 + p_{CM,1} = 2 - p_{PE,1} \\
QY_2 &= 1 + p_{CM,2} + p_{PE,2} p_{CM,1} = 2 - p_{PE,2} p_{PE,1} \\
QY_3 &= 1 + p_{CM,3} + p_{PE,3} p_{CM,2} + p_{PE,3} p_{PE,2} p_{CM,1} = 2 - p_{PE,3} p_{PE,2} p_{PE,1}
\end{aligned} \tag{4.3}$$

The last right-hand side expressions in equation 4.3 indicate that CM occurs for all decay pathways, except for the case in which the electron cools down through all energy levels *via* phonon emission. For any initial energy level  $N$  (with energy such that only one CM event is possible), we can extend equations 4.2 and 4.3 to a general result given by:

$$\tau_N = \prod_{i=1}^N (p_{PE,i}) \sum_{i=1}^N \left( \frac{1}{k_{PE,i}} \right) + \sum_{j=1}^{N-1} \left\{ p_{CM,j} \prod_{k=j+1}^N p_{PE,k} \left[ \frac{1}{k_{CM,j}} + \sum_{k=j+1}^N \left( \frac{1}{k_{PE,k}} \right) \right] \right\} + p_{CM,N} \frac{1}{k_{CM,N}} \tag{4.4}$$

$$QY_N = 2 - \prod_{i=1}^N p_{PE,i} \tag{4.5}$$

We note that equations 4.4 and 4.5 can be modified to include multiple CM events, but they become much more complicated and are not easily fit to the experimental data anymore. We therefore choose to limit ourselves to the situation of a single CM event.

## 4.5 Relating experiment and fits

To fit equations 4.4 and 4.5 to the experimental data in Figure 4.1a and 4.1b, we first need to relate the photoexcitation energy,  $h\nu$ , to the hot electron energy  $\Delta E$  (see Figure 4.2a) above the theoretical energy threshold of CM. A straightforward assumption would be to divide the photon energy in excess of the band gap equally between the electron and hole. This however cannot explain a CM threshold below three times the band gap

energy, such as observed in Figure 4.1b. We therefore choose to give all the photon excess energy over the band gap to the electron as an upper limit. Our previous work indicates the existence of transitions in which the photon excess energy is divided as such.<sup>27,30</sup> With this assumption  $\Delta E$  can be related to the photoexcitation energy using:

$$\Delta E = h\nu - 2E_{bg} = h\nu - 1.9 \text{ eV} \quad 4.6$$

Rescaling the photoexcitation energy according to equation 4.6, the number of the energy level  $N$  can be determined for each photon energy using:

$$N = \frac{\Delta E}{\delta E} \quad 4.7$$

(where  $N$  is rounded up, since the lowest level corresponds to  $N=1$ ). Finally, we prescribe an energy dependence for the phonon emission and CM rate constants of the form:

$$\begin{aligned} k_{PE} &= \alpha_{PE} \Delta E^{\beta_{PE}} \\ k_{CM} &= \alpha_{CM} \Delta E^{\beta_{CM}} \end{aligned} \quad 4.8$$

where the unit of  $\alpha$  is [ $\text{eV}^{-\beta} \text{ps}^{-1}$ ] since we take  $\Delta E$  in [ $\text{eV}$ ] and  $\beta$  is dimensionless. This power law dependence is a heuristic function, that can however describe the general energy dependence suggested by theory quite well.<sup>23</sup> We have carried out the analysis using polynomial functions up to third order as well, but were able to describe the results most accurately using the power law dependence of equation 4.8.

To fit equations 4.4 and 4.5 to the data of Figure 4.1a and 4.1b, we rescale the photoexcitation energy  $h\nu$  to  $\Delta E$  according to equation 4.6. This yields both the relaxation time  $\tau$  and the QY as a function of  $\Delta E$  (the electron excess energy minus one band gap,  $\Delta E = E_N - E_1$  from Figure 4.2a). The relaxation time relevant to CM is however relaxation from the initial electron energy  $\Delta E = h\nu - 2E_{bg}$  down to  $\Delta E = 0$ . The experimental relaxation time in Figure 4.1a equals cooling to the band edge ( $\Delta E = -E_{bg}$ ). Hence, we subtract a constant from the experimental relaxation time, such that it is zero for  $\Delta E = 0$ . Any relaxation below this energy is not relevant for CM. Finally, we perform a global fit of equations 4.4 and 4.5 to the experimental data of the relaxation time and the QY as a function of  $\Delta E$ . We set the highest energy level  $N$  for each data point using equation 4.7 with a distance of  $\delta E = 17 \text{ meV}$  between energy levels, equal to the LO phonon energy in PbSe.<sup>31</sup> The fit parameters we find from this procedure are the fit parameters  $\alpha$  and  $\beta$  from equation 4.8. We note that fitting to only the relaxation time or the QY, there is freedom in the fits of  $k_{CM}$  and  $k_{PE}$  yielding large uncertainties in  $\alpha$  and  $\beta$ . The global fit we perform here with coupled fit parameters does result in an accurate outcome. We have included the code used to fit equations 4.4 and 4.5 to the experimental data of the relaxation time and QY in the Appendix.

#### 4.6 Estimate of the CM and cooling rate constants

Fits to the experimental data points for which  $\Delta E < 0.95 \text{ eV}$  are shown in Figure 4.3a, with

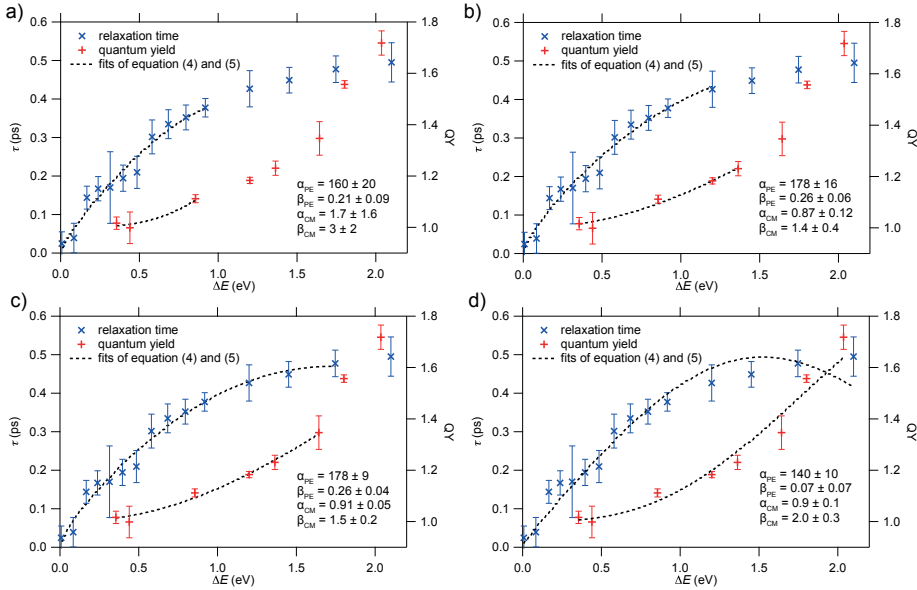


**Figure 4.3.** Fits of equations 4.4 and 4.5 to the experimental data up to **a)**  $\Delta E < 0.95$  eV, **b)**  $\Delta E < 1.4$  eV, **c)**  $\Delta E < 1.7$  eV and **d)**  $\Delta E < 2.1$  eV. Fit parameters from equation 4.8 are presented in the figures. The unit of  $\alpha$  is  $[\text{eV}^{\beta} \text{ps}^{-1}]$  and  $\beta$  is dimensionless.

the fitted parameters indicated in the figure. We choose this limit for  $\Delta E$  because of the validity of our model for only a single CM event, as discussed above. We observe that the fit reproduces the experimental data, but with high uncertainties in the fit parameters up to 100%. The low maximum value of the QY = 1.11 suggests only a small contribution from multiple CM events. We can therefore extend the range of our analysis to experimental data points at  $\Delta E > 0.95$  eV. If we do so, we obtain values of the fit parameters in Figure 4.3b ( $\Delta E < 1.4$  eV) and 4.3c ( $\Delta E < 1.7$  eV) in line with those previously obtained, but decreasing the uncertainty to a maximum of only 15% for the latter case. The maximum value of the QY = 1.35 in Figure 4.3c is evidently still small enough to neglect multiple CM events.

However, the fit becomes worse when we further extend its range to include the full experimental data ( $\Delta E < 2.1$  eV), see Figure 4.3d. Surprisingly, the fitted relaxation time even decreases with energy. This is due to neglecting multiple CM events. When CM occurs, the electron in our model is taken out of the analysis (moved to an energy level  $i < 1$  in Figure 4.2a). For high enough energy however, an electron can undergo CM to an energy level  $i \geq 1$  from which CM can occur again. Therefore, this electron continues to cool down after the first CM event, increasing the total relaxation time. In our model however, this electron is considered to be completely relaxed after the first CM event, resulting in a relaxation time that is shorter in the fit than in the experiment. Additionally, the CM rate constant increases with increasing energy according to equation 4.8. As the CM rate constant increases, on average fewer cooling events take place before the first CM event occurs. If the electron is taken out of the analysis after this first CM event as discussed above, the relaxation time can decrease with increasing energy such as observed in the fit of Figure 4.3d. Neglecting the relaxation time after the first CM event is too

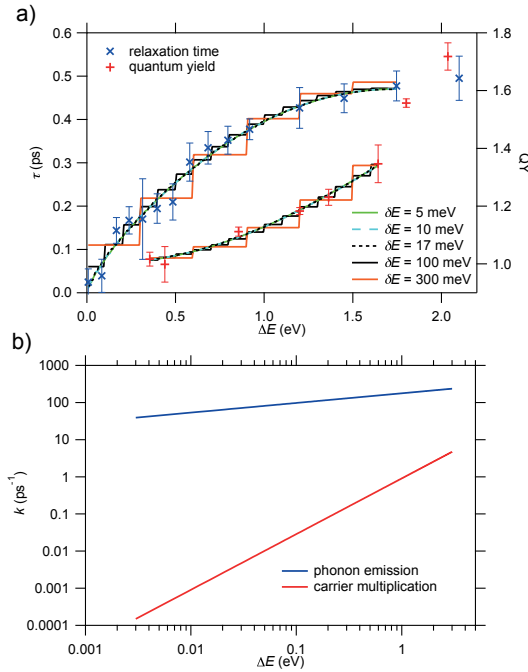


**Figure 4.4.** **a**, Fits to the experimental data using equations (4) en (5) with different values of  $\delta E$ . **b**, Phonon emission rate constant for 17 meV LO phonons and experimental CM rate constant in 3.9 nm PbSe QDs.

severe an approximation to describe the data for the highest  $\Delta E$ . With a measured QY = 1.72 the scenario of multiple CM events is likely. We therefore trust our analysis only up to  $\Delta E < 1.7$  eV.

The distance,  $\delta E$ , between energy levels in the electronic structure of Figure 4.2a has an influence on the fit through equation 4.7. If the distance becomes too large, equations 4.4 and 4.5 will yield a stepwise increase of respectively the relaxation time and the QY as a function of electron excess energy. In Figure 4.4a we show fits to our experimental data using equations 4.4 and 4.5, for different values of  $\delta E$ . We reproduce the fits separately for visibility in the Appendix Figure 4.6. We observe that for large  $\delta E$  in the order of 100 meV, indeed the fits have a stepwise character and do not describe the data as well as the smoother fits for smaller  $\delta E$ . The fits for small  $\delta E$  all yield the same fit parameters  $\alpha_{CM}$ ,  $\beta_{CM}$  and  $\beta_{PE}$ . Only  $\alpha_{PE}$  increases from 355 for  $\delta E = 17$  meV to 605 for  $\delta E = 10$  meV to 1210 for  $\delta E = 5$  meV. This is to be expected, since the phonon emission rate is inversely dependent on the phonon energy  $\delta E$  if the average energy loss rate (i.e. the total relaxation time) remains constant (see equation 4.11 below). Since we argued before that  $\delta E$  represents the phonon energy, these results indicate that cooling in our model can be governed by the most energetic LO phonons with an energy of 17 meV, as well as any other less energetic phonons. We consider LO phonons the most probable, since the most energy can be dissipated per step. Most importantly, the CM rate constant is invariant with the phonon energy  $\delta E$ , if it is small enough.

We finally find a phonon emission rate constant for 17 meV LO phonons and an experimental CM rate constant of:

$$\begin{aligned} k_{\text{PE}} &= (355 \pm 19) \Delta E^{(0.26 \pm 0.04)} \text{ ps}^{-1} \\ k_{\text{CM}} &= (1.8 \pm 0.1) \Delta E^{(1.5 \pm 0.2)} \text{ ps}^{-1} \end{aligned} \quad 4.9$$

in 3.9 nm PbSe QDs, with  $\Delta E$  in eV. We show these rates as a function of  $\Delta E$  in Figure 4.4b. The energy dependence of the CM rate constant should be related to both the Coulomb matrix element for CM at the energy of the hot electron and the density of final bi-exciton states through Fermi's Golden Rule. Theoretical calculations using various methods either find similar<sup>26</sup> or higher<sup>23,24</sup> CM rate constants than the experimental CM rate constant we find. We are uncertain what exactly causes the discrepancy. We note however that the joint DOS for electrons and holes upon photon absorption in a single, parabolic band semiconductor scales with  $(h\nu - E_{\text{bg}})^{0.5}$  and can be higher when more bands are involved.<sup>32</sup> The above method is applicable to any material for which the required experimental data is available, taking into account the following considerations. One should consider carefully how to divide the excess photon energy between electron and hole for materials in which an asymmetric distribution is less likely than in PbSe QDs. Moreover, depending on theoretical insights and the quality of the fits, the prescribed energy dependence of the rate constants as given in equation 4.8 could be chosen differently to suit the material under investigation. Finally, equations 4.4 and 4.5 can be modified to include multiple CM events, although this greatly increases their complexity.

#### 4.7 Estimate of the CM rate constant from the QY

The above analysis yields phonon emission and experimental CM rate constants as a function of electron excess energy from experimental data of the relaxation time and QY in QDs. The major limitation of equation 4.4 is that it requires detailed experimental data of the relaxation time up to high photoexcitation energy. In literature, such data is very rare. The data of the QY needed for equation 4.5 is much more common for many different materials. We therefore discuss here a simplified method to estimate the CM rate constant just above the energetic threshold of CM using only experimental data of the QY. We first need to estimate an energy loss rate. With the experimental data of the relaxation time from Figure 4.1a, we can calculate an average energy loss rate  $\gamma$  in an energy interval  $\Delta E$  using:

$$\gamma = \frac{dE}{dt} = \left[ \frac{d\tau}{d(h\nu)} \right]^{-1} \approx \frac{\Delta E}{\Delta\tau} \quad 4.10$$

where  $\tau$  is the relaxation time and  $h\nu$  the photon energy. We wish to use this average energy loss rate for estimating a phonon emission rate constant in the electronic structure of Figure 4.2a. If relaxation is only governed by phonon emission, then:

$$k_{PE} = \frac{\gamma}{\delta E} = N \frac{\gamma}{\Delta E} \quad 4.11$$

The phonon emission rate in equation 4.11 is inversely dependent on the phonon energy  $\delta E$ , as mentioned before when we discussed Figure 4.4a. Equation 4.11 neglects any energy lost through CM and is therefore only valid below the onset of CM. We however approximate  $k_{PE}$  just above the energetic threshold of CM with  $k_{PE}$  calculated using equation 4.11.

The benefit of equations 4.10 and 4.11 is that an energy loss rate and consequently a phonon emission rate constant can be estimated from experimental data or theoretical calculations. This can then be used to estimate a CM rate constant just above the onset of CM. Of course, this simplified method is not as accurate as applying the entire method discussed above and does not yield a full energy dependence of the CM rate constant, but it aids in further analyzing existing experimental data.

To find a CM rate constant, we next consider how an electron relaxes through the electronic structure of Figure 4.2a. The probabilities given in equation 4.1 that an electron either undergoes CM or cools from a given energy level by emitting a phonon are now constant, because of the average energy loss rate used from equation 4.10. Consequently, the probability that a hot electron created in energy level N does not undergo CM and therefore relaxes to below level 1 by emitting N phonons is equal to  $(p_{PE})^N$ . In all other scenarios, the electron undergoes CM. The total probability of an electron undergoing CM in any of the energy levels is therefore  $1 - (p_{PE})^N$ . As such, the QY is given by (recall that the QY is one plus the yield from CM):

$$QY = 2 - \left( \frac{k_{PE}}{k_{PE} + k_{CM}} \right)^N \quad 4.12$$

Equation 4.12 is used to estimate the CM rate constant from experimental data of the QY. It requires an estimate of the phonon emission rate constant from equation 4.11 as discussed above. Note that according to equation 4.12, the CM rate constant becomes comparable to the phonon emission rate constant if the QY significantly exceeds unity. Since we neglected energy lost through CM in equation 4.11, we again observe that equation 4.12 is only valid just above the onset of CM.

We compare the simplified model discussed above to the full model of equations 4.4 and 4.5 for our experimental data of the relaxation time and QY in 3.9 nm PbSe QDs. We show in Figure 4.5a fits of the full model to the experimental data prescribing constant phonon emission and CM rate constants, up to the first data point of the QY exceeding unity. The fitted rate constants are included in the figure. We observe from Figure 4.5a that the fits of the relaxation time and QY increase linearly with  $\Delta E$ , as expected for constant rate constants.

To use equation 4.12, we need to find reasonable values for  $\gamma$  and N. From Figure 4.5a we observe that for the first QY data point exceeding unity,  $\Delta E = 0.90$  eV. Using equation 4.10 we find from the relaxation time that  $\gamma = 2.5$  eV/ps for  $0 \leq \Delta E \leq 0.90$  eV. With these parameters, we show the QY calculated using equation 4.12 as a function of  $k_{CM}$  in Figure 4.5b for different N.

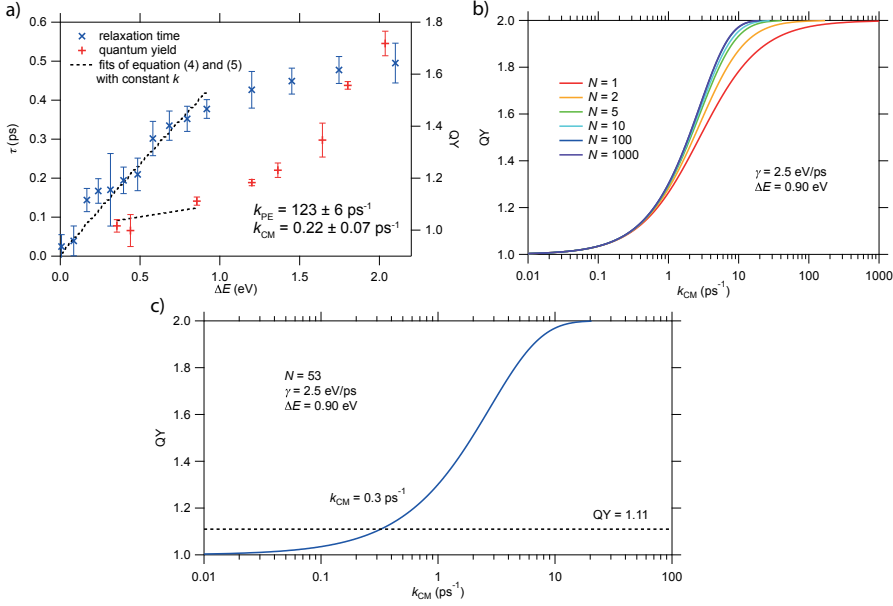


**Figure 4.5.** **a**, Fits to the experimental data using equations 4.4) en 4.5 for constant phonon emission and CM rate constants. **b**, QY as a function of  $k_{CM}$ , calculated using equation 4.12, for  $\gamma = 2.5 \text{ eV/ps}$ ,  $\Delta E = 0.90 \text{ eV}$  and various  $N$ . The QY converges for  $N > 10$ . **c**, QY as a function of  $k_{CM}$ , calculated using equation 4.12, for  $\gamma = 2.5 \text{ eV/ps}$ ,  $\Delta E = 0.90 \text{ eV}$  and  $N = 53$ . The  $QY = 1.11$  is indicated by the black dashed line and intersects the solution from equation 4.12 at  $k_{CM} = 0.3 \text{ ps}^{-1}$ .

From Figure 4.5b we observe that the QY calculated using equation 4.12 depends on  $N$ , but converges for  $N > 10$ . If we consider the distance between energy levels,  $\delta E$ , equal to the LO phonon energy in PbSe of 17 meV as before, we find from equation 4.11 that  $N = 53$  and  $k_{PE} = 147 \text{ ps}^{-1}$ . With these numbers we again show the QY calculated using equation 4.12 as a function of  $k_{CM}$  in Figure 4.5c. We also indicate  $QY = 1.11$  with a black dashed line, equal to the first experimental QY data point exceeding unity. From Figure 4.5c we observe that  $k_{CM} = 0.3 \text{ ps}^{-1}$  for the  $QY = 1.11$ .

We observe from Figure 4.5a and 4.5c that the phonon emission and CM rate constants determined from our full fit procedure with constant rate constants and from using equation 4.12 are equal within the error margin. We therefore find  $k_{CM} = 0.3 \text{ ps}^{-1}$  and  $k_{PE} = 147 \text{ ps}^{-1}$  as an estimate just above the energetic threshold of CM. Note that  $k_{CM}$  is indeed much smaller than  $k_{PE}$ , in agreement with the assumption to obtain equation 4.11.

For  $\Delta E = 0.90 \text{ eV}$ , we find from equation 4.9 that  $k_{CM} = 1.5 \text{ ps}^{-1}$  and  $k_{PE} = 346 \text{ ps}^{-1}$  using the full model of equations 4.4 and 4.5 and both the experimental relaxation time and QY. The simplified method using equation 4.12 therefore significantly underestimates the CM rate constant. It is however useful to estimate an order-of-magnitude for the CM rate constant when only experimental data of the QY is available.


## 4.8 Conclusions

We have presented a method to determine the rate constant of CM for initially hot charge

carriers from experimental data of the relaxation time and QY. We have illustrated this method for electrons in 3.9 nm PbSe QDs, for which we find a CM rate of  $k_{\text{CM}} = (1.8 \pm 0.1) \Delta E^{(1.5 \pm 0.2)} \text{ ps}^{-1}$  with  $\Delta E$  in eV. We have also derived a simplified method to estimate the CM rate constant just above the onset of CM when only experimental data of the QY is available. The method to determine the CM rate constant is generally applicable to analyze the observed CM efficiency in quantum confined and bulk materials. Extraction of a distinct CM rate constant can be useful for screening and direct development of materials with enhanced CM efficiency.

### References

1. Smith, C.; Binks, D. Multiple Exciton Generation in Colloidal Nanocrystals. *Nanomaterials* (Basel) 2014, 4, 19-45.
2. Kershaw, S.; Rogach, A. Carrier Multiplication Mechanisms and Competing Processes in Colloidal Semiconductor Nanostructures. *Materials* 2017, 10, 1095.
3. Padilha, L. A.; Stewart, J. T.; Sandberg, R. L.; Bae, W. K.; Koh, W.-K.; Pietryga, J. M.; Klimov, V. I. Carrier Multiplication in Semiconductor Nanocrystals: Influence of Size, Shape, and Composition. *Acc. Chem. Res.* 2013, 46, 1261-1269.
4. Trinh, M. T.; Houtepen, A. J.; Schins, J. M.; Hanrath, T.; Piris, J.; Knulst, W.; Goossens, A. P. L. M.; Siebbeles, L. D. A. In Spite of Recent Doubts Carrier Multiplication Does Occur in PbSe Nanocrystals. *Nano Lett.* 2008, 8, 1713-1718.
5. Aerts, M.; Suchand Sandeep, C. S.; Gao, Y.; Savenije, T. J.; Schins, J. M.; Houtepen, A. J.; Kinge, S.; Siebbeles, L. D. A. Free Charges Produced by Carrier Multiplication in Strongly Coupled PbSe Quantum Dot Films. *Nano Lett.* 2011, 11, 4485-4489.
6. Sandeep, C. S.; ten Cate, S.; Schins, J. M.; Savenije, T. J.; Liu, Y.; Law, M.; Kinge, S.; Houtepen, A. J.; Siebbeles, L. D. A. High Charge-Carrier Mobility Enables Exploitation of Carrier Multiplication in Quantum-Dot Films. *Nat. Comm.* 2013, 4, 2360.
7. Padilha, L. A.; Stewart, J. T.; Sandberg, R. L.; Bae, W. K.; Koh, W.-K.; Pietryga, J. M.; Klimov, V. I. Aspect Ratio Dependence of Auger Recombination and Carrier Multiplication in PbSe Nanorods. *Nano Lett.* 2013, 13, 1092-1099.
8. Aerts, M.; Bielewicz, T.; Klinke, C.; Grozema, F. C.; Houtepen, A. J.; Schins, J. M.; Siebbeles, L. D. A. Highly Efficient Carrier Multiplication in PbS Nanosheets. *Nat. Comm.* 2014, 5, 3789.
9. Kulkarni, A.; Evers, W. H.; Tomić, S.; Beard, M. C.; Vanmaekelbergh, D.; Siebbeles, L. D. A. Efficient Steplike Carrier Multiplication in Percolative Networks of Epitaxially Connected PbSe Nanocrystals. *ACS Nano* 2018, 12, 378-384.

- 
10. Pijpers, J. J. H.; Ulbricht, R.; Tielrooij, K. J.; Osherov, A.; Golan, Y.; Delerue, C.; Allan, G.; Bonn, M. Assessment of Carrier-Multiplication Efficiency in Bulk PbSe and PbS. *Nat. Phys.* 2009, 5, 811-814.
  11. Gabor, N. M.; Zhong, Z.; Bosnick, K.; Park, J.; McEuen, P. L. Extremely Efficient Multiple Electron-Hole Pair Generation in Carbon Nanotube Photodiodes. *Science* 2009, 325, 1367-1371.
  12. Semonin, O. E.; Luther, J. M.; Choi, S.; Chen, H. Y.; Gao, J. B.; Nozik, A. J.; Beard, M. C. Peak External Photocurrent Quantum Efficiency Exceeding 100% via MEG in a Quantum Dot Solar Cell. *Science* 2011, 334, 1530-1533.
  13. Davis, N.; Bohm, M. L.; Tabachnyk, M.; Wisnivesky-Rocca-Rivarola, F.; Jellicoe, T. C.; Ducati, C.; Ehrler, B.; Greenham, N. C. Multiple-Exciton Generation in Lead Selenide Nanorod Solar Cells with External Quantum Efficiencies Exceeding 120%. *Nat. Comm.* 2015, 6, 8259.
  14. Barati, F.; Grossnickle, M.; Su, S.; Lake, R. K.; Aji, V.; Gabor, N. M. Hot Carrier-Enhanced Interlayer Electron-Hole Pair Multiplication in 2D Semiconductor Heterostructure Photocells. *Nat. Nanotech.* 2017, 12, 1134.
  15. Yan, Y.; Crisp, R. W.; Gu, J.; Chernomordik, B. D.; Pach, G. F.; Marshall, A. R.; Turner, J. A.; Beard, M. C. Multiple Exciton Generation for Photoelectrochemical Hydrogen Evolution Reactions with Quantum Yields Exceeding 100%. *Nat. En.* 2017, 2, 17052.
  16. Kambhampati, P. Hot Exciton Relaxation Dynamics in Semiconductor Quantum Dots: Radiationless Transitions on the Nanoscale. *J. Phys. Chem. C* 2011, 115, 22089-22109.
  17. Stewart, J. T.; Padilha, L. A.; Qazilbash, M. M.; Pietryga, J. M.; Midgett, A. G.; Luther, J. M.; Beard, M. C.; Nozik, A. J.; Klimov, V. I. Comparison of Carrier Multiplication Yields in PbS and PbSe Nanocrystals: The Role of Competing Energy-Loss Processes. *Nano Lett.* 2012, 12, 622-628.
  18. Stewart, J. T.; Padilha, L. A.; Bae, W. K.; Koh, W.-K.; Pietryga, J. M.; Klimov, V. I. Carrier Multiplication in Quantum Dots within the Framework of Two Competing Energy Relaxation Mechanisms. *J. Phys. Chem. Lett.* 2013, 4, 2061-2068.
  19. Park, J.; Joo, J.; Kwon, S. G.; Jang, Y.; Hyeon, T. Synthesis of Monodisperse Spherical Nanocrystals. *Angew. Chem. Int. Ed.* 2007, 46, 4630-4660.
  20. Cho, B.; Peters, W. K.; Hill, R. J.; Courtney, T. L.; Jonas, D. M. Bulklike Hot Carrier Dynamics in Lead Sulfide Quantum Dots. *Nano Lett.* 2010, 10, 2498-2505.
  21. Miaja-Avila, L.; Tritsch, J. R.; Wolcott, A.; Chan, W. L.; Nelson, C. A.; Zhu, X.

- Y. Direct Mapping of Hot-Electron Relaxation and Multiplication Dynamics in PbSe Quantum Dots. *Nano Lett.* 2012, 12, 1588-1591.
22. Spoor, F. C. M.; Tomić, S.; Houtepen, A. J.; Siebbeles, L. D. A. Broadband Cooling Spectra of Hot Electrons and Holes in PbSe Quantum Dots. *ACS Nano* 2017, 11, 6286-6294.
  23. Allan, G.; Delerue, C. Role of Impact Ionization in Multiple Exciton Generation in PbSe Nanocrystals. *Phys. Rev. B* 2006, 73, 205423.
  24. Franceschetti, A.; An, J. M.; Zunger, A. Impact Ionization Can Explain Carrier Multiplication in PbSe Quantum Dots. *Nano Lett.* 2006, 6, 2191-2195.
  25. Rabani, E.; Baer, R. Theory of Multiexciton Generation in Semiconductor Nanocrystals. *Chem. Phys. Lett.* 2010, 496, 227-235.
  26. Velizhanin, K. A.; Piryatinski, A. Numerical Study of Carrier Multiplication Pathways in Photoexcited Nanocrystal and Bulk Forms of PbSe. *Phys. Rev. Lett.* 2011, 106, 207401.
  27. Spoor, F. C. M.; Grimaldi, G.; Delerue, C.; Evers, W. H.; Crisp, R. W.; Geiregat, P.; Hens, Z.; Houtepen, A. J.; Siebbeles, L. D. A. Asymmetric Optical Transitions Determine the Onset of Carrier Multiplication in Lead Chalcogenide Quantum Confined and Bulk Crystals. *ACS Nano* 2018, 12, 4796-4802.
  28. Allan, G.; Delerue, C. Confinement Effects in PbSe Quantum Wells and Nanocrystals. *Phys. Rev. B* 2004, 70, 245321.
  29. An, J. M.; Franceschetti, A.; Dudiy, S. V.; Zunger, A. The Peculiar Electronic Structure of PbSe Quantum Dots. *Nano Lett.* 2006, 6, 2728-2735.
  30. Spoor, F. C. M.; Kunneman, L. T.; Evers, W. H.; Renaud, N.; Grozema, F. C.; Houtepen, A. J.; Siebbeles, L. D. A. Hole Cooling Is Much Faster than Electron Cooling in PbSe Quantum Dots. *ACS Nano* 2016, 10, 695-703.
  31. Geiregat, P.; Delerue, C.; Justo, Y.; Aerts, M.; Spoor, F.; Van Thourhout, D.; Siebbeles, L. D. A.; Allan, G.; Houtepen, A. J.; Hens, Z. A Phonon Scattering Bottleneck for Carrier Cooling in Lead Chalcogenide Nanocrystals. *ACS Nano* 2015, 9, 778-788.
  32. Fox, M., *Optical properties of solids*. Oxford University Press: Oxford, 2001.

## Appendix

### Code used for fitting the carrier relaxation time

The code used for fitting equation 4.4, in the format of a WaveMetrics Igor Pro procedure, is given below. Note that this is an independent fitting routine. The global fit was performed using the global fit procedure incorporated in Igor Pro 6.37.

Function stepwisetimefit(w,energy) : FitFunc

Wave w

Variable energy

//CurveFitDialog/ These comments were created by the Curve Fitting dialog. Altering them will

//CurveFitDialog/ make the function less convenient to work with in the Curve Fitting dialog.

//CurveFitDialog/ Equation:

//CurveFitDialog/ Time with  $k_{CM} = A * \text{energy}^B$  and  $k_{PE} = C * \text{energy}^D$

//CurveFitDialog/ End of Equation

//CurveFitDialog/ Independent Variables 1

//CurveFitDialog/ energy

//CurveFitDialog/ Coefficients 4

//CurveFitDialog/ w[0] = A

//CurveFitDialog/ w[1] = B

//CurveFitDialog/ w[2] = C

//CurveFitDialog/ w[3] = D

Variable bg = 0.95, dE = 0.017

Variable Nmax = ceil(energy / dE)

variable i, j, k, product\_pPE, sum\_tPE, sum\_CM\_AND\_PE, product\_sum\_pPE, sum\_sum\_tPE

Make/N=(Nmax+1)/O/D taufit = 0, pCM = 1, kCM = 0, pPE = 1, kPE = 0, ktot = 0

for (i=1; i<=Nmax; i+=1) // analysis through each energy level i up to Nmax

kCM[i] = w[0] \* (i \* dE)^w[1]

kPE[i] = w[2] \* (i \* dE)^w[3]

ktot[i] = kCM[i]+kPE[i]

pPE[i] = (kPE[i]) / (kPE[i] + kCM[i])

pCM[i] = (kCM[i]) / (kPE[i] + kCM[i])

product\_pPE = 1

sum\_tPE = 0

sum\_CM\_AND\_PE = 0

```
for (j=1; j<=i; j+=1) // sum for only cooling
    product_pPE *= pPE[j]
    sum_tPE += 1/ktot[j]
endfor // sum for only cooling

for(j=1; j<i; j+=1) // sum including CM

    product_sum_pPE = 1
    sum_sum_tPE = 0

    for(k=j+1; k<=i; k+=1) // define the product of pPE and the sum of
tPE for the shorter sum

        product_sum_pPE *= pPE[k]
        sum_sum_tPE += 1/ktot[k]

    endfor

    sum_CM_AND_PE += pCM[j] * product_sum_pPE * (1/ktot[j] +
sum_sum_tPE)

endfor // sum including CM

taufit[i] = pCM[i] * (1/ktot[i]) + product_pPE * sum_tPE + sum_CM_AND_
PE

endfor // analysis through each energy level i up to Nmax

return taufit[Nmax]

End
```

### **Code used for fitting the CM QY**

The code used for fitting equation 4.5, in the format of a WaveMetrics Igor Pro procedure, is given below. Note that this is an independent fitting routine. The global fit was performed using the global fit procedure incorporated in Igor Pro 6.37.

```
Function stepwiseQYfit(w,energy) : FitFunc
    Wave w
    Variable energy
```

```
//CurveFitDialog/ These comments were created by the Curve Fitting dialog.
```

Altering them will

//CurveFitDialog/ make the function less convenient to work with in the Curve Fitting dialog.

//CurveFitDialog/ Equation:

//CurveFitDialog/ QY with  $k_{CM} = A * \text{energy}^B$  and  $k_{PE} = C * \text{energy}^D$

//CurveFitDialog/ End of Equation

//CurveFitDialog/ Independent Variables 1

//CurveFitDialog/ energy

//CurveFitDialog/ Coefficients 4

//CurveFitDialog/ w[0] = A

//CurveFitDialog/ w[1] = B

//CurveFitDialog/ w[2] = C

//CurveFitDialog/ w[3] = D

Variable bg = 0.95, dE = 0.017

Variable Nmax = ceil(energy / dE)

variable i, j, k, product\_pPE

Make/N=(Nmax+1)/O/D QYfit = 1, pCM = 1, kCM = 0, pPE = 1, kPE = 0

Nmax                   for (i=1; i<=Nmax; i+=1) // analysis through each energy level i up to

    kCM[i] = w[0] \* (i \* dE)^w[1]

    kPE[i] = w[2] \* (i \* dE)^w[3]

    pPE[i] = (kPE[i]) / (kPE[i] + kCM[i])

    pCM[i] = (kCM[i]) / (kPE[i] + kCM[i])

    product\_pPE = 1

    for (j=1; j<=i; j+=1) // sum for only cooling

        product\_pPE \*= pPE[j]

    endfor // sum for only cooling

    QYfit[i] = 2 - product\_pPE

endfor // analysis through each energy level i up to Nmax

return QYfit[Nmax]

End

**Influence of the distance  $\delta E$  between energy levels on the fit**

We reproduce the fits of Figure 4.4a in the main text separately for each value of the distance  $\delta E$  between energy levels in Figure 4.6.

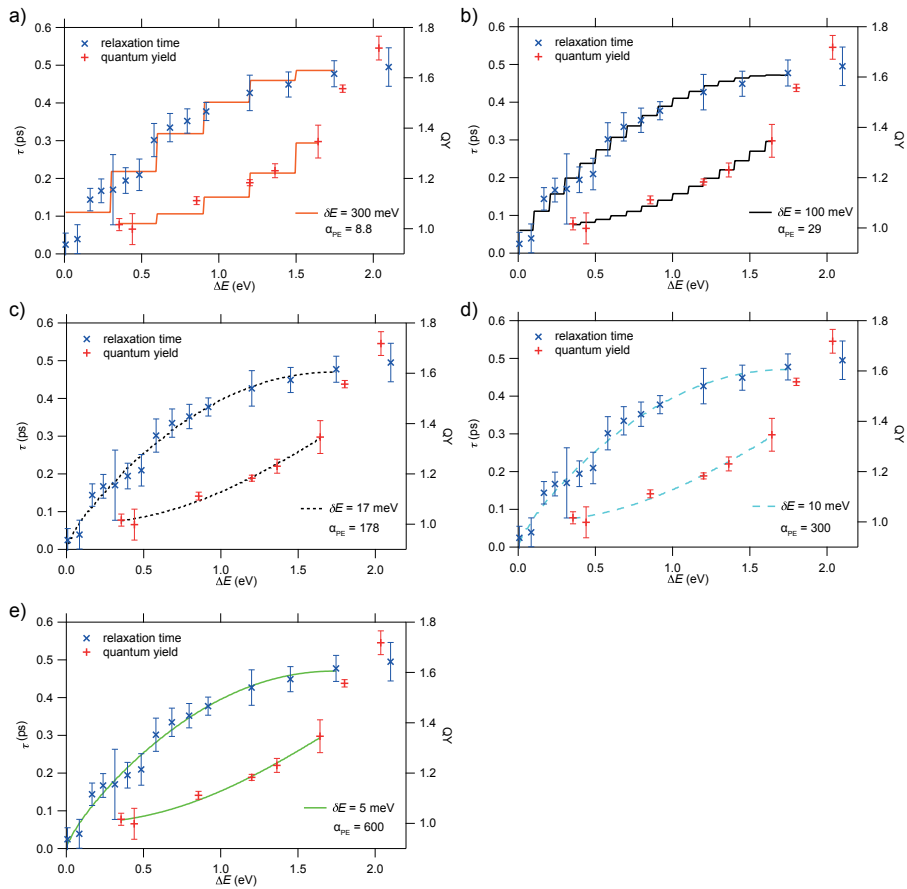


**Figure 4.6.** Fits of Figure 4a in the main text for  $\delta E$  equal to a) 300 meV, b) 100 meV, c) 17 meV, d) 10 meV and e) 5 meV.





# Chapter 5

## Spectroscopic evidence for the contribution of holes to the bleach of Cd-chalcogenide quantum dots

### *Abstract*

In transient-absorption (TA) measurements on Cd-chalcogenide quantum dots (QDs), the presence of a band-edge (BE) bleach signal is commonly attributed entirely to conduction-band electrons in the 1S(e) state, neglecting contributions from BE holes. While this has been the accepted view for more than 20 years, and has often been used to distinguish electron and hole kinetics, the reason for the absence of a hole contribution to the BE bleach has remained unclear. Here, we show with three independent experiments that holes do in fact have a significant impact on the BE-bleach of well-passivated Cd chalcogenide QD samples. Transient absorption experiments on high photoluminescence quantum yield CdSe/CdS/ZnS core-shell-shell QDs clearly show an increase of the band edge bleach as holes cool down to the band edge. The relative contribution of electron-to-hole bleach is 2:1, as predicted by theory. The same measurements on core-only CdSe QDs with lower quantum yield do not show a contribution of holes to the band edge bleach. We assign the lack of hole bleach to the presence of ultra-fast hole trapping in samples with insufficient passivation of the QD surface. In addition, we show measurements of optical gain in core-shell-shell QD solutions, providing clear evidence of a significant hole contribution to the BE transient absorption signal. Finally, we present spectroelectrochemical measurements on CdTe QDs films, showing the presence of a BE-bleach for both electron and hole injection. The presence of a contribution of holes to the bleach in passivated Cd-chalcogenides QDs bears important implications for quantitative studies on optical gain as well as for TA determinations of carrier dynamics.

Based on: Gianluca Grimaldi, Jaco J. Geuchies, Ward van der Stam, Indy du Fossé, Baldur Brynjarsson, Nicholas Kirkwood, Sachin Kinge, Laurens D.A. Siebbeles, Arjan J. Houtepen. *Nano Letters*, 2019, 19 (5), 3002-3010.

## 5.1 Introduction

Cadmium chalcogenide Quantum Dots (QDs) have been among the earliest QD systems to be investigated, and are still at the forefront of QD research, with applications in solar cells<sup>1-3</sup>, transistors<sup>4-6</sup>, LEDs<sup>7,8</sup>, catalysis<sup>9-11</sup> and lasing<sup>12-14</sup>. In particular, recent breakthroughs in electrically-pumped core-shell QD lasers<sup>15</sup> confirm the potentials of these QD materials in low-threshold lasing applications. Understanding the behavior of band-edge (BE) absorption in QDs is a necessary step in the development of optoelectronic applications, and has been the focus of years of spectroscopic investigation<sup>16-21</sup>.

In the presence of excited carriers, the BE absorption of QDs decreases in intensity, an effect called absorption bleach. Numerous reports have claimed that the BE-bleach in Cd chalcogenide QDs seems to be entirely dominated by the presence of electrons in the conduction BE state, with no evidence of a hole contribution to the effect<sup>19,22-25</sup>. This observation has important consequences for both applied and fundamental studies on Cd chalcogenides: the lack of a hole contribution implies a negligible amount of stimulated emission, preventing the realization of optical gain; furthermore, complete assignment of the BE-bleach to electrons has been a widely used assumption in the determination of electron kinetics from transient absorption (TA) measurements of bleach decays<sup>10,26</sup>. Despite the claim on the lack of a hole-induced bleach, the underlying reason remains ambiguous, with studies suggesting the presence of efficient hole trapping<sup>27,28</sup>, a high degeneracy of thermally populated hole states<sup>23,29</sup>, or a combination thereof<sup>22</sup>.

Here we present three independent experiments that clearly demonstrate the presence of a significant hole contribution to the BE-bleach of CdSe and CdTe QDs. According to the present work, the lack of a hole contribution depends on the presence of un-passivated trap states and is not an intrinsic property of II-VI QDs. We performed TA measurements, exciting CdSe/CdS/ZnS core-shell-shell QDs at the 1S [ $1S_{3/2}(h)$ ]-1S(e)] transition and 2S [ $2S_{3/2}(h)$ ]-1S(e)] transition. Comparison of the two bleach dynamics revealed the presence of a  $210 \pm 20$  fs ingrowth upon 2S excitation, while the growth of the 1S signal is limited by the (130 fs) time resolution of the measurement. As the two excitations differ only for the initial hole state, the difference between the two bleach-kinetics demonstrates the presence of a hole contribution to the BE-bleach. The ratio between the electron and hole bleach contribution, extracted from the amplitude of the ingrowth component of the bleach upon 2S excitation, is found to be 2:1. This observation is in excellent agreement with a simple transition-counting model for the bleach of a transition involving a two-fold degenerate electron state and a four-fold degenerate hole state. Interestingly, repeating the measurement on core-only CdSe QDs showed identical kinetics for the two excitations, confirming the role of hole trapping in the removal of the hole contribution from the bleach. The latter explains the absence of the observation of a hole bleach in previous reports<sup>27,28,3,29</sup>.

We provide further evidence for the contribution of holes to the band edge bleach by showing optical gain in solutions of CdSe/CdS/ZnS QDs. The observation of optical gain directly implies the presence of stimulated emission, which in turn is a tell-tale sign of a contribution of holes to the BE bleach. Comparison of the measured gain with predictions from the transition-counting model shows quantitative agreement. Finally, we present

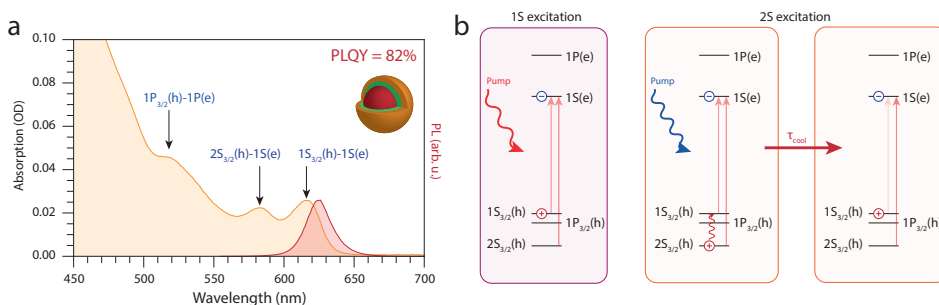


**Figure 5.1. Schematics of optical bleaching and possible scenarios in core-shell-shell CdSe QDs.** **a**, Absorption and photoluminescence spectrum of the CdSe/CdS/ZnS core-shell-shell QDs. The different transitions in the CdSe core are labelled according to the literature<sup>30–32</sup>. **b**, Schematic of the optical transitions in the TA experiments. Upon 1S-excitation, the band-edge absorption transition is bleached instantly due to the presence of an electron in the 1S state and the presence of a hole in the  $1S_{3/2}(h)$  state. Upon 2S-excitation of the  $2S_{3/2}(h) - 1S(e)$  transition, the band-edge bleach should theoretically show an ingrowth over time (sub picosecond), related to fast hole cooling from the  $2S_{3/2}(h)$  to the  $1S_{3/2}(h)$  state.

spectroelectrochemical measurements on films of CdTe QDs. We show that both electron injection (reducing potentials) and hole injection (oxidizing potentials) results in a clear bleach of the BE transition. These results clarify the presence of a hole contribution to the BE-bleach of Cd chalcogenides QD systems, paving the way for quantitative prediction of the gain threshold in this highly-investigated material system.

5

## 5.2 QD synthesis and material properties

We synthesized CdSe/CdS/ZnS QDs with low polydispersity (standard deviation in particle diameter 7%) and high PL performance, following descriptions in recent literature<sup>33,34</sup>. The steady-state absorption and PL spectra of the core-shell-shell QDs are shown in Figure 5.1a, labelled following a multiband effective mass approximation description of electronic states in the strong coupling regime<sup>30–32</sup>. The photoluminescence quantum yield (PLQY) was determined to be 82% (see Supporting Information). The low polydispersity leads to sharp absorption features that allow state selective excitation, which simplifies the analysis of the transient absorption spectra. The high PLQY ensures the sample is hardly affected by carrier trapping.

## 5.3 Evidence of hole contribution to the BE-bleach via ultrafast TA measurements

We attempt to determine the contribution of holes to the BE-bleach by selectively exciting either the 1S [ $1S_{3/2}(h) - 1S(e)$ ] (616 nm) or the 2S [ $2S_{3/2}(h) - 1S(e)$ ] transition (581 nm). Figure 5.1b shows a schematic of the carrier dynamics expected for the two excitations. Upon optical excitation of the 1S transition, both carriers populate the BE levels, immediately contributing to the BE-bleach, while upon 2S-excitation the hole initially populates the  $2S_{3/2}(h)$  state and does not contribute to the BE-bleach. After a certain cooling time ( $\tau_{cool}$ ),

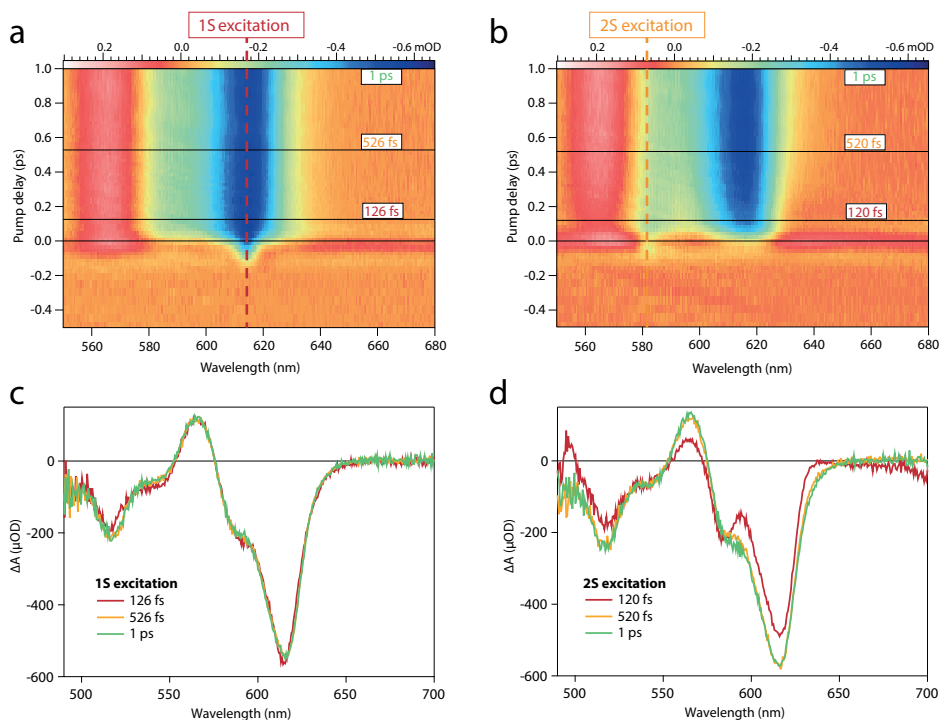


**Figure 5.2. 2D TA measurements on the CdSe/CdS/ZnS QDs during the first picosecond upon 1S- and 2S-excitation.** **(a)**, 2D TA image for excitation resonant with the 1S and **(b)** 2S transition. Excitation of the 1S transition shows an instantaneous appearance of the BE-bleach. **(c)**, Differential absorption of the CdSe QD BE upon 1S- and **(d)** 2S-excitation. Excitation of the 2S transition shows a clear ingrowth of the BE-bleach signal in the first hundreds of femtoseconds after photoexcitation, indicative of hole cooling from the  $2S_{3/2}(h)$  to the  $1S_{3/2}(h)$  state.

the hole relaxes to the  $1S_{3/2}(h)$  state. In this scenario, with carrier dynamics unaffected by trapping, the presence of a hole contribution to the BE-bleach would result in a difference in the kinetics of the ingrowth of the bleach signals in the two excitations.

We performed TA measurements on the sample in the low fluence regime, in which the pump beam excites an average number of excitons per QD much smaller than unity, while vigorously stirring the solution to avoid photocharging effects<sup>35</sup>. Figures 5.2a and 5.2b show 2D TA colormaps for 1S- and 2S-excitation, respectively. Although the two measurements show identical TA signals in the time window between 1 ps and 3 ns after photoexcitation, clear differences between them can be observed in the early-time behavior of the BE-bleach (at 618 nm). To highlight the difference in the two responses, spectral cuts of the 2D TA colormaps are shown in Figure 5.2c and 5.2d, displaying the differential absorption signal for different pump-probe delays. The transient absorption spectrum in the 1S-excitation measurement (Figure 5.2c) remains constant after the coherent artifact response<sup>36</sup>. The 2S-excitation measurement, shown in Figure 5.2d, shows a clear growth of the BE-bleach occurring in the first hundreds of femtoseconds after photoexcitation. As the only difference between the two measurements is the initial hole

state, this clearly demonstrates a significant influence of the hole on the BE-bleach: as holes cool down to the BE state, the BE-bleach increases. Below we perform a quantitative analysis on these transient absorption measurements. We focus only on the region of the 1S transition since spectral overlap between different transitions prevents unambiguous quantitative description of the transient absorption signals at higher energy.

#### 5.4 Quantitative modelling of the hole contribution to the BE-bleach

In order to quantify the impact of the hole on the BE-bleach, we fitted the sum of two Gaussians to the time-dependent differential absorption spectrum close to the energy of the BE absorption (Figure 5.3a), to account for the partial overlap of the 1S and 2S bleach features. Although the description of the TA signal at the energy of the 2S transition is neglecting spectral overlap with higher energy components, the precise shape of the 2S bleach has little influence on the determination of the 1S bleach component (see Appendix). Figure 5.3b shows the time-dependence of the 1S bleach component for 1S- and 2S-excitation. Again, a clear difference is observed in the dynamics of the BE-bleach between the two measurements, with the 2S-excitation showing a clear ingrowth during the first 500 fs, while upon 1S-excitation the BE remains constant after a 130 fs resolution-limited increase. After cooling is completed, the bleach per absorbed photon in the two excitations is the same, confirming that the number of carriers reaching the band-edge in the two excitations is the same (See Appendix). The ingrowth of the BE-bleach in the 2S-excitation measurement is fitted with the sum of a step function (1S electrons) and an exponential increase (1S holes), convolved with a Gaussian Instrument Response Function (IRF, see Appendix). The fit yields a time constant for the ingrowth of  $210 \pm 20$  fs, in agreement with the expected fast dynamics of hole relaxation<sup>37</sup> (see Appendix).

The ratio between the hole bleach ( $\Delta A_h$ ) and the exciton bleach ( $\Delta A_x$ ), extracted from the fit, amounts to  $0.32 \pm 0.03$ . This value can be compared to the prediction based on a widely used model based on state filling of degenerate energy levels<sup>14,15,38,39</sup>, schematically shown in Figure 5.3c. Assuming equal oscillator strength for all the energy-degenerate transitions, the total absorbance is given by a sum over identical contributions  $A^*$  for each transition, represented as red, upwards arrows in Figure 5.3c. The presence of an electron and/or a hole in one of the two states involved in a transition induces state-filling, as well as stimulated emission, both leading to a reduction of the net absorption. In the low-fluence limit relevant for comparisons with the measurements, the steady state absorbance  $A_0$  and the excited state absorbance  $A'$  in the presence of an occupation  $n_e$  and  $n_h$  of the electron and hole states can be written as:

$$A_0 = A^* g_e g_h \quad 5.1$$

$$A' = A^* [(g_e - n_e)(g_h - n_h) - n_e n_h] \quad 5.2$$

where  $g_e$  ( $g_h$ ) represents the electron (hole) degeneracy. The term proportional to  $n_e n_h$  originates from stimulated emission, represented by a green, downwards arrow in Figure 5.3c. It follows from equations 5.1 and 5.2 that the differential absorbance,  $\Delta A = A' - A_0$ , in

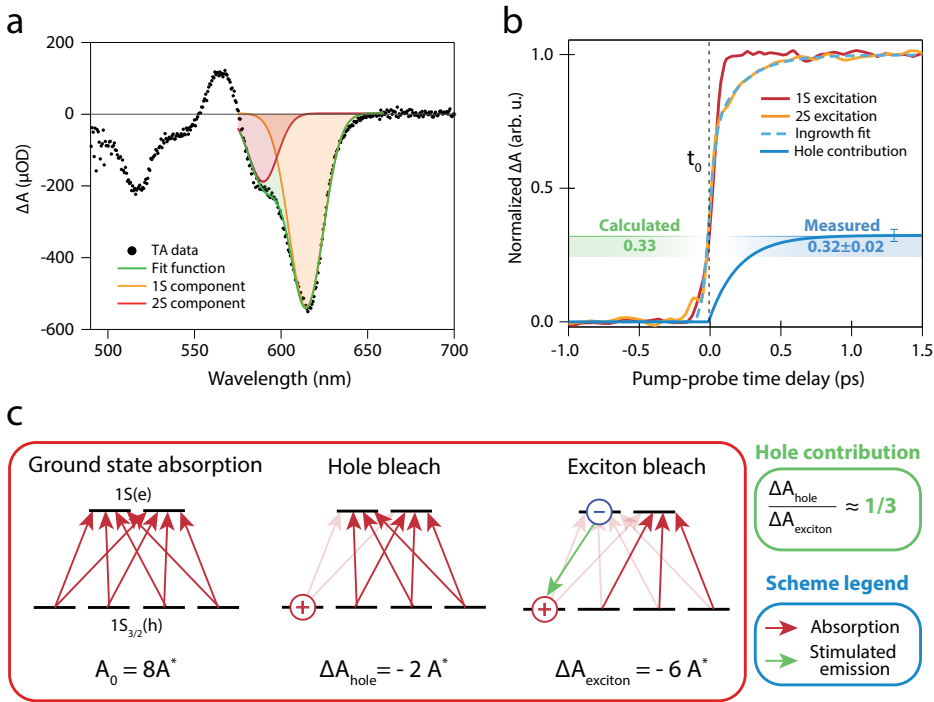


**Figure 5.3.** Analysis of the band-edge bleach in TA experiments upon 1S- and 2S-excitation of the CdSe/CdS/ZnS NCs. **a**, We fit two-Gaussians to the BE-bleach, which correspond to the  $1S_{3/2}(h)$ - $1S(e)$  and  $2S_{3/2}(h)$ - $1S(e)$  transitions, and extract the contribution of each transition to the TA signal for different pump-probe delay times. **b**, Normalized amplitude of the BE-bleach upon exciting the 1S and 2S transition (red and orange). 2S-excitation leads to an ingrowth of the BE-bleach on a timescale of hundreds of femtoseconds, whereas for 1S-excitation the BE-bleach appears instantly. Fitting the 2S-excitation signal with a step increase, due to the electron and an exponential ingrowth due to the hole (convolved with the IRE, see Appendix) produces a good agreement with the data (dotted light-blue) and allows to quantify the time-dependence of the hole contribution (dark blue). **c**, Schematic of the transition counting model used to extract the contributions of the electron and exciton to the magnitude of the BE-bleach.

presence of an exciton ( $n_e=1, n_h=1$ ) and in presence of a hole ( $n_e=0, n_h=1$ ) can be expressed as:

$$\Delta A_x = -A^*(g_e + g_h) \quad 5.3$$

$$\Delta A_h = -A^*g_e \quad 5.4$$

Within this model, the ratio of the hole and exciton BE-bleach,  $(\Delta A_h)/(\Delta A_x) = g_e/(g_e + g_h)$ , is entirely determined by the degeneracy of the band-edge states. Setting the BE degeneracies to the theoretically predicted values ( $g_e = 2$  and  $g_h = 4$ )<sup>40</sup>, results in a ratio of the hole-to-exciton bleach  $(\Delta A_h)/(\Delta A_x) \approx 1/3$ , in quantitative agreement with the value  $(0.32 \pm 0.03)$  we measured. Although the simple model neglects the presence of angular momentum

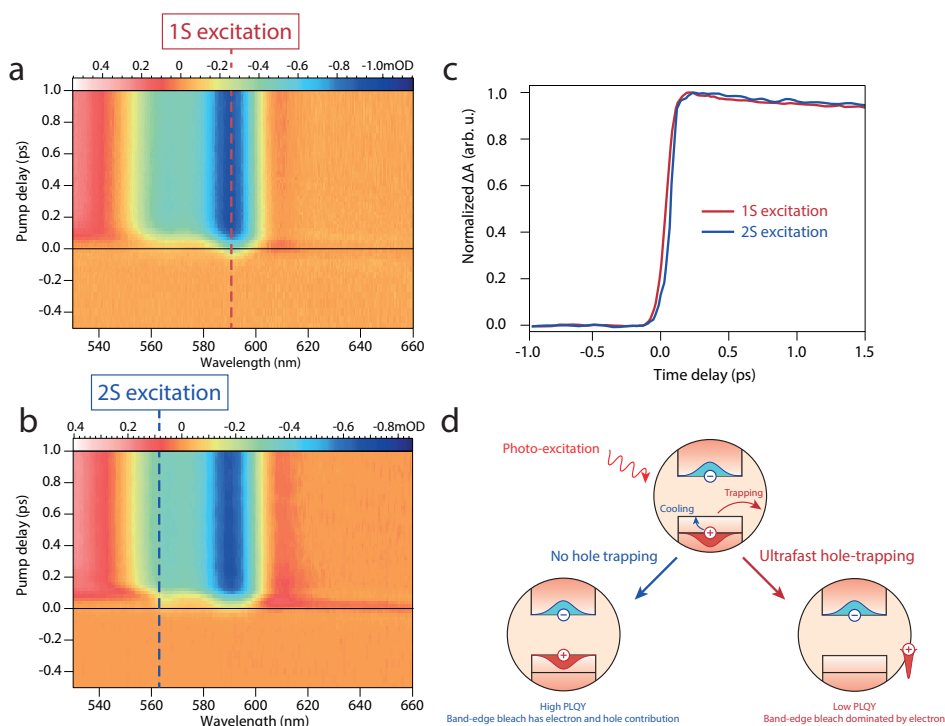


**Figure 5.4. Analysis on the core-only, low PLQY CdSe QDs upon 1S- and 2S-excitation, showing fast hole trapping.** **a**, 2D TA images for 1S- and **(b)** 2S-excitation, up to 1 ps after photoexcitation on the core-only CdSe QDs. In both cases we do not see an ingrowth of the BE-bleach. **c**, Amplitude of the BE-bleach upon exciting the 1S (red) and 2S (yellow) transitions. Note that the bleaches appear simultaneously and instantly after photoexcitation in both cases, i.e. we do not observe the hole cooling, which is in contrast with the band-edge bleach of the high PLQY NCs from Figure 5.4. **d**, Schematic representation of hole relaxation pathways after photo-excitation. In high PLQY samples, with little to no hole trapping, the hole relaxes to the band-edge level  $[1S_{3/2}(h)]$ , where it contributes accordingly to the BE-bleach in the fs-TA experiments. In samples where there is fast hole trapping, the hole is rapidly localized in a trap state, and does not contribute anymore to the BE- bleach signal in our fs-TA experiments.

selection rules for optical transitions, accounting for angular momentum conservation leads to the same quantitative results (see Appendix). We conclude that the bleach dynamics of near-unity PLQY CdSe core-shell QDs can be entirely explained in terms of the commonly accepted values for the BE degeneracies of single-particle electron and hole states in CdSe QDs<sup>14,38,41</sup>, ruling out the presence of a high-degeneracy quasi-continuum of BE hole states.

## 5.5 Absence of hole contribution to the BE-bleach for un-passivated QDs

It is likely that the presence of a high density of surface traps, incomplete surface passivation via thinner shells or lack of time resolution contributed to hide the BE hole

bleach contribution in previous TA studies of CdSe QDs. We studied the importance of good surface passivation for the determination of the hole bleach, via comparison between the high PLQY, core-shell-shell CdSe/CdS/ZnS QDs, shown in Figure 5.3, and low-PLQY (6.5%), core-only CdSe QDs. Recent work by our group<sup>26,42</sup> and others<sup>43</sup> has shown that PL quenching for core-only Cd-chalcogenide QDs is dominated by the presence of localized hole states in the band-gap, leading to ultrafast hole trapping. These trap states originate from undercoordinated chalcogenide atoms at the surface of the QDs<sup>26,42,43</sup>, which can be passivated by Z-type ligands<sup>44</sup>.

Figure 5.4a,b shows 2D TA colormaps for the core-only CdSe NCs, excited at the 1S and the 2S transition, respectively. A striking similarity is observed in the dynamics of the BE-bleach between the two measurements. Figure 5.4c compares the temporal evolution of the BE-bleach for the two excitations, revealing that the bleach components follow the same kinetics in both measurements. This implies that the hole trapping rate exceeds both the cooling rate (i.e.  $\tau_{\text{trap}} \ll \tau_{\text{cool}}$ ) and the time resolution of the measurement (for a more quantitative discussion on the trapping dynamics, see the Appendix, Figure 5.15). Thus, the TA measurement probes QDs populated by a trapped hole and a conduction BE electron, irrespective of the initial excitation. These results demonstrate that the contribution of holes to the BE-bleach is completely obscured by fast hole trapping in low PLQY samples.

## 5

## 5.6 Hole cooling in Z-type ligand (InCl<sub>3</sub>) passivated CdSe core-only QDs

We have attributed the lack of hole-cooling in un-passivated core-only QDs to ultrafast hole trapping, also leading to low PLQY in these samples. This interpretation suggests it should be possible to observe hole cooling in core-only CdSe QDs when their PLQY is high enough, i.e. the hole trapping is sufficiently slow or absent from a portion of the QD population. Below, we show that Z-type ligand passivation of the surface of core-only CdSe QDs increases their PLQY, and allows us to observe the cooling of the hole from the 2S<sub>3/2</sub> into the 1S<sub>3/2</sub> hole state in TA experiments.

Proper passivation of the CdSe QD surface can in principle lead to high PLQY core-only samples<sup>45</sup>. We passivated the surface of CdSe QDs cores with InCl<sub>3</sub>, a Lewis acid that acts as a Z-type ligand, following work that was recently published by our group<sup>44</sup>. The steady-state absorption and PL spectra are shown in Figure 5.5a. After the InCl<sub>3</sub> surface treatment, the PLQY of the CdSe QDs sample increased from 2% to 21%. Figure 5.5b shows the BE bleach for 1S and 2S excitation of these passivated CdSe QDs dispersed in toluene. A clear ingrowth of the BE bleach amplitude is observed when photoexciting the 2S transition, i.e. the hole cools down from the 2S<sub>3/2</sub> hole state to the 1S<sub>3/2</sub> hole state, whereas the growth of the BE bleach upon 1S excitation is limited by the time-resolution. Fitting the data with the same model presented for the high PLQY core-shell-shell QDs, we obtain a ratio for the hole-to-exciton bleach in the InCl<sub>3</sub> passivated CdSe cores of  $0.10 \pm 0.02$ , with a hole cooling time of  $190 \pm 40$  fs, closely matching the value obtained on the core-shell-shell QDs.

We associate the increase in PLQY to the suppression of trapping process in part of

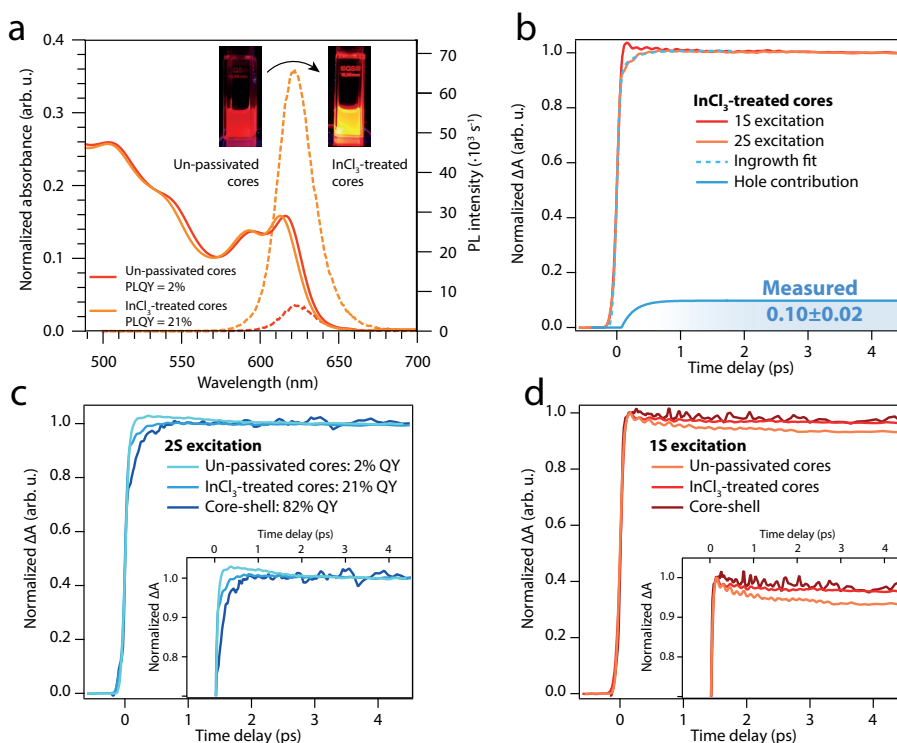


**Figure 5.5. Evidence of hole contribution to the band-edge bleach in Z-type ligand ( $\text{InCl}_3$ ) passivated core-only CdSe QDs with TA.** **a**, Absorption and PL spectra of the un-passivated and  $\text{InCl}_3$  passivated core-only QDs. The PLQY is increased by an order of magnitude. **b**, Comparison between 1S and 2S excitation on CdSe cores which are passivated with  $\text{InCl}_3$ . The ingrowth of the band-edge bleach due to the relaxation of the hole from the 2S to 1S state is clearly visible and constitutes 10% of the total band-edge bleach amplitude. **c**, Comparison of the band-edge bleach amplitude between un-passivated core-only CdSe QDs,  $\text{InCl}_3$  passivated QDs and the core-shell QDs earlier presented in this paper. The inset shows a photograph of the un-passivated (2% PLQY) and  $\text{InCl}_3$  passivated (21% PLQY) QDs. **d**, Band-edge bleach amplitude after 1S excitation on the same samples presented in (c).

the QD population, due to an improved chemical passivation of surface traps<sup>44</sup>. In the passivated QDs, holes contribute to the BE ingrowth, while in the un-passivated portion of the population the BE signal is dominated by the electron contribution. As a result, the amount of hole contribution to the BE signal for the  $\text{InCl}_3$  passivated cores is expected to be lower than in the core-shell-shell sample, in line with the difference in PLQY. Figure 5.5c presents the amplitude of the BE bleach after exciting the 2S transition of the un-passivated QDs, the  $\text{InCl}_3$  passivated QDs and the core-shell-shell QDs. The ingrowth follows a clear trend with increasing PLQY; better passivation of the CdSe QDs leads to a higher contribution of holes to the BE bleach. As we passivate possible hole traps on the surface of the QDs better, a larger fraction of photoexcited holes survive the cooling process from the  $2S_{3/2}$  to the  $1S_{3/2}$  state.

Figure 5.5d shows the amplitude of the BE bleach upon 1S excitation of the un-passivated

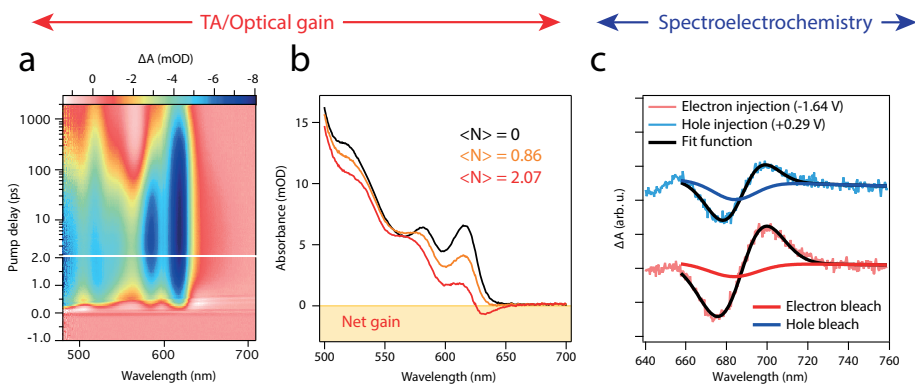


**Figure 5.6. Additional spectroscopic evidence of hole contribution to the BE-bleach.** **a**, High-fluence TA colormap of the CdSe/CdS/ZnS QDs, excited at 400 nm with a fluence of  $6.54 \cdot 10^{14}$  photons/cm<sup>2</sup> per pulse, showing a maximum of the BE-bleach 4.5 picoseconds after photoexcitation. **b**, Comparison between the excited state absorption spectrum ( $A_0 + \Delta A$ ), obtained from the differential absorbance shown in (a) at 4.5 picoseconds, and the steady state absorption ( $A_0$ , black), clearly showing the presence of optical gain at  $\langle N \rangle = 2.07$  excitons/QD. **c**, Spectroelectrochemical measurement on a film of CdTe QDs, showing the differential absorbance spectrum of the sample at reducing potentials (electron injection, red curve) and oxidizing potentials (hole injection, blue curve, offset for clarity). The bleach amplitude was extracted from a fit of the signal with a Gaussian and a derivative-like feature, due to the presence of Stark-shift induced by localized charges<sup>49</sup>.

5

cores, InCl<sub>3</sub>-treated cores and core-shell-shell QDs. Although all samples have a decay component with a picosecond lifetime, InCl<sub>3</sub>-treated cores and un-passivated cores show sign of faster decay components, possibly associated with the ultrafast hole trapping process assumed in our description. However, the presence of multiple coherent bleach oscillations, typically associated with phonon-emission processes<sup>46–48</sup>, and limits in the time-resolution of the measurements prevents quantitative determination of the character of the fastest decay component (See Appendix).

The experiments on these InCl<sub>3</sub>-passivated QDs show that holes do indeed contribute to the BE bleach in CdSe QDs cores, with an amplitude determined by the degree of QD passivation.

### 5.7 Evidence of a hole contribution to the BE-bleach via optical gain and spectroelectrochemistry

Another spectroscopic signature of a significant hole contribution to the BE-bleach can be found in the presence of optical gain at the energy of the 1S transition. Figure 5.6a shows a high-fluence TA measurement on the CdSe/CdS/ZnS QDs, performed exciting the system at 400 nm with a fluence of  $1.86 \cdot 10^{14}$  photons/cm<sup>2</sup> per pulse, resulting in an average of 2.07 excitons per QD. Figure 5.6b compares the steady-state absorbance of the measured sample (black) to excited-state absorbances for different excitation fluences ( $\langle N \rangle = 0.86$  in orange and 2.07 in red), obtained adding the differential absorbance at 4.5 picoseconds after photoexcitation to the steady-state spectrum. For the higher fluence measurement

(red), the excited-state absorbance is negative on the low-energy side of the 1S absorption feature, an effect which would not be possible in the absence of a hole contribution to both stimulated emission and state-filling of the 1S transition. The red trace in Figure 5.6b shows that net gain is observed in the presence of approximately two excitons per QD. In absence of a hole contribution to the BE-bleach, a doubly-excited QD with two-fold degenerate conduction BE should have zero absorption (i.e. the material is transparent at the BE energy), but would not show gain.

We applied the transition-counting model, corrected for Poissonian excitation statistics (see Appendix), to a QD with two-fold degenerate conduction BE and four-fold degenerate valence BE. For an excitation density of  $\langle N \rangle = 2.07$  this model predicts a fractional bleach  $\Delta A/A_0 = 1.21$ , in close agreement with the fractional bleach of 1.19 observed from the TA measurement (see Appendix). This result shows that our quantitative assignment of the hole contribution in the low-fluence BE-bleach remains valid in the high-fluence regime: the transient absorption signal at the BE is well described by the sum of the contributions of electrons, with a degeneracy of 2, and holes, with a degeneracy of 4.

Perhaps the conceptually clearest proof of holes contributing to a BE-bleach comes from experiments where only holes are injected. In principle, hole injection could be done electrochemically and the changes in absorption could be recorded. However, electrochemical hole injection leads to rapid deterioration of CdSe QDs<sup>50</sup>, possibly due to irreversible oxidation of Se surface ions and dissolution of Cd<sup>2+</sup><sup>51</sup>. However, we found that for CdTe QDs stable hole injection is possible, allowing spectroelectrochemical determination of the hole bleach spectrum. The presence of a hole contribution to the BE-bleach should be extendable to other Cd-chalcogenides QDs, as they all share the same character of the BE transition.

Figure 5.6c shows differential absorption spectra obtained during a spectroelectrochemical measurement of a film of CdTe QDs. A potential difference is applied between the sample and a Ag pseudoreference electrode, which allows us to control the Fermi level inside the QD film. Applying both a reducing potential (electron injection, red) and oxidizing potential (hole injection, blue), we observed spectral changes at the BE energy. These spectral changes are caused by the superposition of a bleach feature and of a derivative-like feature, associated with a Stark-shift induced by the presence of trapped electrons.<sup>52</sup> We fitted the BE signal in the two traces, separating the bleach component (red and blue lines in Fig. 5.6c) and the Stark-shift component (see Appendix). The similarity in the spectral shape of the BE signals and the presence of a bleach component in both the spectra demonstrates that holes have a contribution to the BE-bleach similar to the contribution of electrons. Furthermore, we extracted the BE-bleach at each potential from a fit of the differential absorbance spectra, showing the presence of two distinct onsets in the bleach amplitude, corresponding to electron and hole injection (See Appendix). This clearly shows that electrochemical hole injection results in a measurable BE-bleach in CdTe QDs.

## 5.8 Conclusions

To summarize, we have provided three independent pieces of evidence that holes

contribute to the BE-bleach in Cd-chalcogenide QDs. We measured TA in the low-fluence regime on high PLQY CdSe core-shell-shell QD solutions, identifying a component in the bleach kinetics associated with hole cooling. The relative weight of the photogenerated hole to the BE-bleach amounts to half the weight of the electron, consistent with a simple theoretical model for the bleach of degenerate transitions. Measurements on low PLQY CdSe core-only QDs do not show a dependence on the initial hole state. InCl<sub>3</sub>-treated QDs, which have an intermediate PLQY between cores and core-shell-shell particles, show the presence of a hole component in the bleach, with a smaller amplitude than in the core-shell-shell QDs. These observations support the conclusion that ultrafast hole trapping in samples with incomplete passivation obscures the hole contribution to the BE-bleach. We also show that optical gain of the BE transition can be achieved for relatively low excitation densities ( $\langle N \rangle = 2$ ), which implies a significant contribution of a BE hole to the BE-bleach. Furthermore, we measured a bleach upon electrochemical hole injection in CdTe QDs, confirming that holes contribute to the BE-bleach of Cd chalcogenides QDs even in the absence of BE electrons.

5

Once demonstrated, the presence of a hole bleach can be used for spectroscopic analysis, allowing to differentiate between BE and trapped holes. Furthermore, our results suggest that measurements of TA BE-bleach can be employed to investigate the kinetics of hole processes in high PLQY Cd chalcogenides QDs, by monitoring the kinetics of the hole contribution to the bleach. Finally, we showed remarkable agreement between calculations of the fractional bleach in the presence of hole contribution and our experimental results. This observation paves the way to more quantitative studies of the build-up of optical gain in these materials, which will give solid handholds to improve these materials for applications in low-threshold gain media.

## References

1. Ganesan, A.; Houtepen, A.; Crisp, R.; Quantum Dot Solar Cells: Small Beginnings Have Large Impacts. *Appl. Sci.* 2018, 8 (10), 1867.
2. Zhang, H.; Kurley, J. M.; Russell, J. C.; Jang, J.; Talapin, D. V. Solution-Processed, Ultrathin Solar Cells from CdCl<sub>2</sub>-Capped CdTe Nanocrystals: The Multiple Roles of CdCl<sub>2</sub>-Ligands. *J. Am. Chem. Soc.* 2016, 138 (24), 7464–7467.
3. Crisp, R. W.; Pach, G. F.; Kurley, J. M.; France, R. M.; Reese, M. O.; Nanayakkara, S. U.; MacLeod, B. A.; Talapin, D. V.; Beard, M. C.; Luther, J. M. Tandem Solar Cells from Solution-Processed CdTe and PbS Quantum Dots Using a ZnTe–ZnO Tunnel Junction. *Nano Lett.* 2017, 17 (2), 1020–1027.
4. Kagan, C. R.; Lifshitz, E.; Sargent, E. H.; Talapin, D. V.; Murray, C.; Kagan, C.; Bawendi, M. G.; Talapin, D. V.; Lee, J.-S.; Kovalenko, M. V.; et al. Building Devices from Colloidal Quantum Dots. *Science* 2016, 353 (6302), 545–610.

5. Chung, D. S.; Lee, J.-S.; Huang, J.; Nag, A.; Ithurria, S.; Talapin, D. V. Low Voltage, Hysteresis Free, and High Mobility Transistors from All-Inorganic Colloidal Nanocrystals. *Nano Lett.* 2012, 12 (4), 1813–1820.
6. Choi, J.-H.; Oh, S. J.; Lai, Y.; Kim, D. K.; Zhao, T.; Fafarman, A. T.; Diroll, B. T.; Murray, C. B.; Kagan, C. R. In Situ Repair of High-Performance, Flexible Nanocrystal Electronics for Large-Area Fabrication and Operation in Air. *ACS Nano* 2013, 7 (9), 8275–8283.
7. Shirasaki, Y.; Supran, G. J.; Bawendi, M. G.; Bulović, V. Emergence of Colloidal Quantum-Dot Light-Emitting Technologies. *Nat. Photonics* 2013, 7 (1), 13–23.
8. Lim, J.; Park, Y.-S.; Wu, K.; Yun, H. J.; Klimov, V. I. Droop-Free Colloidal Quantum Dot Light Emitting Diodes. *Nano Lett.* 2018, acs.nanolett.8b03457.
9. Wilker, M. B.; Shinopoulos, K. E.; Brown, K. A.; Mulder, D. W.; King, P. W.; Dukovic, G. Electron Transfer Kinetics in CdS Nanorod-[FeFe]-Hydrogenase Complexes and Implications for Photochemical H<sub>2</sub> Generation. *J. Am. Chem. Soc.* 2014, 136 (11), 4316–4324.
10. Utterback, J. K.; Hamby, H.; Pearce, O. M.; Eaves, J. D.; Dukovic, G. Trapped-Hole Diffusion in Photoexcited CdSe Nanorods. *J. Phys. Chem. C* 2018, 122 (29), 16974–16982.
11. Pearce, O. M.; Duncan, J. S.; Damrauer, N. H.; Dukovic, G. Ultrafast Hole Transfer from CdS Quantum Dots to a Water Oxidation Catalyst. *J. Phys. Chem. C* 2018, 122 (30), 17559–17565.
12. Klimov, V. I.; Mikhailovsky, A. A.; Xu, S.; Malko, A.; Hollingsworth, J. A.; Leatherdale, C. A.; Eisler, H.-J.; Bawendi, M. G. Optical Gain and Stimulated Emission in Nanocrystal Quantum Dots. *Science* (80-. ). 2000, 290 (5490).
13. Klimov, V. I.; Ivanov, S. A.; Nanda, J.; Achermann, M.; Bezel, I.; McGuire, J. A.; Piryatinski, A. Single-Exciton Optical Gain in Semiconductor Nanocrystals. *Nature* 2007, 447 (7143), 441–446.
14. Fan, F.; Voznyy, O.; Sabatini, R. P.; Bicanic, K. T.; Adachi, M. M.; McBride, J. R.; Reid, K. R.; Park, Y.-S.; Li, X.; Jain, A.; et al. Continuous-Wave Lasing in Colloidal Quantum Dot Solids Enabled by Facet-Selective Epitaxy. *Nature* 2017, 544 (7648), 75–79.
15. Lim, J.; Park, Y.-S.; Klimov, V. I. Optical Gain in Colloidal Quantum Dots Achieved with Direct-Current Electrical Pumping. *Nat. Mater.* 2017.
16. Bawendi, M. G.; Wilson, W. L.; Rothberg, L.; Carroll, P. J.; Jedju, T. M.; Steigerwald, M. L.; Brus, L. E. Electronic Structure and Photoexcited-Carrier Dynamics in

- Nanometer-Size CdSe Clusters. *Phys. Rev. Lett.* 1990, 65 (13), 1623–1626.
17. Norris, D. J.; Sacra, A.; Murray, C. B.; Bawendi, M. G. Measurement of the Size Dependent Hole Spectrum in CdSe Quantum Dots. *Phys. Rev. Lett.* 1994, 72 (16), 2612–2615.
  18. Norris, D. J.; Bawendi, M. G. Structure in the Lowest Absorption Feature of CdSe Quantum Dots. *J. Chem. Phys.* 1995, 103 (13), 5260–5268.
  19. Guyot-Sionnest, P.; Wehrenberg, B.; Yu, D. Intraband Relaxation in CdSe Nanocrystals and the Strong Influence of the Surface Ligands. *J. Chem. Phys.* 2005, 123 (7), 074709.
  20. Kambhampati, P. Unraveling the Structure and Dynamics of Excitons in Semiconductor Quantum Dots. *Acc. Chem. Res.* 2011, 44 (1), 1–13.
  21. Sercel, P. C.; Efros, A. L. Band-Edge Exciton in CdSe and Other II–VI and III–V Compound Semiconductor Nanocrystals – Revisited. *Nano Lett.* 2018, 18 (7), 4061–4068.
  22. Hunsche, S.; Dekorsy, T.; Klimov, V.; Kurz, H. Ultrafast Dynamics of Carrier-Induced Absorption Changes in Highly-Excited CdSe Nanocrystals. *Appl. Phys. B Laser Opt.* 1996, 62 (1), 3–10.
  23. Klimov, V. I.; McBranch, D. W. Femtosecond  $1\text{P} \rightarrow 1\text{S}$  Electron Relaxation in Strongly Confined Semiconductor Nanocrystals. *Phys. Rev. Lett.* 1998, 80 (18), 4028–4031.
  24. Klimov, V. I.; McBranch, D. W.; Leatherdale, C. A.; Bawendi, M. G. Electron and Hole Relaxation Pathways in Semiconductor Quantum Dots. *Phys. Rev. B* 1999, 60 (19), 13740–13749.
  25. Sewall, S. L.; Cooney, R. R.; Kambhampati, P. Experimental Tests of Effective Mass and Atomistic Approaches to Quantum Dot Electronic Structure: Ordering of Electronic States. *Appl. Phys. Lett.* 2009, 94 (24), 243116.
  26. Boehme, S. C.; Azpiroz, J. M.; Aulin, Y. V.; Grozema, F. C.; Vanmaekelbergh, D. L.; Siebbeles, L. D. A.; Infante, I.; Houtepen, A. J.; Fakultatea, K. Density of Trap States and Auger-Mediated Electron Trapping in CdTe Quantum-Dot Solids.
  27. Knowles, K. E.; McArthur, E. A.; Weiss, E. A. A Multi-Timescale Map of Radiative and Nonradiative Decay Pathways for Excitons in CdSe Quantum Dots. *ACS Nano* 2011, 5 (3), 2026–2035.
  28. Klimov, V. I.; Schwarz, C. J.; McBranch, D. W.; Leatherdale, C. A.; Bawendi, M. G. Ultrafast Dynamics of Inter- and Intraband Transitions in Semiconductor

- Nanocrystals: Implications for Quantum-Dot Lasers. *Phys. Rev. B* 1999, 60 (4), R2177–R2180.
29. Adachi, M. M.; Fan, F.; Sellan, D. P.; Hoogland, S.; Voznyy, O.; Houtepen, A. J.; Parrish, K. D.; Kanjanaboos, P.; Malen, J. A.; Sargent, E. H. Microsecond-Sustained Lasing from Colloidal Quantum Dot Solids. *Nat. Commun.* 2015, 6, 8694.
  30. Ekimov, A. I.; Kudryavtsev, I. A.; Efros, A. L.; Yazeva, T. V.; Hache, F.; Schanne-Klein, M. C.; Rodina, A. V.; Ricard, D.; Flytzanis, C. Absorption and Intensity-Dependent Photoluminescence Measurements on CdSe Quantum Dots: Assignment of the First Electronic Transitions. *J. Opt. Soc. Am. B* 1993, 10 (1), 100.
  31. Norris, D. J.; Bawendi, M. G. Measurement and Assignment of the Size-Dependent Optical Spectrum in CdSe Quantum Dots. *Phys. Rev. B* 1996, 53 (24), 16338–16346.
  32. Sewall, S. L.; Cooney, R. R.; Anderson, K. E. H.; Dias, E. A.; Kambhampati, P. State-to-State Exciton Dynamics in Semiconductor Quantum Dots. *Phys. Rev. B* 2006, 74 (23), 235328.
  33. Chen, O.; Zhao, J.; Chauhan, V. P.; Cui, J.; Wong, C.; Harris, D. K.; Wei, H.; Han, H.-S.; Fukumura, D.; Jain, R. K.; et al. Compact High-Quality CdSe–CdS Core–Shell Nanocrystals with Narrow Emission Linewidths and Suppressed Blinking. *Nat. Mater.* 2013, 12 (5), 445–451.
  34. Boldt, K.; Kirkwood, N.; Beane, G. A.; Mulvaney, P. Synthesis of Highly Luminescent and Photo-Stable, Graded Shell CdSe/Cd<sub>x</sub>Zn<sub>1-x</sub>S Nanoparticles by In Situ Alloying. *Chem. Mater.* 2013, 25 (23), 4731–4738.
  35. McGuire, J. A.; Sykora, M.; Robel, I.; Padilha, L. A.; Joo, J.; Pietryga, J. M.; Klimov, V. I. Spectroscopic Signatures of Photocharging Due to Hot-Carrier Transfer in Solutions of Semiconductor Nanocrystals under Low-Intensity Ultraviolet Excitation. *ACS Nano* 2010, 4 (10), 6087–6097.
  36. Lebedev, M. V.; Misochko, O. V.; Dekorsy, T.; Georgiev, N. On the Nature of “Coherent Artifact.” *J. Exp. Theor. Phys.* 2005, 100 (2), 272–282.
  37. Wang, H. I.; Infante, I.; ten Brinck, S.; Cánovas, E.; Bonn, M. Efficient Hot Electron Transfer in Quantum Dot-Sensitized Mesoporous Oxides at Room Temperature. *Nano Lett.* 2018, acsnano.8b01981.
  38. Bisschop, S.; Geiregat, P.; Aubert, T.; Hens, Z. The Impact of Core/Shell Sizes on the Optical Gain Characteristics of CdSe/CdS Quantum Dots. *ACS Nano* 2018, acsnano.8b02493.

39. Wu, K.; Park, Y.-S.; Lim, J.; Klimov, V. I. Towards Zero-Threshold Optical Gain Using Charged Semiconductor Quantum Dots. *Nat. Nanotechnol.* 2017, 12 (12), 1140–1147.
40. Efros, A. L.; Rosen, M.; Kuno, M.; Nirmal, M.; Norris, D. J.; Bawendi, M. Band-Edge Exciton in Quantum Dots of Semiconductors with a Degenerate Valence Band: Dark and Bright Exciton States. *Phys. Rev. B* 1996, 54 (7), 4843–4856.
41. Korkusinski, M.; Voznyy, O.; Hawrylak, P. Fine Structure and Size Dependence of Exciton and Biexciton Optical Spectra in CdSe Nanocrystals. *Phys. Rev. B* 2010, 82 (24), 245304.
42. Houtepen, A. J.; Hens, Z.; Owen, J. S.; Infante, I. On the Origin of Surface Traps in Colloidal II–VI Semiconductor Nanocrystals. *Chem. Mater.* 2017, 29 (2), 752–761.
43. Giansante, C.; Infante, I. Surface Traps in Colloidal Quantum Dots: A Combined Experimental and Theoretical Perspective. *J. Phys. Chem. Lett.* 2017, 8 (20), 5209–5215.
44. Kirkwood, N.; Monchen, J. O. V.; Crisp, R. W.; Grimaldi, G.; Bergstein, H. A. C.; du Fossé, I.; van der Stam, W.; Infante, I.; Houtepen, A. J. Finding and Fixing Traps in II–VI and III–V Colloidal Quantum Dots: The Importance of Z-Type Ligand Passivation. *J. Am. Chem. Soc.* 2018, jacs.8b07783.
45. Gao, Y.; Peng, X. Photogenerated Excitons in Plain Core CdSe Nanocrystals with Unity Radiative Decay in Single Channel: The Effects of Surface and Ligands. *J. Am. Chem. Soc.* 2015, 137 (12), 4230–4235.
46. Schnitzenbaumer, K. J.; Dukovic, G. Comparison of Phonon Damping Behavior in Quantum Dots Capped with Organic and Inorganic Ligands. *Nano Lett.* 2018, 18 (6), 3667–3674.
47. Sagar, D. M.; Cooney, R. R.; Sewall, S. L.; Dias, E. A.; Barsan, M. M.; Butler, I. S.; Kambhampati, P. Size Dependent, State-Resolved Studies of Exciton-Phonon Couplings in Strongly Confined Semiconductor Quantum Dots. *Phys. Rev. B* 2008, 77 (23), 235321.
48. Cerullo, G.; De Silvestri, S.; Banin, U. Size-Dependent Dynamics of Coherent Acoustic Phonons in Nanocrystal Quantum Dots. *Phys. Rev. B* 1999, 60 (3), 1928–1932.
49. Spoor, F. C. M.; Tomić, S.; Houtepen, A. J.; Siebbeles, L. D. A. Broadband Cooling Spectra of Hot Electrons and Holes in PbSe Quantum Dots. *ACS Nano* 2017, acsnano.7b02506.

50. Gooding, A. K.; Gómez, D. E.; Mulvaney, P. The Effects of Electron and Hole Injection on the Photoluminescence of CdSe/CdS/ZnS Nanocrystal Monolayers. *ACS Nano* 2008, 2 (4), 669–676.
51. Park, S.-M.; Barber, M. E. Thermodynamic Stabilities of Semiconductor Electrodes. *J. Electroanal. Chem. Interfacial Electrochem.* 1979, 99 (1), 67–75.
52. van der Stam, W.; du Fossé, I.; Grimaldi, G.; Monchen, J. O. V.; Kirkwood, N.; Houtepen, A. J. Spectroelectrochemical Signatures of Surface Trap Passivation on CdTe Nanocrystals. *Chem. Mater.* 2018, *acs.chemmater.8b03893*.
53. Kloper, V.; Osovsky, R.; Kolny-Olesiak, J.; Sashchiuk, A.; Lifshitz, E., The Growth of Colloidal Cadmium Telluride Nanocrystal Quantum Dots in the Presence of Cd<sub>0</sub> Nanoparticles. *J. Phys. Chem. C* 2007, 111 (28), 10336-10341.
54. Boehme, S. C.; Vanmaekelbergh, D.; Evers, W. H.; Siebbeles, L. D. A.; Houtepen, A. J., In situ spectroelectrochemical determination of energy levels and energy level offsets in quantum-dot heterojunctions. *J. Phys. Chem. C* 2016, 120 (9), 5164-5173.
55. Tyagi, P.; Cooney, R. R.; Sewall, S. L.; Sagar, D. M.; Saari, J. I.; Kambhampati, P., Controlling piezoelectric response in semiconductor quantum dots via impulsive charge localization. *Nano Lett* 2010, 10 (8), 3062-7.

## Appendix

### Materials used in the QD synthesis

Lithium perchlorate ( $\text{LiClO}_4$ , 99.99%), CdO (99.99%), Cd(II)-acetate (99.995%), Zn(II)-acetate (99.99%), Rhodamine 101 inner salt, Octadecene (ODE, 90%), 1,7-heptanediamine (7-DA, 98%), Oleylamine (OLAM, 99.8%), Oleic acid (OA, 90%), Ferrocene (Fc, 98%), Butanol (BuOH, Anhydrous, 99.8%), Methanol (MeOH, Anhydrous, 99.8%), Hexane (99.8%, Anhydrous), Octadecylphosphonic acid (ODPA, 97%), Trioctyl phosphineoxide (TOPO, technical grade, 90%), Trioctylphosphine (TOP, 97%), 1-Octanethiol (>98.5%), Selenium powder (Se, 99.99%), Tellurium powder (Te, 99.997%), and Acetonitril (99.99%, Anhydrous) were all bought from Sigma-Aldrich and used as received unless specifically mentioned. Acetonitril was dried before use in an Innovative Technology PureSolv Micro column. All other chemicals were used as received, unless specifically mentioned.

## 5

### Synthesis of CdSe core nanocrystals (NCs)

The CdSe core nanocrystals were synthesized according to a method by Chen *et al.*<sup>33</sup>. In a 50 mL three-necked flask, 60 mg of CdO, 280 mg octadecylphosphonic acid (ODPA), 3 g trioctylphosphineoxide (TOPO) and a magnetic stirring bean were added. This mixture of powders was heated up under vacuum to 150°C, where mixture melts. The mixture was vigorously stirred and degassed at this temperature for one hour. The mixture is heated up to 320 °C, where the liquid turned into a clear and colorless solution. 1 mL of trioctylphosphine (TOP) was added to the solution, and the temperature was raised to 380 oC, at which point 0.5 mL of a Se-precursor solution (60mg Se in 0.5mL TOP) was swiftly injected. After a specific growth time the reaction mixture was cooled with an air-gun to room temperature. For the CdSe cores in this work, we used a growth time of 25 seconds. The crude product is washed two times by addition of a 1:1 volume ratio of methyl acetate, followed by centrifugation at 3000 rpm, and redispersion into hexane. The final product is filtered through milipore filters with a pore diameter of 0.2  $\mu\text{m}$  and stored in a nitrogen purged glovebox for further use.

### Synthesis of Cd-oleate and Zn-oleate for CdS and ZnS shell growth

For the Cd-oleate synthesis, 1.32 g of Cd-(acetate)<sub>2</sub> was dissolved in 52.4 g ODE and 7.4 g OA. The mixture was heated up under vacuum to 120°C and left there for three hours. Afterwards, the reaction was cooled down to room temperature and the Cd-oleate solution was stored in a nitrogen purged glovebox for further use.

The Zn-oleate was made in a similar fashion. Zn(II)-(acetate)<sub>2</sub> was mixed with 1g of OA, 1.6 mL ODE and 1.6 mL of OLAM. The oleylamine serves as a stabilizing ligand for the Zn-oleate, since this has the tendency to solidify out of solution at room temperature otherwise. The mixture was heated up in a 20 mL vial inside a nitrogen purged glovebox to 130°C and stored there for further use.

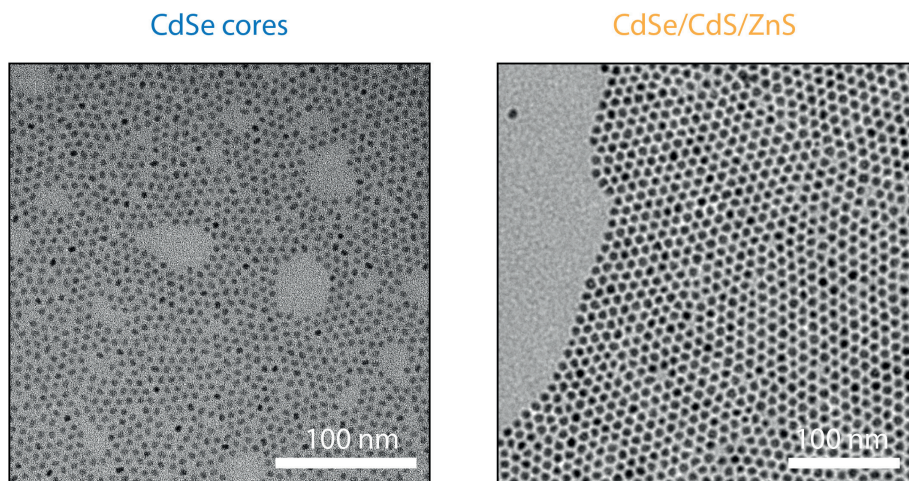


**Figure 5.7.** Characteristic Transmission Electron Microscopy (TEM) images of the core CdSe QDs and small CdSe/CdS/ZnS core-shell-shell QDs.

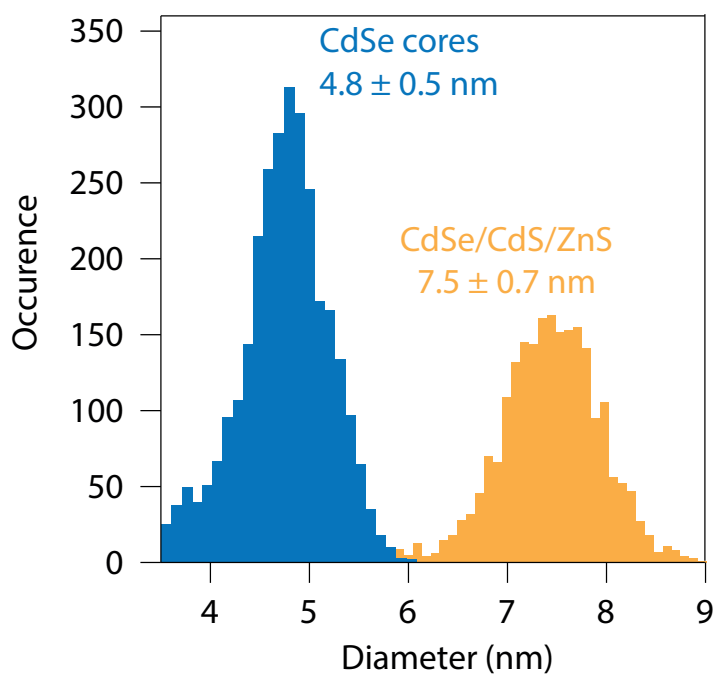


**Figure 5.8.** Size distributions acquired from image analysis using ImageJ. For each of the QD samples, over 3000 nanocrystals were analyzed.

### Shell growth of CdS and ZnS

The shell growth of CdSe QDs into core-shell-shell CdSe/CdS/ZnS nanocrystals was done according to an adapted method by Chen *et al.*<sup>33</sup> and Boldt *et al.*<sup>34</sup>.

For the CdS shell growth, 20 nmol CdSe cores, 2.6 mL octadecene (ODE) and 0.6 mL degassed oleylamine (OLAM) were added to a 100 mL three-necked flask and degassed for one hour at room-temperature (21°C) and for 20 hours at 120°C to completely remove hexane, oxygen and water. After that, the reaction solution was heated up to 310°C under nitrogen flow and magnetic stirring. During the heating, when the temperature reached 240°C, a desired amount of Cd-oleate (diluted in ODE) and 1-octanethiol (diluted in 6 mL ODE) were injected dropwise into the growth solution at a rate of half a CdS monolayer per hour using a syringe pump. We define one CdS monolayer as one full layer of Cd and one full layer of S on the NC surface (i.e. half a unit cell). After the addition of the CdS shell-precursors was finished, 1 mL of oleic acid (OA) was swiftly injected and the solution was annealed at 310°C for one hour. Before the growth of the ZnS shell, the core-shell QDs containing solution was degassed for an hour at 120°C.

For the ZnS shell-growth, the sulfur precursor consisted again out of 1-octanethiol diluted in ODE. The solution with freshly grown CdSe/CdS QDs was heated up to 280°C under nitrogen flow. When the solution reached 210°C, a desired amount of Zn-oleate and 1-octanethiol in 4 mL ODE (in two separate syringes) was injected at a rate of 2 mL/hour. After addition of the precursors, the solution was cooled down to room temperature by removing the heat and with an air-gun.

The solution was washed twice by addition of methanol:butanol (1:2), centrifugation at 3000 rpm for 10 minutes and redispersion of the precipitate in hexane. Finally, the solution was filtered through milipore filters with a pore diameter of 0.2 μm and stored in a nitrogen purged glovebox for further use.

Using the above method, we synthesized a batch of small core-shell-shell CdSe/2CdS/1ZnS QDs.

### Synthesis of CdTe NCs

The CdTe QDs were synthesized using a method by Kloper *et al.*<sup>53</sup>. For the Cd-precursor, CdO (51.5 mg) was mixed with 500 μL OA and 20 mL ODE. The Te-precursor was prepared by dissolving 51 mg Te powder in 1 mL TOP and diluting this yellow solution with 4 mL ODE. The Cd-precursor was first degassed in a three-necked flask under vacuum at 100°C for approximately one hour. After this, the system was heated up under nitrogen to 280°C until the red, turbid solution became transparent and colorless, indicating the formation of Cd(OA)<sub>2</sub>. Subsequently, the temperature was raised to 310°C for roughly 30 minutes. When the first grey precipitate of metallic CdO was observed, the Te-precursor was swiftly injected. Following the resulting nucleation, the color of the solution quickly changed from yellow to black. The QDs were allowed to grow at 260°C for three minutes, after which the mixture was quenched with 5 mL ODE and cooled down to room temperature. The CdO was removed from the reaction mixture by centrifugation and decantation. Washing of the QDs was done by precipitating the solution with a mixture of MeOH and BuOH (QDs:MeOH:BuOH = 1:1:1), centrifuging at 3500 RPM for three minutes, decanting the supernatant and resuspending the QDs in hexane. This was repeated another time, and the resulting solution was stored in a nitrogen purged glovebox for further use.

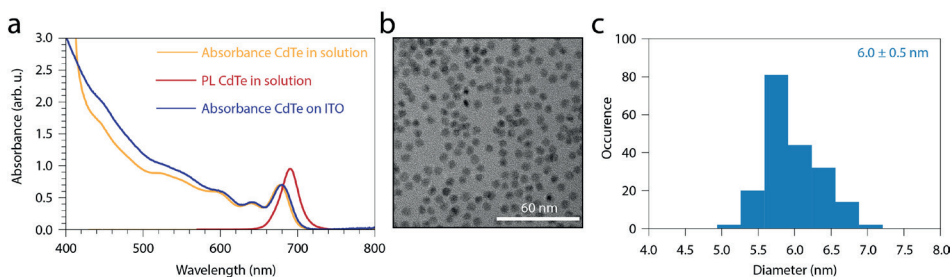


**Figure 5.9. Characterization of the CdTe QDs used for the spectroelectrochemical measurements presented in the main text.** **a**, Absorbance and photoluminescence spectra of the CdTe QDs dispersed in hexane and on an ITO substrate. **b**, Characteristic TEM image of the CdTe QDs. **c**, Histogram of the obtained diameters, revealing an average diameter of  $6.0 \pm 0.5$  nm for the CdTe QDs used in this study.

### Preparation of the CdTe QD film

The CdTe film was prepared via layer-by-layer growth with a mechanical dip-coater (DC Multi-9, Nima Technology), performed inside a nitrogen purged glovebox. Each layer was obtained by dipping ITO covered glass slides for 30 s in a concentrated CdTe-in-hexane solution. After this, the substrate was dipped for 30 s into a 0.1 M solution of 7-DA in MeOH to crosslink the QD film. Finally, the substrate was dipped in a MeOH solution, to wash of any residuals, for 30 s. These three dip-cycles were repeated 7 times to build up a good film on the ITO substrate. Half of the substrate was left uncoated, in order to provide good electrical contact with the electrodes during the electrochemical measurements.

### Z-type ligand passivation of CdSe cores with $\text{InCl}_3$

The preparation of these passivated QDs was done according to recent work by our group<sup>44</sup>. We prepared stock solutions of  $\text{InCl}_3$ -oleylamine in toluene by adding 1 mmol of  $\text{InCl}_3$  with 3 equivalents of oleylamine in a 20 mL vial and stir the solution at 95°C in an  $\text{N}_2$ -filled glovebox. After cooling down this mixture, the desired concentration of the stock solution was reached by further dilution with toluene.

Pre-determined volumes of CdSe QDs, dispersed in toluene, and the  $\text{InCl}_3$ -oleylamine solutions were added to a 10 mL vial to give a final volume of 3 mL. The vials were closed and added into a pre-heated aluminium block at 95°C. The solutions were stirred for 15 minutes, after which they were removed from the heating block and cooled down naturally to room temperature. For the experiments done throughout the main text, we added an equivalent of 90  $\text{InCl}_3/\text{nm}^2$  to 0.456  $\mu\text{mol}$  of CdSe QDs.

### Description of the spectroscopic setups

#### *Steady state absorption and photoluminescence measurements*

Absorption spectra were measured on a double-beam PerkinElmer Lambda 1050 UV/Vis spectrometer. Photoluminescence spectra were recorded on an Edinburgh

Instruments FLS980 spectrofluorimeter equipped with a 450 W Xenon lamp as an excitation source and double grating monochromators.

#### *Transmission Electron Microscopy (TEM)*

TEM images were acquired using a JEOL JEM-1400 plus TEM microscope operating at 120 kV. Samples for TEM imaging were prepared by dropcasting a dilute solution of QDs onto a Formvar and carbon coated copper (400-mesh) TEM grid.

#### *fs-Transient Absorption (TA) spectroscopy*

fs-TA measurements are performed on solutions of the CdSe/(CdS/ZnS) QDs in hexane, loaded inside an air-tight cuvet inside a nitrogen purged glovebox. A Yb-KGW oscillator (Light Conversion, Pharos SP) is used to produce 180 fs photon pulses with a wavelength of 1028 nm and at a frequency of 5 kHz. The pump beam is obtained by sending the fundamental beam through an Optical Parametric Amplifier (OPA) equipped with a second harmonic module (Light Conversion, Orpheus), performing non-linear frequency mixing and producing an output beam whose wavelength can be tuned in the 310-1330 nm window. A small fraction of the fundamental beam power is used to produce a broadband probe spectrum (500-1600 nm), by supercontinuum generation in a sapphire crystal. The pump beam is transmitted through a mechanical chopper operating at 2.5 kHz, allowing one in every two pump pulses to be transmitted. Pump and probe beam overlap at the sample position with a small angle (roughly 8°), and with a relative time delay controlled by an automated delay-stage. After transmission through the sample, the pump beam is dumped while the probe is collected at a detector (Ultrafast Systems, Helios). During the experiments, we make sure the pump and probe beam have orthogonal polarizations (i.e. one of them is vertically polarized, the other horizontally), to reduce the influence of pump scattering into our detector. The differential absorbance is obtained via  $\Delta A = \ln(I_{\text{on}}/I_{\text{off}})$ , where  $I$  is the light incident on the detector with either pump on or pump off. TA data are corrected for probe-chirp via a polynomial correction to the coherent artifact. Pump photon fluence was estimated by measuring the pump beam transmission through a 1-mm-radius pinhole with a thermopile sensor (Coherent, PS19Q).

#### *Photoluminescence quantum yield (PLQY) measurements*

We measured the PLQY of the NC dispersions with respect to a Rhodamine 101 solution in ethanol. The PLQY was calculated using the following equation:

$$PLQY = PLQY_{\text{Rhodamine 101}} \frac{I_{\text{QD solutions}}^{\text{PL}}}{I_{\text{Rhodamine 101}}^{\text{PL}}} \frac{f_{\text{Rhodamine 101}}}{f_{\text{QD solutions}}} \left( \frac{n_{\text{hexane}}}{n_{\text{ethanol}}} \right)^2 \quad 5.5$$

Where  $PLQY_{\text{rhodamine 101}}$  is set to be 95%,  $I_{\text{PL}}$  is the intensity of the photoluminescence signal of either the QD solution or the Rhodamine 101 solution,  $n_{\text{hexane/ethanol}}$  is the refractive index of hexane or ethanol at 530 nm (1.377 and 1.3630) and  $f_x$  is the fraction

of absorbed light of species  $x$ , calculated as  $f_x = 1 - 10^{-OD_x}$ , where  $OD_x$  is the optical density of the solution containing either the QDs or the Rhodamine 101. We determined the PLQY of the CdSe core QDs to be 6.5%, the CdSe/2CdS/1ZnS core-shell-shell QDs to be 81.7% and the CdSe/4CdS/2ZnS core-shell-shell QDs to be 61.3%.

#### *Spectroelectrochemical (SEC) measurements*

The SEC measurements were all performed in a  $N_2$  purged glovebox. As an electrolyte, we used a 0.1 M  $LiClO_4$  solution in acetonitrile, which was dried with an Innovative Technology PureSolv Micro column. The CdTe NC film was immersed in the electrolyte solution, together with a Ag wire pseudoreference electrode and a Pt sheet counter electrode. The potential of the NC film on ITO was controlled with a PGSTAT128N Autolab potentiostat. Changes in the absorption of the NC film as a function of applied potential were recorded simultaneously with a cyclic voltammogram with a fiber-based UV-VIS spectrometer (USB2000, Ocean Optics). For the film, the measurements were started at the open-circuit potential ( $V_{oc} = -0.5V$  with reference to the Ag wire), while scanning with a rate of 50 mV/s. Unless stated otherwise, all potentials are given with reference to the Ag pseudoreference.

5

#### **Determination of the time-dependence of the BE-bleach**

In order to extract the time dependence of the BE-bleach from TA measurements of the small CdSe/CdS/ZnS QDs, we fitted the TA signal in the spectral region close to the BE to a sum of two Gaussians, describing the overlapping 1S and 2S bleach features. Each spectral slice of the TA colormap, corresponding to a set delay time, was fitted in the range between 577 nm and 691 nm. The center of the two Gaussians was determined by a fit to a single spectral cut, obtained for the measurement with 1S resonant excitation (616 nm) after cooling (1 ps), shown in Figure 5.4a. The fit resulted in the following parameters:

$$\lambda_{1S} = 614.8 \pm 0.2 \text{ nm} \quad 5.6$$

$$\sigma_{1S} = 9.5 \pm 0.2 \text{ nm} \quad 5.7$$

$$\lambda_{2S} = 590.7 \pm 0.4 \text{ nm} \quad 5.8$$

$$\sigma_{2S} = 9.3 \pm 0.3 \text{ nm} \quad 5.9$$

Fits of the full TA colormaps for all excitations was performed keeping the set of parameters given by eq. 5.6-5.9, to reduce the number of degrees of freedom. This is performed under the assumption that the position and width of the transition remains constant during the measurement. The amplitude of the 1S Gaussian feature, normalized to the value after 1 picosecond, is then plotted as a function of the delay time, as shown in Figure 5.4b.

### Extracting the hole contribution to the BE-bleach

The apparent dynamics of the normalized BE-bleach amplitude, obtained fitting TA colormaps, is given by a convolution of the real dynamics of the signal by the Instrument Response Function (IRF) of the measurement apparatus. In order to obtain the real dynamics, we obtained an analytical form for the convolution of a function describing the expected signal behavior by a function describing the IRF, and fitting the bleach amplitude by the equation obtained. The IRF was described by a Gaussian function:

$$IRF(t, t_0, \sigma) = e^{-(t-t_0)^2/(2\sigma^2)} \quad 5.10$$

The real signal dynamics was modelled as a step function, multiplied by an exponential ingrowth of a fraction of the signal:

$$F_{real}(t, t_0, \tau, f_h) = \theta(t, t_0) \left[ 1 - f_h e^{-(t-t_0)/\tau} \right] \quad 5.11$$

where  $\theta$  is the Heaviside function and  $f_h$  is the fractional increase of the signal after  $t_0$ . As the growth of the bleach signal after  $t_0$  is associated to hole cooling,  $f_h$  represent the fractional contribution of a hole to the exciton bleach. Convoluting the two functions, one obtains:

$$F_{conv}(t, t_0, \sigma, \tau, f_h) = \frac{1}{2} \left\{ 1 + \operatorname{erf} \left( \frac{t-t_0}{\sqrt{2}\sigma} \right) - f_h \exp \left( \frac{\sigma^2}{2\tau^2} - \left( \frac{t-t_0}{\tau} \right) \right) * \left[ 1 + \operatorname{erf} \left( \frac{(t-t_0)}{\sqrt{2}\sigma} - \frac{\sigma}{\sqrt{2}\tau} \right) \right] \right\} \quad 5.12$$

The model is fitted to the normalized bleach amplitude, with  $t_0, \sigma, \tau$ , and  $f_h$  as fitting parameters.

### Bleach per absorbed fluence for 1S and 2S excitation

In our analysis of the 1S bleach dynamics, we have interpreted the ingrowth of the 1S bleach upon 2S excitation as the consequence of the cooling of carriers (holes), that were instead immediately contributing to the 1S bleach upon 1S excitation. In order to corroborate this assignment, we checked whether the absorption of a photon in the two excitations leads to the same amount of 1S bleach after cooling has occurred. To do so, we rescale the differential absorbance by the absorbed photon fluence:

$$\Delta A' = \frac{\Delta A}{F_a J_0} \quad 5.13$$

where  $F_a$  is the fraction of absorbed light, and  $J_0$  the incoming photon fluence per pulse. The photon fluence was determined measuring the power of the pump beam transmitted

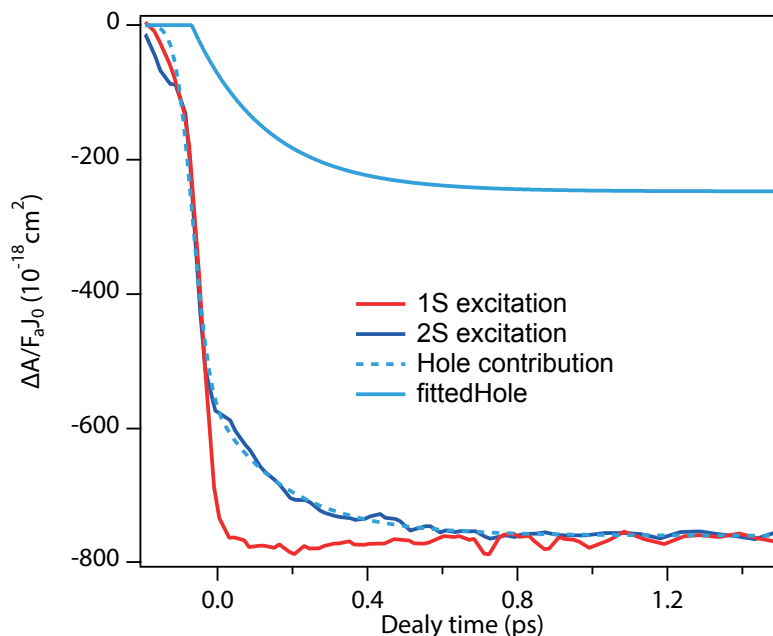


**Figure 5.10. Bleach per absorbed photon fluence per pulse.** Rescaling the bleach 1S bleach obtained for 1S excitation (continuous red line) and 2S excitation (continuous blue line) by the amount of photon fluence absorbed per pulse, the two traces fall on top of each other after cooling. The dashed light-blue line shows the fit of the 2S excitation bleach with the hole cooling model, resulting in a fractional hole contribution of  $0.33 \pm 0.03$  and a cooling time of  $200 \pm 20$  fs, in agreement with the results presented in the main text. The continuous light-blue line represented the hole contribution to the bleach signal, extracted from the fit.

through a circular pinhole with a 1 mm radius, dividing the transmitted power by the area of the pinhole, by the energy of a single photon, and by the repetition rate of the pump beam.

Figure 5.10 displays the bleach per absorbed fluence per pulse for 1S and 2S excitation of the core/shell/shell sample. After cooling has occurred ( $t > 300$  fs), the two bleach traces (continuous lines) fall on top of each other. Fitting of the bleach ingrowth upon 2S excitation, following the approach described in the main text and in the Appendix (Extracting the hole contribution to the BE-bleach), results in a fractional hole contribution of  $0.33 \pm 0.03$  and a cooling time of  $200 \pm 20$  fs, in agreement with the results displayed in the main text. We conclude that the final level of bleach per absorbed photon is the same for different excitation, confirming that the ingrowth observed in the 2S excitation is related to the cooling of carriers that are already at the band-edge upon 1S excitation.

#### Hole contribution for mixed 1S/2S excitations

Figure 5.11 extends Figure 5.4b, showing the effect of hole cooling for measurements

performed with 590 nm and 600 nm excitation. As the excitation wavelength falls in between the position of the two transitions, some QDs in the ensemble will be excited in the 1S transition and some in the 2S transition. As the fraction of QDs excited in the 2S transition will undergo hole cooling, the average normalized bleach is expected to show an ingrowth for all excitations whose wavelength is below the wavelength of the 1S transition, as seen in Figure 5.9. Figure 5.9 also shows that the amount of bleach ingrowth gets smaller as the excitation wavelength approaches the wavelength of the 1S transition. This can be understood in terms of overlapping absorption features, as the 1S feature dominates the absorption for wavelengths around 616 nm, resulting in the excitation of band-edge electrons and holes. As the excitation wavelength decreases, more and more QDs absorb into the 2S feature, leading to the generation of a higher number of hot holes.

Fitting  $F_{\text{conv}}$ , described in eq. 5.12, to the normalized bleach amplitudes for 616 nm, 600 nm, 590 nm and 581 nm excitations, allowed to determine the dependence of the hole contribution  $f_h$  and the ingrowth lifetime  $\tau$  on the excitation wavelength, shown in Table 5.1.

**Table 5.1.** Values for the fitting parameters  $f_h$  and  $\tau$  extracted from a fit of  $F_{\text{conv}}$  to the normalized bleach amplitudes obtained for different excitation wavelengths.

Excitation wavelength (nm)	$f_h$	$\tau$
581	$0.32 \pm 0.03$	$210 \pm 20$
590	$0.26 \pm 0.03$	$190 \pm 20$
600	$0.05 \pm 0.01$	$600 \pm 200$

The values of  $f_h$  reported in Table 5.1 confirm the qualitative trend observed in Figure 5.11. The lifetime of the bleach ingrowth remains approximately constant for 581 nm and 590 nm excitation, suggesting that the ingrowth originates from a single cooling process for both excitations. The difference observed with the fitted lifetime for 600 nm excitations is attributed to the lower accuracy of the parameter determination, due to the presence of only a small amount of signal ingrowth.

We attempted a quantitative comparison between the observed decrease in  $f_h$  and the decrease estimated from the state-filling model for BE-bleach, described in the main text. The fraction of QDs initially photoexcited in the 2S transition was estimated by calculating the contribution of 1S absorption at the different excitation wavelengths. A Gaussian fit of linear absorption spectrum on the lower energy side of the first absorption feature, shown in Figure 5.12a, allowed to determine the shape and intensity of the 1S absorption feature. The fraction of QDs photoexcited in the 2S transition is then estimated as:

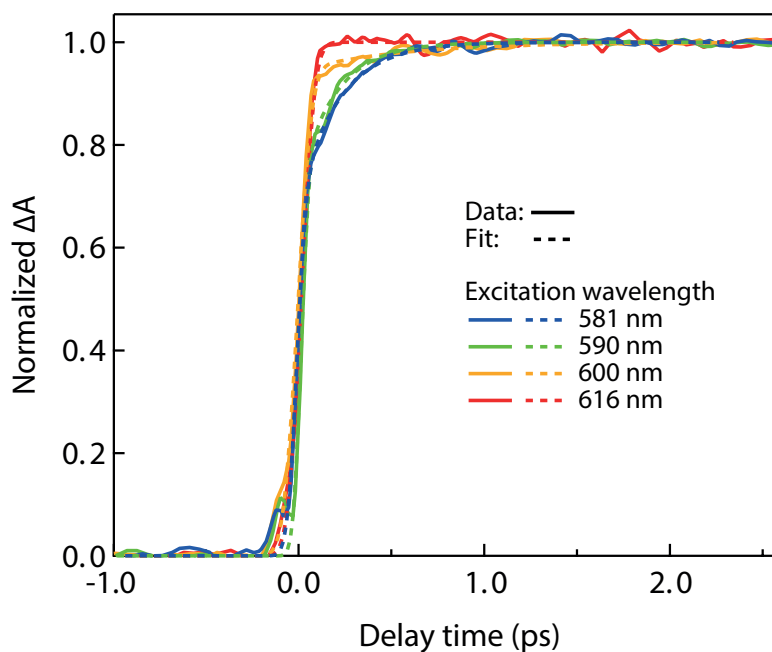


**Figure 5.11. Normalized bleach amplitude for different excitation wavelength.** Solid lines represent the experimental traces, while dotted lines show the results of fits to the data. As the excitation wavelength gets lower, the signal ingrowth decreases in amplitude, and is negligible for resonant 1S excitation.

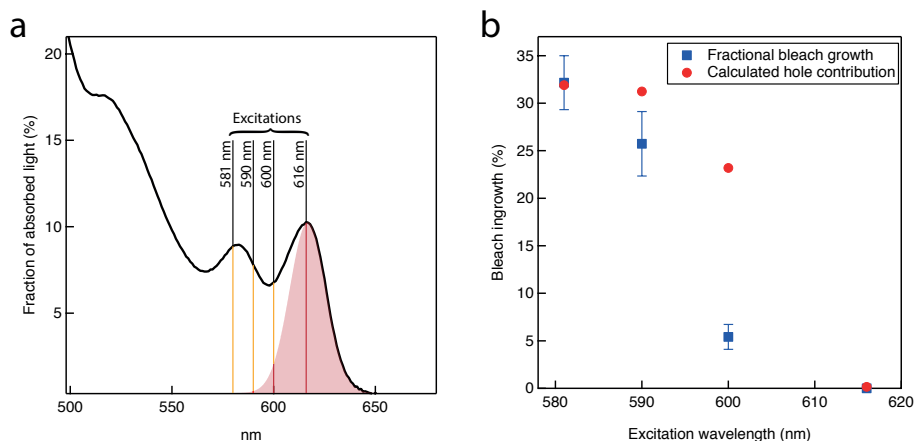


**Figure 5.12. Modeling the bleach ingrowth for mixed 1S/2S excitation.** **a**, Linear absorption spectrum, highlighting the Gaussian fit of the first absorption features (red area) and the fractional excitation of 1S and 2S transition for each excitation wavelength used in the TA measurements (red and orange lines, respectively). **b**, Comparison between calculated and measured bleach ingrowth for different excitation wavelengths. Error bars for the measured bleach growth are obtained from the fit of  $F_{\text{conv}}$  (see “Extracting the hole contribution to the BE-bleach”, Appendix) to TA data. The two estimates follow the same trend in wavelength, while significant difference can be observed for the 600 nm excitation alone.

$$f_{2s} = \left[ 1 - \frac{A_{1s}}{A_0}(\lambda) \right] \quad 5.14$$

The state filling model predicts a value of  $f_h = 0.333$  for pure 2S excitation. In case of mixed 1S/2S excitation of the QD population, the value of the hole contribution can be described as:

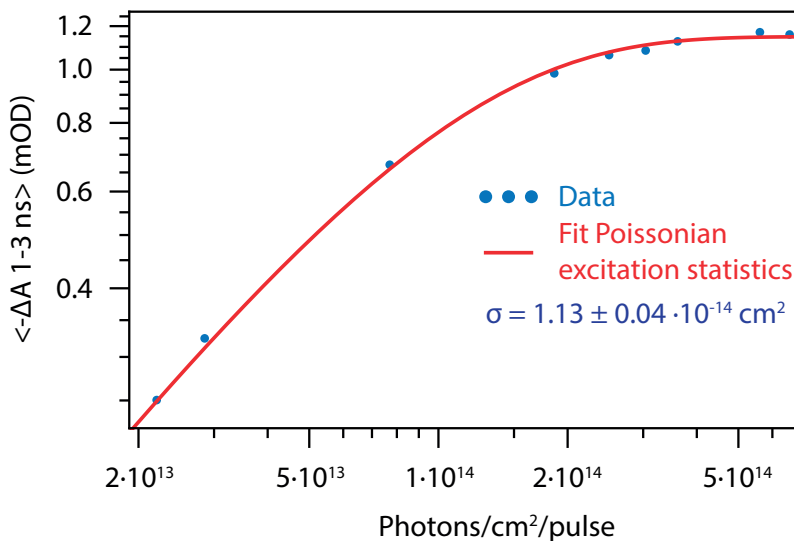
$$f_h = 0.333 * f_{2s} \quad 5.15$$

Figure 5.12b shows the comparison between the measured and calculated hole contributions.

### Determination of the absorption cross section at the pump wavelength (400 nm)

We measure the absorption cross section of the CdSe/CdS/ZnS nanocrystals following Poissonian excitation statistics. The magnitude of the bleach is smaller than directly after photoexcitation, but nonzero, meaning that there still is a finite population of nanocrystals which have excitons in there. The amplitude of the absorption bleach scales with the number of excitons present, and can be estimated via:

$$|\Delta A_{t=3\text{ ns}}| \propto 1 - P_0 = 1 - e^{-\langle N \rangle} \quad 5.16$$



**Figure 5.13. Determination of the absorption cross section at the pump wavelength (400 nm).**

We integrate the bleach magnitude between 1 and 3 nanoseconds, which is the region in which all multiexcitons have decayed, and fit the data assuming Poissonian excitation statistics.

Where  $|\Delta A_{1-3\text{ ns}}|$  is the magnitude of the bleach between 1-3 nanoseconds,  $P_0$  is the Poisson probability of finding zero excitons and  $\langle N \rangle$  is the average exciton population per nanocrystal. In turn,  $\langle N \rangle = \sigma J_0$ , with  $\sigma$  being the absorption cross section, and  $J_0$  the incoming photon fluence. By fitting the data to the above equation, we obtain an absorption cross section at 400 nm of  $1.13 \pm 0.04 \cdot 10^{-14} \text{ cm}^2$ , which we use to calculate  $\langle N \rangle$  per photon fluence used in the TA experiments. We also correct the incoming photon fluence  $J_0$  for absorption throughout the solution:

$$J'_0 = \frac{1 - e^{-\alpha L}}{\alpha L} J_0 \quad 5.17$$

with  $J'_0$  the average of the photon fluence across the solution length. Figure 5.13 shows the fit of  $|\Delta A_{1-3\text{ ns}}|$  with equation 5.16.

### Obtaining the fractional bleach in fs-TA and correcting for Poissonian excitation

To acquire the fractional bleach in the fs-TA experiment, i.e.  $\Delta A/A_0$ , we averaged the band-edge bleach from 596.5 nm to 697.5 nm. To acquire the correct value for  $A_0$ , we fitted the steady-state absorption spectrum to a set of Gaussians, and averaged the fitted Gaussian of the BE transition over the same spectral range as the BE-bleach in TA. In order to compare the experimentally obtained fractional bleach at an average exciton population to a calculated fractional bleach, we corrected for Poissonian excitation statistics:

$$\frac{\Delta A}{A_0} = \sum_{n=0}^{\infty} P(n, \langle N \rangle) * \frac{\Delta A(n)}{A_0} \quad 5.18$$

With  $P(n, \langle N \rangle)$  the Poissonian distribution of excitons throughout the sample, i.e. the chance of finding  $n$  excitons/QD when the average exciton populations equals  $\langle N \rangle$ . We run the summation over  $n$  over the first 20 excitons, since the populations of higher excitonic states become negligible.  $\Delta A(n)$ , the bleach magnitude as a function of the number of excitons was calculated as explained throughout the main text.

### Fit of the spectroelectrochemical measurements of CdTe QD film

We attribute the shape of the differential absorption changes at the BE energy of CdTe QD films to a superposition of a BE bleach feature and a Stark-effect induced derivative-like feature. The latter is due to the presence of trapped carriers, electrostatically shifting the energy of the BE transition without directing populating the BE states. The total fit function used to describe the data is given by:

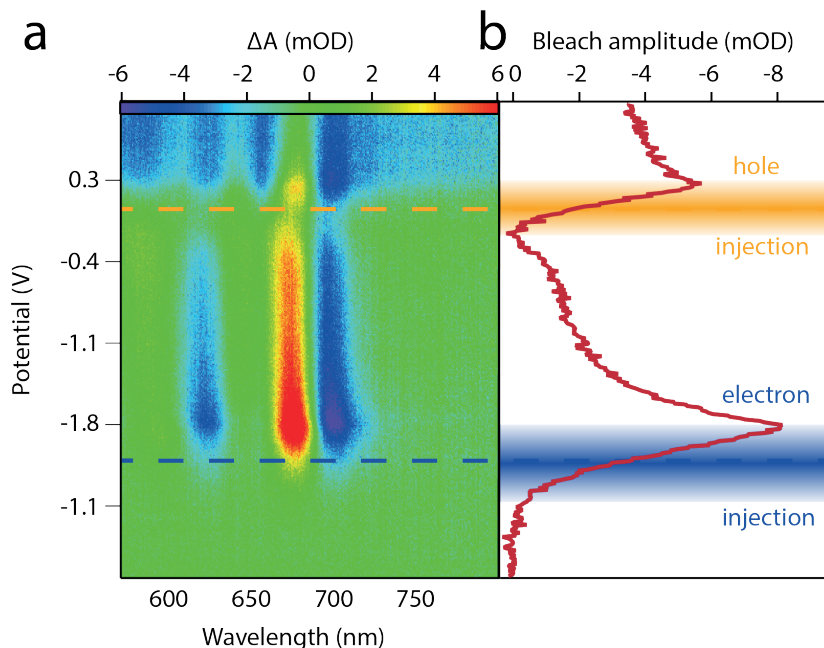


**Figure 5.14. Potential-dependence of the bleach amplitude in a spectroelectrochemical measurement of CdTe QD film.** **a**, Colormap showing the potential dependence of the differential absorbance of a CdTe QD film. **b**, Amplitude of the Gaussian component of the fit function, plotted as a function of the applied potential. The plot shows clearly the presence of two potential regions of bleach increase: one at negative potential, corresponding to electron injection, one at positive potential, corresponding to hole injection.

$$f_{fit}(\lambda) = A_g e^{-\frac{(\lambda-\lambda_0)^2}{2\sigma^2}} + A_{sh} \left( e^{-\frac{(\lambda-\lambda_0-\lambda_{sh})^2}{2\sigma^2}} - e^{-\frac{(\lambda-\lambda_0)^2}{2\sigma^2}} \right) + y_0 + a\lambda \quad 5.19$$

with  $A_g, \lambda_0, \sigma, A_{sh}, \lambda_{sh}, y_0$  and  $a$  used as fitting parameters. The last two terms of the function describe the slowly varying linear background, typically observed in spectroelectrochemical measurements of QD films (See Supporting Information in Boehme *et al.*<sup>54</sup>).

Figure 5.14a shows a colormap of the differential absorbance of a CdTe QD film. To extract the potential-dependence of the bleach amplitude, we fitted each differential absorbance spectrum, obtained at a fixed potential. Figure 5.14b shows the potential dependence of the amplitude of the bleach component. The bleach amplitude increases both for negative potentials and for positive potentials. As the Open-Circuit Voltage in the system was -0.5 V, the two potential regions correspond, respectively, to the electron and hole injection. This demonstrates that the BE bleach in CdTe QD has contributions from both electrons and holes.

### Modelling the effect of hole trapping on the ingrowth of the TA signal at short delay times

We do not see a decay of the band-edge bleach upon 1S and 2S excitation of the CdSe core-only QDs. We interpret this to mean that the hole trapping rate is faster than our Instrument Response Function. To give an upper estimate of the hole trapping time, we model the effect of ultrafast hole trapping on the ingrowth of the TA signal after optical excitation by convolving a Gaussian function, which serves as our IRF, with the sum of a hole and electron contributing term:

$$I(t, t_0, \tau_{\text{trap}}) = e^{-\frac{(t-t_0)^2}{2\sigma_{\text{IRF}}^2}} * \left( \frac{1}{3} e^{-\frac{t-t_0}{\tau_{\text{trap}}}} \theta(t, t_0) + \frac{2}{3} \theta(t, t_0) \right) \quad 5.20$$

We use a characteristic width of the instrument response time  $\sigma_{\text{IRF}}$  of 55 fs, as obtained on the TA data of the core-only CdSe QDs. The second half of the function is built up out of two parts; a hole contribution term, which has an amplitude of 1/3, a decaying exponential with a characteristic hole trapping time  $\tau_{\text{trap}}$ , which is multiplied with the Heaviside step function. The second half contains the electron contribution, with an amplitude of 2/3, multiplied with the Heaviside step function. We varied the trapping time in Figure 5.15. A characteristic time for hole trapping of roughly 30 fs is required to

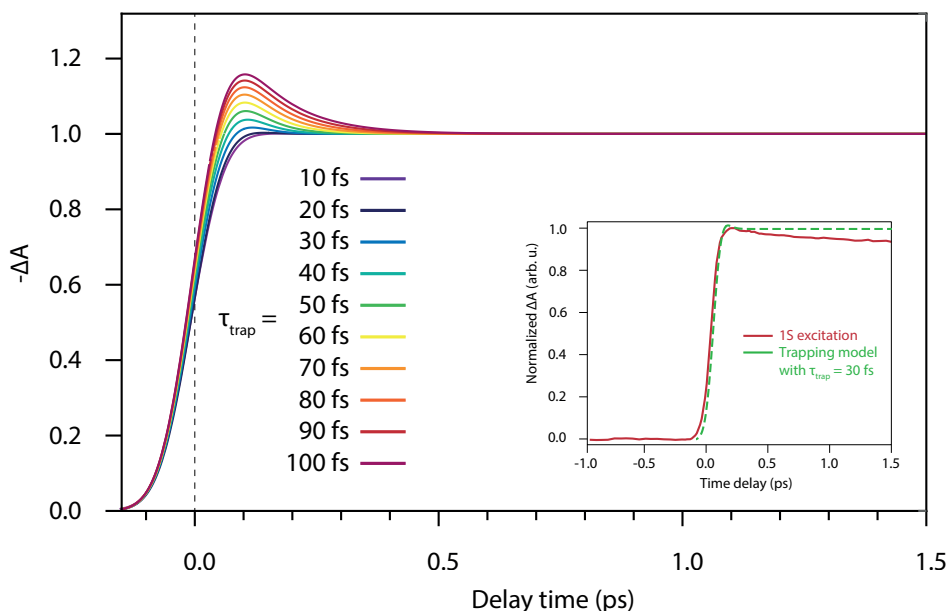


**Figure 5.15. Modelling the dynamics of the BE bleach with different hole trapping times  $\tau_{\text{trap}}$ .** The IRF is modelled as a Gaussian function, which is convolved with an exponentially decaying function to describe the hole trapping. The inset shows the experimental data from Figure 5.4 in the main text, on which the function with the 30 fs trapping time is superimposed.

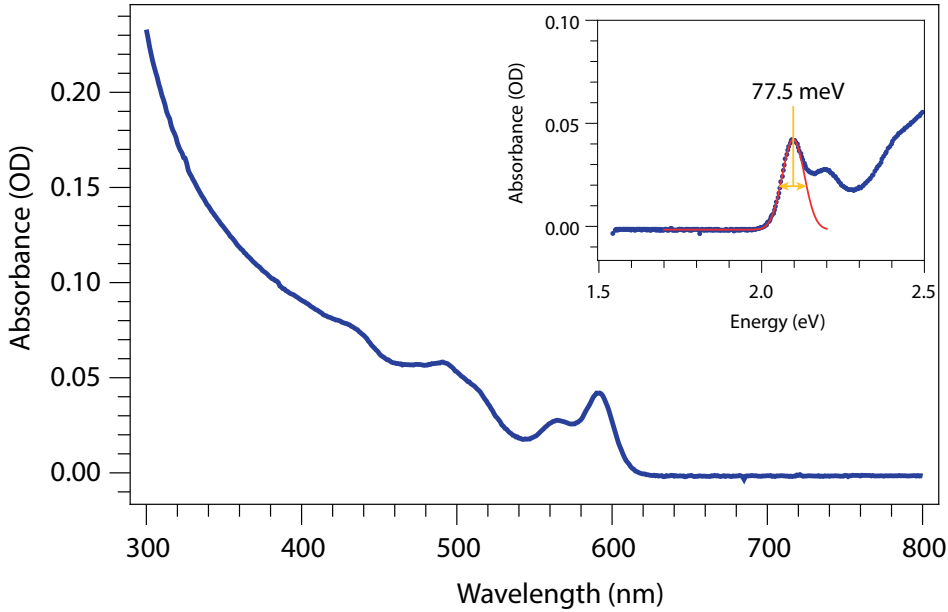


**Figure 5.16. Steady-state absorption spectrum of the CdSe core QDs.** The inset shows the same absorption spectrum plotted versus photon energy. The  $\sigma$  of the 1S transition equals 32 meV. According to the Heisenberg principle, a trapping time of 30 fs would lead to a broadening of the peaks  $\Delta E$  of roughly 11 meV.

more-or-less have an instantaneous ingrowth of the signal (broadened by the IRF).

### Independence of the relative hole contribution to the exciton bleach on angular momentum selection rules

In the transition-counting model employed in the main text, all transitions between hole and electron states are allowed. However, angular momentum selection rule for optical transitions should allow only transitions for which the change in the projection of the total angular momentum along a given axis,  $M$ , is equal to the projection of the total angular momentum of the photon.

For linearly polarized light, the quantum number for the total angular momentum of the photon,  $L$ , and the quantum number for its projection along the  $z$ -axis,  $M$ , are respectively 1 and 0. Thus, only transitions involving  $\Delta L=1$  and  $\Delta M=0$  will be allowed. For the transitions between the hole states and the electron states this implies the only allowed transitions are transitions from the  $M=\pm 1/2$  state of the hole to the  $M=\pm 1/2$  state of the electron. In the transition-counting model, considering the same oscillator strength for the two transitions, we can express the steady-state absorption as:

$$A_0 = A(h=1/2, e=1/2) + A(h=-1/2, e=-1/2) = 2A^* \quad 5.21$$

In the presence of an exciton, different excited-state absorption values will be obtained for different location of the hole in the four available states. If the hole is populating states with  $|M| = 3/2$ , then the absorption is affected only via state filling of one of the electron states:

$$A'(h = \pm 3/2) = 2A^* - A^* = A^* \quad 5.22$$

If the hole is in the  $|M|=1/2$  states, then either both transitions are blocked by state-filling (electrons and holes have different  $M$  quantum numbers) or the sum of state filling and stimulated emission leads to no absorption:

$$A'(h = \pm 1/2) = 2A^* - 2A^* = 0 \quad 5.23$$

Upon 2S excitation, the hole has equal probability to cool in any of the four hole states. Thus, the excited state absorbance for a population of QDs excited in resonance with the 2S absorption is going to be an average of the 4 possible hole configurations:

$$A'_{ex} = \frac{A^* + A^* + 0 + 0}{4} = \frac{A^*}{2} \quad 5.24$$

The differential absorbance of the QD population in the presence of one exciton per QD will then be:

$$\Delta A_{ex} = \frac{A'_{ex} - A_0}{A_0} = -\frac{3}{4} A^* \quad 5.25$$

In the presence of only a hole, one more transition is allowed for each hole configuration:

$$A'(h = \pm 3/2) = 2A^* \quad 5.26$$

$$A'(h = \pm 1/2) = 2A^* - A^* = A^* \quad 5.27$$

$$A'_h = \frac{2A^* + 2A^* + A^* + A^*}{4} = \frac{3}{2} A^* \quad 5.28$$

The difference absorbance for one hole per QD is given by:

$$\Delta A_h = \frac{A'_h - A_0}{A_0} = -\frac{1}{4} A^* \quad 5.29$$

from which follows:

$$\Delta A_{\text{ex}} / \Delta A_{\text{h}} = 3 \quad 5.30$$

We can conclude then that in the presence of angular momentum selection rules the hole contribute to 1/3 of the exciton bleach, exactly the same number computed in the absence of selection rules.

### Comparing different fit strategies for the determination of the band-edge bleach

In order to disentangle the 1S bleach from the background of TA features, we fitted the TA signals around the band-edge energy with two Gaussians, representing respectively the 1S and 2S bleach features. While the 1S bleach is well described by a single Gaussian, the spectral overlap of multiple TA features around the energy of the 2S transition complicates the assignment of the spectral shape of the 2S bleach. To assess the effect of imperfect description of the 2S bleach shape on the determination of the 1S bleach, we repeated the fitting of the TA response employing a single Gaussian feature. Since the TA response deviates from the single Gaussian shape on the high-energy side of the 1S bleach, the spectral range of the fit was limited to the low-energy side of the 1S bleach and a small portion of the high-energy side. For the core/shell/shell sample, the fitting range extended from 610 nm to 670 nm, while for the core-only sample the fitting range extended from 585 nm to 637 nm. The central wavelength of the standard deviation of the Gaussian peak was determined via a fit of the single TA spectral cut, and held constant in the subsequent global fit of the full TA measurement. For the core/shell/shell sample, the parameters of the Gaussian feature are:

$$\begin{aligned} \lambda &= 615.0 \pm 0.1 \text{ nm} \\ \sigma &= 9.4 \pm 0.1 \text{ nm} \end{aligned} \quad 5.31$$

For the core-only sample, the parameters of the Gaussian feature are:

$$\begin{aligned} \lambda &= 592.63 \pm 0.04 \text{ nm} \\ \sigma &= 8.73 \pm 0.05 \text{ nm} \end{aligned} \quad 5.32$$

Figure 5.17a-d shows the comparison between the 1S bleach amplitude extracted from a fit employing two Gaussians (continuous red lines) and a fit employing one Gaussian (dashed black lines). The two fit procedures yield very similar results, with minor differences in the bleach amplitude and the same signal dynamics. We can conclude that our analysis of the hole contribution to the 1S bleach is largely unaffected by the precise account of the 2S bleach.

### Phonon-related oscillation in the band-edge bleach of CdSe QDs upon resonant 1S excitation

In the first picoseconds after photoexcitation, the dynamics of the BE bleach is affected by signal oscillations. Figure 5.18a shows the bleach oscillations for the un-passivated cores and for the  $\text{InCl}_3$ -treated cores, obtained subtracting the experimental signal from

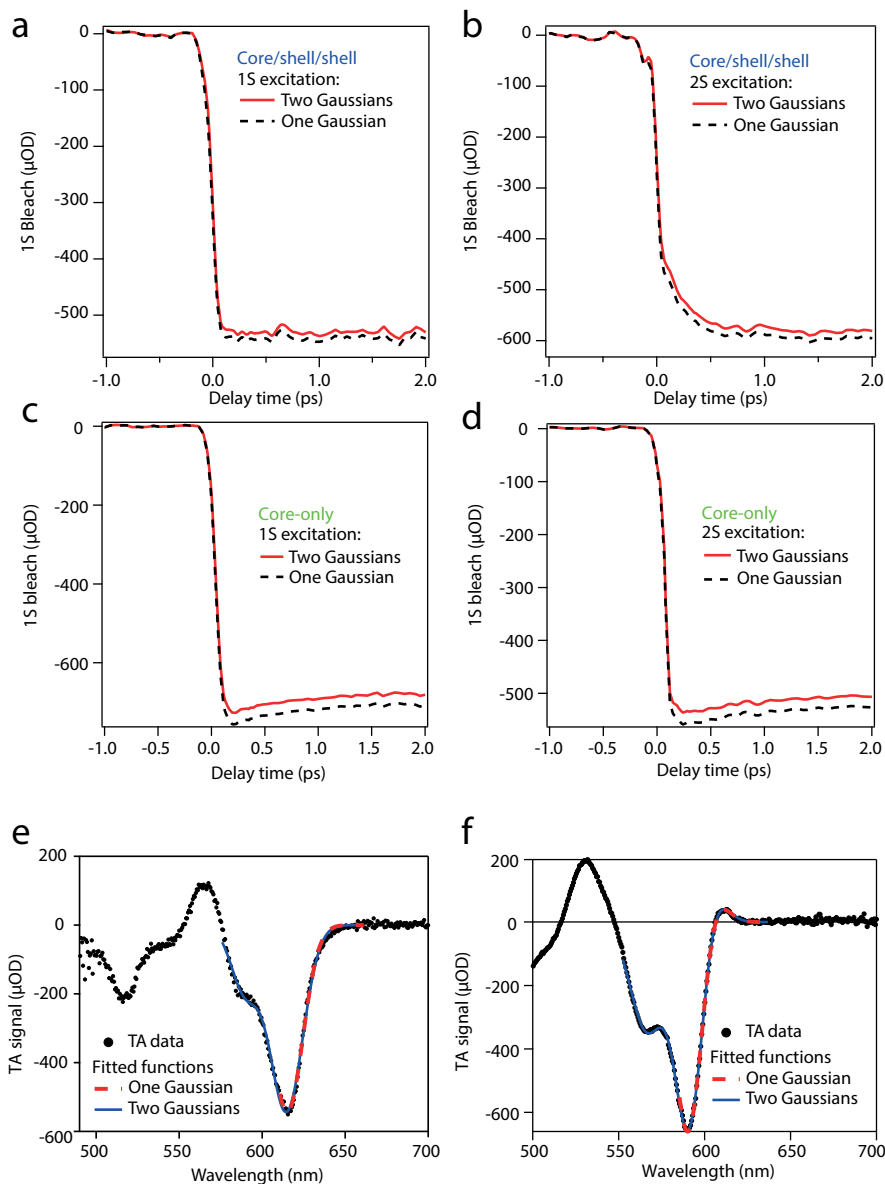


**Figure 5.17. Effect of 2S fit on the determination of the 1S bleach.** **a**, Time-dependence of the bleach dynamics for the core/shell/shell sample excited resonantly with the 1S transition, obtained from a fit of the TA measurement with two Gaussians (continuous red line) or with one Gaussian feature (dashed black line). Panels **(b-d)** show the same time-dependence of the 1S bleach estimated with the two fitting approaches, obtained for 2S excitation of the core/shell/shell sample **(b)**, 1S excitation of the core-only sample **(c)**, and 2S excitation of the core-only sample. Panels **(e-f)** show the comparison between the fitted functions and the TA data, for the core/shell/shell sample **(e)**, and for core-only sample **(f)**, highlighting that both fit functions describe correctly the 1S bleach.

the result of a bi-exponential fit. The presence of oscillatory modulation in transient absorption measurements has been observed in numerous studies<sup>46,48,55</sup>, and has been associated with the excitation of longitudinal optical (LO) and longitudinal acoustic (LA) phonons in the QDs. Figure 5.18b shows the result of a Fourier analysis on the oscillatory signal, showing the presence of a strong frequency components at  $212\text{ cm}^{-1}$  and  $16\text{ cm}^{-1}$ , in agreement with previous measurements of LO and LA phonon frequency in CdSe QDs<sup>47</sup>. In particular, Tyagi *et al.*<sup>55</sup> have identified trapping of holes on the surface of CdSe QDs as the mechanism that launches the LA phonon oscillations, occurring on a sub-ps timescale, in line with our interpretation of the hole dynamics in core-only CdSe QDs.

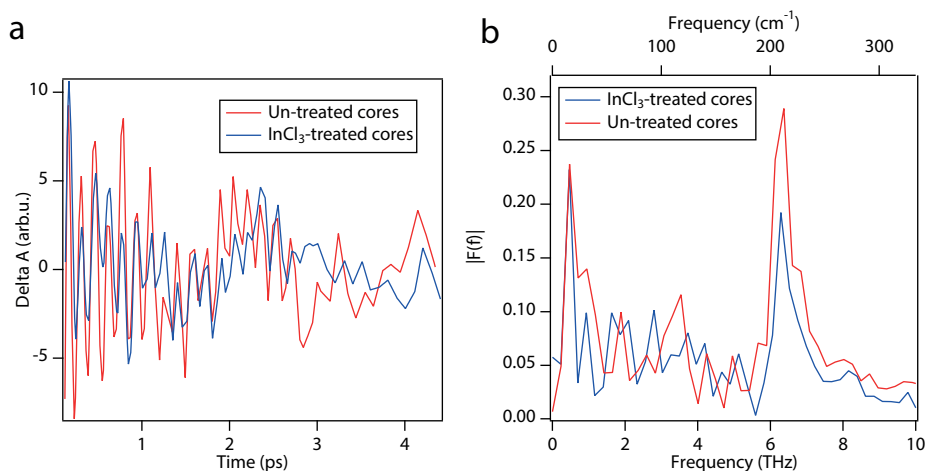


**Figure 5.18. BE-bleach oscillations upon 1S excitation of core-only QDs.** **a**, Time-dependence of the bleach oscillations, obtained subtracting a bi-exponential fit from the bleach signal. **b**, Fourier analysis of the oscillation in (a), showing the presence of two dominant frequency component, at  $16\text{ cm}^{-1}$  and  $212\text{ cm}^{-1}$ .





# Chapter 6

## Kinetic Monte Carlo modelling of temperature dependent spectral diffusion in InP QD films

### *Abstract*

Controlling and understanding carrier transport in quantum-dot (QD) solids is of both applied and fundamental interest. Here we apply Kinetic Monte Carlo (KMC) modelling of spectral diffusion in transient absorption data on conductive InP QD solids to extract the charge carrier mobilities. These mobilities are benchmarked with time-resolve microwave conductivity measurements on the same films. The comparison reveals a satisfactory agreement between the two approaches, with extracted mobilities within a factor  $\sim 5$  in films with different ligand treatments and mobilities spanning three orders of magnitude for various ligand treatments. This validates the use of KMC to study carrier transport in QD solids.

Using both KMC and TRMC, the carrier mobility in InP QDs is shown to be temperature deactivated. We discuss the causes of the mobility trend, suggesting that describing the hopping process in the context of the Marcus charge transfer model provides a closer description for the measured temperature trends, therefore proving the importance of a detailed description of the hopping process in the context of temperature-dependent mobility studies.

Our results provide experimental confirmation of the validity of the KMC-modeling approach to mobility estimates in QD solids, while shedding light on the nature of the temperature-dependent trends reported with this approach.

Based on: Gianluca Grimaldi, Jaco J. Geuchies, Ward van der Stam, Indy du Fossé, Baldur Brynjarsson, Nicholas Kirkwood, Sachin Kinge, Laurens D.A. Siebbeles, Arjan J. Houtepen. *Nano Letters*, 2019, 19 (5), 3002-3010.

## 6.1 Introduction

Colloidal quantum dot (QD) solids are a promising system for development in optoelectronic applications, with applications in transistors<sup>1-3</sup>, solar cells<sup>3-5</sup>, LEDs<sup>3, 6-7</sup> and photodetectors<sup>3, 8-10</sup>. The potential of QD materials for devices is often limited by the properties affecting charge transport within QD solids. In particular, suboptimal carrier mobility leads to significant losses in QD based solar cells, impacting the diffusion length of carriers, limiting the optimal thickness of the devices and thus putting an upper limit to the amount of sunlight absorbed.

Spectroscopic investigation of QD solids allows to obtain information on the material properties before optimization of a working QD-based device, thus allowing fast screening of possible material candidates. Recent developments by Gilmore *et al.*<sup>11</sup> have shown the possibility to estimate carrier mobilities from Transient Absorption (TA) measurements, using a Kinetic Monte-Carlo (KMC) model for carrier diffusion to fit the experimental data. This approach allows to extract useful information about carrier transport in QD solids from a facile and contact-less measurement, and has been quickly adopted in studies of QD electronic transport<sup>12-13</sup>.

Despite the rapid adoption of this spectroscopic approach, to date no direct comparison has been performed between mobility estimates obtained from the KMC-modeling approach and alternative contact-less techniques. Spectroscopic techniques such as Time Resolved Microwave Conductivity (TRMC) or Terahertz conductivity have been established as a reliable approach to contact-less mobility estimate, probing carrier motion on a local scale. Assessing the validity of the KMC-based mobility estimate *via* comparison with one of these techniques would provide important insights over the reliability of the information extracted from KMC-modeling.

Furthermore, Gilmore *et al.* have shown a temperature deactivated behavior of mobilities in PbS QD films obtained with the KMC-modeling of cryogenic TA measurements<sup>12</sup>. Very recently, Chen *et al.* have also observed a temperature deactivated mobility extracted from similar analysis of TA measurement on PbS QD solids heated up to 150°C<sup>14</sup>. In both studies, the observed mobilities were not sufficiently high to explain the effect in terms of a transition to band-like transport and were rather explained by a reduction of the interparticle distance induced by a contraction of the ligand shell. Although both reports highlight the possibilities of changes in the QD spacing as the major factor for the temperature dependence, further characterization is needed to pinpoint the source of this behavior.

In this study, we present a direct comparison between charge carrier mobilities extracted from KMC-modeling of TA measurements and TRMC measurements. We performed TA and TRMC measurements on InP QD samples capped with short, conductive ligands, leading to conductive QD samples with TRMC mobilities spanning three orders of magnitude. We extracted mobility estimates by a fit of a KMC model to the TA data, and compared the obtained mobilities to the estimates provided by the TRMC measurements. We find good, but not perfect, agreement between the two techniques, reproducing the same order of magnitude for the mobility in all the samples characterized. This validates

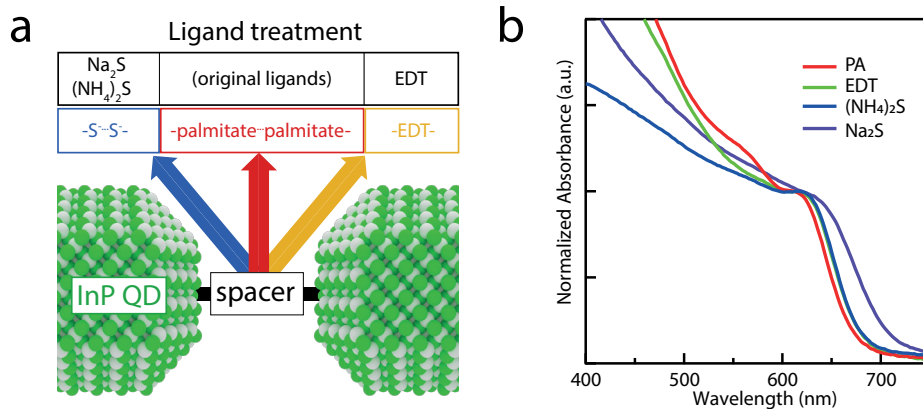


**Figure 6.1. Conductive InP QD films via ligand exchange.** **a**, Scheme representing the different ligand treatments employed to functionalize the QD surface, indicating the QD spacers provided by each treatment. **b**, steady-state absorption spectra of the films, showing the presence of broadening and redshift of the first absorption feature for the ligand-treated films.

the KMC modelling of TA data to estimate the charge carrier mobilities, although it also demonstrates further improvements of the KMC modelling are possible.

Furthermore, we characterized the temperature dependence of KMC- and TRMC-mobilities in the InP QDs solids. In line with the recent results mentioned above on PbS QD solids we observe with both measurement techniques a temperature deactivation of carrier mobility, in a wide range of samples. We discuss this temperature dependent mobility showing first in a quantitative way that the trend cannot be explained by a Miller-Abrahams description of carrier hopping with constant interparticle distance. However, employing a Marcus description for electron transfer rates in the system, we show an enhanced agreement with the observed temperature trend. In this case we do not need to invoke a change of the interparticle distance to describe the observed trend in mobility. This demonstrates the importance of a detailed description of the charge transfer mechanism. Our results confirm the possibility to provide meaningful estimates of carrier mobilities *via* the KMC-modeling approach, for constant and varying temperature. Furthermore, they shed light into the nature of temperature-dependent mobilities observed in literature, providing insights to improve current KMC-based approaches to mobility estimates.

## 6.2 Film preparation

Conductive InP QD films were obtained *via* ligand exchange of the palmitate ligands present on the QD surface after synthesis for shorter ligands, as described in our previous work.<sup>15</sup> The scheme in Figure 6.1a shows the ligand treatment used in this study, highlighting the QD spacer delivered by each ligand treatment. Figure 6.1b shows the effect of the different ligand treatments on the absorption spectra. The first absorption feature of the ligand exchanged films are broadened and redshifted with comparison to the palmitate capped sample, as typically observed for films ligand exchanged with small linkers<sup>16-19</sup>.

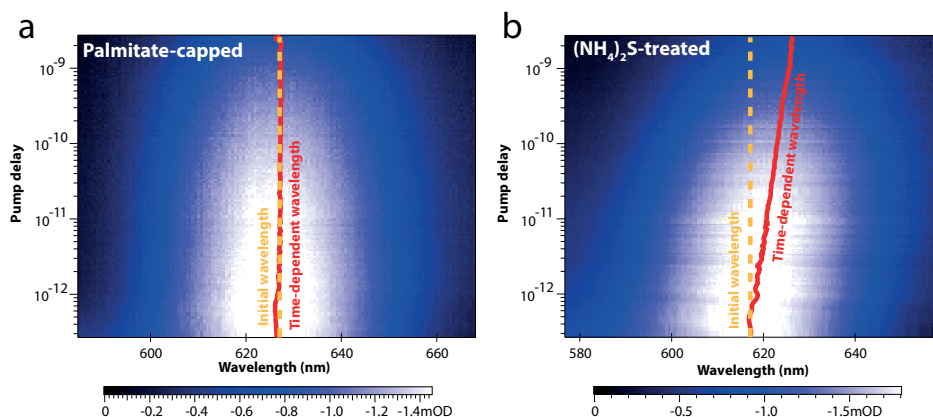


**Figure 6.2. Transient Absorption (TA) red-shift of first absorption feature.** a,b) TA colormap showing the differential absorbance of InP QD films: a) the as-synthesized palmitate-capped QDs (PA) and b) QDs treated with ammonium sulfide ( $(\text{NH}_4)_2\text{S}$ ). Dashed-orange lines indicate the initial position of the bleach central wavelength, while the red lines show the time-dependence of the bleach wavelength. While PA-capped QDs show change in the bleach wavelength, a significant red-shift is observed for the  $(\text{NH}_4)_2\text{S}$ -treated film.

## 6

### 6.3 Transient absorption measurements on InP QD films

We performed TA measurements on InP QD solids capped with palmitate ligands, with ethanedithiolate ligands (EDT), or treated with sulfur salts ( $\text{Na}_2\text{S}$ ,  $(\text{NH}_4)_2\text{S}$ ) to provide  $\text{S}^-$  ions on the QD surface. To avoid multi-excitonic effects, the measurements were performed in the low-power regime, with an average number of excitons per QD,  $\langle N \rangle$ , much smaller than one.

Figure 6.2a and 6.2b show TA colormaps for the PA-capped and  $(\text{NH}_4)_2\text{S}$ -treated sample, showing the presence of a negative change in absorbance at the band-edge energy of the InP QDs, called a band-edge bleach. While the two measurements show a similar decay of the bleach in time, the position of the bleach in the  $(\text{NH}_4)_2\text{S}$ -treated sample shows a redshift in time, while the bleach position is constant for the PA-capped sample. The red lines in Figure 6.2a and 6.2b show the center of a Gaussian function fitted to the bleach signal, while the dotted orange line marks the initial position of the bleach after photoexcitation. The central bleach wavelength for the  $(\text{NH}_4)_2\text{S}$ -treated sample at the end of the 3 ns time-window differs significantly from the initial value, while no appreciable change is observed for the PA capped sample.

The redshift of the band edge bleach feature, also called spectral diffusion, is commonly observed in disordered conductive materials<sup>11, 20-23</sup> and its cause is depicted schematically in Figure 6.3 for a QD solid. Due to quantum confinement, large QDs have a lower energy for electrons (and holes) than smaller QDs. This, and other sources of disorder (e.g. electrostatic disorder) gives rise to a fluctuation in energy levels. As carriers move through the film, downwards energy transitions are favored over upwards energy transition, since

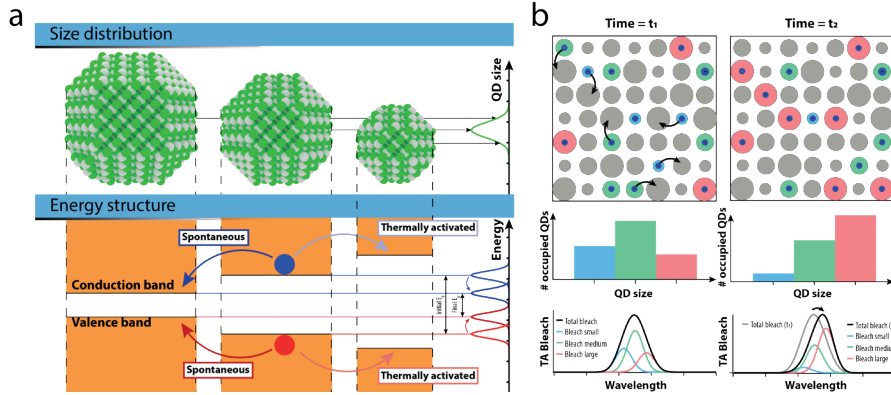


**Figure 6.3. Effect of electron diffusion on the absorption bleach.** **a**, Schematic of the effect of particle size on the conduction and valence band energies. Due to the difference in hopping rates between upwards and downwards energy steps, electrons will preferentially hop to larger (lower band-gap) QDs. **b**, Schematics of the effect of electron diffusion on a uniformly excited QD population. As carrier hop preferentially towards larger QDs, the distribution of occupied QDs shifts towards larger QD sizes. The absorption bleach of the entire population is given by the sum of the bleaches of the different QD sizes. As time passes, the larger QDs constitute a higher fraction of the occupied QDs, and consequently the total bleach shifts towards lower energy (higher wavelength) values.

the latter require heat absorption from the surrounding medium. Figure 6.3b shows a 2D scheme exemplifying the effect of this asymmetry in transition rate on the distribution of carriers in a photoexcited QD solid. While initially distributed randomly throughout the film, after a certain time carriers will preferentially occupy the largest, smaller band-gap QDs, bleaching the absorption from the large QDs more than the rest of the population. As a result, the total bleach shift towards lower energy. How quickly this happens, and hence what the timescale is of the spectral diffusion, depends on the mobility of electrons and holes.

## 6.4 Monte Carlo modelling of TA energy shifts

To relate the observed spectral diffusion of the band-edge bleach to the charge carrier mobility we used Monte Carlo modeling of electron hopping.<sup>11</sup> The QD film is represented in the simulation by lattice sites with randomly assigned energies following a Gaussian distribution. The rate constant of electron hops between QDs are set by a Miller-Abrahams model:

$$k = k_0 \begin{cases} \exp\left(-\frac{E_f - E_i}{k_b T}\right), & \text{for } E_f > E_i \\ 1, & \text{for } E_f \leq E_i \end{cases} \quad 6.1$$

where  $E_i$  and  $E_f$  are the initial and final energy of the carrier. For simplicity the TA signal is assumed to be entirely due to the electron, motivated by the lower degeneracy of electron

band-edge states in InP QDs<sup>24</sup>, and the simulation models the diffusion of the electron alone. Electron diffusion is simulated by evolving the system in time with a Kinetic Monte Carlo scheme (see Methods), keeping track of the electron energy as it hops to different sites. Averaging over numerous electron trajectories allows to reconstruct the energy evolution of the electron population. The calculated energy shifts can then be fitted to the experimental redshifts, optimizing for the hopping prefactor  $k_0$  and for the width of the electron's energy distribution,  $\sigma$ .

Figure 6.4a shows the comparison between the experimental (continuous lines) and the computed (dotted lines) energy shifts for EDT-capped, Na<sub>2</sub>S-treated, and (NH<sub>4</sub>)<sub>2</sub>S-treated samples. The fit shows a very good agreement for the EDT-capped sample, while the higher conductivity S<sup>-</sup>-capped samples show deviation from the computed behavior, likely associated with neglected contributions to the bleach dynamics (i.e. hole contribution to the bleach, and excitonic effects) or an energy landscape that is more complicated than the single Gaussian function that is used in the modelling. The best values for the fitting parameters are shown in Table 6.1. The best values for the width of the energy distribution  $\sigma$  are in line with values obtained by Gilmore *et al.* for PbSe QDs<sup>11</sup>, but appear to be lower than the width of the first absorption feature of the InP QD films, 130 meV for the EDT and (NH<sub>4</sub>)<sub>2</sub>S sample and 150 meV for the Na<sub>2</sub>S sample. The total width of the first absorption feature is broadened with respect to the width of the energy distribution by the convolution with the homogenous absorption linewidth. Furthermore, the presence of excitons, not contributing to spectral diffusion, would reduce the estimate of  $\sigma$  (See Appendix for a discussion of the effects of excitons on the spectral shift).

6

**Table 6.1.** Best values for the fit parameters of the KMC model.

	EDT	Na <sub>2</sub> S	(NH <sub>4</sub> ) <sub>2</sub> S
$k_0$	$2.33 \pm 0.15 \cdot 10^8$	$1.20 \pm 0.09 \cdot 10^{10}$	$8.7 \pm 0.8 \cdot 10^9$
$\sigma$	$13.7 \pm 0.2$	$20.98 \pm 0.13$	$23.6 \pm 0.2$

During the simulations, we kept track of the electron mean square displacement (MSD) during each trajectory. Once the electrons have reached thermal equilibrium, their motion can be described by a stochastic walk, for which the MSD should increase linearly with time, following the relation:

$$MSD = 6Dt \quad 6.2$$

where  $D$  is the diffusion coefficient. Hence the linear increase of the MSD indicates thermal equilibrium has been established and the slope of the MSD vs. time gives the diffusion coefficient. Finally, the mobility can be extracted from Einstein-Smoluchowski equation, valid at thermal equilibrium:

$$\mu = \frac{eD}{k_b T} \quad 6.3$$

where  $e$  is the elementary charge. Figure 6.4b shows the MSD as a function of time

computed for the EDT, Na<sub>2</sub>S, and (NH<sub>4</sub>)<sub>2</sub>S samples using optimized values for the fitting parameters, together with the fit obtained using eq. 6.2 (dotted lines). The faster dynamics of the spectral diffusion observed for the S<sup>-</sup>-capped samples translates into a faster growth of the MSD, and consequently into a higher mobility. The extracted mobilities are shown as the green bars in Figure 6.4c. We obtained a mobility of 1.7·10<sup>-3</sup> cm<sup>2</sup>/(V·s) for the EDT treated sample, 60·10<sup>-3</sup> cm<sup>2</sup>/(V·s) for the Na<sub>2</sub>S-treated sample, and 39·10<sup>-3</sup> cm<sup>2</sup>/(V·s) for the (NH<sub>4</sub>)<sub>2</sub>S-treated sample.

## 6.5 Comparison between TRMC and KMC mobility estimates

To assess the validity of the KMC analysis, we compared the mobility estimates obtained above with those obtained from the well-established TRMC approach (see Method section). In TRMC spectroscopy, the absorption of microwave radiation by free charges in the sample is related to the photoconductivity of the free charges. This technique has been applied to a broad range of semiconductor materials<sup>25-28</sup>, including QD solids<sup>29-32</sup>. Recently we have performed an extensive TRMC study on films of InP QDs with the same ligand treatments that were used above for the TA measurements<sup>15</sup>. Figure 6.4c shows a comparison of the electron mobilities estimated with the KMC model (green bars) and the sum of electron and hole mobilities estimated from TRMC measurements (red bars). From the figure, it is clear that both measurements give similar mobility values and that both reproduce the trend of a decreasing mobility with increasing ligand length.

One can observe that the KMC estimate is generally somewhat higher than the TRMC estimate. To account for the differences between the two datasets, we need to focus on the way the approximations entering mobility estimates in the two approaches. In our previous work on InP QD films, we reported evidence of carrier trapping for low fluence measurements. As TRMC signals provide a measurement of the product between the sum of the carrier mobility and the yield of free carriers, assumption on the values of the free carrier yield need to be made in order to extract mobility estimates. The TRMC mobilities shown in Figure 6.4c assume unity free carrier yield, thus providing a lower limit for the sum of the electron and hole mobilities. Any carrier recombination or trapping process occurring within the rise time of the TRMC signal (12 ns) reduces the value of the TRMC mobility estimate compared to the true carrier mobility.

To quantify the effect of charge carrier trapping on the TRMC mobilities, we obtained an estimate of the fraction surviving carriers from the decay of the bleach signal in the TA experiments. A biexponential decay function plus a constant background was fitted to all TA traces:

$$\Delta A = y_0 + A_1 \exp\left(-\frac{t}{\tau_1}\right) + A_2 \exp\left(-\frac{t}{\tau_2}\right) \quad 6.4$$

The lifetimes obtained for the decay components are ~100 ps and ~1 ns (See Appendix, Figure 6.6), which is much shorter than the time-resolution of the TRMC measurement. Thus, we assume that carriers involved in the decay processes observed in the bleach

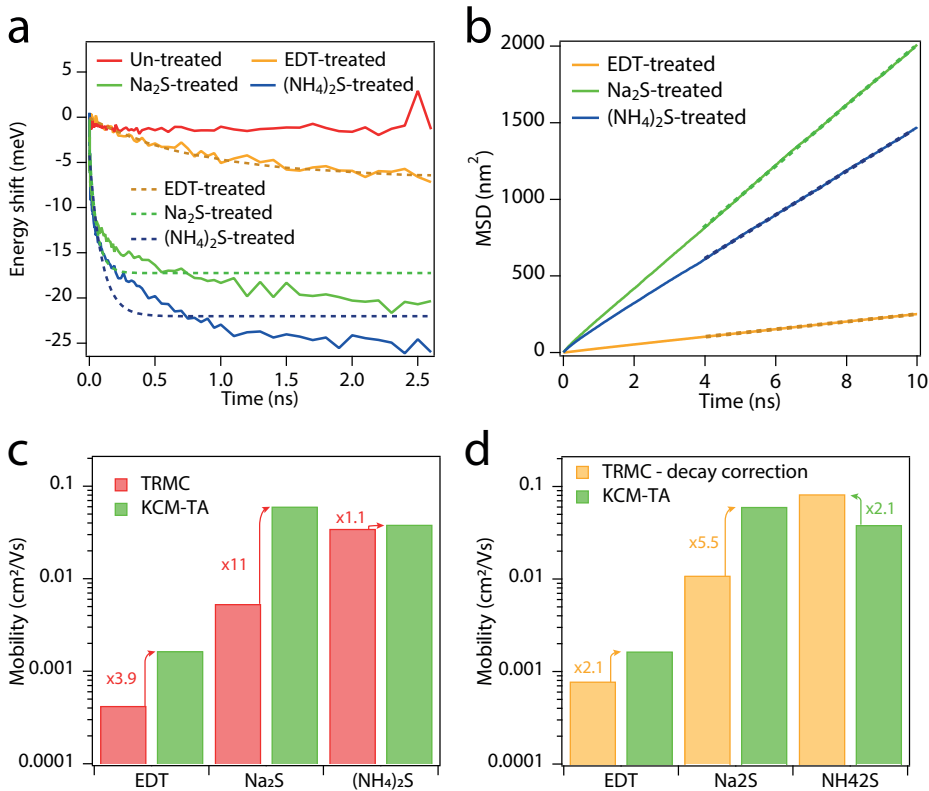


**Figure 6.4. Kinetic Monte Carlo (KMC) modelling of TA redshifts.** **a**, Comparison between experimental energy shift and the energy shift obtained from a fit of the KMC model to the experimental data. The PA-capped sample was not fitted due to lack of a significant redshift. **b**, Mean square displacement (MSD) obtained for the KMC fits of the samples exhibiting redshift. The thermalized long time increased of the MSD is fitted to obtain the diffusion coefficient and the mobility in the system. **c**, Comparison between the mobilities obtained by the KMC modeling of TA data and from TRMC measurements. **d**, Comparison between the TA mobility estimates and TRMC mobilities corrected for the sub-resolution signal decay inferred from the TA measurements. The correction leads to a remarkable agreement between the TRMC and TA estimates for the EDT and  $(\text{NH}_4)_2\text{S}$  samples (i.e.: a factor 2 difference between the two measurements), and a larger discrepancy for the  $\text{Na}_2\text{S}$  sample (i.e.: a factor 5 difference).

signal do not contribute to the TRMC signal. The ratio between the amplitude of the constant component  $\gamma_0$  and the initial bleach amplitude gives the fraction of the initially photogenerated charges contributing to the TRMC signal. Figure 6.4d compares KMC-TA mobilities with the TRMC mobilities rescaled by the estimated carrier yield, showing an improved agreement between the two mobilities for the EDT and  $(\text{NH}_4)_2\text{S}$  samples.

In comparing TA and TRMC mobilities we relied on the assumption that both estimates are dominated by the electron contribution. The hole contribution is assumed to be negligible on grounds of the prevalent electron contribution to the bleach<sup>24</sup> and the high ratio between the hole and electron effective mass in InP<sup>33</sup> suggesting a higher electron

mobility due to a higher tunneling rate between neighboring QDs<sup>34</sup>. However, our recent observation of a hole contributions to the band-edge bleach of cadmium chalcogenides<sup>35</sup>, with a band structure similar to InP QDs, suggests hole diffusion might contribute to the bleach redshift. Furthermore, the dynamics of excitons dissociation during the TA measurements might affect the observed spectral diffusion, and is not accounted in our model. Lastly, we considered a Gaussian distribution of the QD energies, but the energies of the QD population might be following another type of distribution, which would affect the shape of the calculated spectral diffusion. Indeed, the deviation of the S-capped spectral diffusion from the fitted behavior (see Figure 6.4a) suggest that hopping of a single carrier species in a Gaussian energy landscape does not fully capture the spectral diffusion. However, the good quantitative agreement between TRMC and KMC estimates suggests that the simple KMC model is sufficient to capture the main transport properties of carriers inside the QD solids we characterized.

Summarizing, although quantitative differences are observed between the KMC-TA and TRMC approach for mobility estimates in QD solids, overall the two methods yield comparable results, confirming that reliable measurements of carrier mobilities in QD solids can be obtained from KMC modelling of TA measurements.

## 6.6 Temperature dependence of carrier mobility

We performed TA measurements as a function of temperature between 77K and 293K, monitoring the spectral diffusion. Figure 6.5a shows the effect of temperature on the time-dependent energy shift measured for the sample treated with EDT (thin lines). As the temperature is lowered, the energy shift initially increases in amplitude, as predicted for hopping diffusion in a Gaussian energy distribution<sup>21</sup>, in which the energy shift between the initial and thermalized energy distribution increases as the spread of the Boltzmann distribution reduces, and is given by<sup>21</sup>:

$$\Delta E = -\frac{\sigma^2}{k_b T} \quad 6.5$$

For further negative temperatures the amplitude of the shift decreases, due to the decreasing number of free carriers generated after photoexcitation and the low diffusivity of excitons (see Appendix).

To quantify the dynamics of the hopping process at varying temperatures (i.e. carrier mobility and diffusion coefficient), we fitted the KMC model to the experimental data (thick lines in Figure 6.5a). The blue dots in Figure 6.5b show the temperature dependence of the mobility obtained with the abovementioned approach, showing an increase in carrier mobility for lower temperatures. To confirm the temperature trend extracted from the KMC-modeling approach, we performed TRMC measurement as a function of temperature on the same EDT treated sample. The mobilities obtained *via* TRMC measurements are displayed in Figure 6.5b (red dots), confirming the increase in carrier mobility for decreasing temperature.

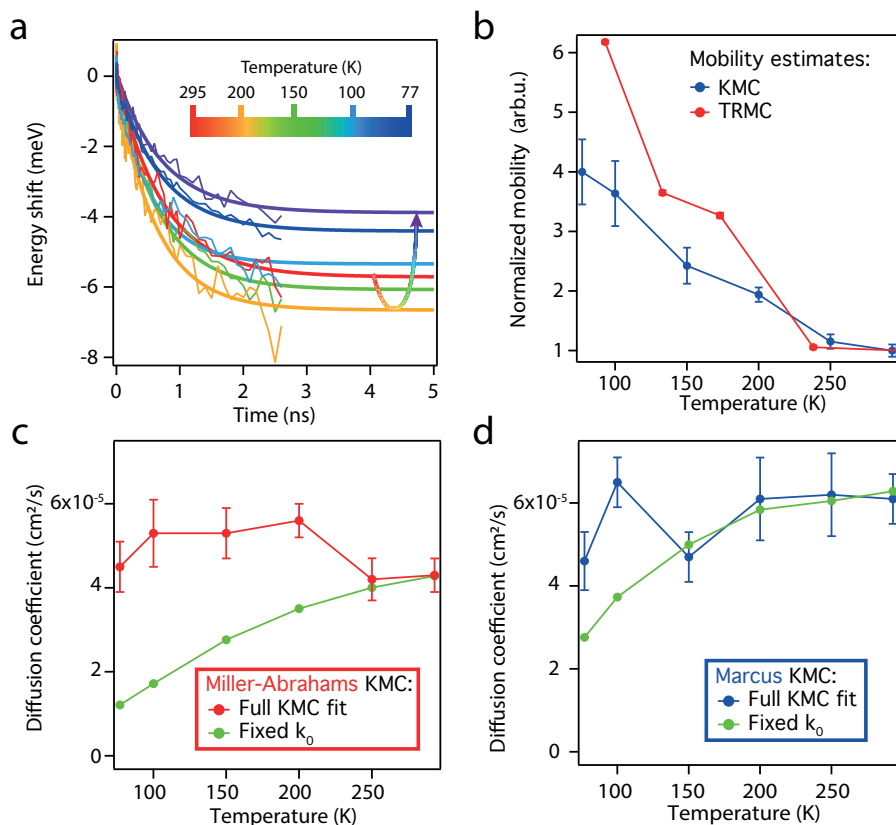


**Figure 6.5. Temperature-dependence of mobility in InP QD films.** **a**, energy shifts obtained from a EDT-treated InP QD films measured at different temperatures (thin lines), showing an effect of temperature on both the amplitude and the dynamics of the energy shift. The most notable change is an initial increase in the shift amplitude as temperature decreases, predicted for hopping of free carriers in a Gaussian energy distribution, followed by an amplitude decrease, associated to the decreasing number of free carriers at lower temperature (see discussion in section 6.6). The thick lines indicate the best fit of the KMC-model to the data. **b**, Temperature trends of the mobility estimates extracted from KMC-modeling of TA data (blue dots), compared with mobility estimates obtained *via* TRMC measurements (red dots). The two datasets are normalized to 1 at room temperature. **c**, Diffusion coefficient estimated fitting the KMC model to the spectral diffusion for each temperature (red dots), compared to the temperature dependence predicted for Miller-Abrahams hopping using a constant value of the hopping prefactor  $k_0$  (green dots). **d**, Diffusion coefficient obtained using Marcus model instead of Miller-Abrahams for the rate calculation, displaying a better agreement between the temperature-dependence predicted from the model (green dots) and the one extracted from the fit (blue dots).

Such a temperature deactivated mobility is not typically expected for hopping transport, but it agrees with recent reports on the temperature dependent mobility of PbS QD films obtained *via* KMC-modeling<sup>12,14</sup>. In those reports the unexpected temperature dependence of the mobility was attributed to a contraction of the ligand shell, resulting in decreased

interparticle distances and a concomitant increase in the hopping rate  $k_0$ . While we do not dispute that this can be a factor of importance, we consider here various possible causes for the observed temperature deactivated transport.

As pointed out by Guyot-Sionnest<sup>36</sup>, it is not impossible for hopping transport to show a temperature deactivated mobility. The reason for this lies in the Einstein-Smoluchowski relation, eq. 6.3, which relates the mobility to  $1/T$  times the diffusion coefficient. Since the average hopping rate constant,  $\langle k \rangle$ , scales linearly with the diffusion coefficient ( $D = k\Delta^2/6$ , where  $\Delta$  is the center-to-center interparticle distance<sup>11,20,36</sup>) it is more convenient to assess the temperature dependence of the diffusion coefficient. The red dots in Figure 6.5c show the diffusion coefficients associated *via* eq. 6.3 to the mobility values displayed in Figure 6.5b. The values of the diffusion coefficient, and consequently the average hopping rates, are substantially temperature independent, in contrast with the activated hopping rate that is expected from the Miller-Abrahams formalism (eq. 6.1). The green dots in Figure 6.5c represent the diffusion coefficients obtained running the KMC simulation with a fixed value for the hopping-prefactor  $k_0$ , showing that in the absence of changes in  $k_0$  Miller-Abrahams hopping predicts a temperature activated diffusion coefficient.

We can explain the temperature trend either assuming that the hopping prefactor increases as a function of temperature, as assumed by Gilmore *et al.*<sup>11</sup>, or assuming that the Miller-Abrahams model does not correctly predict the temperature-dependence of carrier hopping in our system. For systems in which the electronic states are strongly influenced by the polarization of the surrounding environment or by interaction with phonon modes, charge transfer is typically described using Marcus theory, predicting an electron transfer rate given by:

$$k = \frac{k_0}{\sqrt{TE_\lambda}} e^{-\frac{(\Delta E - E_\lambda)^2}{4k_B TE_\lambda}} \quad 6.6$$

where  $E_\lambda$  is the reorganization energy, i.e. the energy required to rearrange atoms to accommodate for the change in the electron position. Atomistic calculations on CdSe QDs supercrystals, performed by Chu *et al.*<sup>37</sup>, identified multi-phonon assisted transfer, described by Marcus theory, as the dominant transfer mechanism in their system. As can be seen from equation 6.6, Marcus rates have a  $T^{-1/2}$  factor contributing to the thermal deactivation of the electron transfer process, originating from the temperature dependence of the number of phonon-modes able to assist the electron in the transfer process.

To see how hopping would be influenced by a Marcus-like transport mechanism we performed KMC simulations substituting the Miller-Abrahams rates given by equation 6.1 with the Marcus rates obtained *via* equation 6.6. We first obtained an estimate of  $E_\lambda$  by fitting equation 6.6 to the temperature dependence of the diffusion coefficients displayed in Figure 6.5d (see Appendix), obtaining a value of  $7.4 \pm 0.4$  meV, in the same order of magnitude as the value calculated by Chu *et al.* for CdSe QDs<sup>37</sup>. We then used this reorganization energy as a constant, non-adjustable parameter in the KMC simulations. The blue dots in Figure 6.5d show the diffusion coefficient obtained by these Marcus-rate

based KMC simulations.

Firstly, one can notice that the diffusion coefficient obtained with the two Marcus-rate KMC simulations are remarkably similar to the values obtained from Miller-Abrahams-rate KMC simulations (see Appendix, Figure 6.8 for direct comparison). This confirms that the KMC approach provides a good estimate of temperature-dependent carrier diffusion coefficients and mobilities regardless of the particular choice for the charge transfer model.

However, the Marcus approach sheds light on the inverse temperature dependence of the carrier mobility. Performing a Marcus-rate KMC simulation with a fixed value of the  $k_0$  prefactor, we obtain the green dots in Figures 6.5d, showing a close agreement with the temperature trend of the diffusion coefficients extracted from the fits. Analogously, the reduced temperature activation of the diffusion coefficient expected for constant  $k_0$  leads to a temperature-dependence of the carrier mobility closely matching the mobilities extracted from the fits (See Appendix, Figure 6.9).

These results show that, describing electron transfer with Marcus theory, the temperature dependence of carrier diffusion coefficient and mobility can be described without a change of the  $k_0$  prefactor. Since the value of  $k_0$  is related to the characteristics of the tunneling barrier between QDs, a Marcus description of charge transfer accounts for the temperature trend without invoking a modification of the tunneling barrier, such as a reduced interparticle distance (reducing the barrier length) or a change in dielectric screening (reducing the barrier height).

The discussion above certainly does not rule out that changes to the tunnel barrier can occur as temperature changes, for instance caused by a contraction of the ligand shell. It does however show that any discussion of the temperature dependence of hopping transport is very sensitive to the exact functional form of the hopping rate, which in turn depends on the exact energy fluctuations (e.g. phonon modes) responsible for creating resonance between the initial and final site in the hopping process.

## 6.7 Conclusions

We benchmarked KMC-modeling of carrier mobility in conductive QD films by applying the method to TA measurements on conductive InP QD films and comparing the extracted mobilities with values obtained from TRMC measurements. The comparison revealed a reasonable agreement between the two approaches, reproducing the same order of magnitude of the mobility in films with different ligand treatments and mobilities spanning three orders of magnitude.

We then determined the temperature dependence of the carrier mobility in the InP QDs samples, revealing a temperature deactivated mobility, similar to recent reports for PbS QD films. We discuss the causes of the mobility trend, suggesting that describing the hopping process in the context of the Marcus charge transfer model provides a closer description for the measured temperature trends, therefore proving the importance of a detailed description of the hopping process in the context of temperature-dependent mobility studies.

Our results provide experimental confirmation of the validity of the KMC-modeling

approach to mobility estimates in QD solids, while shedding light on the nature of the temperature-dependent trends reported with this approach.

## 6.8 Methods

**Quantum Dot (QD) synthesis and film fabrication.** The sample preparation was performed following the recipe presented in Crisp *et al.*, including both QD synthesis and film fabrication<sup>15</sup>.

Transient absorption spectroscopy (TA). TA measurements were obtained measuring the change in light transmitted through a photoexcited sample. The output of a femtosecond pulsed laser (Light Conversion, Pharos SP, 1030 nm wavelength, 5 kHz) is split in two components. The first component is sent to an Optical Parametric Amplifier (OPA) equipped with a second harmonic module (Light Conversion, Orpheus), tuning the wavelength of the fundamental laser output between 320 and 1600 nm. The OPA output is then sent through a mechanical chopper rotating at a frequency of 2.5 KHz (i.e., blocking one every two laser pulses) and sent on the sample as excitation pulse. The second laser component is reflected on mirrors mounted on a remote-controlled mechanical stage, allowing to shorten or to extend the laser's path length by controlling the position of the mirrors on the stage. The second component is subsequently focused on a sapphire crystal, producing a white-light continuum, and finally sent on the sample, where it serves as a probe pulse. Excitation and probe pulses are overlapped at the sample position. After transmission through the sample the probe pulse is measured by a detector, recording the intensity spectrum of the transmitted light. A half-wave plate placed in the probe-path allows to rotate the polarization of the probe beam with respect to the excitation beam. A linear polarizer placed in the detection path allows to transmit only light polarized along the polarization direction of the probe pulse, preventing scattered excitation light to be measured at the detector. Since two probe pulses are transmitted for every excitation pulse, the detector measures the transmitted probe spectrum in the presence of an excitation pulse ( $I_{on}$ ) followed by the same spectrum measured in the absence of an excitation pulse ( $I_{off}$ ). The changes in the absorbance of the sample due to photoexcitation can be obtained from:

$$\Delta A = \log_{10} \left( \frac{I_{on}}{I_{off}} \right) \quad 6.7$$

Changes in the probe's path length are used to control the relative time of arrival of the two pulses, thus allowing to measure  $\Delta A$  as a function of the time elapsed after photoexcitation.

**Time-resolved microwave conductivity (TRMC).** In TRMC spectroscopy, the absorption of microwave radiation by free charges in the sample is related to the photoconductivity of the free charges. The measurements are performed placing a substrate coated with a QD film in a microwave cavity. Microwave radiation, reflected back and forth in the cavity, forms a standing wave, with one of the amplitude maxima occurring at the sample position. The sample is exposed to nanosecond laser pulses, exciting electrons in the QD film. If the excitation leads to the creation of free carriers (unbound electrons and holes), they can be accelerated by the microwave's electric field, resulting in a net microwave absorption. We can relate the absorption of microwave power to the change in photoconductance ( $\Delta G$ ) *via*:

$$\frac{\Delta P}{P} = -K \Delta G \quad 6.8$$

where  $P$  is the microwave power reflected back from the cavity in the unexcited measurement,  $\Delta P$  is the change in microwave power induced by photoexcitation and  $K$  is the sensitivity factor, determined

by the geometry of the cavity and by its optical properties. The conductance change can be linked to physical quantities associated with electronic motion *via*:

$$\Delta G = e\beta I_0 F_a \Phi (\mu_e + \mu_h) \quad 6.9$$

where  $\beta$  is the ratio between the transverse and longitudinal dimensions of the waveguide,  $I_0 F_a$  is the absorbed photon fluence,  $\Phi$  is the yield of free carrier formation and  $\mu_e$  ( $\mu_h$ ) is the electron (hole) mobility. Knowledge of the cavity geometry and of the photoexcitation conditions allows to convert the microwave changes in a product of the photogeneration yield and the sum of the electron and hole<sup>28,38</sup>. Assuming a unity  $\Phi$  (i.e., every absorbed photon leads to the generation of a free electron and a free hole), we obtain then an estimate for the sum of the electron and hole mobilities, which was used as an upper limit for the actual sum of the mobilities in the sample.

**Kinetic-Monte-Carlo modeling of TA measurements.** TA spectral shift were analyzed with a Kinetic-Monte-Carlo (KMC) model, following the approach reported in Gilmore *et al.*<sup>11</sup>, in order to extract mobility estimates from TA results. The QD assembly was represented by a BCC arrangement of electronic sites, whose energies are randomly distributed and follow a Gaussian distribution with  $\sigma$  standard deviation. Each simulation run is started at a different, randomly selected electronic site. The rates of transition between the current site and all of the nearest-neighbor sites is determined according to a Miller-Abrahams hopping model:

$$k = k_0 \begin{cases} \exp\left(-\frac{E_f - E_i}{k_b T}\right), & \text{for } E_f > E_i \\ 1, & \text{for } E_f \leq E_i \end{cases} \quad 6.10$$

where  $\epsilon$  are site energies,  $k_b$  is the Boltzmann constant,  $T$  is the temperature in Kelvin, and  $k_0$  is the hopping prefactor. Each evolution step is calculated following a KMC scheme. In its first step, the algorithm determines the destination site of the electron's hop. This is done summing the transition rates of all neighbouring sites, and multiplying by a random number  $r$  in the interval  $[0,1)$ :

$$k^* = r \sum_{NN} k_i \quad 6.11$$

A partial sum of the transition rate is performed, and continues while the sum is smaller than  $k^*$ . When the addition of the rate  $k_i$  makes the partial sum bigger than  $k^*$ , the sum is stopped and the electron is moved to the  $i$ th nearest neighbour. Once determined the destination site, the algorithm computes the time required to complete the transition. The time step corresponding to the transition is calculated *via* the formula:

$$\Delta t = -\frac{\ln r}{\sum_{NN} k_i} \quad 6.12$$

and the current time of the simulation set to  $t_{\text{current}} = t_{\text{old}} + \Delta t$ . The KMC scheme described above is iterated until  $t_{\text{current}}$  exceeds 3 ns. At each hop, energy and mean square displacement (MSD) of the electron are recorded. The time-dependence of the electron energy can then be fitted to the experimentally determined TA spectral shift, using  $k_0$

and  $\sigma$  as fitting parameters. The optimal values of the fit parameters are then used to run again the KMC scheme, obtaining the time-dependence of the MSD, which shows an approximately linear increase as a function of time. The long-time slope of the MSD,  $\alpha$ , can be related, by definition, to the diffusion coefficient  $D$ :

$$\alpha = 6D \quad 6.13$$

In turns the diffusion coefficient of a system in thermal equilibrium can be related to the mobility of the diffusing electrons by the Einstein-Smoluchowski relation:

$$D = \frac{\mu k_B T}{e} \quad 6.14$$

where  $e$  is the fundamental electric charge, and  $\mu$  the electron mobility. Thus, fitting the long-time MSD time-dependence provides an estimate of the electron mobility.

Each KMC trajectory is stochastic, reproducing the hopping behavior of a single electron in the QD film. Since the TA spectral shift results from the average behavior of all electrons moving in the QD film, the time-dependence of the physical quantities calculated along a KMC run (energy and MSD) need to be averaged over many different runs.

## References

1. Ganesan, A.; Houtepen, A.; Crisp, R.; Quantum Dot Solar Cells: Small Beginnings Have Large Impacts. *Appl. Sci.* 2018, 8 (10), 1867.
2. Zhang, H.; Kurley, J. M.; Russell, J. C.; Jang, J.; Talapin, D. V. Solution-Processed, Ultrathin Solar Cells from CdCl<sub>2</sub> 3 – -Capped CdTe Nanocrystals: The Multiple Roles of CdCl<sub>2</sub> – Ligands. *J. Am. Chem. Soc.* 2016, 138 (24), 7464–7467.
3. Crisp, R. W.; Pach, G. F.; Kurley, J. M.; France, R. M.; Reese, M. O.; Nanayakkara, S. U.; MacLeod, B. A.; Talapin, D. V.; Beard, M. C.; Luther, J. M. Tandem Solar Cells from Solution-Processed CdTe and PbS Quantum Dots Using a ZnTe–ZnO Tunnel Junction. *Nano Lett.* 2017, 17 (2), 1020–1027.
4. Kagan, C. R.; Lifshitz, E.; Sargent, E. H.; Talapin, D. V.; Murray, C.; Kagan, C.; Bawendi, M. G.; Talapin, D. V.; Lee, J.-S.; Kovalenko, M. V.; *et al.* Building Devices from Colloidal Quantum Dots. *Science* 2016, 353 (6302), 545–610.
5. Chung, D. S.; Lee, J.-S.; Huang, J.; Nag, A.; Ithurria, S.; Talapin, D. V. Low Voltage, Hysteresis Free, and High Mobility Transistors from All-Inorganic Colloidal Nanocrystals. *Nano Lett.* 2012, 12 (4), 1813–1820.
6. Choi, J.-H.; Oh, S. J.; Lai, Y.; Kim, D. K.; Zhao, T.; Fafarman, A. T.; Diroll, B. T.; Murray, C. B.; Kagan, C. R. In Situ Repair of High-Performance, Flexible

- Nanocrystal Electronics for Large-Area Fabrication and Operation in Air. *ACS Nano* 2013, 7 (9), 8275–8283.
7. Shirasaki, Y.; Supran, G. J.; Bawendi, M. G.; Bulović, V. Emergence of Colloidal Quantum-Dot Light-Emitting Technologies. *Nat. Photonics* 2013, 7 (1), 13–23.
  8. Lim, J.; Park, Y.-S.; Wu, K.; Yun, H. J.; Klimov, V. I. Droop-Free Colloidal Quantum Dot Light Emitting Diodes. *Nano Lett.* 2018, acs.nanolett.8b03457.
  9. Wilker, M. B.; Shinopoulos, K. E.; Brown, K. A.; Mulder, D. W.; King, P. W.; Dukovic, G. Electron Transfer Kinetics in CdS Nanorod-[FeFe]-Hydrogenase Complexes and Implications for Photochemical H<sub>2</sub> Generation. *J. Am. Chem. Soc.* 2014, 136 (11), 4316–4324.
  10. Utterback, J. K.; Hamby, H.; Pearce, O. M.; Eaves, J. D.; Dukovic, G. Trapped-Hole Diffusion in Photoexcited CdSe Nanorods. *J. Phys. Chem. C* 2018, 122 (29), 16974–16982.
  11. Pearce, O. M.; Duncan, J. S.; Damrauer, N. H.; Dukovic, G. Ultrafast Hole Transfer from CdS Quantum Dots to a Water Oxidation Catalyst. *J. Phys. Chem. C* 2018, 122 (30), 17559–17565.
  12. Klimov, V. I.; Mikhailovsky, A. A.; Xu, S.; Malko, A.; Hollingsworth, J. A.; Leatherdale, C. A.; Eisler, H.-J.; Bawendi, M. G. Optical Gain and Stimulated Emission in Nanocrystal Quantum Dots. *Science* (80-. ). 2000, 290 (5490).
  13. Klimov, V. I.; Ivanov, S. A.; Nanda, J.; Achermann, M.; Bezel, I.; McGuire, J. A.; Piryatinski, A. Single-Exciton Optical Gain in Semiconductor Nanocrystals. *Nature* 2007, 447 (7143), 441–446.
  14. Fan, F.; Voznyy, O.; Sabatini, R. P.; Bicanic, K. T.; Adachi, M. M.; McBride, J. R.; Reid, K. R.; Park, Y.-S.; Li, X.; Jain, A.; *et al.* Continuous-Wave Lasing in Colloidal Quantum Dot Solids Enabled by Facet-Selective Epitaxy. *Nature* 2017, 544 (7648), 75–79.
  15. Lim, J.; Park, Y.-S.; Klimov, V. I. Optical Gain in Colloidal Quantum Dots Achieved with Direct-Current Electrical Pumping. *Nat. Mater.* 2017.
  16. Bawendi, M. G.; Wilson, W. L.; Rothberg, L.; Carroll, P. J.; Jedju, T. M.; Steigerwald, M. L.; Brus, L. E. Electronic Structure and Photoexcited-Carrier Dynamics in Nanometer-Size CdSe Clusters. *Phys. Rev. Lett.* 1990, 65 (13), 1623–1626.
  17. Norris, D. J.; Sacra, A.; Murray, C. B.; Bawendi, M. G. Measurement of the Size Dependent Hole Spectrum in CdSe Quantum Dots. *Phys. Rev. Lett.* 1994, 72 (16), 2612–2615.

18. Norris, D. J.; Bawendi, M. G. Structure in the Lowest Absorption Feature of CdSe Quantum Dots. *J. Chem. Phys.* 1995, 103 (13), 5260–5268.
19. Guyot-Sionnest, P.; Wehrenberg, B.; Yu, D. Intraband Relaxation in CdSe Nanocrystals and the Strong Influence of the Surface Ligands. *J. Chem. Phys.* 2005, 123 (7), 074709.
20. Kambhampati, P. Unraveling the Structure and Dynamics of Excitons in Semiconductor Quantum Dots. *Acc. Chem. Res.* 2011, 44 (1), 1–13.
21. Sercel, P. C.; Efros, A. L. Band-Edge Exciton in CdSe and Other II–VI and III–V Compound Semiconductor Nanocrystals – Revisited. *Nano Lett.* 2018, 18 (7), 4061–4068.
22. Hunsche, S.; Dekorsy, T.; Klimov, V.; Kurz, H. Ultrafast Dynamics of Carrier-Induced Absorption Changes in Highly-Excited CdSe Nanocrystals. *Appl. Phys. B Laser Opt.* 1996, 62 (1), 3–10.
23. Klimov, V. I.; McBranch, D. W. Femtosecond  $1P_{-1}$  to  $1S$  Electron Relaxation in Strongly Confined Semiconductor Nanocrystals. *Phys. Rev. Lett.* 1998, 80 (18), 4028–4031.
24. Klimov, V. I.; McBranch, D. W.; Leatherdale, C. A.; Bawendi, M. G. Electron and Hole Relaxation Pathways in Semiconductor Quantum Dots. *Phys. Rev. B* 1999, 60 (19), 13740–13749.
25. Sewall, S. L.; Cooney, R. R.; Kambhampati, P. Experimental Tests of Effective Mass and Atomistic Approaches to Quantum Dot Electronic Structure: Ordering of Electronic States. *Appl. Phys. Lett.* 2009, 94 (24), 243116.
26. Boehme, S. C.; Azpiroz, J. M.; Aulin, Y. V.; Grozema, F. C.; Vanmaekelbergh, D. L.; Siebbeles, L. D. A.; Infante, I.; Houtepen, A. J.; Fakultatea, K. Density of Trap States and Auger-Mediated Electron Trapping in CdTe Quantum-Dot Solids.
27. Knowles, K. E.; McArthur, E. A.; Weiss, E. A. A Multi-Timescale Map of Radiative and Nonradiative Decay Pathways for Excitons in CdSe Quantum Dots. *ACS Nano* 2011, 5 (3), 2026–2035.
28. Klimov, V. I.; Schwarz, C. J.; McBranch, D. W.; Leatherdale, C. A.; Bawendi, M. G. Ultrafast Dynamics of Inter- and Intraband Transitions in Semiconductor Nanocrystals: Implications for Quantum-Dot Lasers. *Phys. Rev. B* 1999, 60 (4), R2177–R2180.
29. Adachi, M. M.; Fan, F.; Sellan, D. P.; Hoogland, S.; Voznyy, O.; Houtepen, A. J.; Parrish, K. D.; Kanjanaboos, P.; Malen, J. A.; Sargent, E. H. Microsecond-Sustained Lasing from Colloidal Quantum Dot Solids. *Nat. Commun.* 2015, 6, 8694.

30. Ekimov, A. I.; Kudryavtsev, I. A.; Efros, A. L.; Yazeva, T. V.; Hache, F.; Schanne-Klein, M. C.; Rodina, A. V.; Ricard, D.; Flytzanis, C. Absorption and Intensity-Dependent Photoluminescence Measurements on CdSe Quantum Dots: Assignment of the First Electronic Transitions. *J. Opt. Soc. Am. B* 1993, 10 (1), 100.
31. Norris, D. J.; Bawendi, M. G. Measurement and Assignment of the Size-Dependent Optical Spectrum in CdSe Quantum Dots. *Phys. Rev. B* 1996, 53 (24), 16338–16346.
32. Sewall, S. L.; Cooney, R. R.; Anderson, K. E. H.; Dias, E. A.; Kambhampati, P. State-to-State Exciton Dynamics in Semiconductor Quantum Dots. *Phys. Rev. B* 2006, 74 (23), 235328.
33. Chen, O.; Zhao, J.; Chauhan, V. P.; Cui, J.; Wong, C.; Harris, D. K.; Wei, H.; Han, H.-S.; Fukumura, D.; Jain, R. K.; *et al.* Compact High-Quality CdSe–CdS Core–Shell Nanocrystals with Narrow Emission Linewidths and Suppressed Blinking. *Nat. Mater.* 2013, 12 (5), 445–451.
34. Boldt, K.; Kirkwood, N.; Beane, G. A.; Mulvaney, P. Synthesis of Highly Luminescent and Photo-Stable, Graded Shell CdSe/Cd<sub>x</sub>Zn<sub>1-x</sub>S Nanoparticles by In Situ Alloying. *Chem. Mater.* 2013, 25 (23), 4731–4738.
35. McGuire, J. A.; Sykora, M.; Robel, I.; Padilha, L. A.; Joo, J.; Pietryga, J. M.; Klimov, V. I. Spectroscopic Signatures of Photocharging Due to Hot-Carrier Transfer in Solutions of Semiconductor Nanocrystals under Low-Intensity Ultraviolet Excitation. *ACS Nano* 2010, 4 (10), 6087–6097.
36. Lebedev, M. V.; Misochko, O. V.; Dekorsy, T.; Georgiev, N. On the Nature of “Coherent Artifact.” *J. Exp. Theor. Phys.* 2005, 100 (2), 272–282.
37. Wang, H. I.; Infante, I.; ten Brinck, S.; Cánovas, E.; Bonn, M. Efficient Hot Electron Transfer in Quantum Dot-Sensitized Mesoporous Oxides at Room Temperature. *Nano Lett.* 2018, *acs.nanolett.8b01981*.
38. Bisschop, S.; Geiregat, P.; Aubert, T.; Hens, Z. The Impact of Core/Shell Sizes on the Optical Gain Characteristics of CdSe/CdS Quantum Dots. *ACS Nano* 2018, *acs.nano.8b02493*.
39. Wu, K.; Park, Y.-S.; Lim, J.; Klimov, V. I. Towards Zero-Threshold Optical Gain Using Charged Semiconductor Quantum Dots. *Nat. Nanotechnol.* 2017, 12 (12), 1140–1147.
40. Efros, A. L.; Rosen, M.; Kuno, M.; Nirmal, M.; Norris, D. J.; Bawendi, M. Band-Edge Exciton in Quantum Dots of Semiconductors with a Degenerate Valence Band:

- Dark and Bright Exciton States. *Phys. Rev. B* 1996, 54 (7), 4843–4856.
41. Korkusinski, M.; Voznyy, O.; Hawrylak, P. Fine Structure and Size Dependence of Exciton and Biexciton Optical Spectra in CdSe Nanocrystals. *Phys. Rev. B* 2010, 82 (24), 245304.
  42. Houtepen, A. J.; Hens, Z.; Owen, J. S.; Infante, I. On the Origin of Surface Traps in Colloidal II–VI Semiconductor Nanocrystals. *Chem. Mater.* 2017, 29 (2), 752–761.
  43. Giansante, C.; Infante, I. Surface Traps in Colloidal Quantum Dots: A Combined Experimental and Theoretical Perspective. *J. Phys. Chem. Lett.* 2017, 8 (20), 5209–5215.
  44. Kirkwood, N.; Monchen, J. O. V.; Crisp, R. W.; Grimaldi, G.; Bergstein, H. A. C.; du Fossé, I.; van der Stam, W.; Infante, I.; Houtepen, A. J. Finding and Fixing Traps in II–VI and III–V Colloidal Quantum Dots: The Importance of Z-Type Ligand Passivation. *J. Am. Chem. Soc.* 2018, jacs.8b07783.
  45. Gao, Y.; Peng, X. Photogenerated Excitons in Plain Core CdSe Nanocrystals with Unity Radiative Decay in Single Channel: The Effects of Surface and Ligands. *J. Am. Chem. Soc.* 2015, 137 (12), 4230–4235.
  46. Schnitzenbaumer, K. J.; Dukovic, G. Comparison of Phonon Damping Behavior in Quantum Dots Capped with Organic and Inorganic Ligands. *Nano Lett.* 2018, 18 (6), 3667–3674.
  47. Sagar, D. M.; Cooney, R. R.; Sewall, S. L.; Dias, E. A.; Barsan, M. M.; Butler, I. S.; Kambhampati, P. Size Dependent, State-Resolved Studies of Exciton-Phonon Couplings in Strongly Confined Semiconductor Quantum Dots. *Phys. Rev. B* 2008, 77 (23), 235321.
  48. Cerullo, G.; De Silvestri, S.; Banin, U. Size-Dependent Dynamics of Coherent Acoustic Phonons in Nanocrystal Quantum Dots. *Phys. Rev. B* 1999, 60 (3), 1928–1932.
  49. Spoor, F. C. M.; Tomić, S.; Houtepen, A. J.; Siebbeles, L. D. A. Broadband Cooling Spectra of Hot Electrons and Holes in PbSe Quantum Dots. *ACS Nano* 2017, acsnano.7b02506.
  50. Gooding, A. K.; Gómez, D. E.; Mulvaney, P. The Effects of Electron and Hole Injection on the Photoluminescence of CdSe/CdS/ZnS Nanocrystal Monolayers. *ACS Nano* 2008, 2 (4), 669–676.
  51. Park, S.-M.; Barber, M. E. Thermodynamic Stabilities of Semiconductor Electrodes. *J. Electroanal. Chem. Interfacial Electrochem.* 1979, 99 (1), 67–75.

52. van der Stam, W.; du Fossé, I.; Grimaldi, G.; Monchen, J. O. V.; Kirkwood, N.; Houtepen, A. J. Spectroelectrochemical Signatures of Surface Trap Passivation on CdTe Nanocrystals. *Chem. Mater.* 2018, *acs.chemmater.8b03893*.
53. Kloper, V.; Osovsky, R.; Kolny-Olesiak, J.; Sashchiuk, A.; Lifshitz, E., The Growth of Colloidal Cadmium Telluride Nanocrystal Quantum Dots in the Presence of Cd<sub>0</sub> Nanoparticles. *J. Phys. Chem. C* 2007, 111 (28), 10336-10341.
54. Boehme, S. C.; Vanmaekelbergh, D.; Evers, W. H.; Siebbeles, L. D. A.; Houtepen, A. J., In situ spectroelectrochemical determination of energy levels and energy level offsets in quantum-dot heterojunctions. *J. Phys. Chem. C* 2016, 120 (9), 5164-5173.
55. Tyagi, P.; Cooney, R. R.; Sewall, S. L.; Sagar, D. M.; Saari, J. I.; Kambhampati, P., Controlling piezoelectric response in semiconductor quantum dots via impulsive charge localization. *Nano Lett* 2010, 10 (8), 3062-7.
56. Bäessler, H., Charge Transport in Disordered Organic Photoconductors. *Phys. Status Solidi B* 1993, 175, 15-56.

## Appendix

### Carrier lifetime in room temperature Transient Absorption measurements on ligand-treated InP QDs films

In order to estimate the amount of carrier decay occurring during the ingrowth of the Time Resolved Microwave Conductivity (TRMC) signal, occurring on a  $\sim 10$  ps timescale, we fitted the decay of the InP QD band-edge bleach during a Transient Absorption (TA) measurement. Figure 6.6 shows the fit of the TA bleach decays for (a) the EDT sample, (b) the  $\text{Na}_2\text{S}$  sample, and (c) the  $(\text{NH}_4)_2\text{S}$  sample. Since all the lifetimes involved in the decay process are shorter than the TRMC signal rising time ( $\sim 10$  ns), the surviving fraction of excited species sampled in the TRMC measurement,  $\phi_{\text{TRMC}}$ , is estimated from the ratio of the constant component of the fit to the total initially amplitude of the signal.

Sample	$\phi_{\text{TRMC}}$
EDT	$0.580 \pm 0.006$
$\text{Na}_2\text{S}$	$0.485 \pm 0.007$
$(\text{NH}_4)_2\text{S}$	$0.417 \pm 0.012$

The TRMC experiment provide a measurement of  $\phi \Sigma \mu$ , where  $\phi$  is the yield of free carrier and  $\Sigma \mu$  the sum of the electron and hole mobilities. The value of  $\phi$  has an upper bound in the value of  $\phi_{\text{TRMC}}$ . Assuming that all the photoexcited species surviving the decay are free carriers, we can estimate the sum of the carrier mobilities dividing the TRMC signal by  $\phi_{\text{TRMC}}$ . The amplitudes of the TRMC signal rescaled by  $\phi_{\text{TRMC}}$  are presented in the maintext in Figure 6.4d.

6

### Temperature dependence of the energy shift amplitude

The bleach signal observed in a TA measurement on conductive QD solids can be

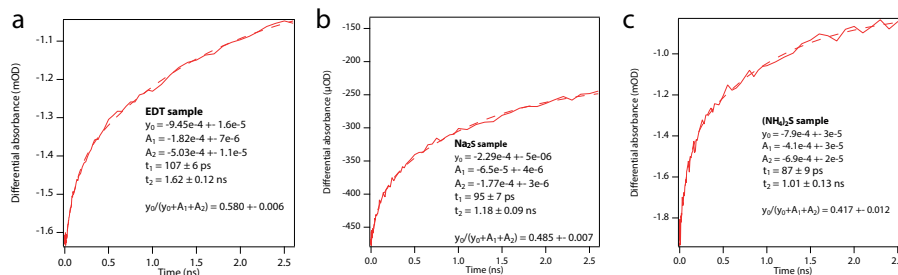


**Figure 6.6. Biexponential fit to the Transient Absorption (TA) band-edge bleach decay.** **a**, EDT sample, excited with a 530 nm pump wavelength, photon fluence of  $4.4 \cdot 10^{12}$  photons/cm<sup>2</sup> per pulse. **b**,  $\text{Na}_2\text{S}$  sample, excited with a 570 nm pump wavelength, photon fluence of  $2.4 \cdot 10^{12}$  photons/cm<sup>2</sup> per pulse. **c**,  $(\text{NH}_4)_2\text{S}$  sample, excited with a 530 nm pump wavelength, photon fluence of  $2.3 \cdot 10^{13}$  photons/cm<sup>2</sup> per pulse.

expressed as the sum of two components:

- an exciton bleach, whose average energy remains constant in time-range of the experiment (i.e.: neglecting energy transfer processes on the experiment timescale).
- a free carrier bleach, whose average energy changes due to carrier hopping towards lower energy sites.

Considering a Gaussian distribution for the band-edge energies, and random photoexcitation of the energy distribution, the two bleaches can be described by two Gaussians distributions:

$$\Delta A_f(E,t) = a_f \exp\left(-\frac{(E - E_f(t))^2}{2\sigma_f^2}\right) \quad 6.15$$

$$\Delta A_x(E,t) = a_x \exp\left(-\frac{(E - E_x)^2}{2\sigma_x^2}\right) \quad 6.16$$

with  $E_f(t=0) = E_x$ .

The mean value of the sum of two Gaussians is given by:

$$\bar{E}(t) = \frac{a_f \sigma_f E_f(t) + a_x \sigma_x E_x}{a_f \sigma_f + a_x \sigma_x} \quad 6.17$$

At  $t=0$ , the total bleach is exactly described by a Gaussian function. If the standard deviation of the two bleach components remain larger than the energy shift between the two components at every time, and if  $\sigma_f \approx \sigma_x$ , the total bleach at a generic time in the measurement can be described by a Gaussian function, whose central energy is given by:

$$\bar{E} \approx \frac{a_f E_f(t) + a_x E_x}{a_f + a_x} = f_f E_f(t) + f_x E_x \quad 6.18$$

where  $f_{f/x}$  are the fraction of excitations resulting in electron-hole pairs (f) / excitons (X). Denoting with  $\Delta E(t)$  the shift of the total bleach from its energy at  $t=0$ , it can be expressed as:

$$\begin{aligned} \Delta \bar{E}(t) &= \bar{E}(t) - \bar{E}(0) = f_f (E_f(t) - E_f(0)) + f_x (E_x(t) - E_x(0)) \\ &= f_f \Delta E_f(t) \end{aligned} \quad 6.19$$

where  $\Delta E_f(t)$  represents the shift of the free carrier bleach.

For carrier hopping in a Gaussian energy distribution, the total energy shift between the initial energy distribution and the thermalized energy distribution,  $\Delta E_f(\infty)$ , is given by<sup>56</sup>:

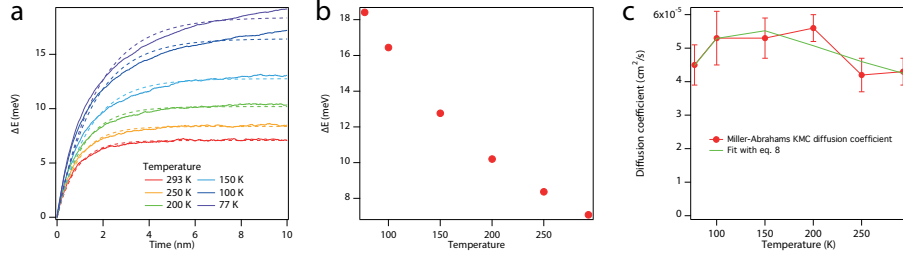


**Figure 6.7.** Estimate of the reorganization energy from the temperature dependence of the diffusion coefficient in an EDT-treated InP QD film. **a**, Average energy difference between the electron and the neighbouring electronic states (continuous line), compared to an exponential fit (dotted line). **b**, thermalized value of the average energy difference, extracted from the exponential fits in (a). **c**, Fit of the diffusion coefficient shown in Figure 6.5c with a Marcus scaling of the diffusion coefficient, given by equation 6.22 (green line).

$$\Delta E_i(\infty) = -\frac{\sigma_f^2}{k_b T} \quad 6.20$$

Thus, the amplitude of the energy shift of the total bleach between its initial and thermalized state is given by:

$$\Delta \bar{E}(\infty) = -f_i(T) \frac{\sigma_f^2}{k_b T} \quad 6.21$$

Thus, although reducing the temperature increases the amplitude of the energy shift of the free carrier component, reduction in the exciton dissociation, thermally activated, can lead to an overall decrease of the energy shift of the total bleach.

### Estimate of the reorganization energy in an EDT-treated InP QD film

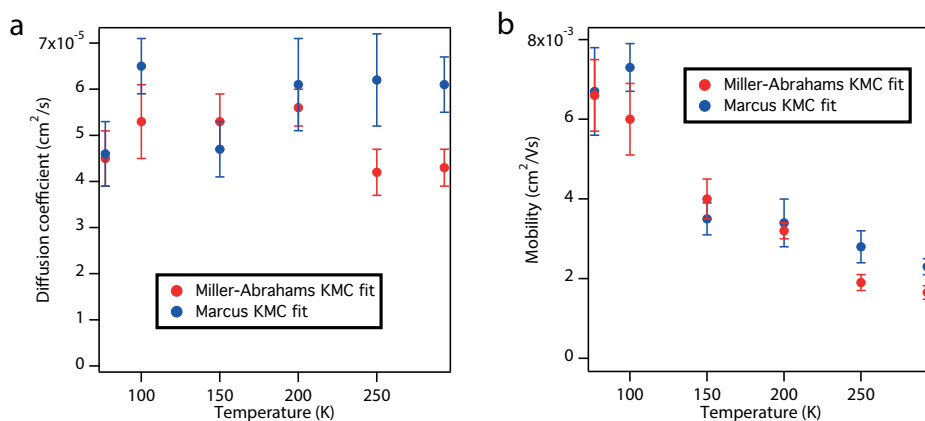
In order to obtain an estimate of the reorganization energy to be used for the Marcus-based KMC model, we fitted the temperature-dependence of the diffusion coefficient displayed in the main-text in Figure 6.5c with the functional dependence:

$$D = \frac{D_0}{\sqrt{TE_\lambda}} e^{-\frac{(\Delta E - E_\lambda)^2}{4k_b TE_\lambda}} \quad 6.22$$

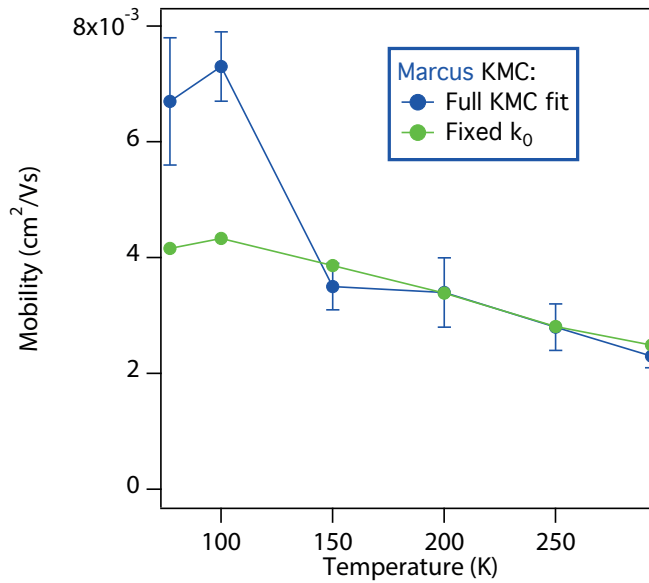
where  $\Delta E(T)$  represent the average energy offset for the thermalized system at temperature  $T$ . The average energy offset changes as a function of temperature, as the Boltzmann distribution for the electron energies becomes narrower (see eq. 6.5 in the main-text). To account for the way that  $\Delta E(T)$  changes in the simulation at different temperatures, we recorded the average energy difference between the populated electron state and the electron states in the neighbouring QDs during the KMC simulation. Figure 6.7a shows

the time dependence of  $\Delta E(T)$ . We extracted the thermalized value of  $\Delta E(T)$  from an exponential fit of the time-dependent average energy difference. Figure 6.7b shows the temperature dependence of the thermalized  $\Delta E(T)$ , showing an increase for lower temperature. We fitted the temperature dependent of the diffusion coefficient shown in Figure 6.5c with equation 6.22, using the estimate for  $\Delta E(T)$  and optimizing for the reorganization energy  $E_\lambda$ . Figure 6.7c shows the result of the fit to the diffusion coefficient (green line). The best value of the reorganization energy, extracted from the fit, was  $7.4 \pm 0.4$  meV.

### Comparison of mobilities and diffusion coefficients extracted from the Miller-Abrahams and Marcus models



**Figure 6.8.** **a**, Comparison between diffusion coefficients extracted from the full KMC fit of the temperature-dependent spectral shift of the EDT-treated samples, obtained using Miller-Abrahams rates (red dots) and Marcus rates (blue dots). **b**, Comparison between mobilities extracted from the full KMC fit of the temperature-dependent spectral shift of the EDT-treated samples, obtained using Miller-Abrahams rates (red dots) and Marcus rates (blue dots). For both mobilities and diffusion coefficients, the two approaches provide remarkably similar estimates.

**Comparison between Marcus mobilities extracted from the full fit and from a fit with fixed hopping prefactor**

**Figure 6.9.** Temperature-dependence of electron mobility obtained using Marcus rates in the KMC model, comparing the values obtained performing a full fit of the KMC model (blue dots) to the values obtained from a fit performed holding a constant hopping prefactor  $k_0$  (set to the value obtained at room temperature in the full fit). The good agreement between the two traces shows that the temperature activated mobility extracted from the KMC fit using Marcus rates does not require a strong temperature-dependence of the hopping prefactor.



# Summary

---

The generation of excited carrier via light absorption (photogeneration) and their ability to propagate in space in Quantum Dot (QD) films affect critically the performance of QD-based optoelectronic devices. The work performed in this thesis is aimed at increasing the understanding of fundamental processes occurring in QD solutions and QD films, providing the groundwork for future optimization of QD-based devices.

We employed a combination of ultrafast spectroscopy techniques (transient absorption spectroscopy and spectroelectrochemistry) and computational methods (Monte-Carlo and Density Functional Theory simulations), to obtain information about the energy of electronic levels and the dynamics of carrier transport, relaxation and transfer between different materials. Our results provide evidence of previously unreported effects: hot-electron transfer between different QD species, a hole contribution to the bleach of cadmium chalcogenide QDs and the presence of a temperature de-activated mobility for carrier hopping in InP QD films. Furthermore, we demonstrate the possibility to achieve band-alignment in QD heterojunction via control of the ligand passivation on the QD surface.

Chapter 1 introduces the main concepts used in the rest of the thesis and broadly motivates the interest in nanostructures, in general, and in semiconductor Quantum Dots, in particular. The main electronic properties of QD systems and their absorption properties are derived from a simple quantum mechanical model. The chapter then discusses the presence of surface effects in QDs, the properties of QD heterostructures and gives a framework for the interpretation of electron transport in QD films. Finally, the use of QD for solar cell applications is discussed, introducing the processes that could give QD systems an advantage over bulk solar cell materials.

In Chapter 2, we report the presence of hot-electron transfer between CdSe and PbSe QDs, assembled in a heterojunction QD film. We characterised the transfer process by looking at the bleaching of optical transitions in CdSe QDs occurring upon selective excitation of PbSe QDs in a heterojunction QD film. The efficiency of the transfer process is determined as a function of excitation wavelength, revealing an increase as the excess energy of the photon increases. Density Functional Theory (DFT) simulations of a CdSe-PbSe heterojunction showed the presence of electron states delocalized over the heterojunction. Furthermore, time-dependent DFT simulations confirmed the presence of a hot-electron transfer process occurring on a sub-ps timescale between the PbSe and the CdSe QDs.

In Chapter 3, we report the effect of different ligand treatments on the band-alignment between PbSe and CdSe QDs in a heterojunction QD film. The band-alignment between the two QD materials is determined both via spectroelectrochemical measurements and transient absorption measurements. Our measurements showed the possibility to select

ligand with different dipole moments to switch the band-alignment of the two materials from a type-I alignment, observed in bulk, to a type-II alignment. Transient absorption measurements on a type-II-aligned PbSe-CdSe heterojunction QD film showed the presence of a high density of trap states, that needed to be saturated to allow electron transfer between the two components.

In Chapter 4, we develop a model to extract Carrier Multiplication (CM) rates from experimental measurements of the CM yield and carrier relaxation times. Additionally, a simplified model allowed to obtain an estimate for the CM rates from utilizing CM yield data and a value for the carrier energy-loss rates, typically available in literature. Obtaining CM rates can play an important role in the optimization of the CM process, while facilitating the screening of materials displaying desirable CM properties.

In Chapter 5, we demonstrate the presence of a hole contribution to the bleach of cadmium chalcogenide QDs. We measured the bleach dynamics upon resonant excitation of the 2S feature of CdSe QDs, leading to the excitation of a band-edge electron and of a hot hole. Observing the increase in the bleach as the hole undergoes cooling, we could confirm the presence of a hole contribution to the bleach and quantify its amplitude. Spectroelectrochemical measurements of CdTe QDs showed the presence of a bleach feature upon electrochemical injection of holes. Furthermore, we showed a lack of hole contribution in CdSe QD samples characterized by low photoluminescence, associating the absence of a hole bleach with the presence of efficient hole trapping. Our findings resolve a long-lasting controversy in the field of ultrafast QD spectroscopy.

In Chapter 6, we employ a Kinetic Monte Carlo (KMC) model to describe the spectral shifts observed in temperature-dependent Transient Absorption measurement of InP QD films, allowing to determine the temperature-dependence of carrier mobility in the system. Our results show the presence of a temperature de-activated mobility, in contrast with the predictions arising from the Miller-Abrahams description of carrier hopping. We compared the mobility extracted from the KMC model considering Miller-Abrahams rates with those obtained using a Marcus description for the transfer, obtaining a better agreement between the model's predictions and the experimental trend. Our results suggest that a Marcus description of the hopping rates might explain the temperature de-activated mobility in InP QD systems, without requiring changes in interparticle distance or the presence of band-like transport.

---

## Summary

---



# Samenvatting

---

Het genereren van ladingen in de aangeslagen toestand door absorptie van licht, en de mogelijkheid van deze ladingen om door films van kwantum-stippen te bewegen, heeft een sterke invloed op de prestaties van apparaten gemaakt met kwantum-stippen. Het werk dat in dit proefschrift beschreven staat is gericht op het verhogen van ons begrip over fundamentele processen die in oplossingen en films van kwantum-stippen plaatsvinden. Dit legt de basis voor de toekomstige optimalisatie van apparaten gemaakt met kwantum-stippen.

We hebben gebruik gemaakt van een combinatie van ultrasnelle spectroscopische technieken (transiente absorptie spectroscopie en spectroelektrochemie) en computationele methodes (Monte-Carlo en Dichtheids Functionaal Theorie simulaties), om informatie te verkrijgen over de energie van elektronische toestanden en de dynamiek van ladingstransport, relaxatie en ladingsoverdracht tussen verschillende materialen. Onze resultaten laten effecten zien die tot nu toe nog niet geobserveerd zijn: de overdracht van hete elektronen tussen verschillende kwantum-stip materialen, de bijdrage van een gat aan de uitdoving van optische overgangen in Cd-chalcogenide kwantum-stippen, en de aanwezigheid van een temperatuurs gedeactiveerde mobiliteit voor het hopen van ladingen in films van InP kwantum-stippen. Verder demonstreren we de mogelijkheid om de band-uitlijning in heterojuncties gemaakt van kwantum-stippen aan te passen door de oppervlaktes van de kwantum-stippen met verschillende liganden te passiveren.

Hoofdstuk 1 introduceert het onderzoek en de onderliggende ideeën die door het proefschrift beschreven worden, en beschrijft waar de interesse in nanostructuren en in kwantum-stippen vandaan komt. De elektronische eigenschappen van systemen opgebouwd uit kwantum-stippen, en de daaruit volgende optische eigenschappen, worden afgeleid vanuit een simpel kwantum-mechanisch model. Het hoofdstuk bespreekt vervolgens de invloed van oppervlakte defecten op de optische prestaties van kwantum-stippen, de eigenschappen van heterostructuren van kwantum-stippen en geeft een kader voor de interpretatie van elektron transport in films gemaakt van kwantum-stippen. Als laatste wordt het gebruik van kwantum-stippen voor toepassingen in zonnecellen beschreven, waarbij de processen worden uitgelicht die deze nanodeeltjes een voordeel geven over zonnecellen die gemaakt zijn van bulk materialen.

In hoofdstuk 2 beschrijven we de observatie van de overdracht van 'hete-elektronen' tussen CdSe en PbSe kwantum-stippen, die geassembleerd zijn in een heterojunctie film. We hebben het overdrachtsproces van de elektronen gekarakteriseerd door te kijken naar het uitdoven van optische overgangen in CdSe deeltjes, die plaatsvinden door selectief de PbSe deeltjes in de heterojunctie film aan te slaan. De efficiëntie van het overdrachtsproces is bepaald als functie van de excitatie golflengte, waaruit een interessante toename in efficiëntie is te zien naarmate de overmaat aan energie van de fotonen toeneemt. Dichtheids Functionaal Theorie (DFT) simulaties van een CdSe-PbSe heterojunctie laten de aanwezigheid van gedelocaliseerde elektron toestanden zien, die over de gehele

heterojunctie verspreid zijn. Door middel van tijds-afhankelijke DFT is ook de overdracht van een heet elektron bevestigd, die in een tijdsspan van minder dan een picoseconde tussen de PbSe en CdSe kwantum-stippen plaatsvindt.

In Hoofdstuk 3 laten we het effect zien van verschillende ligand behandelingen op de energetische posities van de banden in CdSe en PbSe kwantum-stippen in een heterojunctie film. De band-uitlijning tussen de twee materialen is bepaald door een combinatie van spectro-elektrochemie en transiente-absorptie metingen. Onze metingen laten zien dat, door de keuze van liganden met verschillende dipool momenten aan de nanodeeltjes te hechten, het mogelijk is om de band-uitlijning te veranderen van een type-I uitlijning, wat ook in bulk varianten van deze materialen te zien is, naar een type-II uitlijning. Transiente absorptie metingen aan een type-II uitgelijnde PbSe-CdSe heterojunctie film laten de aanwezigheid van een hoge dichtheid aan defect-toestanden zien. Deze moeten verzadigd worden om elektron overdracht tussen de PbSe en CdSe lagen te observeren.

In Hoofdstuk 4 hebben we een model ontwikkeld om de Ladings-Vermenigvuldigings (LV) snelheden uit metingen van de LV opbrengst en de ladings relaxatie tijden te halen. Een vereenvoudigd model stond ons toe om een schatting te maken van de LV snelheden, met als input de LV opbrengst en een waarde voor de ladings energie-verlies snelheid (die typisch in de literatuur te vinden is). Het verkrijgen van LV snelheden kan een belangrijke rol spelen in de optimalisatie van het LV proces; materialen kunnen snel gecontroleerd worden om te kijken of ze de juiste eigenschappen voor LV bezitten.

In Hoofdstuk 5 demonstreren we de bijdragen van een 'gat' aan de uitdovingen van optische overgangen in CdSe kwantum-stippen. We hebben de uitdovings dynamiek gemeten na resonante excitatie van de 2S overgang in de CdSe deeltjes, wat leidt tot een elektron aan de conductieband-rand en een heet gat. Terwijl het gat afkoelt naar de de valentieband-rand, observeren we een toename in de uitdoving van de eerste optische overgang in CdSe, die gekwantificeerd is op basis van de theoretisch voorspelde eigenschappen van CdSe deeltjes. Spectroelektrochemische metingen op een film van CdTe kwantum-stippen laten de uitdoving van de eerste optische overgang zien na elektrochemische injectie van gaten. Verder laten we een gebrek aan bijdrage van het gat aan de optische uitdoving zien voor CdSe nanodeeltjes met weinig luminescentie. Dit wordt geassocieerd met zeer efficiënte afvang van gaten door defecten aan het oppervlak van deze nanodeeltjes. Deze bevindingen lossen een langdurig openstaande vraag op in het veld van ultrasnelle spectroscopie aan kwantum-stippen.

In Hoofdstuk 6 gebruiken we een Kinetisch Monte Carlo (KMC) model om de spectrale verschuivingen te verklaren in temperatuurs-afhankelijke transiente absorptie metingen van InP films. Dit stelt ons in staat om de temperatuurs-afhankelijkheid van de mobiliteit van ladingen in deze systemen te meten. Onze resultaten laten zien dat de mobiliteit temperatuurs gedeactiveerd is, in tegenstelling tot voorspellingen uit de Miller-Abrahams beschrijving voor het hopen van ladingen. We hebben de mobiliteit uit het KMC model verkregen door snelheden uit de Miller-Abrahams theorie met die uit de Marcus theorie te vergelijken, waarbij de laatstgenoemde een betere overeenkomst laat zien met de experimentele data. Onze resultaten laten zien dat de Marcus beschrijving voor

het hoppen van lading de temperatuurs-gedeactiveerde mobiliteit in InP systemen kan beschrijven, zonder dat de afstand tussen de deeltjes veranderd of dat er band-transport aanwezig moet zijn.



# List of publications

This thesis was based on the following publications:

Gianluca Grimaldi, Ryan W. Crisp, Stephanie ten Brinck, Felipe Zapata, Michiko van Ouwendorp, Nicolas Renaud, Nicholas Kirkwood, Wiel Evers, Sachin Kinge, Ivan Infante, Laurens D. A. Siebbeles and Arjan J. Houtepen, "Hot-electron transfer in quantum-dot heterojunction films". *Nature Communications*, 2018, 9 (1), 2310.

Frank C. M. Spoor\*, Gianluca Grimaldi\*, Sachin Kinge, Arjan J. Houtepen and Laurens D. A. Siebbeles, "Model To Determine a Distinct Rate Constant for Carrier Multiplication from Experiments". *ACS Applied Energy Materials*, 2019, 2 (1), 721-728.  
(\*shared first authors)

Gianluca Grimaldi, Jaco J. Geuchies, Ward van der Stam, Indy du Fossé, Baldur Brynjarsson, Nicholas Kirkwood, Sachin Kinge, Laurens D.A. Siebbeles and Arjan J. Houtepen, "Spectroscopic Evidence for the Contribution of Holes to the Bleach of Cd-Chalcogenide Quantum Dots". *Nano Letters*, 2019, 19 (5), 3002-3010.

Gianluca Grimaldi, Mark van den Brom, Ryan Crisp, Nicholas Kirkwood, Solrun Gudjonsdottir, Jaco J. Geuchies, Sachin Kinge, Laurens D.A. Siebbeles and Arjan J. Houtepen, "Engineering the band-alignment in QD heterojunction films via ligand exchange". In preparation.

Gianluca Grimaldi, Ryan W. Crisp, Amy van Leiden, Nicholas Kirkwood, Sachin Kinge, Laurens D. A. Siebbeles, and Arjan J. Houtepen, "Kinetic Monte Carlo modelling of temperature dependent spectral diffusion in InP QD films". In preparation.

Other publications:

Jannika Lauth, Gianluca Grimaldi, Sachin Kinge, Arjan J. Houtepen, Laurens D. A. Siebbeles, Marcus Scheele, "Ultrafast Charge Transfer and Upconversion in Zinc beta-Tetraaminophthalocyanine-Functionalized PbS Nanostructures Probed by Transient Absorption Spectroscopy". *Angewandte Chemie International Edition*, 2017, 56 (45), 14061-14065.

Ryan W. Crisp, Gianluca Grimaldi, Luca De Trizio, Wiel H. Evers, Nicholas Kirkwood, Sachin Kinge, Liberato Manna, Laurens D. A. Siebbeles and Arjan J. Houtepen, "Selective antimony reduction initiating the nucleation and growth of InSb quantum dots". *Nanoscale*, 2018, 10 (23), 11110-11116.

---

## List of publications

---

Ryan W. Crisp, Nicholas Kirkwood, Gianluca Grimaldi, Sachin Kinge, Laurens D. A. Siebbeles and Arjan J. Houtepen, "Highly Photoconductive InP Quantum Dots Films and Solar Cells". *ACS Applied Energy Materials*, 2018, 1 (11), 6569-6576.

Ward van der Stam, Indy du Fossé, Gianluca Grimaldi, Julius O. V. Monchen, Nicholas Kirkwood and Arjan J. Houtepen, "Spectroelectrochemical Signatures of Surface Trap Passivation on CdTe Nanocrystals". *Chemistry of Materials*, 2018, 30 (21), 8052-8061.

Frank F. C. Spoor, Gianluca Grimaldi, Christophe Delerue, Wiel H. Evers, Ryan W. Crisp, Pieter Geiregat, Zeger Hens, Arjan J. Houtepen and Laurens D. A. Siebbeles, "Asymmetric Optical Transitions Determine the Onset of Carrier Multiplication in Lead Chalcogenide Quantum Confined and Bulk Crystals". *ACS Nano*, 2018, 12 (5), 4796-4802.

Nicholas Kirkwood, Julius O. V. Monchen, Ryan W. Crisp, Gianluca Grimaldi, Huub A. C. Bergstein, Indy du Fossé, Ward van der Stam, Ivan Infante and Arjan J. Houtepen, "Finding and Fixing Traps in II-VI and III-V Colloidal Quantum Dots: The Importance of Z-Type Ligand Passivation". *Journal of the American Chemical Society*, 2018, 140 (46), 15712-15723.

Ward van der Stam, Gianluca Grimaldi, Jaco Geuchies, Solrun Gudjonsdottir, Pieter T. Uffelen, Mandy van Overeem, Baldur Brynjarsson, Nicholas Kirkwood and Arjan J. Houtepen, "Electrochemical Modulation of the Photophysics of Surface-Localized Trap States in Core/Shell/(Shell) Quantum Dot Films". Submitted.

Ryan W. Crisp, Fatemeh S. M. Hashemi, Jordi Alkemade, Nicholas Kirkwood, Gianluca Grimaldi, Sachin Kinge, Laurens D. A. Siebbeles, Ruud van Ommen and Arjan J. Houtepen, "Atomic Layer Deposition of ZnO on InP Quantum Dot Films for Charge Separation, Stabilization, and Solar Cell Formation". Submitted.

Pieter Geiregat, Ivo Tanghe, Renu Tomar, Shalini Singh, Gianluca Grimaldi, Jorick Maes, Arjan J. Houtepen and Zeger Hens, "Optically Induced Stark Effect and the Exciton Oscillator Strength in quasi-2D Colloidal CdSe Nanoplatelets". In preparation.

---

## List of publications

---



# Acknowledgments

---

I want to start thanking my promotors, Dr. Arjan J. Houtepen and Prof. Laurens D.A. Siebbeles.

**Arjan**, these four years working in your research group have been special to me, largely thanks to the collaborative environment you fostered, your inspiring scientific ambition and your care for the well-being of your PhD and postdocs. You have been an invaluable point of reference for me in these four years, helping me grow scientifically and as a person. Rarely have I left your office without hearing that something could be improved, and just as rarely without hearing an encouragement. Your ability to turn criticism into support, feedbacks into spontaneous enthusiasm reveals how much passion and commitment you put in your work. Our scientific discussions, originating from practical problems and progressing to increasingly abstract territories, were among the most enriching moments of my PhD. Thank you for your guidance, perseverance, and patience (and for your guitar, too!). If it feels sad to part ways, it's because it has been really a tremendous time.

**Laurens**, your deep knowledge and insight were crucial for the completion of my PhD project. You always welcomed my questions with keen curiosity and were remarkably available for impromptu blackboard explanations. I found inspiration in your interest for the meeting point between experiments and theory, and in your careful distinction between what is scientifically novel and what is repackaging of attested science. Furthermore, I think your interest on hearing the issues of PhD students in the OM section, and hearing their feedbacks, was crucial to ensure a good work environment in the section. Thanks for your contribution in this thesis and for your supervision and support.

In my mind, the time in Delft all but coincides with the time spent with dr. Ryan Crisp. **Ryan**, you were there since the very beginning, since a dinner in the only cash-only restaurant in Delft (tough start), in which I hadn't yet heard any of your countless jokes and you hadn't yet heard any of my attempts to translate nonsensical Italian idioms. You were the reassuring presence inside an old chemistry lab (that to a first year PhD student with a physics background looked not entirely different from a graveyard at midnight), mentoring my early attempts at producing quantum dots, while firmly reminding me of the many benefits of not creating explosions. And when a couple of month later, in the new lab (reassuringly different from a graveyard), I didn't feel out of place between fume hoods and gloveboxes, I know it is thanks to the help and inspiration you gave me. In short, I hope you realize you made my PhD-life tremendously easier. But if in the years to come the work-related memories might fade a little (we both know how my memory works!), I'm sure the overflowing amount of memories outside of the lab will more than

---

## Acknowledgement

---

compensate for that. A few examples: from running at night through twisty German streets in the look for an unfindable pub, to my interminable pauses between Blokus moves; long discussions on everything at Salvatore's, half-heartedly refusing a continuous supply of limoncello; rock climbing next to the sea in Sardinia or running to the last train back from Amsterdam on weekends. I know in the future we'll keep adding entries to this list. In the meantime, thanks for everything.

**Nico**, you probably know that you were invaluable for the whole OM section. Coming to scientific questions from a theoretical angle, you nevertheless make it deceptively easy for an experimentalist to follow your reasoning. Thanks a lot for sharing with me your scripts on rate equation modelling, laying the groundwork for the analysis in Chapter 2 and giving me a great example of how to write organized and concise programs. I learnt very quickly to appreciate your balance and your wit, your irony and your understatements. Thanks for teaming up with Ryan in introducing me to rock climbing, and in saving Silvia's hands when they got stuck in the belaying device (and, consequently, my lower body). A big thanks to you and Rianne for inviting us to your beautiful wedding, especially for the snake accident associated, that (with a bit of narrative freedom) makes for a great story of heroism in the face of adversity! I wish the best for both of you!

**Nick** and **Steph**, I don't know when this thesis will make its way to you, but if the Australian custom doesn't stop it (it is, after all, the *fruit* of four years of work) I want you to know that it was terrific to get to know you. As enthusiasm for one's work can at times turn into drudgery, the constant presence of friends like you greatly helped me to look with enthusiasm at the time ahead. Nick, thanks for all your help in the lab, for our strangely satisfying conversations on all the world's problems, and for introducing me to the kiwi accent. I'm jealous for those PhD students in Melbourne getting to work with such a talented scientist, and overall great guy!

**Frank**, thanks for your fundamental contribution in this thesis, in my Transient Absorption training, and in my development as a PhD student. Beside your pungent remarks and automatic one-upmanship (let's not deny it!), you are a great friend, a brilliant scientist, and have always been there for me, in and out of the lab. I had a lot of fun discussing science, chatting about tennis matches, and getting beaten up at pool (with some reservation on this last one). I've learnt a lot from you, and I am not surprised at all by your successful career outside academia, as your limits are only set by how much you want something (and by physical laws, strictly speaking).

**Jannika**, when I came as a freshly started PhD in the postdoc-only office, I must have been at first confused and intimidated, but you were immediately welcoming, to the point that I hardly felt out of place. I liked a lot our chats, in which our good-spirited pessimism made each other laugh. I miss already the tennis matches with you and Ryan, where we might not have excelled in the quality of the shots, but had lots of fun botching them. I'm grateful for our collaboration, for all your suggestions and insights on academia and how to survive it.

**Sólrún**, you have been the smiling center of gravity of our group, encouraging all of us to be more than co-workers. I think the best example of how you try to make everything around you better is my desk plant being still alive, thanks to your periodic watering it (since I regularly forgot to do it). Thanks for all your help with the electrochemical measurements, and all the effort you put in making sure the chemistry lab remains in a functioning state. I had a great time sharing an office with you!

**Ward**, it was a pleasure to work with you. Your extremely specific and rather obscure Italian sentences always manage to get a laugh out of me, and made me wonder how did you manage to learn them in your short stay in Italy. Perhaps it helps that you are extremely bright and sociable! You are competitive out of love for the game, whether it is football, science, or crushing a record of consecutive racket ball passes on the beach (that almost costed you an injury). Thanks for letting me play around with the modeling of your amazing electrochemistry data, I enjoyed our collaboration and had a great time with you!

**Hamit**, thanks for the numerous lunch together, evidence of our shared Mediterranean inclination for good (or decent) food, good conversation, a certain lack of planning, and a moderate dose of financial irresponsibility. I really appreciate your ability to go out of your way to help a friend, and your humility in front of criticism. I did *not* appreciate the cheering against Federer at the tennis tournament, who does that?! It was great to be colleagues, and I wish you all the best for the lunches to come!

**Jaco**, we started casually chatting about data and theory, and before we knew it we had something interesting to say about “rude” excitations in Quantum Dots (the... *band edge* holes). The work in Chapter 5 would not be there without your amazing input, your help and your encouragement. I cannot say I was surprised though, since great things happens around you and you manage to get the best out of people. If it wasn't for your charisma, there would hardly be a Jogging And Chat Organization (and it would likely have another name). Nor would I have accepted to run at midnight through a (surprisingly) hilly part of the Netherlands. Beside your ability to guilt-trip people into outdoor activities, you are a catalyst for good time in the lab and outside. Thanks for all the pictures of laser-shooting cats!

I want to extend my gratitude to all of the people in the OM group, for the amazing experience I had working with all of you! **Kevin, Maria, Magnus, Prashant, Silke, Alexander, Natalie, Francesca, Aditya, Cancel, Dengyang, Sourav, Michele, Deepika, Indy, Jence, Valentina, Maryam**, I'm proud of having been part of this group! Thanks to **Ferdinand** and **Tom** for their precious feedback in group meetings and presentations.

---

## Acknowledgement

---

My gratitude goes to **Wiel** and **Jos**, without you everything I've done in my PhD outside of my office would have been impossible. Thanks for your invaluable help in the lab, and for being always approachable.

**Emanuele**, although it feels like I have always known you, it wasn't long time ago that we were just perplexed Bachelor students in Palermo, a bit skeptical about the possibilities ahead of us. Even though we went separate ways early on, meeting again always brought me back to those months of exams stretching across the Sicilian summer, a sense of fellowship between two people walking together a stretch of road. You discovered first the perks of this low-lying country, and you are one of the main reasons I came to the Netherlands, suggesting I should check out the Quantum Dot research-group in Delft. A big thanks for that (except for those weeks of uninterrupted rain, those are hard to love). I'm continuously impressed by your ability to fully engage in your research and in your free time, by your quiet ambition and by your intelligence, allowing it to convert your dreams into solid reality. You've been always an inspiration to me, and will continue to be one wherever our respective paths will lead us.

Thanks to all my table tennis teammates, **Jeroen**, **Samenda** and **Max**. Thanks for including me in your team and making me feel part of it. Although my Dutch conversational skills didn't extend much further than "ja" and "precies", although I might have been somewhat "hot-headed" during matches, you were open and supportive. I had a lot of fun skidding on the dusty floor of the Delft gym, and hopefully my outburst provided some entertaining at times!

To **Silvia**, that knows what goes on behind the scenes, with immense gratitude for the camaraderie, the chatter and the silence, the collaborative drafting of a vocabulary of two, the meticulous charting and the uncertain exploration of our shared territory. In the ebbs and flows of these four years, the current keeps washing us up on the same sheltered shore. We take our time, we sip a long, lazy, Saturday breakfast, and off we go again, in the current.

To my **brother**, always heading for the shortest path to the core of things, for our conversations inadvertently spilling into the night and the morning, enthusiastic attempts to find truth while sitting at a table, half asleep.

To my **father** and my **mother**, whose actions, inactions, interests, distastes, set me rolling down this slope, whether knowingly or not. Thanks for your support, like a discrete humming sound in the background, ineffable but clear, subdued but ubiquitous, hushed enough to not claim attention to itself, and yet present. You taught me how to think and how to laugh, when to take the world with a frown and when with a smile, sheltered me gently and patiently. These lines are a short attempt to try to break through the curtains of

---

## Acknowledgement

---

self-irony and circumspection, to deliver a simple message: thank you.



# Curriculum Vitae

---

Gianluca was born on April 24th, 1991, in Chicago (USA). He obtained his Bachelor Degree in Physics at the University of Milano-Bicocca (Milan, Italy), in 2012. During his Master Degree studies at the University of Milano-Bicocca, he studied for six months at the Technische Universität München (Munich, Germany) within the Erasmus program. He performed the experimental work for his Master thesis in the Walter Schottky Institute, in Munich, and obtained his Master Degree in 2015.



In October 2015, he started working on the PhD project “Stable and Non-Toxic Nanocrystal Solar Cells” in the Optoelectronic Material section at the Delft University of Technology (TUDelft), under the supervision of dr. Arjan J. Houtepen. In September 2017, he won the Energy & Environmental Science Poster Prize of the nanoGe September Meeting conference.

In his spare time, Gianluca enjoys watching (and discussing) movies and tennis matches. He enjoys running, until his knees allow it, and playing table tennis. He likes reading novels and playing guitar and piano (although rarely and with debatable results).

